ABSTRACT

MOBARREZ, MAZIAR. DC Microgrids: Architectures, Control and Economic Analysis. (Under the direction of Dr. Subhashish Bhattacharya.)

In existing AC PV systems, PV generates DC voltage, this DC voltage is inverted to AC through a grid-tied inverter and on the load side the AC voltage is converted to DC once again. This AC power system requires two energy conversion steps, DC/AC conversion at the PV side and AC/DC conversion at the DC load side. Approximately 10% of PV generation is lost in these conversion steps. Renewable energy resources like solar and fuel cells generate DC power, on the other hand a large and increasing portion of loads use DC voltage internally such as LED lights, VFDs, battery chargers, and power supplies. There is a possibility to eliminate the costly and inefficient power inverters and install a DC network linking DC loads to the DC sources. DC microgrids and DC distribution power systems offer efficiency improvement, higher reliability better expandability and stability over their equivalent AC systems.

The aim of this work is to accelerate the deployment of DC systems by quantifying the benefits of DC systems compared to AC ,removing the technical barriers and addressing the issues related to safety and protection.

First, the two most popular architectures of DC microgrids are presented and the pros and cons of each configuration are discussed. Then, an emerging architecture for PV plus storage DC microgrids for commercial buildings is studied, which provides power to the DC loads from a local PV source without the need for a dedicated PV Maximum Power Point Tracking inverter or DC/DC converter. Moreover, control and topologies of DC microgrid's individual components including: DC/DC and AC/DC converters are discussed. Finally, three possible power balancing strategies for DC microgrids including: centralized,

distributed and distributed with higher level of supervision are explained.

Also, a comparative study between AC PV systems and a specific architecture of DC PV systems are presented. The study examines the DC system energy performance in different locations across the U.S. for several commercial building types and operating profiles. The results from this comparative study are expanded to the generic DC systems.

DC microgrid control algorithm has to maintain stable power balance between generation and consumption. While ensuring power balance, the control algorithm should also control power sharing among sources and allow for multiple slack sources for redundancy Also it should be able to reliably mitigate the impact of PV and load variations in the microgrid from transferring to the AC power grid, when the microgrid is interacting with the main AC grid. This work introduces two power balancing methods that satisfies the requirements mentioned above. Then, the feasibility and effectiveness of the proposed strategies are verified in either lab scale system setup or using control hardware-in-the-loop simulations.

One of the purposes of this work is to quantitatively examine the stability and performance of the DC system. For the mentioned purpose, the model of the DC system including: all the components and their controllers are described in terms of mathematical models. Then, the mathematical model is used to properly set the response time of the components controller to ensure stability of the system in all different operation modes.

One of the limitations in using DC networks is the issues related to the current-limiting devices and circuit breakers. In this work, six configurations of DC circuit breakers from three categories are evaluated and the results are compared in terms of the time required by the breakers to interrupt the fault current, maximum DC breaking current, rated voltage, efficiency and current state of development. These six configurations include solid state circuit breaker, hybrid solid state circuit breaker with mechanical dis-connector, hybrid solid state circuit breaker with fast mechanical switch, mechanical circuit breaker with LC

resonance path and a hybrid fault current limiting circuit breaker. Also a control approach for protection of voltage source converters when the fault happens at close to the converter's terminal is proposed. In the remainder, we examine the different grounding methods and system architectures and discuss the design trade-offs in terms of safety, reliability, detection, mitigation, noise, and cost. Moreover, impedance grounding, isolation, and bi-polar architectures are examined and their benefits with respect to these criteria are discussed.

DC Microgrids: Architectures, Control and Economic Analysis

by
Maziar Mobarrez

A dissertation submitted to the Graduate Faculty of
North Carolina State University
in partial fulfillment of the
requirements for the Degree of
Doctor of Philosophy

Electrical Engineering

Raleigh, North Carolina

2018

APPROVED BY:

Dr. Mesut Baran	Dr. David Lubkeman
Dr. Xiangwu Zhang	Dr. Daniel J. Fregosi External Member

Dr. Subhashish Bhattacharya
Chair of Advisory Committee

DEDICATION

To my family members Alireza Mobarrez, Mitra Rezaei and Niloufar Mobarrez for their unconditional love and support.

BIOGRAPHY

Maziar Mobarrez was born in Tehran, Iran, in 1987 and grew up in Sari, Iran. He received his B.Sc. and M.Sc. degrees both in electrical engineering from K. N. Toosi University of Technology, Tehran, Iran in 2010 and Chalmers University of Technology, Gothenburg, Sweden in 2012, respectively. He is currently pursuing his Ph.D. in power electronics at North Carolina State University, FREEDM Systems Center, Raleigh, NC, USA. He worked as graduate industrial trainee at Robert Bosch LLC, Building Grid Technology (BGT) division between 2015 and 2017, where he was involved in developing world's first commercial DC microgrid for commercial buildings. His research interests are applications of power electronics in power system, AC and DC Microgrids, DC Circuit Breakers and wide bandgap devices. Maziar will begin working for the U.S. ABB Corporate Research Center in Raleigh, NC.

ACKNOWLEDGEMENTS

This work has been carried out at the Department of Electrical and Computer Engineering at North Carolina State University, Future Renewable Electric Energy Delivery and Management (FREEDM) Systems center.

First of all, I would like to express my sincere appreciation to my advisor, Prof. Subhashish Bhattacharya, for his trust in me, his constant support and encouragement. He taught me how to think independently and overcome obstacles. I hope to be privileged to benefit from his mentorship and collaboration throughout my future career.

I am grateful to my committee members, Prof. Mesut Baran, Dr. David Lubkeman, Dr. Daniel Fregosi, Dr. Sudipta Chakraborty and Dr. Xiangwu Zhang for their valuable suggestions and helps.

A very special thank to my Bosch colleague, mentor and friend, Dr. Daniel Fregosi for his constant support, availability and great discussions.

It has been a great pleasure to work at the FREEDM Systems Center. Thanks to all the students, employees and staff at the center for making my thesis work a pleasant stay. I would like to thank my colleagues Dr. Mohammad Etemadrezaei, Dr. Mahsa Kashani, Dr. Maziar Vanouni, Dr. Jiahong Yan, Dr. Sarah Hambridge, Dr. Nima Yousefpoor, Dr. Saman Babei, Dr. Ghazal Falahi, Dr. Govind Chavan, Mr. Adam Morgan, Mr. Sayan Acharya, Mr. Anup Anurag, Mr. Rushikesh Agashe, Mr. Alireza Afiat Milani, Mr. Alireza Dayerizadeh, Mrs. Niloofar Ghanbari and many others.

I would like to thank my true friends for standing by my side in happiness and sadness: Sina Larimian, Vahid Zarandi, Atefeh Morsali, Mohammadreza Sadeghi, Sebo Avedian, Ebrahim Ghazisaeedi, Hani Vahedi, Kayvan Mojtahedzadeh, Hossein Zarrini, Hessam Khorasani, Sohrab Mikanik, Omid Rostamian and Leila Cotrone.

Finally, I would like to express my deepest gratitude from all my heart to my parents and my sister for their endless love, continuous support, and inspiration.

TABLE OF CONTENTS

LIST OF TABLES

LIST OF FIGURES

CHAPTER

1

INTRODUCTION

Climate change is one of the most urgent and complex challenges we face today [1]. Excessive greenhouse gases leading to an enhanced greenhouse effect which warms the planet to a temperature above normal, known as global warming [2]. Majority of the climate scientists agree that greenhouse gas emissions from human activities is the main cause of global warming [3]. Based on the data from United States Environmental Protection Agency (EPA), the primary sources of greenhouse gas emissions in the U.S. are electricity production, transportation, industry, commercial and residential, agriculture, land use and forestry [4]. The primary greenhouse gas emitted through human activities is carbon dioxide (CO_2). One of the main activities that emits CO_2, is the combustion of fossil fuels to generate electricity. According to the EPA's data, electricity itself accounts for about 37% of total U.S.

CO_2 emissions and almost 31% of total U.S. greenhouse gas emissions in 2013 [4]. Primary sources of greenhouse gas emissions in the U.S. and their shares are shown in Figure1.1.

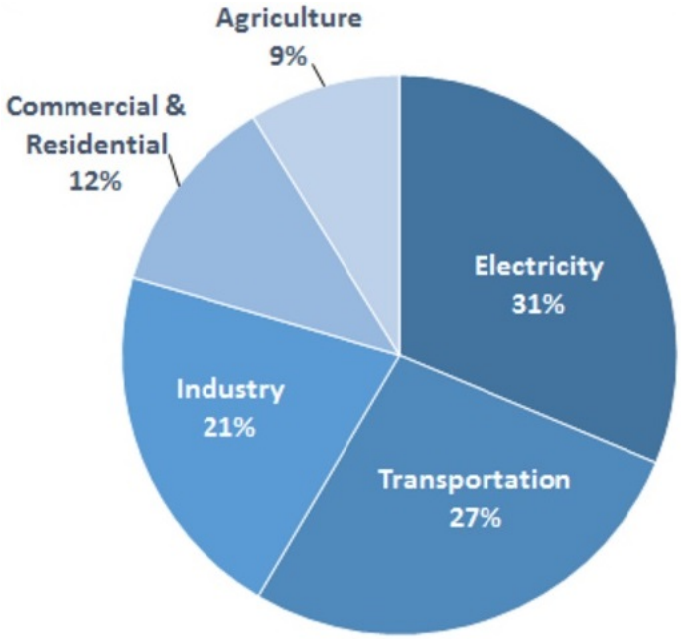

Figure 1.1 Primary sources of greenhouse gas emissions in the U.S. [4].

Therefore, industrial countries have started taking aggressive actions to cut their greenhouse gas emissions to stabilize earth's climate. These actions resulted in high penetration of distributed energy resources, specially from renewable sources like wind and solar, into the power grid [5], [6] and [7]. Wind and solar energy vary based on the availability of wind and sun and therefore, they are referred to as variable generation sources. Besides the variability in wind and solar generation, there are other sources of variation in the power grid like the demand for electricity (load). However, the load variations are better understood than wind and solar variations. Problem arises when the level of power generation and power demand need to be matched. Large-scale deployment of distributed renewable energy has to provide utilities and grid operators the capability to safely and reliably mitigate the impact of

intermittency on the distribution infrastructure. According to National Renewable Energy Laboratory (NREL), most U.S. jurisdictions limit solar photovoltaic (PV) asset penetration to 15% of peak load, after which interconnections are either limited or allowed after an expensive impact study [8]. This requirement limits the amount of distributed renewable energy penetration on the utility grid, impacting the achievement of carbon reduction goals which were discussed earlier. Therefore, there is a common consensus that the power grid needs to be upgraded and modernized to accommodate more renewable sources like wind and solar.

On the other hand, the nation's electricity grid is facing a crisis. It is outdated and its assets are getting aged. A familiar example of such assets are the power transformers which are the key and very robust components of every power systems. It has been reported that the average age of transformers in the U.S. is 40 years although they are made for 30 years of reliable operation [9]. According to U.S. Energy Information Administration (EIA) , there is an increasing trend in power outages from 2008 to 2009 just due to transformer operational mechanism.

All economics and societal progress depends on a reliable and efficient electric grid. Anyone living in North America was certainly aware of, if not affected by, the 14^{th} of August 2003 blackout. The investigation into the blackout shows that the cause was an unfortunate chain of events that disrupted power flow to key areas of load and resulted in confusion over the status of the power delivery network. Electric demand continued, and without an effective way to move power into major metropolitan areas, the system became unstable [10]. The vulnerability of the power grid to the natural disasters has been increasing during the last decade. Natural disasters have severe impact on the supply, generation and delivery of power to large areas of the country due to the interconnected nature of power grid. A recent investigation from Climate Central shows that the majority of power outages and disturbances that occurred between 2003 and 2012, were caused by severe weather

including: storms, hurricanes, heat waves and tornadoes [11]. Figure1.2 shows the number of power outages over a 28 years period.

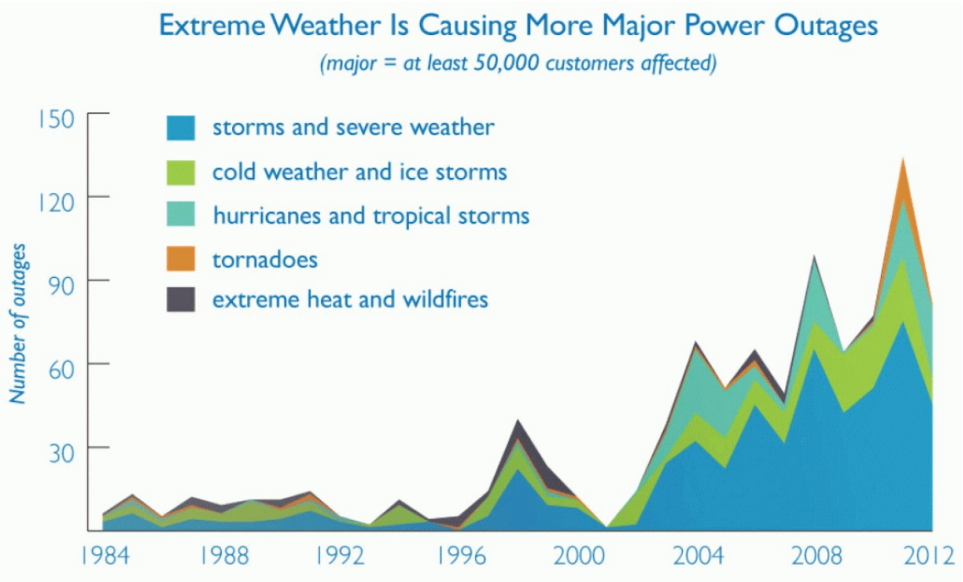

Figure 1.2 Number of major power outages due to the extreme weather and natural disasters [11].

Power outages related to weather, take out between $20 billion to $55 billion annually from the nation's economy. Analysis of industry data found that these storms are a growing threat to, and the leading cause of outages in the U.S. electric grid [12]. The past decade saw power outages related to bad weather increase, which means that the electric grid requires extensive upgrades to effectively and reliably meet the nation's energy demands.

Advances in the power electronics and technology are changing the way electricity is produced, delivered and consumed. To overcome the issues related to high penetration of renewable sources into the grid and the aged grid infrastructure, the future power grid needs to be more decentralized and will be highly relied on dynamically controlled microgrids [13], [14] and [15]. The Microgrid, as defined by the U.S. Department of Energy (DOE) is: "a group of interconnected loads and distributed energy resources (DERs) within clearly defined

electrical boundaries that acts as a single controllable entity with respect to the grid and can connect and disconnect from the grid to enable it to operate in both grid-connected or island mode."[16]. This definition matches with the formal definition developed by the International Council on Large Electric Systems (CIGRE): "Microgrids are electricity distribution systems containing loads and distributed energy resources (such as distributed generators, storage devices or controllable loads) that can be operated in a controlled, coordinated way while connected to the main power network or while islanded." [17].

Microgrids are the key component in the 21st-century smart electric grid envisioned by the DOE Smart Grid Research & Development Program. One of the 2020 goals of the program is to: develop market-deployable advanced electric transmission and distribution technologies and facilitate expansion of the nation's electricity infrastructure capacity, and identify, prioritize, coordinate and improve the protection and restorative capability of national and international critical infrastructure assets and key resources [18]. Utility-interactive microgrids can manage the widespread penetration of renewable energy sources and DERs in the power grid [19] and therefore, have become a widely accepted concept for connecting DERs into the power grid [20].

1.1 State of the Art

Mircrogrid categories and architectures are fluid and they can vary significantly in terms of scale, sources, voltage levels and complexity. Following are four main types of microgrids that currently exist

1. **Campus Microgrids**: Military bases, university or corporate campuses utilize this type of microgrid. And the facility owner owns, maintains and control the microgrid power system. Although, the campus microgrid is connected to the local power grid, but it allows the facility to operate independently in grid outages [21].

2. **Community Microgrids**: This type of microgrid uses the same technology as the *campus microgrid*. However, the utility controls the microgrid and its DERs and it is integrated into utility network rather than located behind the facility's meter.

3. **Islanded Microgrids**: The *islanded or off-grid microgrid* operates independent from the power grid with no connection to the utility. However, they use the same DERs, energy storage units and controllers as utility-interactive microgrids. Their main application is to provide power to remote and isolated areas where the power grid is not available or it does not make economic sense to transmit power to.

4. **Nanogrids**: Some microgrids provide power to a military base or a university campus. But there are microgrids that only serve a single building or a load, they are called *nanogrid* to differentiate them from the microgrids.

Considering the growing interest in microgrid deployment, the research on microgrids gained popularity during the recent years. Following are different aspects of research on microgrids

- Issues related to renewable sources and deployment of Energy Storage Systems (ESS) in microgrids [22], [23] and [24].

- Impact of the microgrids on the performance of power grid including reliability, resiliency and power quality [25], [26] and [27].

- Application of power electronics in microgrids, as various DERs and ESS interact with each other through power electronic converters [28], [29] and [30].

- Microgrid economics and issues related to microgrid scheduling, demand side management (DSM), market pricing, and optimal planning [31], [32] and [33].

- Microgrid operation and control in grid-tied and islanded modes [34], [35] and [36].

- Control of microgrid clusters, where more than one microgrid are interacting with each other and share power among themselves [37], [38] and [39].
- Protection of microgrids including protection of power electronic converters, ground fault protection and etc [40], [41] and [42].

Figure 1.3 show a schematic diagram for a solar plus storage microgrid in which the PV and energy storage systems connect to separate inverters that share a connection to a common AC bus.

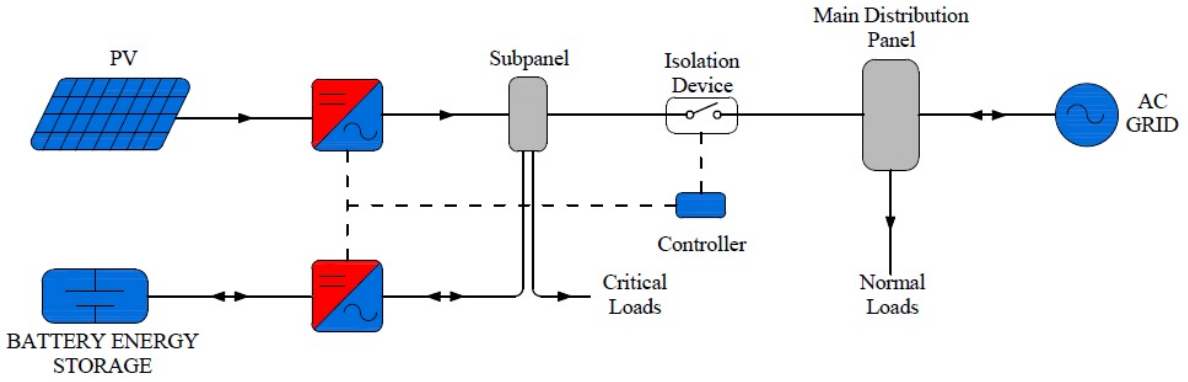

Figure 1.3 Typical configuration of an AC-coupled solar-plus-storage AC microgrid.

Renewable sources like solar and fuel cells generate DC power, on the other hand a large and increasing portion of loads use DC voltage internally like Light Emiting Diodes (LED), Variable Frequency Drives (VFD), battery chargers, and power supplies. There is a possibility to eliminate the costly and inefficient power inverters and install a DC network linking DC loads to the DC sources. Across the world, data centers that are significant users of electricity (2%-3% of total energy usage in the US based on various industry reports) have realized the benefits of using DC and are transitioning to DC power distribution. Figure 1.4 shows the schematic of a typical DC microgrid. As it can be seen, all the loads and sources

are connected to a common DC bus and interacting through DC/DC converters.

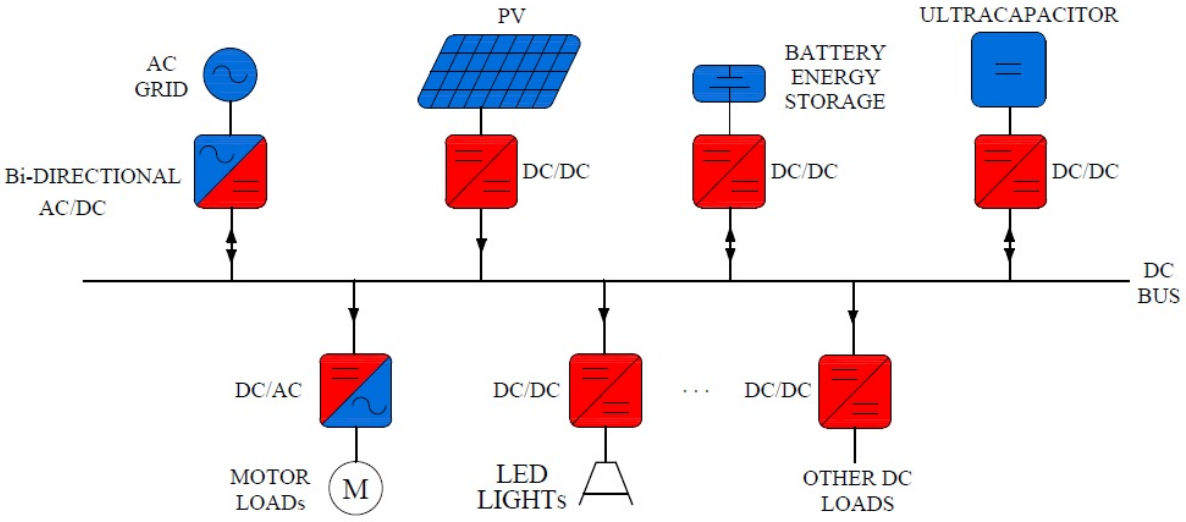

Figure 1.4 Typical configuration of a building scale low voltage (LV) DC Microgrid.

DC Microgrids and distributed generation offer efficiency improvement [43],[44], reliability [45],[46],[47],[48], better expandability [49] and stability [50],[51] over the conventional AC systems.

The combination of lowering the cost of solar and energy storage, improving the energy efficiencies of the loads and smoothing distributed PV output that is enabled by the DC Microgrid system provides a more attractive economic value proposition for electricity rate payers when compared to existing technologies, and thus promotes the penetration of those technologies to better serve emission reduction goals, and achieve the Zero Net Energy (ZNE) target.

Residential and commercial buildings consume almost 40% of primary energy and approximately 70% of the electricity in the U.S [52]. To achieve net zero energy in these buildings, the adoption of energy efficient loads will reduce the building energy usage by 60 to 70% [53]. And the remaining 30 to 40% must come from on-site renewable energy sources

like wind and solar. The aim of this research is to enable DC microgrids by simplifying project-specific design, installation, and commissioning, allowing designers and installers to unlock the benefits of microgrids for their customers. To ensure reliable and efficient operation of a DC microgrid during fault, it should be equipped with a protection system to detect, isolate and ideally clear the fault in case of emergency. Therefore, another important section of this work is dedicated to overcurrent/ground-fault protection devices/methods and grounding schemes which have not been covered clearly in literature.

platform is designed to

1.2 Outline of the Research

1.2.1 Goals and Objectives

The objective of this project is to explore and validate the efficacy of DC electric power distribution incorporating distributed renewable energy generation (DREG) and battery energy storage systems (BESS). This research employed an interdisciplinary approach incorporating engineering research and technology demonstration to produce the knowledge, tools, and metrics that can be applied to the power grid where this game changing technology can have measurable energy and cost saving impacts.

Goals and objectives of this work can be summarized as following

1. **Investigate the existing and emerging PV plus storage DC microgrid architectures.**
2. **Conduct a comparative study between DC and AC distribution systems.**
3. **Demonstrate improvement in electrical system efficiency in the DC system over a conventional AC design.**

4. **Identify and quantify the economic value of DC microgrids for different types of facilities in various locations.**

5. **Design, modeling and control of a functional and scalable DC distribution system that incorporates energy storage and solar generation.**

6. **Control Hardware-in-the-Loop demonstration of a decentralized power and energy management scheme for DC microgrids to facilitate deployment of DC microgrids.**

7. **Develop mathematical model of the DC distribution system for stability and performance analysis purposes.**

8. **Explore overcurrent protection methods including: mechanical, solid state and hybrid DC circuit breakers and hybrid fault current limiter.**

9. **Design and selection of appropriate grounding schemes for DC systems in terms of safety of personnel and equipment as well as the ability to ride-through the ground fault.**

To fulfill the above objectives, this dissertation is organized as following

- In chapter 2, the two most popular architectures of DC microgrids are presented and the pros and cons of each configuration are discussed. Then, an emerging architecture for PV plus storage DC microgrids for commercial buildings is studied, which provides power to the DC loads from a local PV source without the need for a dedicated PV Maximum Power Point Tracking (MPPT) inverter or DC/DC converter. Moreover, control and topologies of DC microgrid's individual components including: DC/DC and AC/DC converters are discussed. Finally, three possible power balancing strategies for DC microgrids including: centralized, distributed and distributed with higher level of supervision are explained.

- Chapter 3 discusses the benefits and drawbacks of potential DC microgrid relative to their AC counterparts according to the study performed by Los Alamos National Lab study. Then, a comparative study between AC PV systems and a specific architecture of DC PV systems are presented. The study examines the DC system energy performance in different locations across the U.S. for several commercial building types and operating profiles. Later in the chapter, the results from the comparative study are expanded to the generic DC systems.

- DC microgrid control algorithm has to maintain stable power balance between generation and consumption. While ensuring power balance, the control algorithm should also control power sharing among sources and allow for multiple slack sources for redundancy Also it should be able to reliably mitigate the impact of PV and load variations in the microgrid from transferring to the AC power grid, when the microgrid is interacting with the main AC grid. Chapter 4 proposes two power balancing methods that satisfies the requirements mentioned above. Then, the feasibility and effectiveness of the proposed strategies are verified in either lab scale system setup or using control hardware-in-the-loop simulations.

- The purpose of this chapter is to quantitatively examine the stability and performance of the DC microgrid platform developed in Chapter 4. For the mentioned purpose, the model of the DC system including: all the components and their controllers are described in terms of mathematical models. Then, the mathematical model will be used to properly set the response time of the components controller to ensure stability of the system in all different operation modes.

- One of the limitations in using DC networks is the issues related to the current-limiting devices and circuit breakers. In chapter 6, six configurations of DC circuit breakers from three categories are evaluated and the results are compared in terms of the time

required by the breakers to interrupt the fault current, maximum DC breaking current, rated voltage, efficiency and current state of development. These six configurations include solid state circuit breaker, hybrid solid state circuit breaker with mechanical dis-connector, hybrid solid state circuit breaker with fast mechanical switch, mechanical circuit breaker with LC resonance path and a hybrid fault current limiting circuit breaker. Also a control approach for protection of voltage source converters (VSC) when the fault happens at close to the converter's terminal is proposed. In the remainder of this chapter, we examine the different grounding methods and system architectures and discuss the design trade-offs in terms of safety, reliability, detection, mitigation, noise, and cost. Moreover, impedance grounding, isolation, and bi-polar architectures are examined and their benefits with respect to these criteria are discussed.

- Lastly, the thesis is concluded and future work is discussed in chapter 7.

CHAPTER

2

AN OVERVIEW OF ARCHITECTURES AND CONTROL METHODS OF DC MICROGRIDS

2.1 Introduction

Climate change is one of the most urgent and complex challenges we face today [1] and most of the climate scientists agree that greenhouse gas emissions from human activities is the main cause of global warming [4]. The primary greenhouse gas emitted through human activities is CO_2. One of the main activities that emits CO_2 is the combustion of fossil fuels

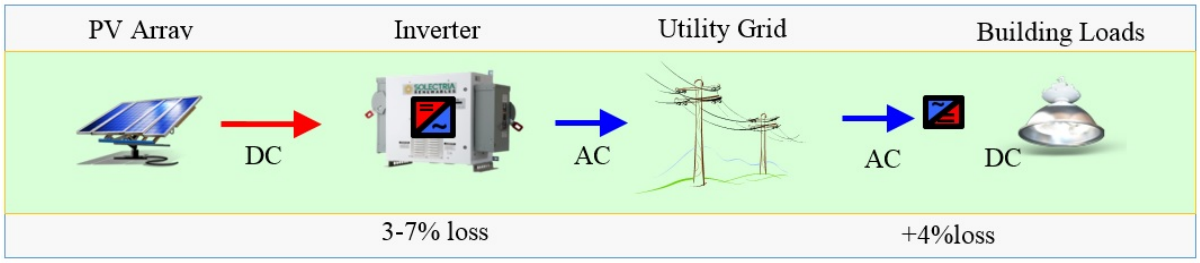

Figure 2.1 Typical configuration of an AC PV system for residential and commercial buildings.

to generate electricity. Based on the data from EPA, electricity accounts for about 37% of total U.S. CO_2 emissions and almost 31% of total U.S. greenhouse gas emissions in 2013 [4]. Therefore, U.S. has started to take aggressive actions, like net-zero energy building, to cut its greenhouse gas emissions to stabilize earth's climate. Residential and commercial buildings consume almost 40% of primary energy and approximately 70% of the electricity in the U.S [52]. To achieve net zero energy in these buildings, the adoption of energy efficient loads will reduce the building energy usage by 60 to 70% [53]. And the remaining 30 to 40% must come from on-site renewable energy sources like wind and solar.

Figure 2.1 shows a typical configuration of the AC PV systems for residential and commercial buildings [54]. PV generates DC voltage, this DC voltage is inverted to AC through a grid-tied inverter and on the load side the AC voltage is converted to DC once again. This AC power system requires two energy conversion steps, DC/AC conversion at the PV side and AC/DC conversion at the DC load side. Approximately 10% of PV generation is lost in these conversion steps [54].

Renewable energy sources like solar and fuel cells generate DC power, on the other hand a large and increasing portion of loads use DC voltage internally such as LED lights, VFDs, battery charge controllers, and power supplies. There is a possibility to eliminate the costly and inefficient power inverters and install a DC network linking DC loads to the DC sources. Across the world, data centers that are significant users of electricity (2%-3% of

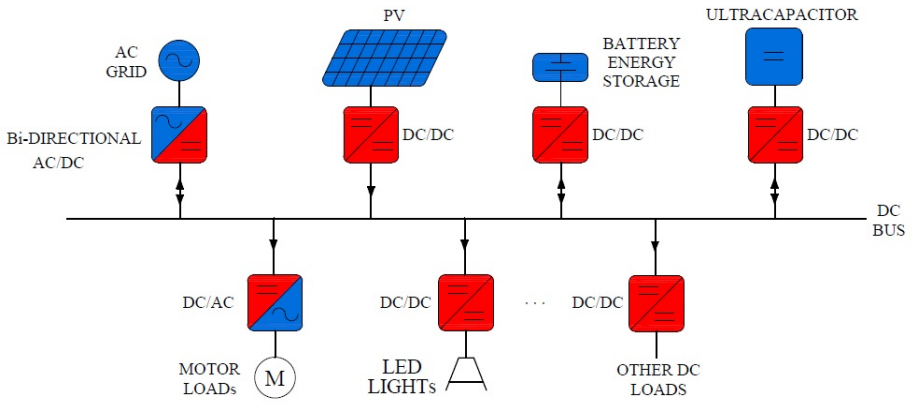

Figure 2.2 Typical configuration of a building scale PV plus battery LV DC microgrid.

total energy usage in the U.S., based on various industry reports) have realized the benefits of using DC and are transitioning to DC power distribution.

DC microgrids and distributed generation offer efficiency improvement [43],[44], reliability [45],[46],[47],[48], better expandability [49] and stability [50],[51] over the equivalent AC systems.

Different configurations of DC microgrids have been widely investigated in the literature, and all agree that DC microgrid is more reliable, more efficient and less costly than the equivalent AC microgrids [55], [56], [57] and [58]. Figure 2.2 shows the typical configuration of a DC microgrid with local PV source and BESS. In this configuration, all the sources and loads are connected to a common DC bus through power converters.

In this chapter, the two most popular architectures of DC microgrids are presented and the pros and cons of each configuration are discussed. Moreover, an emerging architecture for PV plus storage DC microgrids for commercial buildings is studied. Then, control of DC microgrids's individual components including: DC/DC and AC/DC converters are discussed. Finally, three possible power balancing strategies for DC microgrids including: centralized, distributed and distributed with higher level of supervision are explained.

2.2 Architectures of DC Microgrids

A DC microgrid must have multiple terminals, and power converters are generally used to interface individual loads, distributed energy sources and distributed energy storage systems including: PV panels, small wind turbines, fuel cells and micro-turbines, batteries, flywheel and etc. A DC microgrid can have any arbitrary circuit configuration. However, the two most common configurations are **Star** and **Mesh**. The circuit schematic of these two configurations are shown in Figure 2.3 and 2.4. Each of these configurations have their own pros and cons which are discussed in the following.

2.2.1 Star

Star microgrids, shown in Figure 2.3, are the most common type of DC microgrids. In this configuration, all the sources, storage and loads are routed and connected to a common bus. The circuit breaker in each branch, protects that branch against short circuit and overcurrent faults. Star DC microgrid offers advantages such as simple and practical design, low cost and simple protection. On the other hand, this configuration is not fault tolerant, meaning that if a short circuit occurs on the main bus, all the circuit breakers trip and the entire system will be de-energized. The system can only be re-energized when the fault is located and cleared. Similarly, if one line to the ground fault happens on the main bus, all the sources and loads must be disconnected from the main bus to clear the fault which means temporary power outage.

2.2.2 Mesh

It was mentioned earlier that, DC microgrids with star configuration are vulnerable to the faults on main bus and such faults will result in entire shut down of the system. Figure 2.4

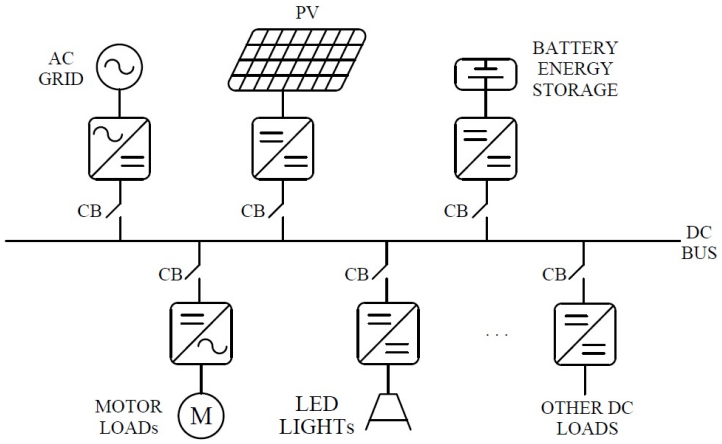

Figure 2.3 Typical DC microgrid with star configuration.

shows mesh (ring-bus) DC microgrid which was proposed to resolve this issue. When a DC fault happens on the main bus, depending on the location of the fault, two circuit breakers will isolate the faulted segment and the system keeps operating. As an example, if fault happens between circuit breaker 1 and 2 (CB1 and CB2), these two circuit breakers will trip and isolate the fault, and they can be re-closed once the fault is cleared. In order to ensure reliable operation of the microgrid under short circuit fault, fast detection, location and isolation of fault is required, otherwise the fault will affect all the sources and loads. In [59], a fault detection and location method is proposed, the proposed method consists of one master controller, two slave controllers, and freewheeling branches between each line and ground. The slave controllers read the current at each end of the bus segment connecting two components and send it to the master controller. They also operate the bidirectional solid-state switches on the bus segment and the freewheeling branch according to the commands from the master controller. In the course of normal operations, the currents measured at each end of the bus segment should be nearly identical and the master controller sends commands to put the bus switches on normal positions. When their input and output current are not identical, a fault is detected and a turn off command

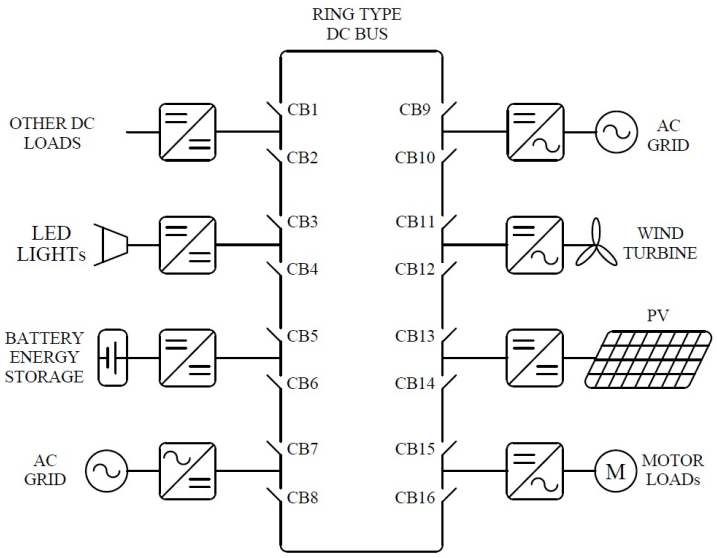

Figure 2.4 Typical DC microgrid with mesh (ring-bus) configuration.

is sent to the corresponding breakers to isolate the fault [59]. Although the mesh type DC microgrid is fault tolerant, but it adds complexity to the design and increases the initial cost and investment. It should be noted that the two discussed configurations are identical in terms of power converter controls and power balancing strategies. In this dissertation, only DC microgrids with star configuration is considered due to the popularity, lower initial investment and simpler protection schemes.

2.2.3 Floating DC Bus Voltage

Typical DC PV systems, as it was shown in Figure 2.2, require two energy conversion steps, DC/DC conversion at PV side for PV MPPT and DC/DC conversion on the load and battery sides. Although the DC/DC converters are generally more efficient than the AC/DC converters, but the PV generation is lost in these two energy conversion steps.

In contrast, Robert Bosch LLC (Bosch) has developed an innovative DC microgrid platform which provides power to the DC loads from a local PV source without the need for

a dedicated PV MPPT inverter or DC/DC converter. The novel DC microgrid platform is designed to maximize the energy efficiency while offering high reliability, redundancy and safety and low cost compared to the equivalent AC and DC microgrids [54]. In this section, system architecture and operation principle of Bosch patented DC microgrid solution are explained. Then, the experimental results from one of the demonstration projects in Charlotte, North Carolina, USA validate the system feasibility. It should be noted that this system architecture falls under the star DC microgrid architecture.

There are two possible configurations of this patented system which are shown in Figure 2.5 and 2.6. Figure 2.5 shows the version that uses PV to power local DC loads while the AC/DC gateway regulates the DC bus voltage by importing power from the grid or exporting power to the grid depending on the solar power output and the load power. The other version as shown in Figure 2.6 benefits from BESS and other types of energy storage systems such as ultracapacitors. This version enable features such as peak shaving, load shifting and can operate in island mode. The concept in both version is to provide power to the DC loads directly from local PV without the need for a dedicated PV MPPT converter. The key feature of these systems is the floating DC bus voltage, which allows the gateway AC/DC to perform MPPT for the PV array by minimizing the power required from the grid. In the first version, the PV source is sized so that the AC/DC gateway is able to regulate the DC bus voltage according to the maximum power voltage of the PV array at all the times. In the second version, unlike the first system, either the AC/DC gateway or BESS charge controller can perform DC bus voltage regulation and track the PV maximum power. A single high efficiency DC/DC conversion between the load and renewable source significantly reduces the power loss, thus improving the overall energy usage of solar energy by 7-10% as compared to the conventional AC systems [54].

The discussed DC system operates at a nominal voltage of $380 V_{dc}$. However, it was mentioned earlier that one of the key features of this system is the floating DC bus voltage,

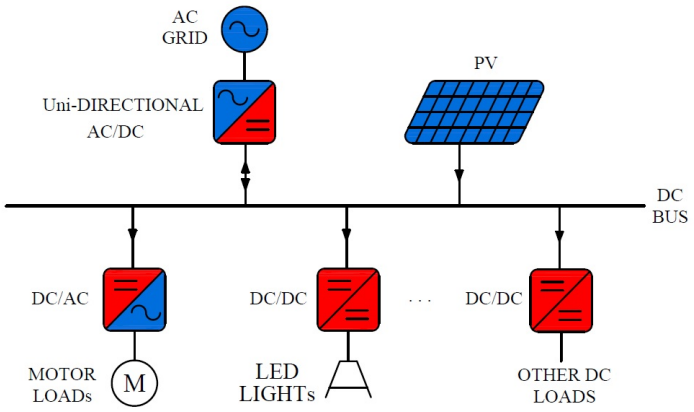

Figure 2.5 Bosch DC PV system architecture (no energy storage).

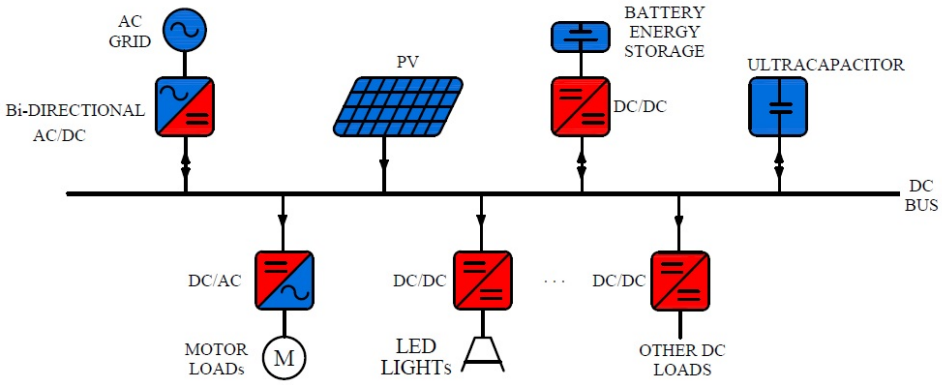

Figure 2.6 Bosch DC microgrid architecture.

which allows the AC/DC gateway or BESS perform MPPT for the PV array.

2.2.3.1 System Implementation

Bosch has tested the feasibility and effectiveness of the proposed DC microgrid platform by several pilot projects in the country. In this part, hardware setup and experimental results from one of the installations located in Charlotte, North Carolina, USA are presented. This system was built to verify and validate the patented DC PV system shown in Figure 2.5. For this project, the PV was sized in such a way that its maximum output power remains always less than the load so that the AC/DC gateway can be unidirectional (rectifier) and

only exports power from the grid .

2.2.3.2 System Overview

The components of the pilot DC system are shown in Figure 2.7. The master controller reads the power measurements and sends the voltage command to the rectifier in order to minimize the power drawn from the grid (MPPT). A $15kW$ rectifier provides the balance of power required to operate the loads and regulates the DC bus voltage based on the command from master controller. Figure 2.7(a) shows $10kW$ of rooftop mounted solar panels and Figure 2.7(b) shows $10kW$ of DC loads including 44 DC high bay LED lights and 4 industrial ceiling fans (to demonstrate the motor load). The $15kW$ rectifier, system management and controller unit and the Combiner and measurement unit are shown in Figure 2.7(c), (d) and (e), respectively.

2.2.3.3 Experimental Results

The experimental results from the system described above are shown in Figure 2.8 and 2.9. Figure 2.8(a) shows the total DC load power over a period of one day in December, when the DC bus voltage is fixed at $380V_{dc}$ with no MPPT controller in the system. Figure 2.8(b) shows the DC bus voltage and the PV output power and the power coming from the grid over a period of one day in December, when the DC bus voltage is fixed at $380V_{dc}$ with no MPPT controller in the system.

Figure 2.9(a) shows the total DC load power over a period of one day in December, when the DC bus voltage is varying to track the maximum power of the PV. Figure 2.9(b) shows the DC bus voltage and the PV output power and the power coming from the grid over a period of one day in December, when the DC bus voltage is varying to track the maximum power of the PV. It can be seen that before $7:30AM$ and after $4:30PM$ when there is no PV generation, the DC bus voltage is fixed at $380V_{dc}$. And between $7:30AM$ and $4:30PM$

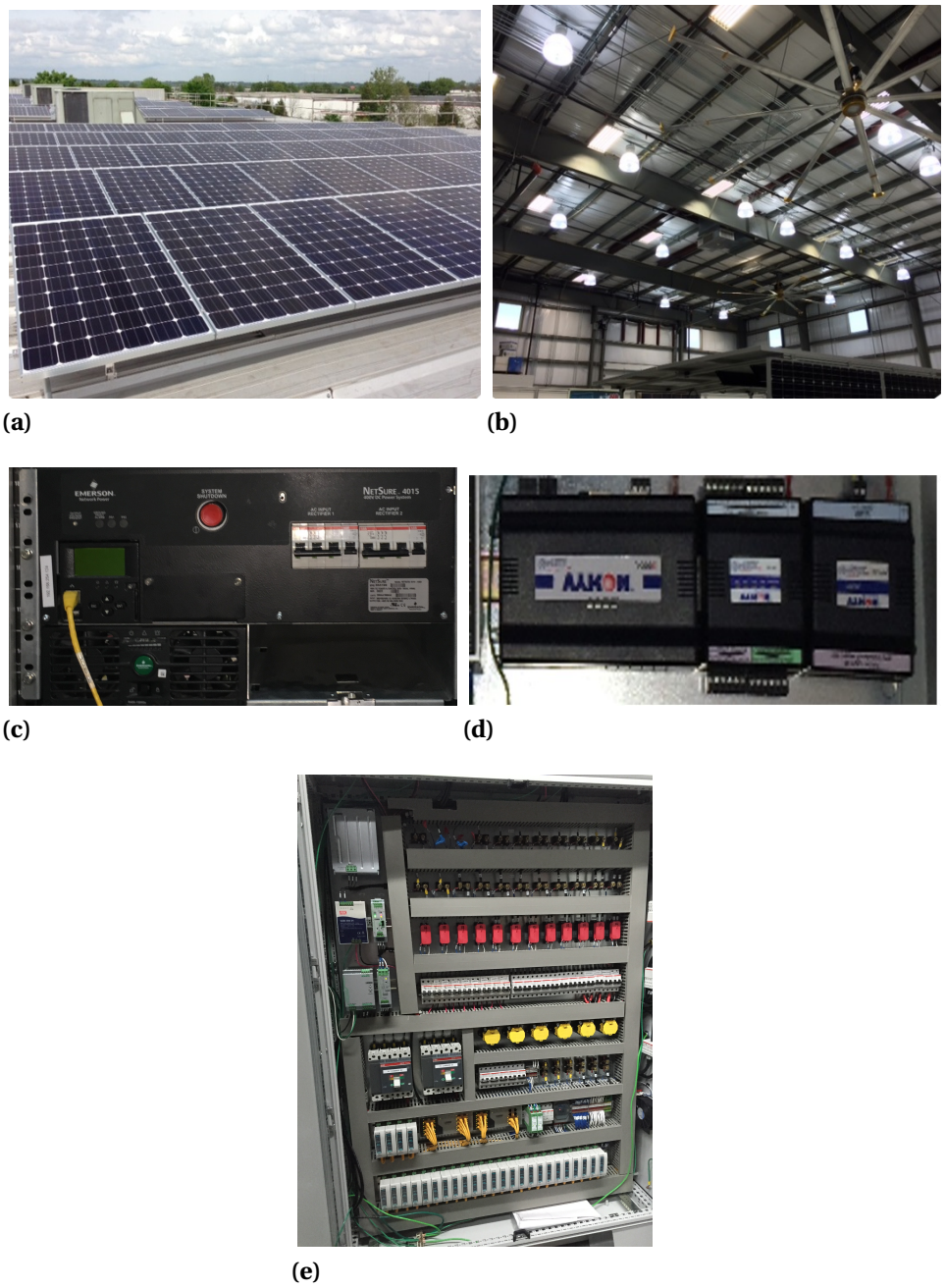

Figure 2.7 Experimental setup for demostrating the unidirectional DC microgrid. (a): $10kW$ of rooftop mounted solar panels. (b): $10kW$ of DC loads including 44 high bay LED lights and 4 industrial ceiling fans. (c): $15kW$ rectifier to provide the required power to the loads. (d): System management and controller unit. (e): Combiner unit, where all the sources and loads connect to the DC bus.

the DC bus voltage is varying to capture the maximum power from PV. The **perturb and observe** algorithm was implemented for performing MPPT. The rectifier changes the bus voltage in order to minimize the power drawn from the grid. It can be seen that the PV generation starts increasing from $7:30AM$ and reaches to its maximum value around $1:00PM$. The sudden drop of PV power from $1:00PM$ is because of the cloudy condition on the day of data collection.

2.3 Power Electronics Converters of DC Microgrids

2.3.1 AC/DC Gateway

Grid interactive DC microgrids require AC/DC gateways to transfer power from or to the AC grid. Especially in the power grids with high penetration of renewable energies, the utility companies require the renewable asset managers to adjust their import or export power according to the utilities's need. Therefore, a well-designed AC/DC gateway with bidirectional power flow capability is required. On the other hand, the AC/DC interface should provide controllable dc-link voltage, high power quality, high transient performance, high efficiency and galvanic isolation to limit the leakage and common mode currents and prevent having current path between the AC grid and microgrid in case of a fault. Although AC/DC converters have been widely investigated in literature, there are a few studies on the suitable AC/DC converters for DC microgrids. In this section, three possible topologies for AC/DC converters are presented and they are compared together. Finally, control method of a three-phase VSC in dq reference frame is explained and the simulation results are presented.

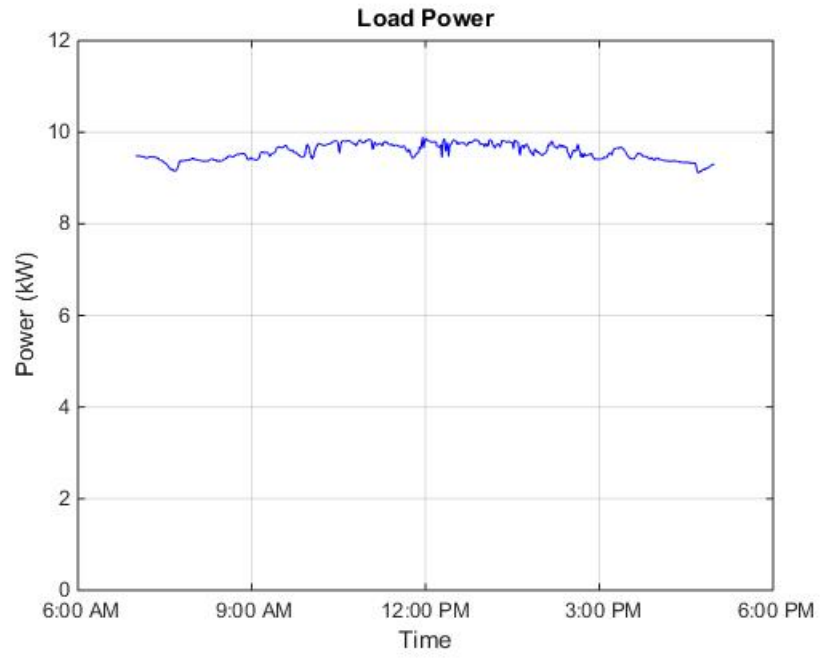

(a)

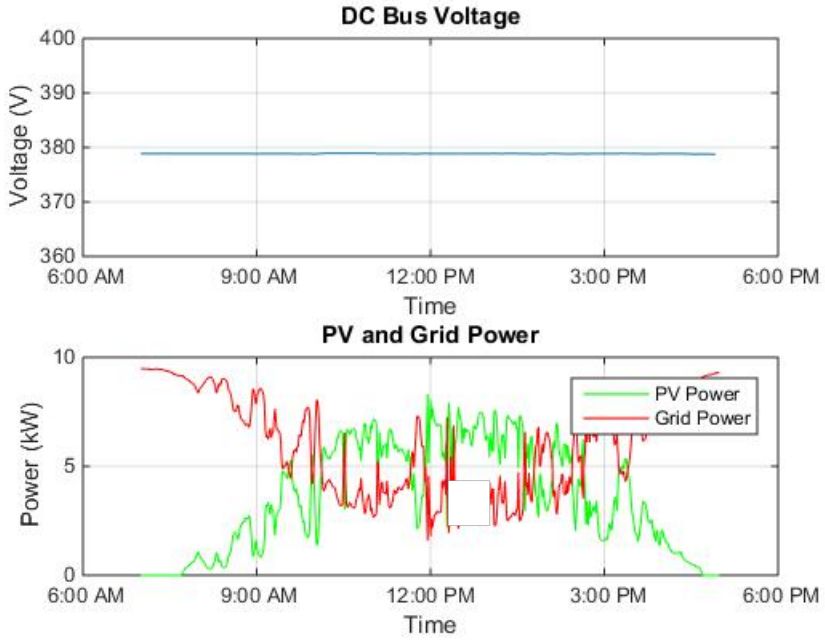

(b)

Figure 2.8 (a): Total DC Load power for a typical day from 7:00AM to 5:00PM when the bus voltage is fixed at $380 V_{dc}$. (b): DC bus voltage (top). PV and Grid power for a typical day from 7:00AM to 5:00PM when the bus voltage is fixed at $380 V_{dc}$ (bottom).

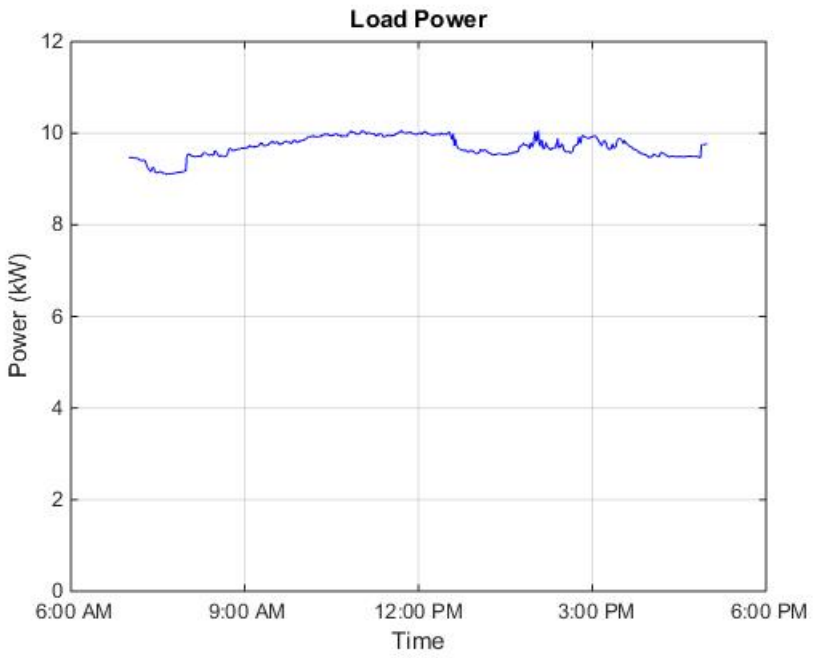

(a)

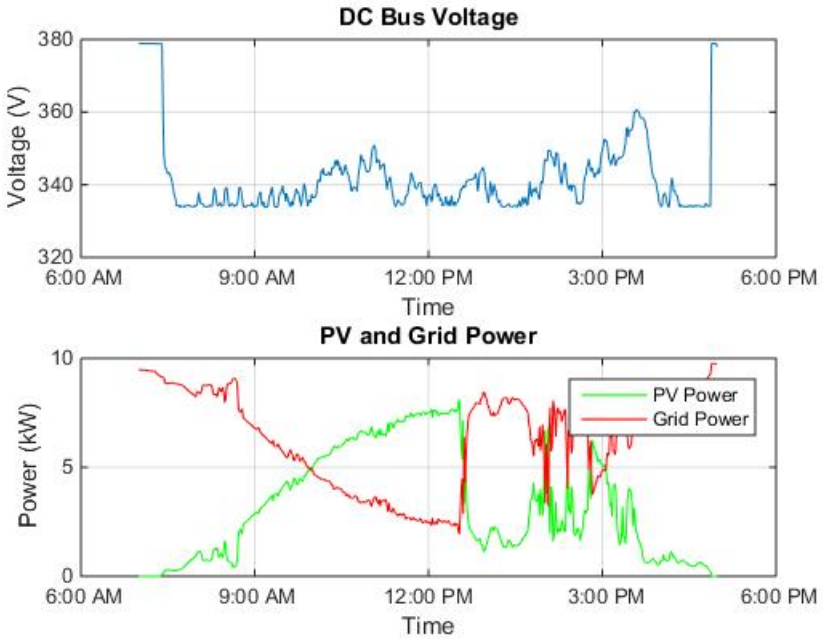

(b)

Figure 2.9 (a): Total DC Load power for a typical day from 7:00AM to 5:00PM when the bus voltage is varying to track the PV maximum power. (b): DC bus voltage (top). PV and Grid power for a typical day from 7:00AM to 5:00PM when the bus voltage is varying to track the PV maximum power (bottom).

2.3.1.1 Three-Phase ,Two-Level VSC

Figure 2.10 shows a three-phase two-level VSC which employs six semiconductor switches, two on each leg. This gives the converter bidirectional power flow capability. However, this topology suffers from high leakage and common mode current/voltage due to the lack of galvanic isolation between the AC and DC grids. Also the minimum DC-link voltage is determined by the AC grid voltage, meaning the DC-link voltage cannot be anything lower than the peak value of the line to line voltage. As an example, if the rectifier is connected to a $3ph$ $480V_{ac}$, the DC-link voltage would be $678V_{dc}$ or higher, this becomes an issue for commercial and residential LV DC microgrids which has DC voltages in order of $380V_{dc}$. A transformer on the AC side can resolve the issues related to the voltage level and leakage current. However, low frequency transformers are bulky and require regular maintenance. Figure 2.11 shows the DC bus voltage and leakage current in a three-phase VSC without isolation transformer (a) and in a three phase VSC with isolation transformer (b). In the test system, the VSC is regulating the DC bus voltage to $800V_{dc}$ and the high resistance midpoint grounding scheme is considered for this simulations. As it can be seen in Figure 2.11(a), although the DC bus voltage (green) does not show any oscillation, but the AC grid oscillation is reflected to the DC bus voltage and negative bus voltage with respect to the ground which causes high leakage current. Figure 2.11(b) shows the same system when an isolation transformer is placed between the converter and the AC grid, it can be observed that the isolation transformer does not let the AC grid oscillations get reflected to the DC side and consequently, also the leakage current is reduced significantly.

2.3.1.2 Three-Phase, Two-Level, Two-Stage VSC

The three-phase VSC discussed in the previous section, has limited output voltage. By adding a buck converter in series with the VSC converter, as shown in Figure 2.12, better

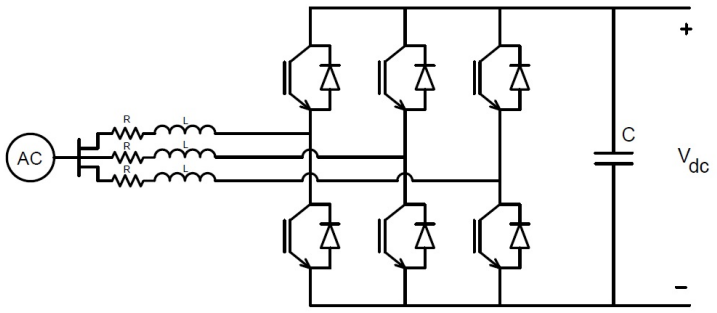

Figure 2.10 Three-phase, two-level VSC.

controllability of the DC bus voltage can be achieved. This configuration still benefits from bidirectional power flow but does not provide galvanic isolation. Moreover, two conversion steps increase the power loss and affects the overall efficiency of the converter.

2.3.1.3 Three-Phase, Two-Level, Two-Stage Isolated VSC

Figure 2.13 shows a three-phase, two-stage VSC with galvanic isolation. This topology consists of a three-phase VSC in series with a dual active bridge (DAB) DC/DC converter. This configuration benefits from bidirectional power flow while offers wide output DC voltage and galvanic isolation. Also since the isolation transformer is a high frequency transformer, does not affect the physical size of the converter. However, the cost and efficiency of this converter is affected by the high number of semiconductor switches.

All the discussed converters are potential candidates for a grid interactive DC microgrids, with different trade-offs between price, efficiency and performance. Depending on the requirements for each application, the appropriate AC/DC converter can be selected.

2.3.2 Control of Three-Phase, Two-Level AC/DC Gateway

In this section, high performance control method of the three phase VSC in dq reference frame is studied and simulation results are presented. The method is based on the transfor-

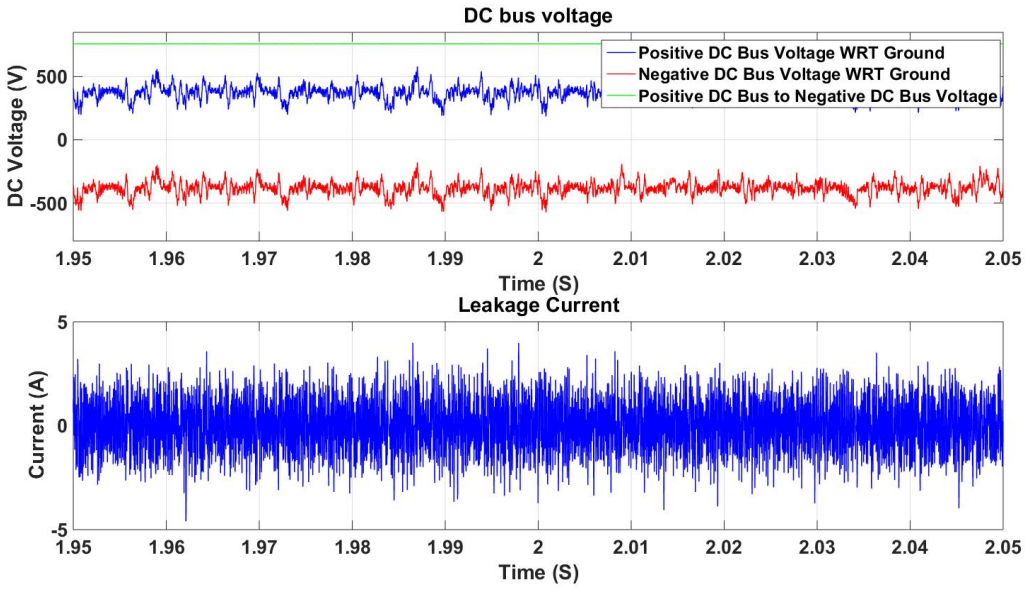

(a)

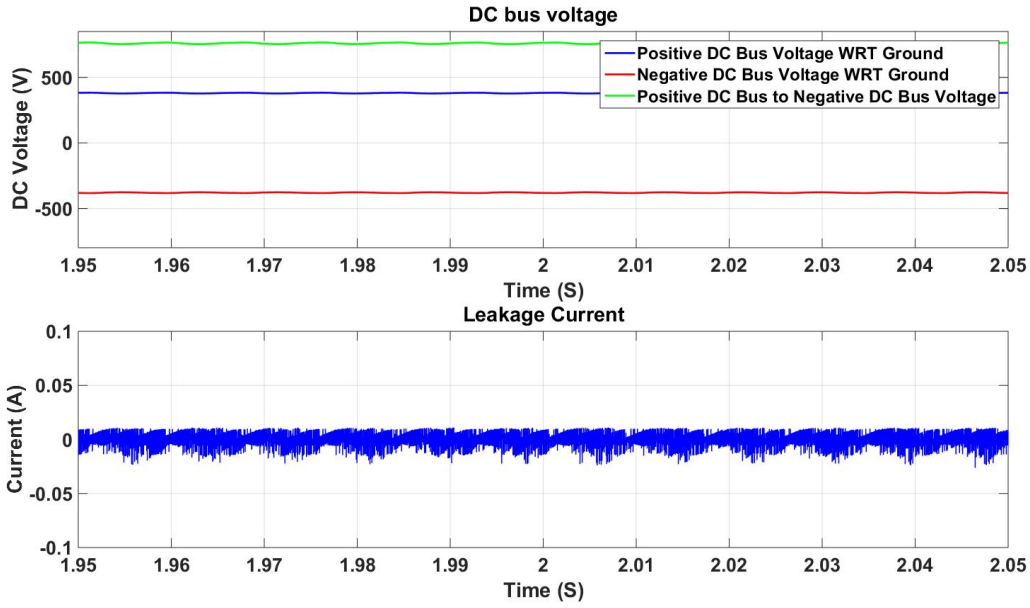

(b)

Figure 2.11 (a): DC bus voltage and leakage current in a non-isolated system. (b): DC bus voltage and leakage current in an isolated system.

mation between stationary coordinates and synchronous rotating coordinates (dq). This strategy guarantees

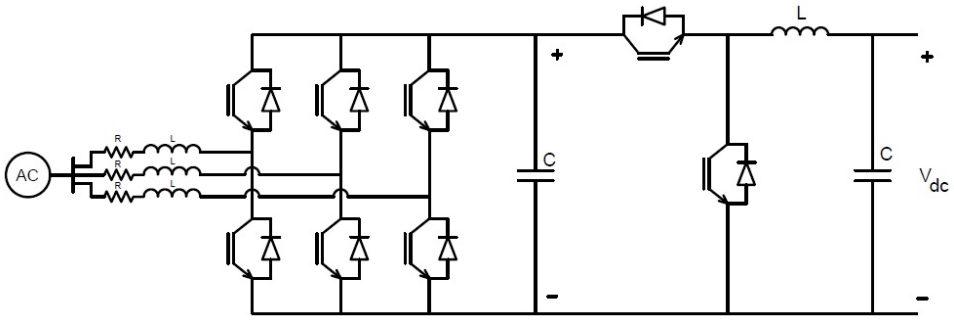

Figure 2.12 Three-phase, two-level, two-stage VSC.

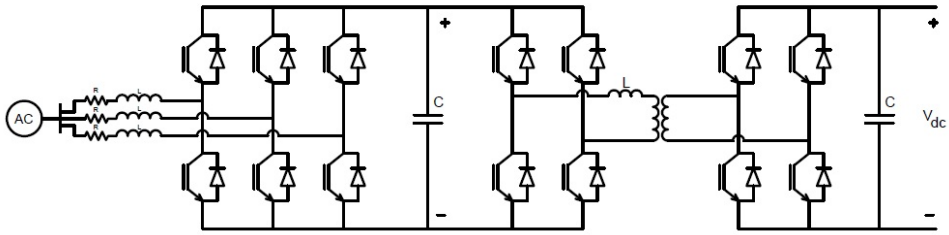

Figure 2.13 Three-phase, two-level, two-stage isolated VSC.

1. Fast transient response.

2. High static performance via internal current control loop.

Consequently, the performance depends on the quality of the current control loop. We can find several strategies that can be applied for current control. A widely used scheme for high performance current control is the dq synchronous controller, where the regulated currents are DC quantities. This eliminates the steady-state errors. Figure 2.14 shows the control scheme of the three-phase VSC in dq reference frame. It should be noted that this control scheme is for controlling the DC bus voltage. However, in many applications, like grid interactive microgrids, the control method should be able to control the active and reactive power that being imported from the grid or exported to the grid. The modified control scheme for this case is shown in Figure 2.15.

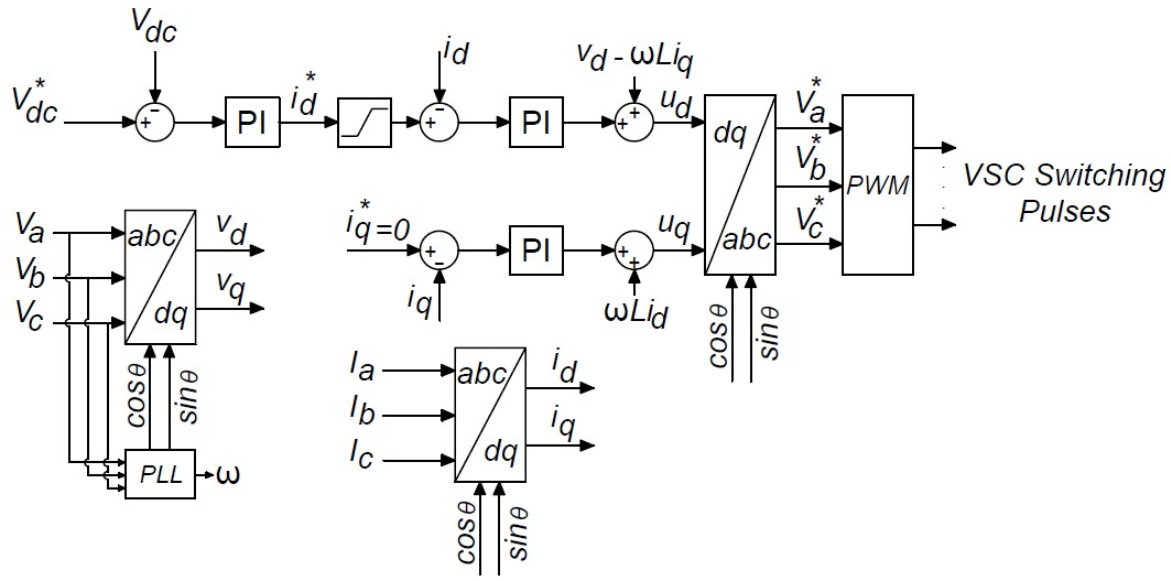

Figure 2.14 Three phase VSC voltage control scheme in dq reference frame.

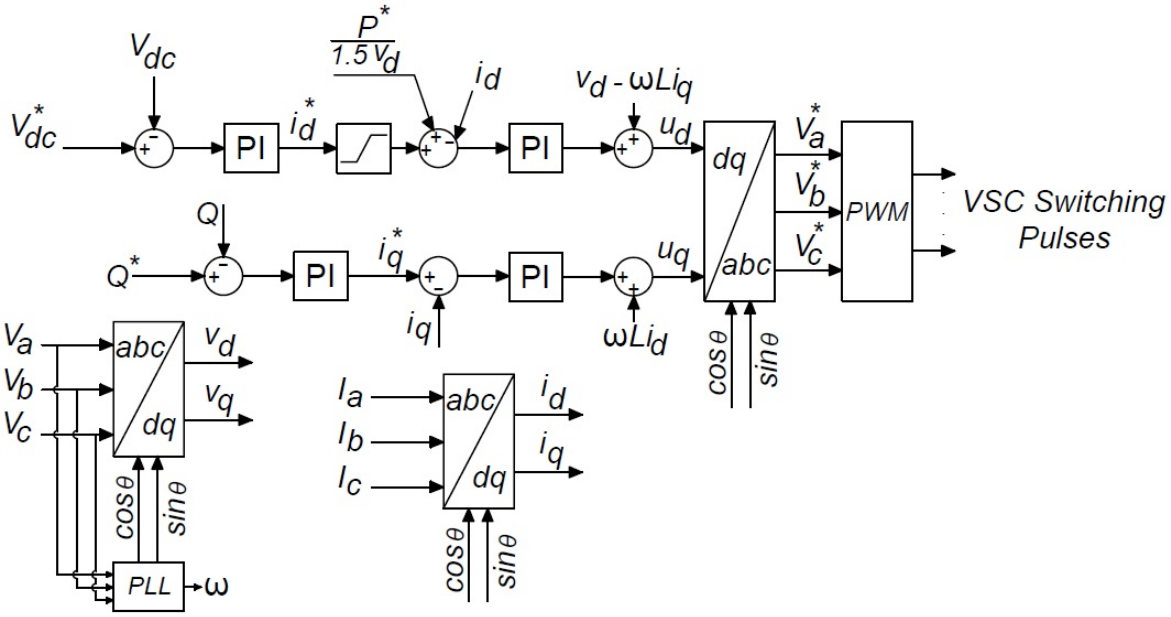

Figure 2.15 Three phase VSC voltage/power control scheme in dq reference frame.

2.3.2.1 Reference Current Calculations

i_d^* and i_q^* can be calculated using the following explanations, these values will be used in the voltage/power control scheme in the dq reference frame discussed earlier. But before that,

the grid voltages and the dq/abc and abc/dq transformation matrices which has been used in this report are explained. The grid voltages has been considered to be sinusoidal as following

$$V_a = V_p sin(\omega t), \quad V_b = V_p sin(\omega t - 120), \quad V_c = V_p sin(\omega t + 120) \tag{2.1}$$

And the transformation from dq to abc reference frame and vice versa are like the following

$$\begin{bmatrix} x_d \\ x_q \\ x_0 \end{bmatrix} = \sqrt{\frac{2}{3}} \begin{bmatrix} sin(\omega t) & sin(\omega t - 120) & sin(\omega t + 120) \\ cos(\omega t) & cos(\omega t - 120) & cos(\omega t + 120) \\ \frac{\sqrt{2}}{2} & \frac{\sqrt{2}}{2} & \frac{\sqrt{2}}{2} \end{bmatrix} \begin{bmatrix} x_a \\ x_b \\ x_c \end{bmatrix} \tag{2.2}$$

$$\begin{bmatrix} x_a \\ x_b \\ x_c \end{bmatrix} = \sqrt{\frac{2}{3}} \begin{bmatrix} sin(\omega t) & cos(\omega t) & \frac{\sqrt{2}}{2} \\ sin(\omega t - 120) & cos(\omega t - 120) & \frac{\sqrt{2}}{2} \\ sin(\omega t + 120) & cos(\omega t + 120) & \frac{\sqrt{2}}{2} \end{bmatrix} \begin{bmatrix} x_d \\ x_q \\ x_0 \end{bmatrix} \tag{2.3}$$

With this definition, d component would be responsible of controlling the active power and q component is responsible for controlling the reactive power.

Since the converter usually work in unity power factor condition, then $Q = 0$ and P =desired value. Therefore, i_q^* is considered to be zero and i_d^* can be calculated as

$$P = \frac{3}{2} V_d I_d \tag{2.4}$$

Table 2.1 Specifications of the modeled three-phase VSC in Matlab/Simulink.

AC system frequency (Hz)	60
AC system line-neutral voltage peak (V)	155
AC system resistance ($m\Omega$)	1
AC system inductance(mH)	1.8
Average DC voltage (V)	700
Switching frequency (kHz)	1.26
DC link capacitance (μF)	500
Active power transfer (kW)	50
Power Factor	1

2.3.2.2 Simulation Results

A three-phase VSC converter with the control scheme discussed earlier is modeled in Matlab/Simulink. The frequency of AC system is $60Hz$, and its line-neutral voltage is $155V$ peak. The converter is controlled by sine-triangle comparison PWM. The triangle frequency is fixed at 21 times the fundamental frequency. The converter is operated so the average real power transferred from grid to the DC loads is $50kW$, and unity power factor operation is considered ($Q = 0$). The system impedance values and specs are shown in Table 2.1.

Since the converter should work in unity power factor condition, then $Q = 0$ and $P = 50kW$. Therefore, i_q^* is considered to be zero and i_d^* can be calculated as

$$P = \frac{3}{2} V_d I_d \tag{2.5}$$

where $P = 50kW$, $V_d = \sqrt{\frac{3}{2}} V_p = 189.83$ and consequently $i_d^* = 263.38$

Also a voltage controller is needed to maintain $700V_{dc}$ on the DC side. The control scheme shown in Figure 2.15 was used for this simulations. The reference values are trans-

formed to the abc reference frame and after normalization are sent to the PWM block to generate the firing pulses for the converter's switches.

Figure 2.16 shows the DC bus reference voltage and the measured voltage. It can be seen that the control regulates the voltage at $700 Vdc$.

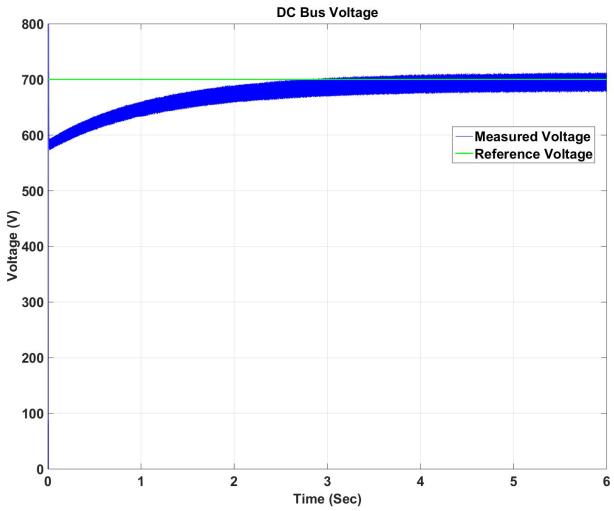

Figure 2.16 Output DC voltage of the three-phase VSC.

Three-phase voltages and currents are shown in Figure 2.17, it can be seen that there is no phase shift between the voltages and currents and the system is working in unity power factor.

Based on the three phase voltage and currents shown in Figure 2.17, the instantaneous real power, $p(t)$ and instantaneous reactive power $q(t)$ are calculated the corresponding DC and AC components are shown in Figure 2.18.

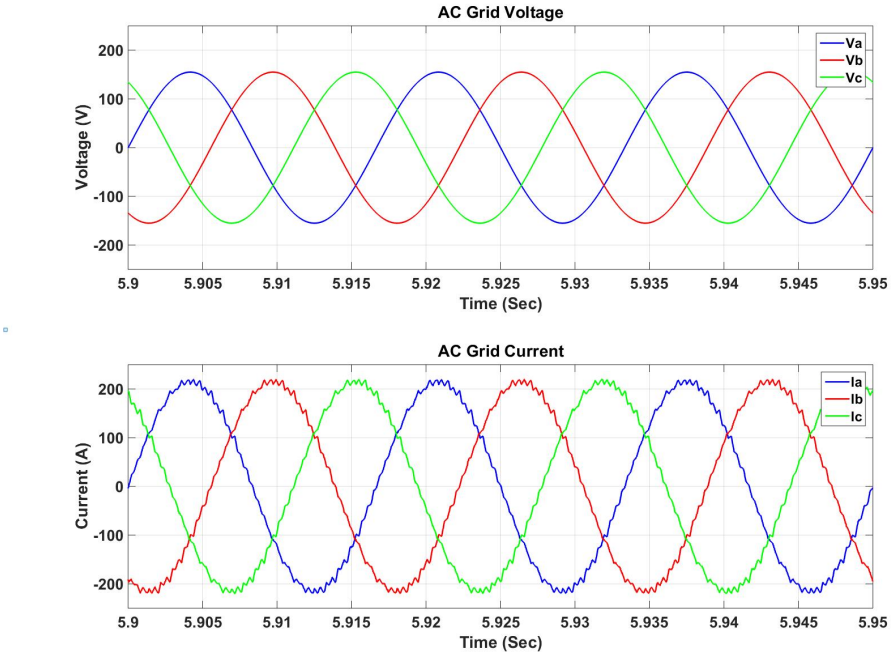

Figure 2.17 AC side voltages and currents of the three-phase VSC.

2.3.3 DC/DC Converters

DC/DC converters are required to link DC sources and DC loads with different voltage levels. Generally, DC/DC converters are more efficient and have simpler topologies compared to the AC/DC converters. Depending on the voltage level of sources and loads, buck, boost, buck-boost converters can be used. These converters can be either isolated such as DAB and flyback converters or they can be non-isolated such as buck, boost and buck-boost [60], [61], [62].

All the DC/DC converters in a DC microgrid are working in either current control mode or voltage control mode. In current control mode, the converter regulates its current to match with the reference current. In this mode, converter is considered as a current source. On the other hand, in voltage control mode, the converter regulates its voltage to match with the reference voltage. Converter is considered as a voltage source in this mode. What

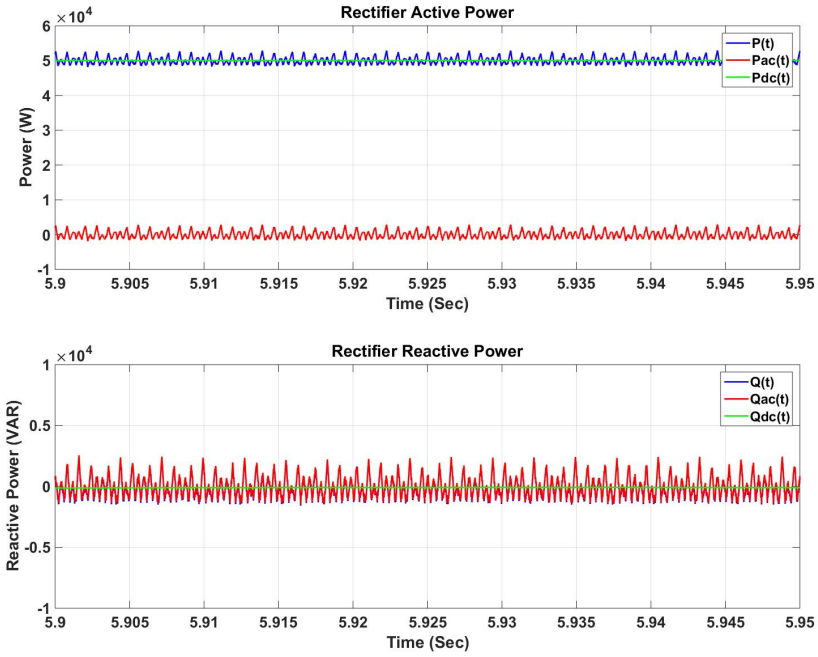

Figure 2.18 Instantaneous active and reactive power of the three-phase VSC.

differentiates between different control methods is the way that reference current or voltage are being calculated.

Figure 2.19(a) shows the current control scheme for a typical DC/DC converter, where the reference current (i^*_{ref}) is compared with the measured current (i_m) and the error goes to a PI controller then the duty cycle for converter switches are determined according to the output of the PI controller. Figure 2.19(b) shows the voltage control scheme for a typical DC/DC converter, where the reference voltage (V^*_{dc}) is compared with the measured voltage (V_{dc}) and the error goes to a PI controller to calculate the reference current (i^*_{ref}), then the reference current goes to a current control loop to determine the duty cycle for the switches.

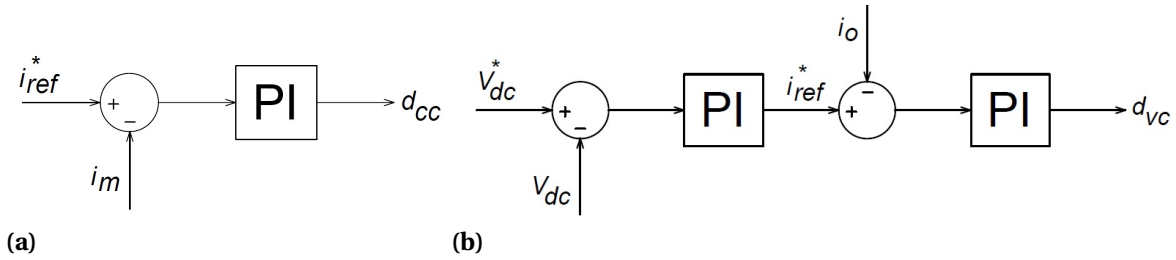

Figure 2.19 (a): Current control scheme of a typical DC/DC converter. (b): Voltage control scheme of a typical DC/DC converter.

2.4 Power Balancing in DC Microgrids

Normally a DC microgrid consists of several DERs, energy storage systems and DC loads which are connected to a common DC bus through power converters. To ensure stable operation of the DC microgrids, the sum of generated power needs to be equal to the power drawn from the common bus. Equation 2.6 shows the power balance between sources and loads. Too much generation will result in overvoltage, and not enough generation causes the DC bus voltage to collapse.

$$P_{Generation} = P_{Consumption} \tag{2.6}$$

Therefore, the controller of a DC microgrid needs to ensure that all the power converters maintain the power balance equation shown in Equation 2.6. There are several possible power balancing strategies which are discussed in the this sections.

Power balancing strategies in a microgrid can be classified as centralized, distributed and distributed with higher level of supervision. Each of these strategies have their own advantages and disadvantages and have their own applications. In the remainder of this section, these three different strategies are explained and their differences are mentioned.

2.4.1 Centralized

In the centralized strategy, all the system information and data are collected by a central controller and the controller makes control decisions such as scheduling tasks [63] [64]. Therefore, there is a need for high speed communication links between each power converter in the system and the master controller. For that reason, this strategy is highly relied on communication links and the master controller, meaning the reliability of the system is related to the reliability of the communication network, and any fault in the communication network will affect the microgrid's operation.

2.4.2 Distributed

The issue related to the communication network which discussed in the previous section, can be avoided by employing distributed power balancing strategy. The most common distributed power balancing strategies fall under voltage droop-based control and current droop-based control or the combination of these two [65], [66]. The current droop-based control is also known as DC bus signaling (DBS). In the distributed power balancing strategies, the power converters operate based on local quantity measurements such as their output voltages or currents.

Figure 2.20 shows the $I-V$ characteristics of two DC/DC converters connected in parallel to a common bus and regulate the bus voltage employing voltage droop control. When two converters are connected in parallel, any voltage difference between the two sources will cause circulating current. In order to reduce the circulating current, we can program a virtual output resistance by using droop control. This concept can be expressed as Equation 2.7.

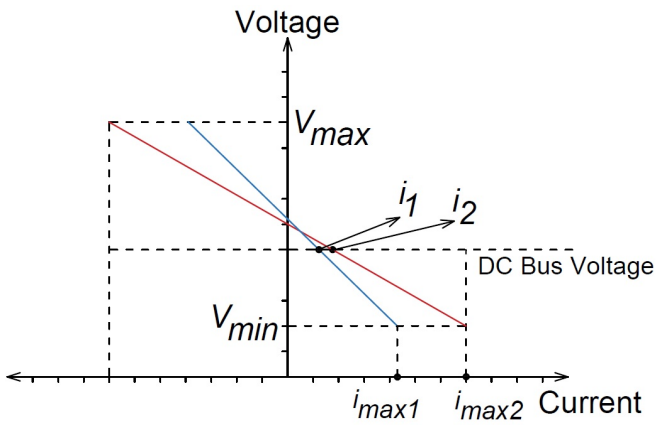

Figure 2.20 Voltage droop characteristics of two DC/DC converters with different droop coefficients.

$$V_{ref} = V_{nominal} - R_d.i_{dc} \tag{2.7}$$

where $V_{nominal}$ is the nominal output voltage of the converter, V_{ref} is the calculated reference output voltage, i_{dc} is the converter's output current and R_d is the virtual resistance or droop coefficient. Also the control block diagram of a voltage droop control is shown in Figure 2.23(a).

In current droop-based control method or DBS, converters sense the bus voltage continuously and set their output current based on the bus voltage. This means that all the systems converter are operating in current control mode unlike the voltage droop control, where the converters were operating in voltage control mode. Figure 2.21 shows the $I-V$ characteristics of two DC/DC converters connected in parallel to a common bus and regulate the bus voltage employing current droop control. In this control method, since all the converters are operating in current control mode, the circulating current issue does not exist. The control block fiagram of a current droop control is shown in Figure 2.23(b). There are two drawbacks associated with this control method. Firstly, the number of sources and

storage (converters) is limited by the number of voltage levels On the other hand, adding sources with higher priority involves changing the states of all other sources with a lower priority, which restrains the realization of "plug and play".

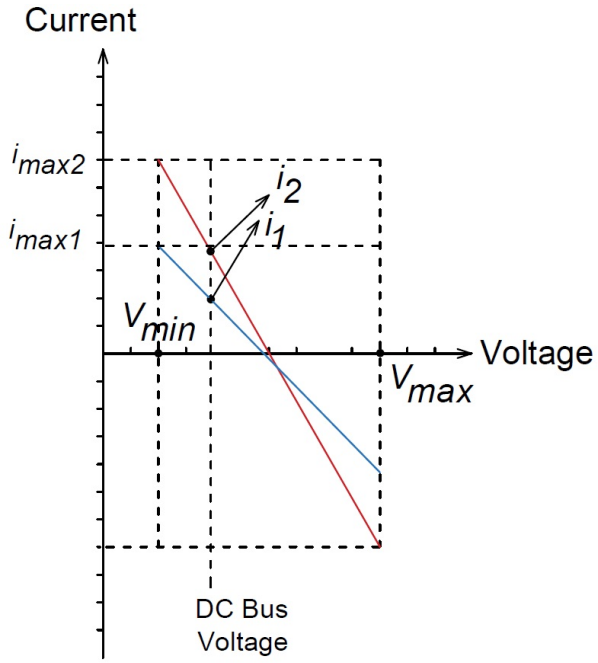

Figure 2.21 Current droop characteristics of two DC/DC converters with different droop coefficients.

As it was mentioned earlier, these two modes can be combined to enable microgrids with features such as islanding, demand response and PV output smoothing. As an example, different voltage levels can be defined to distinguish between different system operation modes. The converters sense the bus voltage continuously and set their operation mode while the amount of power transferred with the microgrid are handled by the voltage droop controller. Figure 2.22 shows $I-V$ characteristics of a bidirectional converter employing voltage and current droop control in a DC microgrid. As it can be seen in the figure, whenever the DC bus voltage is between V_1 and V_2, converter does not exchange any power with

the microgrid. When the bus voltage drops below V_2, converter imports power to the grid according to its voltage droop $I-V$ profile. And when the bus voltage gets higher than V_1, converter exports power to the grid according to its voltage droop $I-V$ profile. Voltage drops and spikes happens due to the change in generation or consumption in a DC microgrid. Obviously, the characteristics of a converter can be set according to its application and the characteristics shown in Figure 2.22 is just an example.

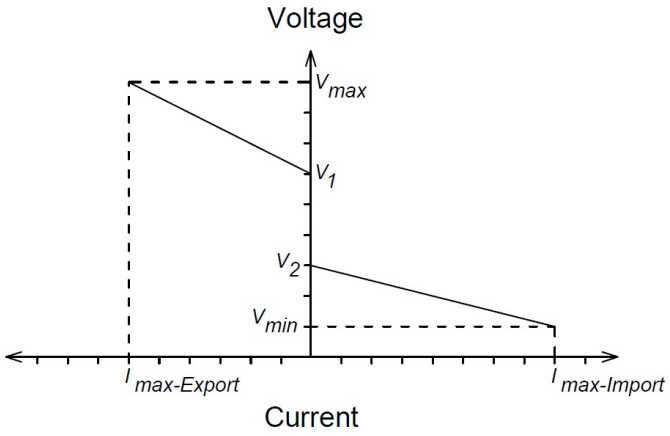

Figure 2.22 $I-V$ characteristics of a bidirectional converter employing a combination of voltage and current droop controls.

A simple DC microgrid has been modeled in Matlab/SIMULINK to demonstrate the feasibility of voltage and current droop control methods. The DC microgrid consists of $18kW$ of solar (6 strings of PV panels, each string with 12 panels in series) which is connected to the DC bus through a MPPT converter. It is assumed that the MPPT converter keeps the solar at its maximum power continuously and works as a variable current source converter. Also there are two voltage source converters, one connecting to the AC grid and one controlling the charge of a battery.

Figure 2.24 shows the results of the mentioned DC microgrid when voltage droop control scheme is implemented. The maximum and minimum DC bus voltage is set to $380V_{dc}$

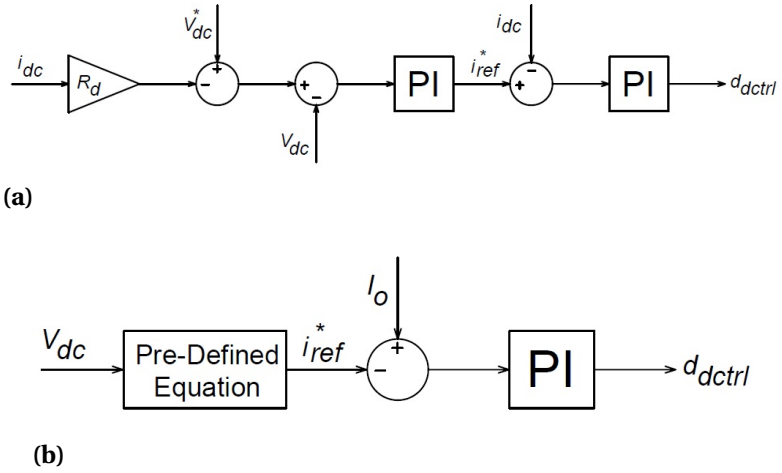

Figure 2.23 (a): Voltage droop control block diagram of a typical DC/DC converter. (b): Current droop control block diagram of a typical DC/DC converter.

and $320 V_{dc}$ respectively. And the maximum current of converter 1 is set to $100A$ and the maximum current of the converter 2 is set to $300A$. These voltage and current values were used to calculate the droop coefficients. As it can be seen in Figure 2.24, the PV power is $7kW$ at the beginning and the two converters regulate the voltage at $332 V_{dc}$ by sharing the current according to their droop slope. At $t = 1s$, the PV output is increased due to the change in the solar irradiance. The converters adjust their power based on the available power and regulate the bus voltage at $344 V_{dc}$.

Figure 2.25 shows the results of the DC microgrid when current droop control scheme is implemented. In this simulations, both converters sense the bus voltage all the time and set their current reference according to a predefined equation. Initially, the DC bus voltage is $350 V_{dc}$ and the converters are drawing $50A$ and $25A$ respectively. When the bus voltage increases (this can be because of change in the generation), converters change their power based on the new value of the DC bus voltage.

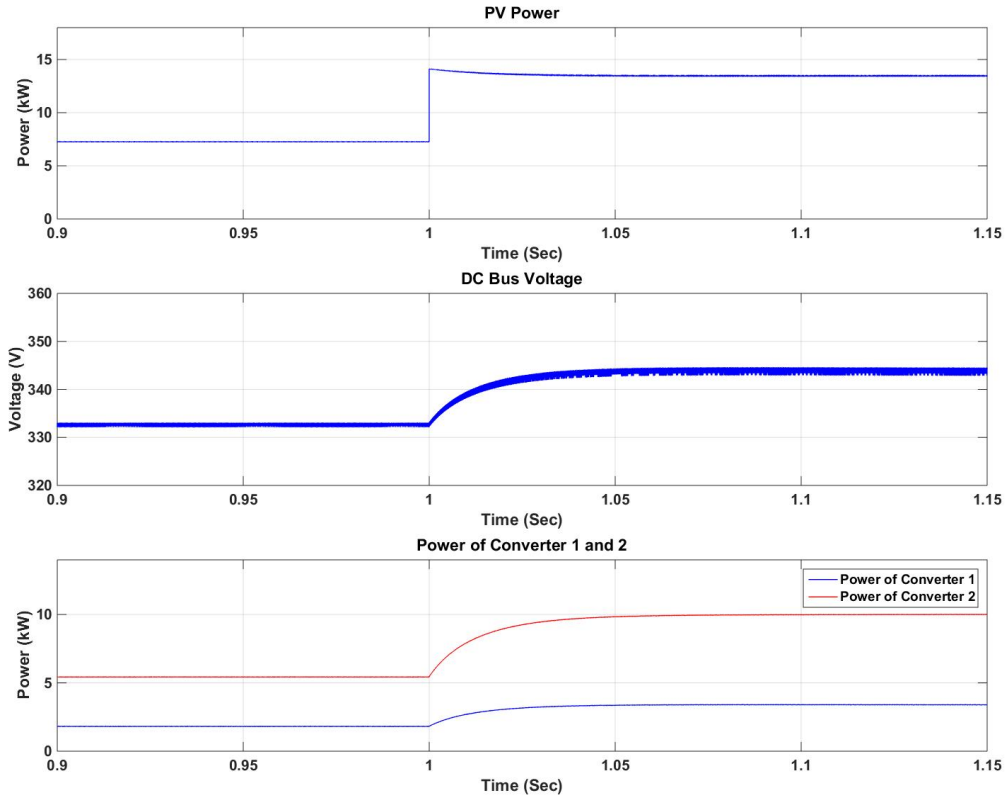

Figure 2.24 PV power (top). DC bus voltage (middle) and power change of two paralleled voltage droop controlled DC/DC converter with change in PV power (bottom).

2.4.3 Distributed with Higher Level of Supervision

The droop control methods discussed in the previous section has two major drawbacks. On one hand, due to the practical limitations, the nominal voltage of different power converters in the system are not exactly equal. Even a small error in nominal voltages will result in significant deviation of current from their required values. To illustrate this issue, the droop characteristic of two paralleled converters in a DC microgrid are shown in Figure 2.26. The two converters have the same droop coefficients. However, due to the voltage sensing, there is an error between the nominal voltages. It can be seen that this small error causes

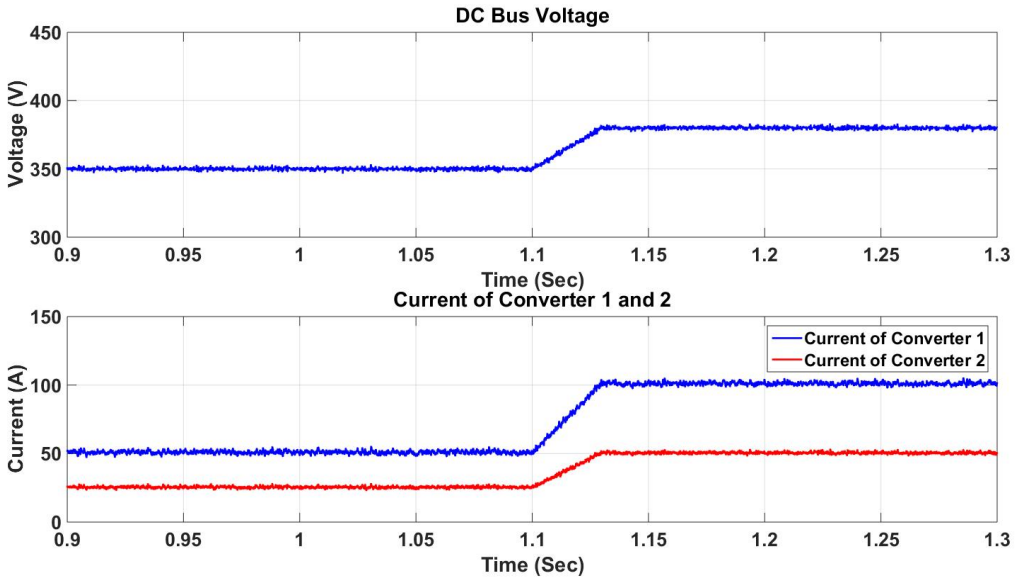

(a)

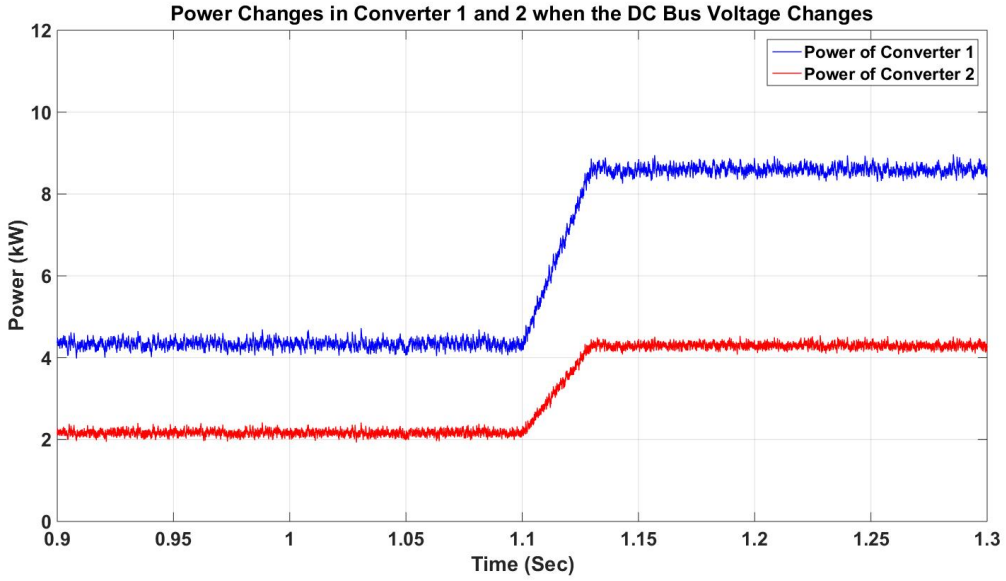

(b)

Figure 2.25 Power change in two paralleled converter sharing power according to current droop control scheme.

unequal load sharing between the converters. This issue can be avoided by increasing the droop coefficient as it is shown in Figure 2.26(a). However, the voltage variation window will

become large and may not be accepted by the loads. To avoid high voltage drop and ensure equal load sharing between the power converters of the system, a distributed control with higher level of supervision is proposed in [65]. In this method, the droop coefficient is set to be high to ensure the equal load sharing among converters, to avoid the voltage drop issue, the droop characteristics is shifted up to compensate for voltage drop (Figure 2.26(b)) in high load conditions. For this purpose, a secondary controller is needed to monitor the state of the system and update the droop characteristics of the converters in the system.

The second drawbacks of the droop control is that in a large microgrid where the line resistances are not negligible, the load sharing will be affected by the line resistances. Therefore, high droop slopes are needed and a second layer of control consequently.

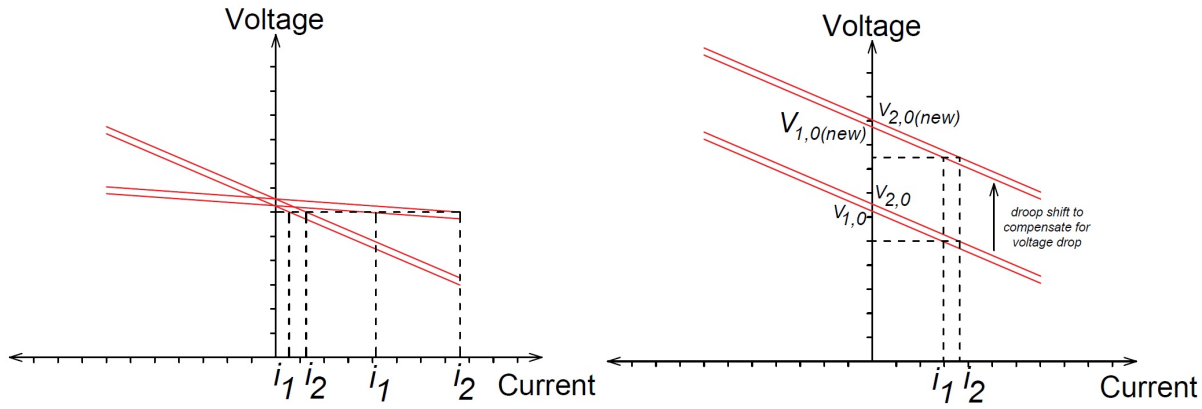

Figure 2.26 (a): Unequal load sharing due to error in nominal voltages of two parallel DC/DC converters. (b): Droop profile shifting for voltage drop compensation.

Moreover, in a cluster of microgrids where power sharing among them is needed, a tertiary level of control is needed to change the bus voltage in adjacent microgrids according to the required power flow among them.

Therefore, a higher level of supervision is required in distributed control to ensure that

the system is operating as it is expected. More desired features can be added to a system by using distributed control with a layer of communication.

CHAPTER

3

COMPARATIVE STUDY OF DC AND AC MICROGRIDS

Microgrids and specifically DC microgrids are the key components in the 21st-century's smart grid and deployment of microgrids are expanding rapidly in the U.S. power system. DC microgrids have demonstrated higher reliability, better power quality and better utilization of on-site generations compared to their AC counterparts. This is mainly due to linking DC sources to the DC loads with less conversion steps. Although the benefits of DC systems are clear, an accurate analytical study is required to quantify the benefits of DC systems which can be used for economic analysis.

In the remainder of this chapter, the benefits and drawbacks of potential DC microgrid

relative to their AC counterparts are presented according to the study done by Los Alamos National Lab study. Then, a comparative study between AC PV systems and a specific architecture of DC PV systems are disused. Finally, the results from the comparative study expands to the generic DC PV systems.

3.1 Estimate of Technical and Economic Benefits

Los Alamos National Lab has provided a preliminary examination of the benefits and drawbacks of potential DC power systems relative to their AC counterparts. They compared the performance of conventional AC architecture and mentioned DC architecture using several metrics. Results show that the DC microgrid architecture shown in Figure 2.2 enjoys 2-3% efficiency increase over the equivalent AC architecture assuming that the renewable energy sources are sized so that the need for exporting power is minimized [67].

Several national labs performed a study for DOE and compared the performance of mentioned AC and DC microgrids using several metrics including: safety and protection, reliability, capital cost, energy efficiency, operating cost, engineering costs, environmental impact, power quality, and resilience. For the initial comparison, generic AC and DC microgrid configurations (Figure 3.1) have been considered.

Results of a study on the AC and DC microgrids configurations shown in Figure 3.1 are summarized in Table 3.1 [67]. In Table 3.1, a "+" ("−") indicates that DC is expected to outperform (underperform) the AC architecture, while a "0" indicates that, at this level of analysis undertaken, the metric does not distinguish between the architectures. In addition to applications requiring high power quality, DC microgrids are expected to outperform their AC counterparts in applications where there is a large amount of DC-based generation and the export from the DC microgrid to the bulk AC system is limited by design or is simply absent, e.g. in remote small-scale power systems. These two architectural properties

combine to lower both capital and operating costs of DC relative to AC microgrids [67].

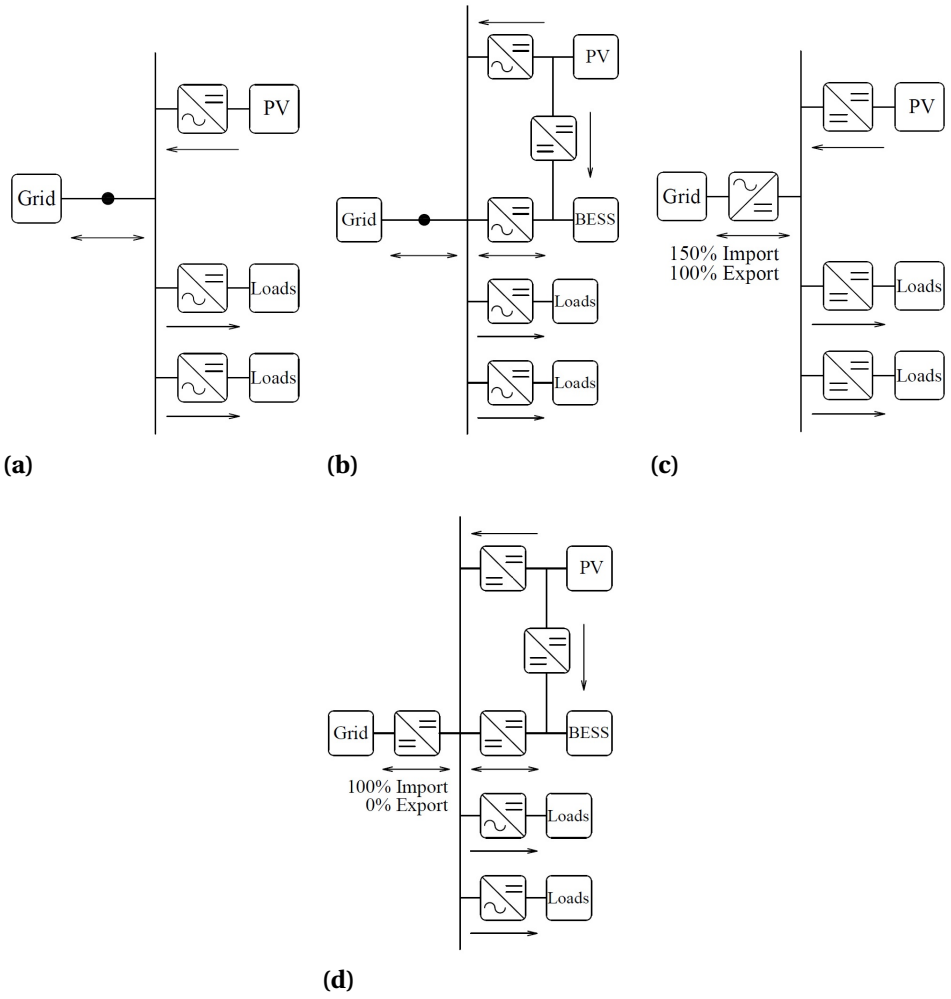

Figure 3.1 Four power system architectures. (a): AC network. (b): AC PV+ Battery microgrid. (c): DC network. (d): DC PV+Battery microgrid.

Table 3.1 Typical ratings and present development status of the full solid state DC circuit breaker.

Metric	**Rank**	**Comparison of DC to AC Architecture**
Safety and protection	0	Both AC and DC have adequate protection devices
Reliability	0	Assuming power electronics at AC/DC interface are sized appropriately to account for potential failures
Capital cost	+/-	DC architecture for a PV+Battery microgrid enjoys \$1/W lower cost for power electronics if the energy assets are sized so that power export is not required while N-1 reliability is maintained. However, DC architectures for the PV Network have 0.60/W higher cost for power electronics under similar reliability and sizing assumptions
Energy efficiency	+	The DC microgrid architectures enjoy a 2-3% efficiency increase over AC architectures assuming that the microgrid energy assets are sized so that power export is not required.
Operation cost	0	Under the assumption of the study, energy efficiency improvements count toward reductions in capital cost.
Engineering cost	+	Primary (distributed) control systems for DC architectures are potentially more universal, which may lower engineering costs
Environmental impact	0	Under the assumption of the study, energy efficiency improvements count toward reductions in capital cost, not towards less fossil-generated electricity purchased. If efficiency improvements were credited to lower marginal CO_2 emissions reductions, the monetary value is not large
Power quality	+	Power electronics at the AC/DC interface provides buffer against external disturbances
Resilience	0	Similar properties

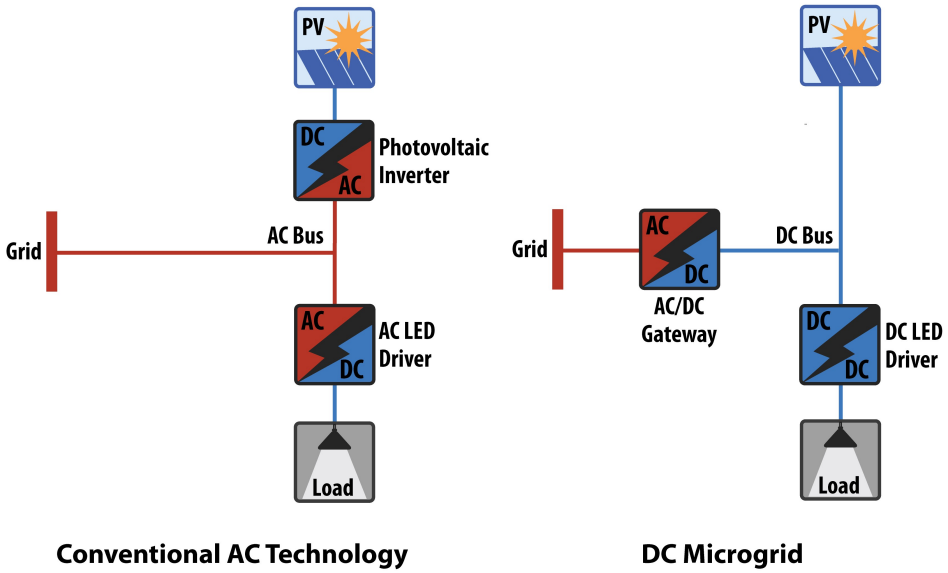

Figure 3.2 Left: Conventional AC PV system. Right: DC system.

3.2 A Comparative Study of DC and AC Microgrids in Commercial Buildings

The National Renewable Energy Laboratory (NREL) performed a simulation study to analyze the energy performance of both the unidirectional and bidirectional versions of the system discussed in Section 2.2.3 for several scenarios in different locations throughout the U.S [54]. Figure 3.2 shows a conventional AC PV system and the studied DC system.

3.2.1 Energy Analysis Model

In this analysis, a simple DC system containing only a PV array, DC LED lights, and an AC/DC rectifier was assumed. NREL simulated the performance of this system in a variety of scenarios resulting from the combination of

- Four building types: retail, supermarket, refrigerated warehouse, and non-refrigerated

warehouse.

- Five operating schedules: 6 a.m.-10 p.m. 5 days/week, 6 a.m.-10 p.m. 7 days/week, 8 a.m.-8 p.m. 7 days/week, 24 hours/day 5 days/week, and 24 hours/day 7 days/week.
- Two DC microgrid types: unidirectional and bidirectional.
- Two DC microgrid types: unidirectional and bidirectional.
- Five PV array sizes: 100%, 125%, 150%, 200%, and 250% of installed high bay lighting load capacity.
- Five hundred fifty-four geographic locations: 544 in the contiguous United States and 10 in Hawaii.

3.2.2 Evaluation Framework

An accurate comparison between conventional AC system and an equivalent DC systemof in terms of energy performance requires that the definitions of energy inputs and outputs be consistent between the two system types. Figure 3.3 presents a generic schematic of a building power network that contains a PV array, DC loads, and a connection to the AC power grid. This model can be used for an accurate comparison between AC and DC distribution systems.

Three possible converter locations are shown in Figure 3.3: at the PV source, at the load, and at the grid interconnection. Depending on the type of distribution system, the wiring between these converters may be either AC or DC. The figure also identifies the power measurement points, P_a, P_b, P_c, P_d, P_e, P_f.

The generic network of Figure 3.3 can represent either a conventional AC system or the DC microgrid depending on how converters are placed . In the AC case, there is no central AC/DC converter and $P_e = P_f$. The PV system uses a conventional PV inverter and

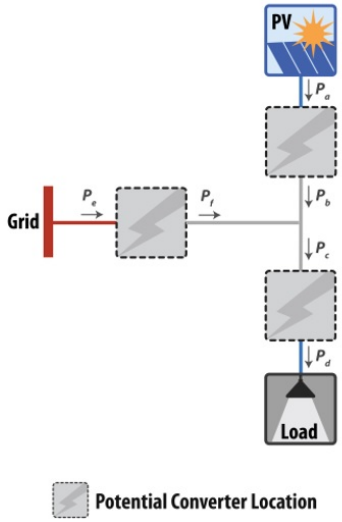

Figure 3.3 Schematic of a building electric power network with local PV generation, DC loads, and grid connection.

the load uses an AC/DC converter. In the DC case, there is instead no converter at the PV source and therefore $P_a = P_b$ (except in cases of curtailment). A DC/DC converter matches voltage between the PV source and the DC load. In this case, the grid-tied AC/DC converter provides the balance of power. Curtailment represents a special case for the DC microgrid in which $P_b < P_a$. Curtailment occurs if the available generation exceeds the combined load demand and export capacity of the gateway inverter. In such cases, the model represents the curtailed energy conceptually as a system loss between points a and b.

3.2.3 Definition of Performance Metrics

To compare the energy performance of the DC microgrid with a conventional AC system, seven energy performance metrics were developed by NREL. Four of these metrics describe the energy performance of the electric power system including: grid energy intensity, energy efficiency, PV utilization fraction, and grid utilization fraction. The remaining three are site metrics that describe the changes in site energy for a building employing a DC microgrid

compared to a building with a conventional AC system including: change in electricity Intensity, change in natural gas intensity, change in total energy intensity.

In defining the mentioned metrics, t represents an arbitrary time period in a set of time periods $T = [1, 2, ..., T]$ that span an entire year, each with duration $\triangle t$. Within each time period, the system is assumed to operate at steady-state (powers P_{at} to P_{ft} are constant) such that $E_{at} = P_{at} \triangle t$, $E_{bt} = P_{bt} \triangle t$, and so forth. The notation $t \in T$ indicates an operation that occurs over all time periods in set T.

Given these definitions, the grid energy intensity is the annual grid electricity consumption of the DC loads normalized by the floor area (A_{Floor}).

$$\text{Grid Energy Intensity} = \frac{\sum_{t=1}^{T} E_{et}}{A_{Floor}} \tag{3.1}$$

This metric varies significantly with PV system size and therefore it must be used for comparing scenarios with identically sized PV arrays. Because it measures total energy consumption, this metric provides the fairest point of comparison from a cost perspective.

The system energy efficiency is the ratio of total output (load) energy to total input (source) energy, including energy from both the electric grid and the PV array.

$$\text{Energy Efficiency} = \eta_E = \frac{\sum_{t=1}^{T} E_{dt}}{\sum_{t=1}^{T} (E_{et} + E_{at})} \tag{3.2}$$

1 It should be noted that, the energy efficiency differs from power efficiency. Energy efficiency is equivalent to weighted average power efficiency with weights proportional to system load at each time step.

The PV utilization fraction is a PV-specific energy efficiency metric defined as the fraction

of PV energy that serves a useful purpose; that is, the fraction that is either delivered to the load or exported to the electric grid.

$$\text{PV Utilization Fraction} = \frac{\sum_{t\in T|E_{ft}\leq 0}(E_{dt} - Eet) + \sum_{t\in T|E_{ft}>0}(\frac{E_{dt}}{E_{ct}})E_{bt}}{\sum_{t\in T}E_{at}} \tag{3.3}$$

The numerator of equation 3.3 sums all useful PV energy: energy delivered to the load (E_d) and exported to the grid ($-E_e$) whenever PV generation exceeds load, plus the PV array's portion of energy delivered to the load whenever load exceeds PV generation. The denominator sums all PV generation.

The grid utilization fraction is the counterpart to the PV utilization fraction, it provides a measure of the efficiency of grid-to-load energy transfer.

$$\text{Grid Utilization Fraction} = \frac{\sum_{t\in T|E_{ft}>0}(\frac{E_{dt}}{E_{ct}})E_{ft}}{\sum_{t\in T|E_{ft}>0}E_{et}} \tag{3.4}$$

The metric applies during grid import operation only; the numerator sums the grid's part of energy delivered to the load whenever load exceeds PV generation.

To assess the whole building (site) impact of the distribution system type, NREL simulated the performance of the entire building using the internal heat gains associated with each system type: the AC baseline and the DC microgrid. This process yielded net annual site electricity, natural gas, and total energy consumption for each system type ($E_{SiteElectric}, E_{SiteNaturalGas}, and E_{SiteEnergy}$, respectively). The three site performance metrics summarize the site impacts normalized by floor area.

$$\text{Site Change in Electricity Intensity} = \frac{E_{\text{Site Electric, DC}} - E_{\text{Site Electric, AC}}}{A_{\text{Floor}}} \tag{3.5}$$

$$\text{Site Change in Natural Gas Intensity} = \frac{E_{\text{Site Natura lGas, DC}} - E_{\text{Site Natural Gas, AC}}}{A_{\text{Floor}}} \tag{3.6}$$

$$\text{Site Change in Total Energy Intensity} = \frac{E_{\text{Site Energy, DC}} - E_{\text{Site Energy AC}}}{A_{\text{Floor}}} \tag{3.7}$$

The site change in electricity intensity includes the change in grid energy intensity of the high bay lighting subsystem rather than being in addition to it. The site change in total energy intensity combines the direct and indirect effects of the DC microgrid on electricity and gas consumption into a single metric.

3.2.4 Analysis Results

Figure 3.4 and 3.5 show show that buildings with continuous daily operation, the DC distribution system significantly improves the energy performance of the system compared to an equivalent AC system . Also the DC system improved PV utilization from approximately 0.90 for the AC to approximately 0.97 for the DC and improved annual energy efficiency from approximately 92% for the AC baseline to approximately 95% for the DCMG.

As it can be seen in Figure 3.6 and 3.7, in nearly all locations, the net indirect impact of the DC system was a reduction of site energy compared to the AC baseline.Moreover, The bidirectional DC system, performed well for all simulation scenarios. In contrast, the unidirectional DC system performed well only for system designs and building operating

schedules that did not result in significant curtailment of PV production. Finally, this analysis provides evidence that the DC distribution systems in commercial buildings can produce significant energy savings.

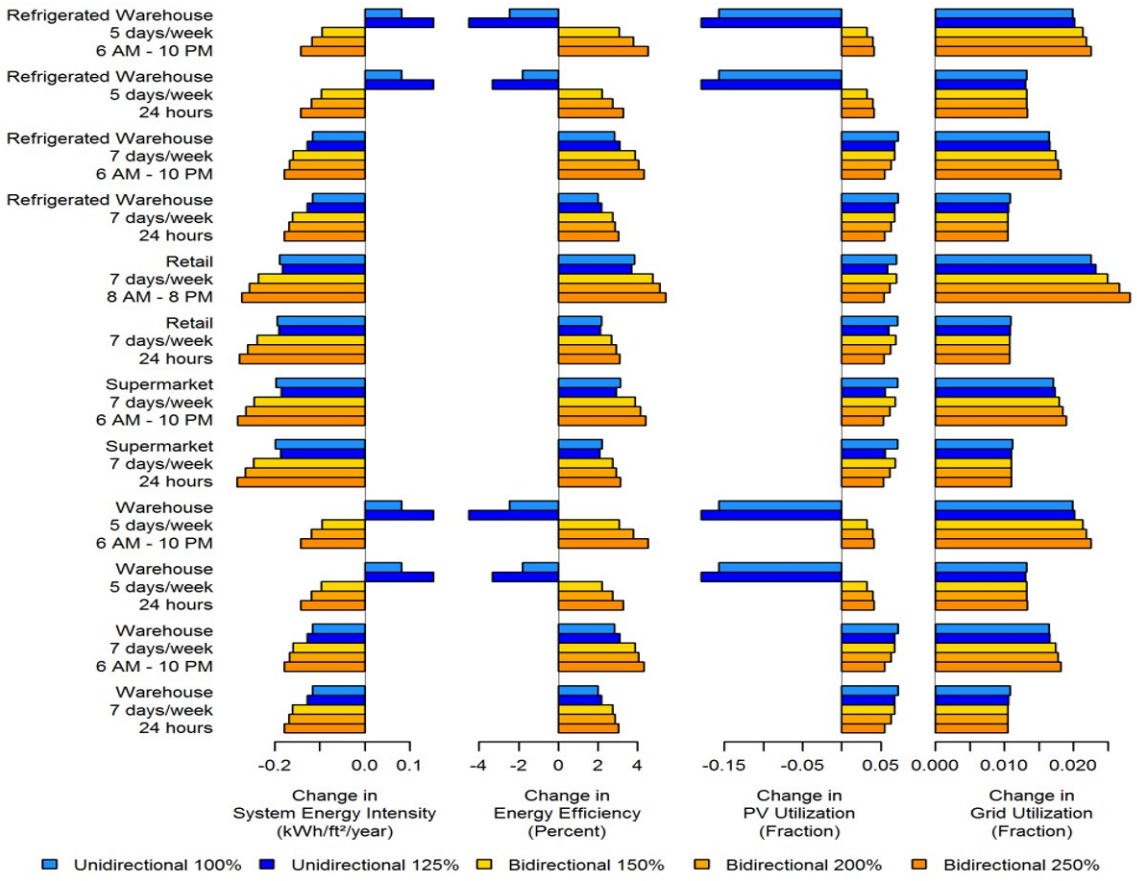

Figure 3.4 Average changes in system energy performance metrics for buildings with seven days per week operation: DC microgrid compared to AC baseline [68],[54].

3.3 Expanding Results to Generic DC PV Systems

The energy analysis discussed in the previous section, compares a very specific DC PV system architecture shown in Figure 3.8(b) with a typical AC PV system shown in Figure

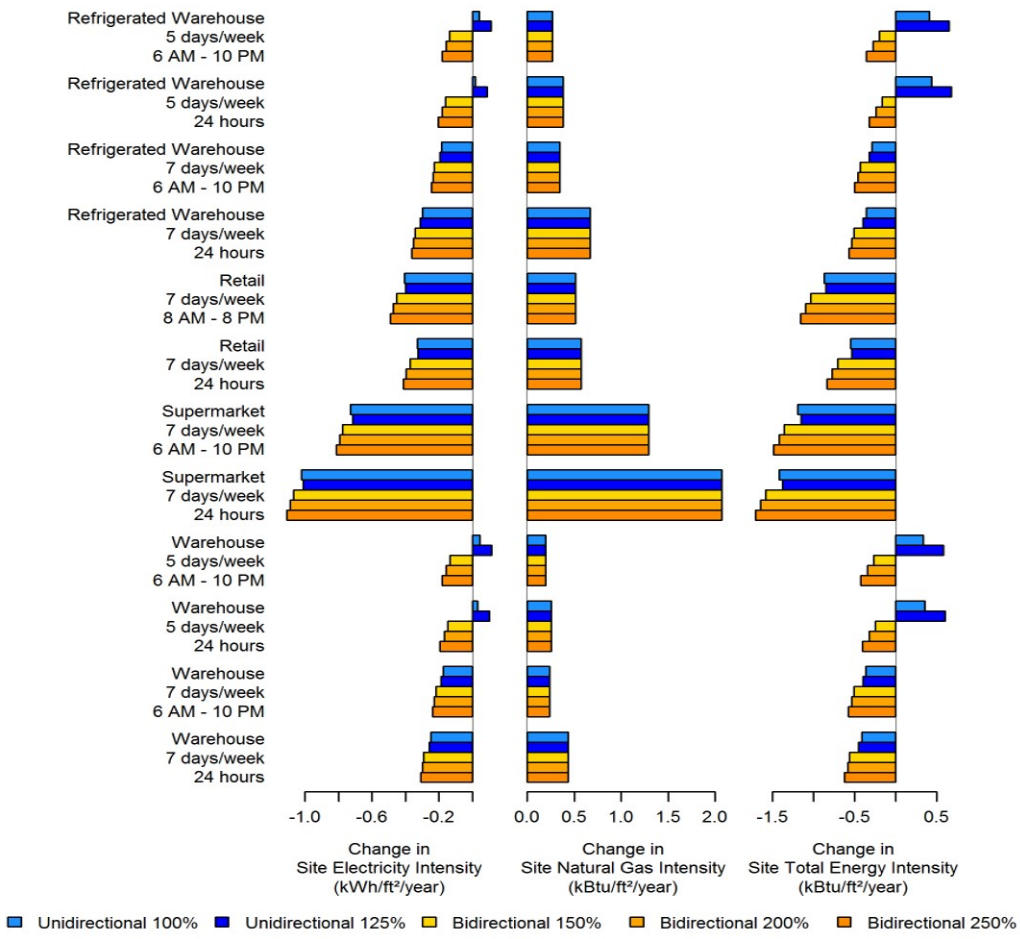

Figure 3.5 Average changes in site energy performance metrics for buildings with seven days per week operation: DC microgrid compared to AC baseline [68],[54].

3.8(a). In this section, we examine if the results from the previous section can be expanded to a more common DC PV system architecture as shown in Figure 3.8(c) or not. They key difference between the systems shown in Figure 3.8(b) and (c) is the lack of PV MPPT converter in (b) which makes this system inherently more efficient than the system shown in Figure 3.8(c). From this explanation, it might conclude that the results from the previous section cannot be expanded for the typical DC PV systems. However, a significant trend in recent years is the migration from $600\,V_{dc}$ PV systems to $1000\,V_{dc}$ systems. The $1000\,V_{dc}$ PV system is well-recognized by the utilities to reduce the installations cost and improve

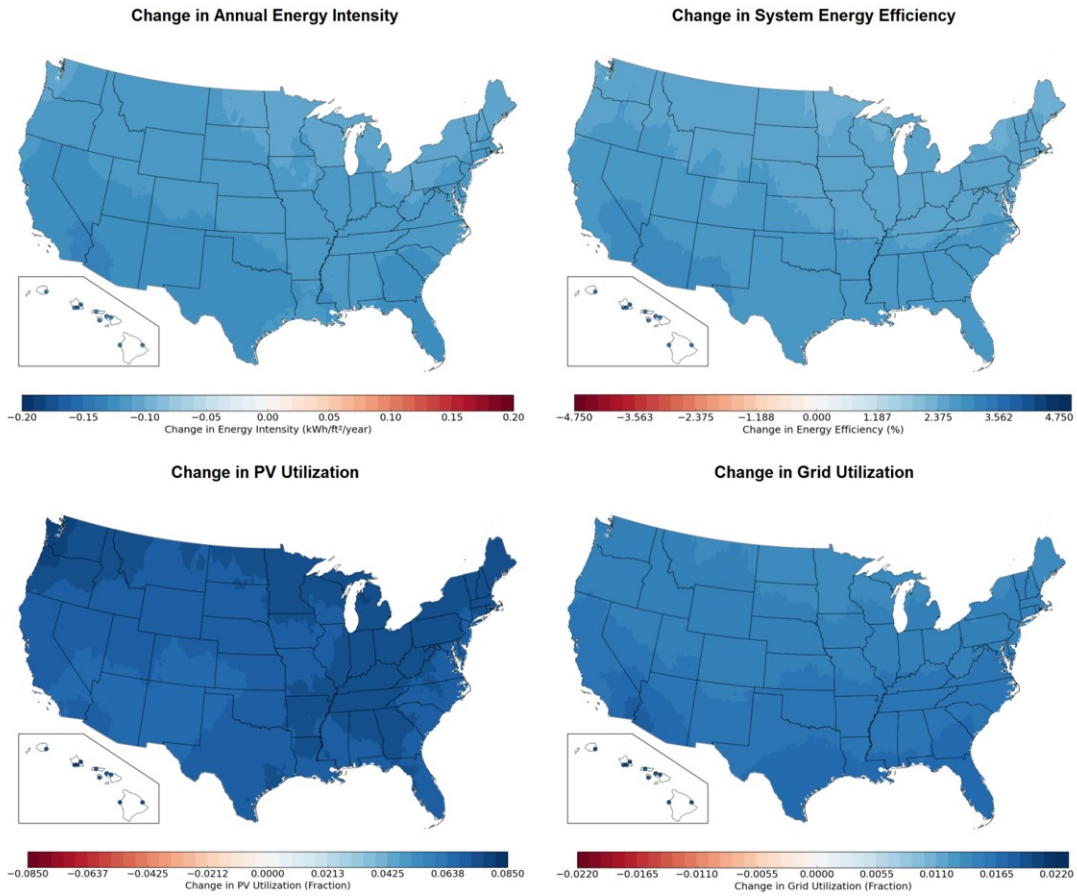

Figure 3.6 Performance comparison map of system energy intensity (DC microgrid compared to AC baseline): warehouse, 6 a.m.-10 p.m. operation, 7 days/week, unidirectional DC microgrid, 100% array scaling factor [68],[54].

the performance. To benefit from these advantages, more and more commercial systems are adopting $1000\,V_{dc}$ systems. As one of the advantages, ohmic wiring losses of a $1000\,V_{dc}$ system is $\approx 0.6\%$ less than the same-size $600\,V_{dc}$ PV system [69] and [70]. Therefore, there is a possibility that ohmic loss reduction in $1000\,V_{dc}$ PV system compensate for the losses in the PV MPPT converter. In the other words, the PV utilization factor for a $1000\,V_{dc}$ PV system with the schematic shown in Figure 3.8(c) might be similar to the $600\,V_{dc}$ PV system with schematic shown in Figure 3.8(b). In the reminder of this chapter, the PV systems with $600\,V_{dc}$ and $1000\,V_{dc}$ are compared. Then a comparison study between the $600\,V_{dc}$ and

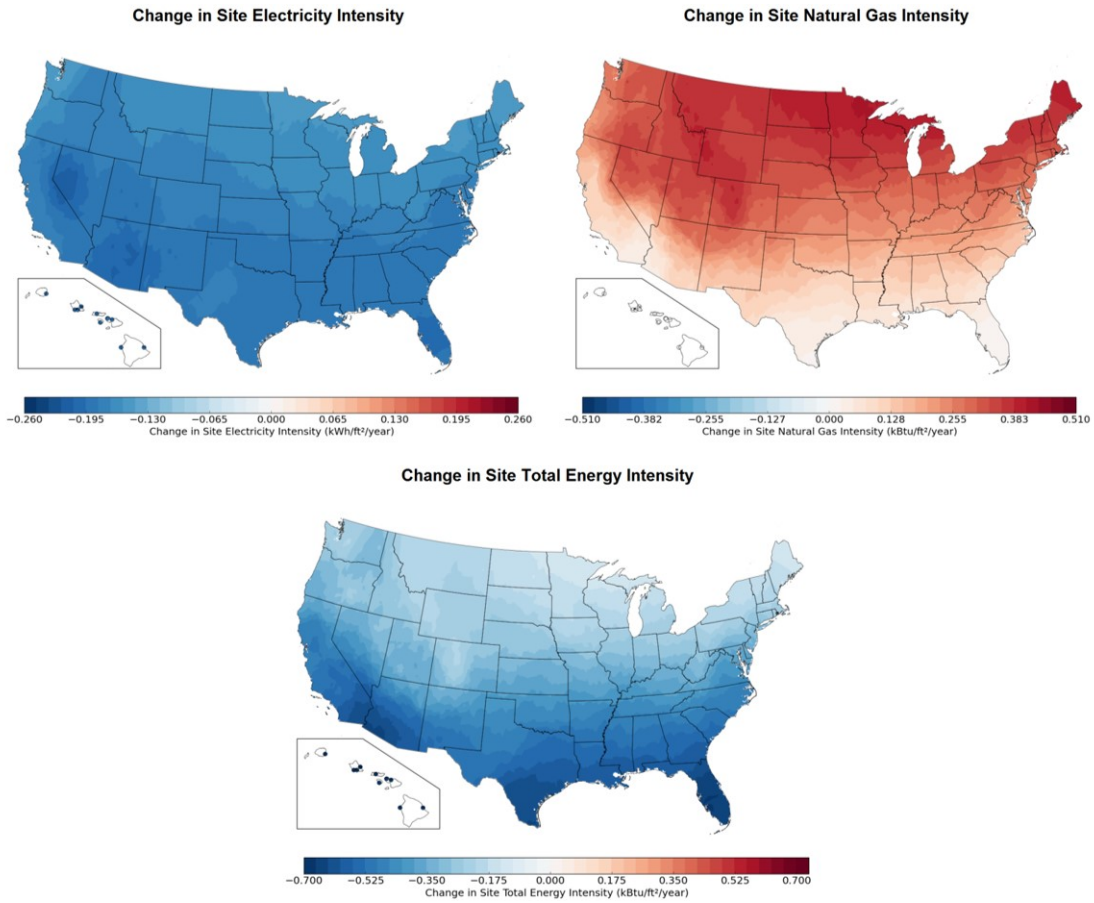

Figure 3.7 Performance comparison map of site energy intensity (DC microgrid compared to AC baseline): warehouse, 6 a.m.-10 p.m. operation, 7 days/week, unidirectional DC microgrid, 100% array scaling factor [68],[54].

$1000\,V_{dc}$ PV systems in terms of PV utilization factor will be performed.

3.3.1 600V PV System vs. 1000V PV System

$1000\,V_{dc}$ PV design and technology allows integrators to realize increased energy production, material cost savings and a lower levelized cost of energy. However, due to the lack of high quality UL listed products, legacy designs at $600\,V_{dc}$ and reluctant inspector acceptance the adoption of $1000\,V_{dc}$ was slow. Recently, those barriers have been removed by a growing number of high quality UL listed modules, components and DC/DC optimizer/inverters

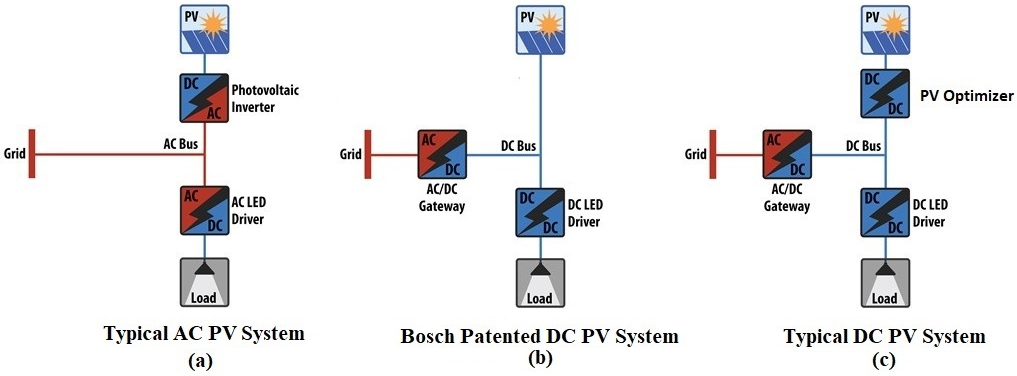

Figure 3.8 (a): Schematic of a typical AC PV system. (b): Schematic of Bosch patented DC PV system. (c): Schematic of a typical DC PV system.

Table 3.2 Benchmark between a conventional 600 V_{dc} system and a 1000 V_{dc} system.

1 MW DC	1MW DC
750kW MPPT Converter	750kW MPPT Converter
4140 PV modules	4140 PV modules
1000 VDC	600 VDC
20 modules per string	12 modules per string
207 strings	345 strings
9 combiners/ home runs	15 combiners/home runs

driven mainly by the utility segment, along with the code to support 1000 V_{dc} for commercial applications [70].

According to the SMA, "The Commercial Promise of 1000 VDC PV Design" white paper, the benefits of 1000 V_{dc} can be summarized as the following

1. **Financial Benefits:** The higher voltage results in lower installation costs, greater DC/DC optimizer/inverter efficiency, less system power loss and reduced balance of system (BoS) components. Table 3.2 uses as a benchmark for comparison between the conventional 600 V_{dc} system with a 1000 V_{dc} system.

   The savings mainly comes from reduced wiring need as shown in Table 3.3

   By putting the dollar amount on to the numbers shown in Table 3.3, the 1000 V_{dc}

Table 3.3 Wiring need comparison between a conventional $600 V_{dc}$ system and a $1000 V_{dc}$ system.

BoS Wiring Quantity	**600V DC**	**1000 V DC**	**Difference**
Modules (number per string*strings)	12*345	20*207	No Difference
String combiner boxes, home runs	15	9	(6)
10 AWG wire module to combiner	46 618 ft	27 340 ft	(19 278)
350 MCM wire combiner to inverter	4 703 ft	2 500 ft	(2 203)
300 MCM wire	943 ft	1 466 ft	523
4/0 AWG wire	665 ft	0	(665)

Table 3.4 Ohmic loss comparison between a conventional $600 V_{dc}$ system and a $1000 V_{dc}$ system.

Line Loss Summary	**600V DC**	**1000 V DC**	**Difference**
Lost watts	10 435	6 390	(4 045)
Percentage of system size	1.39%	0.85%	(0.54%)

system saves more than $20,000 on wiring costs alone, not including conduit or labor savings. When all factors are considered, a $0.02 to $0.03/watt savings can be achieved at installation [70].

2. **Improved Performance:** System can achieve additional improvement such as reduced ohmic losses due to higher level of voltage. Table 3.4 comparing line losses through a voltage drop calculator showed the following for the same 750 kW AC example.

   With 0.54% efficiency gain due to lower line loss, total energy harvest is improved. This number will be used later in this chapter to perform comparative study between the $600 V_{dc}$ direct PV connected system and $1000 V_{dc}$ regular PV system in terms of PV utilization factor.

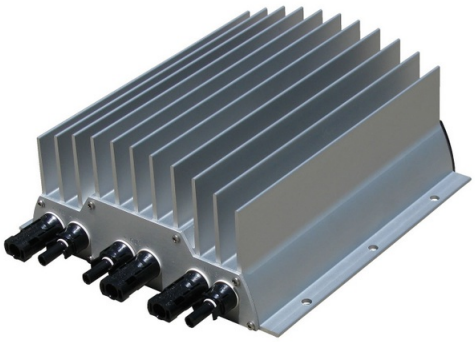

Figure 3.9 $1kV$ PV DC/DC optimizer developed by Ampt.

3.3.2 PV Utilization Factor Comparison

In this section, the PV utilization factor of direct connected $600V_{dc}$ PV system is compared with a regular $1000V_{dc}$ PV system. The initial thought is that the reduction in ohmic losses in $1000V_{dc}$ system will compensate for losses in the PV MPPT converter and therefore, $600V_{dc}$ direct PV connected system and regular $1000V_{dc}$ system get the same PV utilization factors.

The PV utilization factor is defined as the percentage of PV output power that reaches to the DC bus. In a $600V_{dc}$ direct PV connected system the only source of PV power loss is the ohmic losses which is 1.39% according to [70] meaning that PV utilization factor is 98.61%. For the regular $1000V_{dc}$ PV system on the other hand, the is PV power loss in lines as well as the PV MPPT converter. Line losses are 0.85% according to [70]. In the reminder of this section, the power loss in the MPPT converter is calculated.

With recent advances in semiconductor switches and introduction of wide bandgap devices such as SiC MOSFETs and IGBTs, the overall efficiency of power converters have increased significantly [71]. Ampt a leader in PV power technology, introduced $1kV$ string level PV optimizer with 99.5% efficiency. Figure 3.9 shows a $30kW$ $1kV$ Ampt DC/DC optimizer. Also Figure 3.10 shows the efficiency of the mentioned converter over the full range of output power based on CEC data.

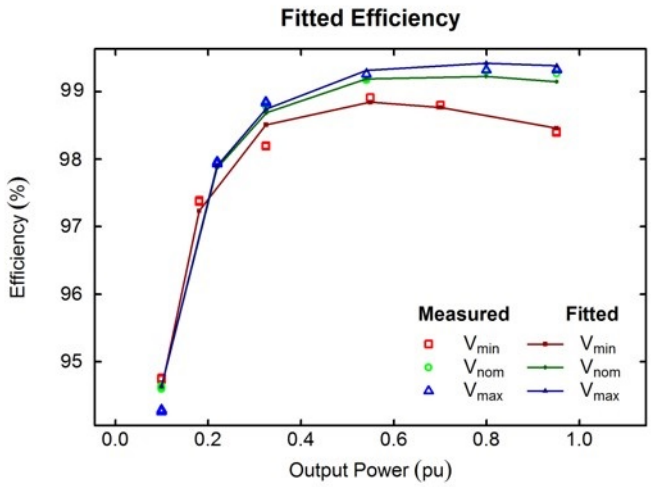

Figure 3.10 Efficiency of $1kV$ Ampt DC/DC PV optimizer over the full range of output power.

As it is shown in Figure 3.10 the converter efficiency varies depending on its output power, and the output power of the converter is determined by the available PV power. Figure 3.11 shows the available PV power during a typical sunny day. As it can be seen, PV power starts from zero and gets to its peak value around noon and then goes back to zero by sunset. This means that the PV MPPT converter does not operate at its maximum efficiency all the time. Therefore, only a weighted efficiency has to be used to calculate the accurate PV power loss in the MPPT converter.

In order to calculate the weighted efficiency of the PV MPPT converter, the PV power during a day is divided into 14 sections each with constant power as it is shown in Figure 3.12. Weight of each section in efficiency calculation is the power of that section in percentage, and the efficiency of each section can be found from Figure 3.10. For instance, weight of section 4 is 0.6 and the efficiency of that section is 99.3%. With this explanation, the weighted efficiency of the MPPT converter can be calculated as following

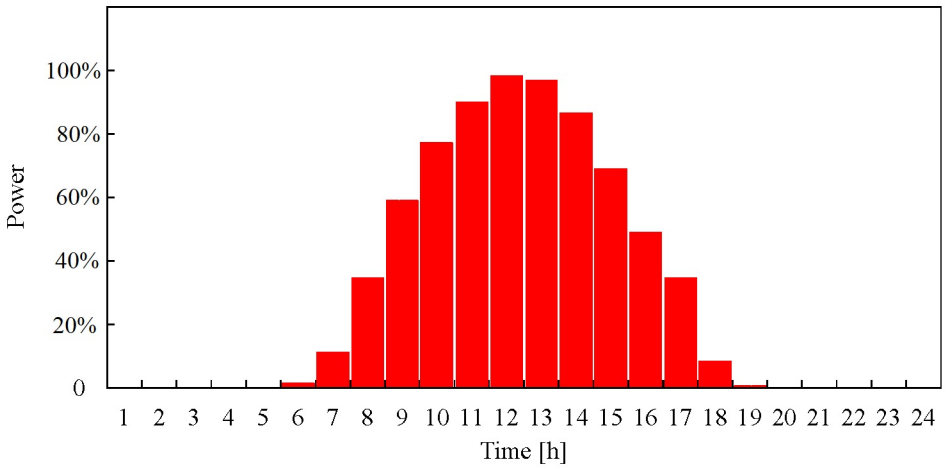

Figure 3.11 Typical PV output power over a day.

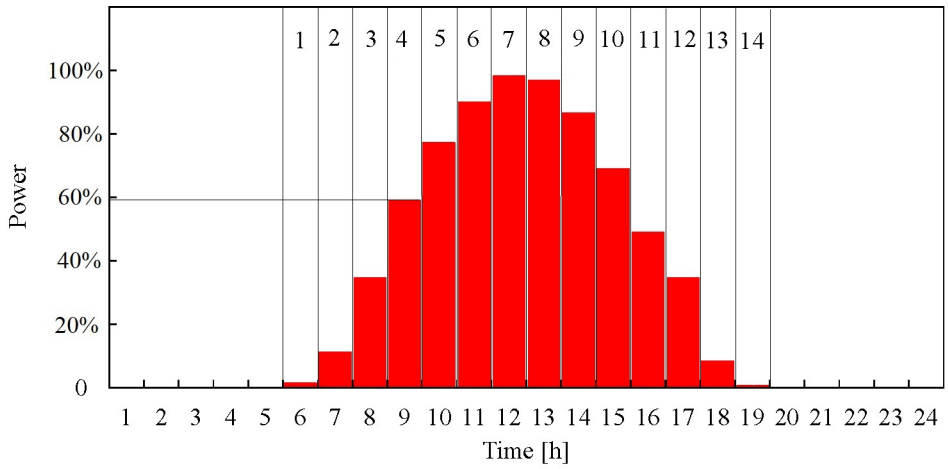

Figure 3.12 Sectionized PV production over a day.

$$\bar{\eta} = \frac{\sum_{i=1}^{14} \omega_i \eta_i}{\sum_{i=1}^{14} \omega_i} \tag{3.8}$$

where $\bar{\eta}$ is the weighted efficiency of the PV MPPT converter, ω_i is the weight of i^{th} section in percentage and η_i is the efficiency of the i^{th} section. Applying equation 3.8 on the data shown in Figure 3.11 and 3.10 the weighted efficiency of the PV MPPT converter will be calculated 99.4%.

This study shows that in a regular $1000\,V_{dc}$ PV system, 0.6% and 0.85% of the PV power is lost in the MPPT converter and the lines, respectively. Resulting in PV utilization factor of 98.55%. Also it was mentioned that the PV utilization factor in a direct connect $600\,V_{dc}$ PV system is 98.61%. As it can be seen these two system have almost similar PV utilization factors which means that the energy analysis results presented in the previous section of this chapter can be expanded to a regular $1000\,V_{dc}$ PV system and this system will benefit from all the energy improvement of the $600\,V_{dc}$ system with direct connection of PV to the DC bus.

CHAPTER

4

POWER BALANCING METHODS IN DC MICROGRIDS

One of the challenges associated with employing microgrids is to implement a reliable control algorithm that ensures distributed power converters maintain power balance to regulate the bus voltage in a desired window. To ensure stable operation of a microgrid, the sum of the generated power needs to be equal to the power drawn from the common bus at all times. This is more straightforward in a DC system since no synchronization is necessary. While ensuring power balance, the control algorithm should also control power sharing among sources and allow for multiple slack sources for redundancy. Moreover, A well-designed control algorithm should enable features such as scalability, redundancy,

grid resiliency, and storage features like peak shaving, load shifting, and demand response. On top of all these requirements , large-scale deployment of distributed renewable energy resources like solar in the microgrids, has to provide utilities and grid operators the capability to safely and reliably mitigate the impact of solar and loads intermittency on the main AC power grid. Therefore, the control algorithm should be able to reliably mitigate the impact of PV and load variations in the microgrid from transferring to the AC power grid, when the microgrid is transferring power with the AC grid.

In this chapter we propose two power balancing methods that satisfies the requirements mentioned above. Then, the feasibility and effectiveness of the proposed strategies are verified in either lab scale system setup or using control-HIL (C-HIL) simulations.

4.1 Distributed with Direct Connection of Energy Storage

In this section, a novel distributed power balancing strategy with a layer of supervision is proposed for the LV DC microgrids. The goal of this power balancing strategy is to harvest the maximum power from the renewable sources (solar in our case) and minimize the effect of solar variations on the main AC grid and smooth out the solar output by using BESSs. This is achieved by implementing a distributed power balancing strategy. In this control strategy, different voltage levels are predefined to distinguish between different system operations modes. The converters in DC microgrid, sense the DC bus voltage continuously and set their operating mode and amount of power transfer with the microgrid accordingly [72]. In the remainder of this section, the mentioned power balancing strategy and the control algorithm is explained in details. Then, laboratory-scale implementation of the discussed control algorithm and the experimental results will be presented.

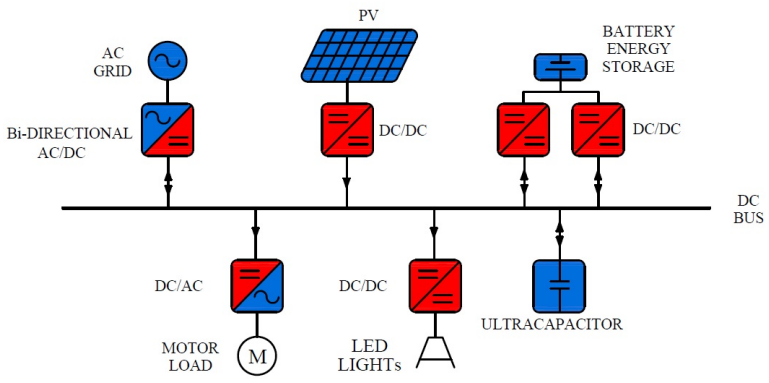

Figure 4.1 Schematic of a DC microgrid with direct connection of energy storage.

4.1.1 Control Algorithm

Reliable and stable operation of a DC microgrid relies on coordinated control of multiple sources, BESSs and loads. A proper controller is responsible for maintaining the DC bus voltage in a specific window, balancing the power between the power electronic converters of the system and enabling some features such as solar output smoothing, islanding and etc. The control algorithm can be divided into two sections. First, the proposed distributed power balancing strategy is explained and. The second part, discusses a layer of communication that is implemented to optimize the BESSs operation and compensate for voltage drop/rise due to employing linear droop.

4.1.1.1 Distributed Power Balancing Strategy

The power balancing strategy that will be proposed in this section, is applicable to any grid-tied PV plus energy storage DC microgrid.

Figure 4.1 shows a typical DC microgrid with local PV source and BESS. It can be seen that the microgrid is connected to the main AC grid through a bidirectional AC/DC inverter. This inverter enables the export of surplus PV generation to the electric grid, when the BESS are fully charged and there is not enough loads to consume generated power by PV. It

is also responsible for importing power from the main grid in case PV and BESS are not capable of providing sufficient power to the loads. Also a MPPT DC/DC converter is used to connect the PV array to the DC bus. The MPPT converter regulates the PV's voltage to the maximum power voltage, V_{mp}, to maximize the PV output power, and therefore, it is considered as a variable current source from the DC microgrid point of view. Bidirectional DC/DC converters are used to exchange power between battery and the main DC bus. Also, an ultracapacitor is connected directly to the DC bus to absorb the transient variations in PV/loads and prevent the battery micro cycles charging and discharging due to the small variations in solar output and loads. Finally, for demonstrating the parallel operation of DC/DC converters in the microgird, two paralleled DC/DC converters are used between the battery and the microgrid. As it was mentioned earlier, the goal of the proposed power balancing strategy is to maximize the power coming from the renewable resources (solar in our case) and to smooth out the PV variation. These goals are achieved by implementing a distributed power balancing strategy with a layer of communication [72]. In this power balancing strategy, four different voltage levels are predefined like the following to distinguish between different system operations modes.

$$V_{min} < V_1 < V_2 < V_{max} \tag{4.1}$$

Converters of the DC microgrid sense the DC bus voltage continuously and set their operation mode and the amount of power transfer with the microgrid accordingly.

Whenever the bus voltage is between V_1 and V_2 , battery converters and the gridâĂŞtied inverter are at standby and the voltage can vary between V_1 and V_2 according to the available PV power and load. In order to avoid frequent battery charge and discharge, an ultracapacitor is connected directly to the bus to slow down the voltage variations. In case of overgeneration, the bus voltage increases slowly, as soon as the voltage reaches to V_2, the

battery converters start drawing power from the microgrid to store the surplus energy. To equally distribute the voltage regulation capacity of the battery converters, a linear droop is adopted as

$$V_{ci}^{*} = V_2 - R_{dci} I_{ci} \tag{4.2}$$

Where V_{ci}^{*} is the reference voltage of the i^{th} converter's voltage control loop, R_{dci} and I_{ci} are the droop coefficient and the output current of the i^{th} converter, respectively. It should be noted that in this work, all the currents going to the microgrid, are considered as positive currents and all the currents drawn from the microgrid are considered as negative. The battery and the DC/DC converters should be sized large enough to have enough capacity and power to regulate the bus voltage in overgeneration conditions. However, in rare conditions when the battery is fully charged or the load is too low, battery will not be able to store all the excess energy, and the voltage increases to V_{max}. The grid-tied inverter senses the bus voltage continuously and as soon as the voltage reaches to V_{max}, it starts regulating the bus voltage by exporting the excess energy to the main AC grid. Similarly, in case of undergeneration, the bus voltage decreases slowly, as soon as the voltage reaches to V_1, the battery converters start importing power to the microgrid by discharging the battery. To equally distribute the voltage regulation capacity of the battery converters, a linear droop is adopted as

$$V_{ci}^{*} = V_1 - R_{dci} I_{ci} \tag{4.3}$$

Where V_{ci}^{*} is the reference voltage of the i^{th} converter's voltage control loop, R_{dci} and I_{ci} are the droop coefficient and the current of the i^{th} converter, respectively. The battery should be sized large enough to have enough capacity to regulate the bus voltage in undergeneration conditions. However, in rare conditions when the battery is fully discharged or

the load is too high, battery will not be able to provide enough power to keep the bus voltage from collapsing, and therefore, the bus voltage keeps dropping. The grid-tied inverter senses the bus voltage continuously and as soon as the voltage reaches to V_{min}, it starts regulating the bus voltage by importing power from the main AC grid. Different operation modes of the systemâĂŹs converters are summarized in the following. Also the $V-I$ characteristics of PV DC/DC optimizer, battery DC/DC converters as well as grid-tied inverter are shown in Figure 4.2.

- **Mode I:** $V_1 < V_{Bus} < V_2$ **:** battery DC/DC converters and grid-tied inverter are at standby. The DC bus voltage is determined by the load and available PV power. The ultracapacitor is the slack terminal in this mode.

- **Mode II:** $V_2 < V_{Bus} < V_{max}$ **:** battery DC/DC converters are slack terminals and regulate the DC bus voltage by drawing power from the microgrid following a droop profile.

- **Mode III:** $V_{min} < V_{Bus} < V_1$ **:** battery DC/DC converters are the slack terminals and regulate the DC bus voltage by drawing power from the microgrid following a droop profile.

- **Mode IV:** $V_{Bus} < V_{min}$ **:** battery DC/DC converters discharge to the microgrid to keep the voltage above V_{min} but since they are not able to do that, the grid-tied inverter becomes the slack terminal and regulates the DC bus voltage by importing power from the AC grid.

- **Mode V:** $V_{max} < V_{Bus}$**:** battery DC/DC converters draw power from the grid to keep the voltage below V_{max} but since they are not able to do that, the grid-tied inverter becomes the slack terminal and regulates the DC bus voltage by exporting power to the AC grid.

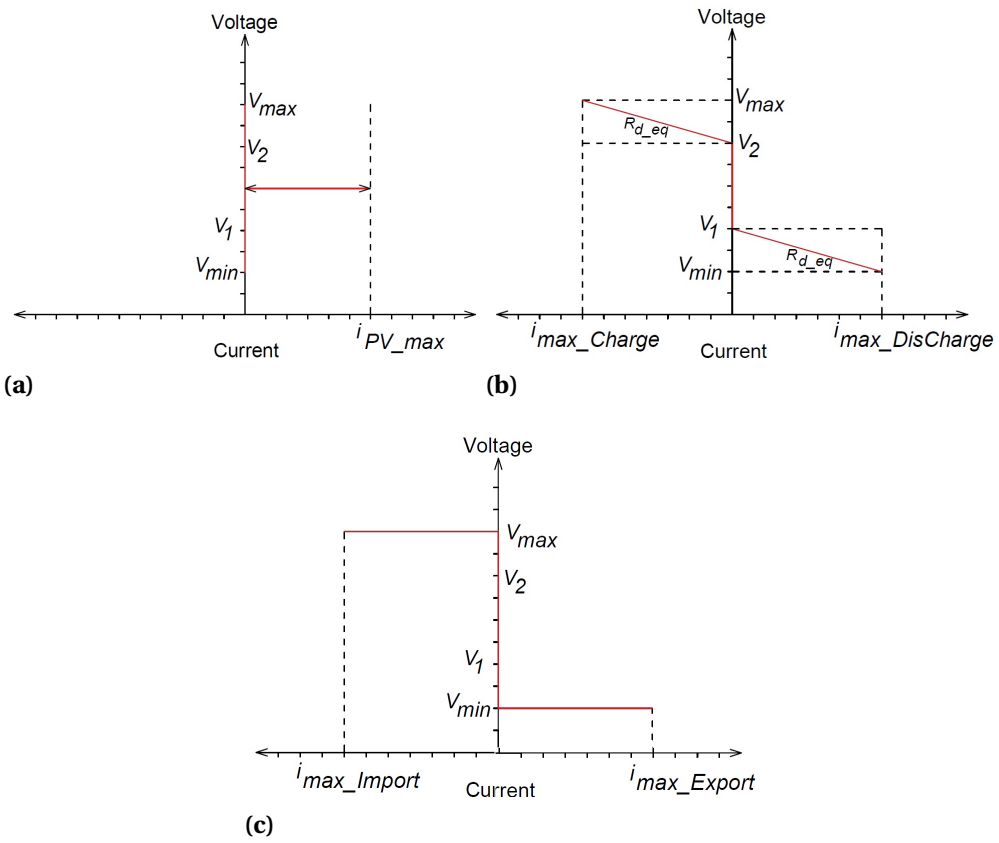

Figure 4.2 (a): V-I characteristic of PV DC/DC optimizer. (b): Equivalent V-I characteristics of battery DC/DC converters ($R_{d_{eq}}$ is the equivalent droop coefficient of the battery converters. (c): V-I characteristic of grid-tied bidirectional inverter.

4.1.1.2 Supervision Layer

The control algorithm discussed in the previous section is able to keep the power balance among converters of the system without a need for communication. However, to ensure the optimal operation of the system, a layer of low-bandwidth communication is added to the control algorithm which will be discussed in this section.

1. The linear droop control method used for battery converters has two major drawbacks. On one hand, due to the practical limitations, the nominal voltage of different power converters in the system are not exactly equal. Even a small error in nominal voltages

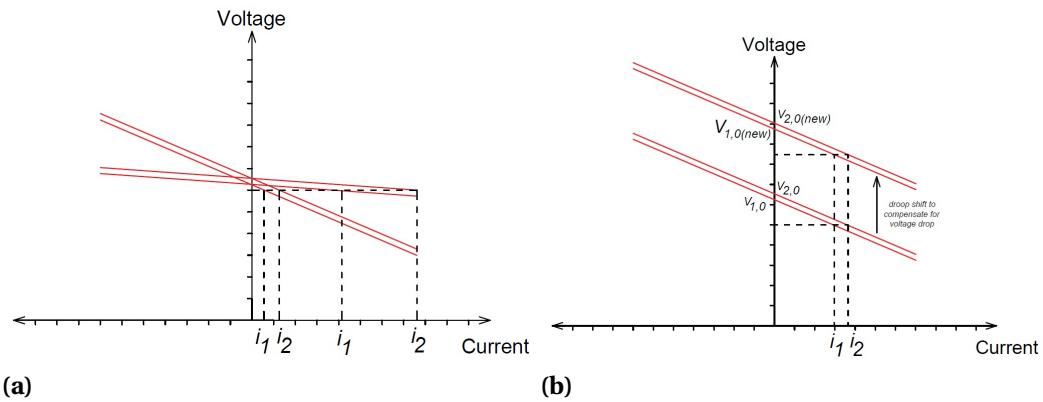

Figure 4.3 (a): V-I characteristic of PV DC/DC optimizer. (b): Equivalent.

will result in significant deviation of current from their required values. To illustrate this issue, the droop profile of two paralleled converters in a DC microgrid are shown in Figure 4.3. The two converters have the same droop coefficient. However, due to the voltage sensing error, there is an error between the nominal voltages. It can be seen that this small error causes unequal load sharing between the converters. This issue can be avoided by increasing the droop coefficient as it is shown in Figure 4.3(a). However, the voltage variation window will become large and may not be accepted by the loads. The second drawbacks of the droop control is that in a large microgrid where the line resistances are not negligible, the load sharing will be affected by the line resistances. Therefore, again high droop coefficients are needed. To resolve the issue related to high droop slope and avoid high voltage drop/rise and ensure equal load sharing between the power converters of the system, the droop slope is set to be high to ensure the equal load sharing among converters, to avoid the voltage drop (rise) issue, the droop characteristics is shifted up (down) to compensate for voltage drop (rise) (Figure 4.3(b)) in high load conditions. For this purpose, a communication layer is needed to monitor the state of the system and to update the droop characteristics of the converters in the system.

2. BESSs of the system are responsible to regulate the voltage by charging whenever $V_2 < V_{Bus} < V_{max}$ and by discharging whenever $V_{min} < V_{Bus} < V_1$. Although the DC microgrid discussed in this paper only has one BESS, but it is very likely the larger microgrids have multiple BESSs. Therefore, coordination among different BESSs is necessary in the microgrids with multiple BESSs. There are different charging/discharging control schemes that can be implemented based on the specific application. In this report, the control scheme that discussed in [73] is used. The control objective of this scheme is to keep the State of Charges (SoC) of all the BESSs at the same level. This is achieved by comparing the SoC of each BESS with the average SoC of the batteries and have the BESSs with higher SoC contribute more in discharging and the batteries with lower SoCs contribute more in charging.

$$\beta_i = \frac{SoC_i}{\frac{1}{n}\sum_i^n SoC_i} \tag{4.4}$$

where β_i is the ratio of SoC of i^{th} BESS to the average SoC of all BESSs of the system. And n is the total number of BESSs. High β_i means high SoC while low β_i corresponds to low SoC. This information is used to adjust the droop coefficient of the battery converters as following

$$R_{di}^n = \begin{cases} \beta_i R_{di} & if \quad i_{ci} < 0 \\ \frac{R_{di}}{\beta_i} & if \quad i_{ci} > 0 \end{cases} \tag{4.5}$$

Where R_{di}^n is the new droop coefficient of the i^{th} converter. R_{di} is the current droop coefficient of the i^{th} converter and i_{ci} is the output current of the i^{th} converter. Equation 4.5 means that batteries with higher SoCs contribute more in discharging and less in charging. Similarly, batteries with lower SoCs, contribute less in discharging

and more in charging. To be able to implement the mentioned charge/discharging control scheme, a communication layer is needed.

4.1.2 Implementation and Experimental Results

To demonstrate the feasibility and effectiveness of the proposed power balancing strategy, a lab-scale DC microgrid, with the configuration shown in Figure 4.1, has been implemented. In this section, hardware setup and experimental results of the five different operation modes discussed earlier are presented. Since the implemented microgrid has only one BESS and the length of wires between two paralleled DC/DC converters and the main DC bus is short, there was no need for adding the communication layer. Therefore, only the results from the power balancing without communication layer is presented. Figure 4.4 shows the implemented lab-scale test setup. In this setup, a $5kW$ bidirectional inverter used as an interface between the microgrid and the main grid. The inverter has a voltage controller built in that enabled it to regulate the DC bus voltage in both directions. A $10kW$ solar array emulator represents the solar. The solar operates at MPPT all the time and is considered as a variable current source. To store surplus of PV generation and use it in off-grid mode or for peak shaving, a $100kWh$ flow battery energy storage system is used. Two paralleled DC/DC converters are used to enable the power exchange between the battery and the microgrid. The parallel operation is achieved by implementing a linear voltage droop control, with droop coefficient of 0.8. To prevent microcycle charge and discharge on the battery, a $10F$ ultracapacitor is connected directly to the bus. $4.3kW$ of DC LED lights and industrial ceiling fans were used as the loads. To be able to set the thresholds and droop profiles on different converters of the system, a master controller was employed. Finally, all the sources and loads are combined in a combiner/monitoring panel where all the measurement devices, overcurrent protection, surge protection and the main DC bus are located. For this experiments, the predefined voltage levels: V_{min}, V_1 , V_2 and V_{max} are

considered to be $320V_{dc}$, $340V_{dc}$,$360V_{dc}$ and $380V_{dc}$, respectively. Components of the pilot DC microgrid are shown in Figure 4.4. Also, results from the five operation modes of the microgrid are presented in Figure 4.5-4.9.

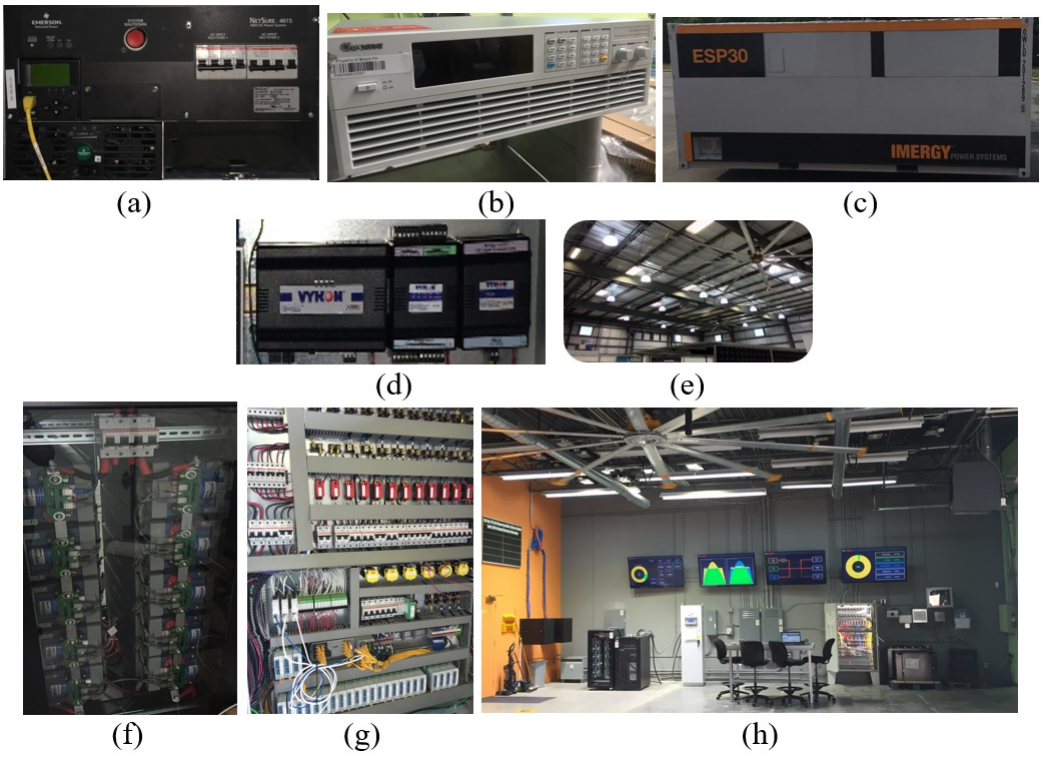

Figure 4.4 DC microgrid setup. (a): $5kW$ Grid-tied bidirectional inverter. (b): $10kW$ solar array emulator. (c): $100kWh$ Flow battery. (d): Master controller. (e): $4.3kW$ of DC LED lights + industrial fan. (f): $10F$ ultracapacitor. (g): Monitoring and combiner units. (h): DC microgrid laboratory.

- **Mode I:** As it was discussed earlier, inverter and the battery are at stand by in this mode and the voltage slowly changes between $340V_{dc}$ and $360V_{dc}$ based on the available PV power and the load on the bus. Figure 4.5 shows the results from this mode. It can be seen that the ultracapacitor reacts to the PV variation and slows down the voltage changes to prevent the battery from microcycle charging and discharging.

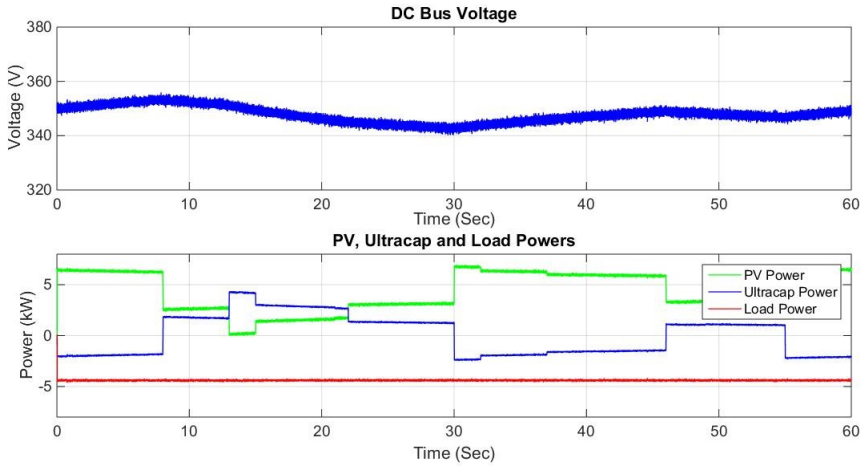

Figure 4.5 Operation Mode I: Battery and the grid-tied inverter at stand by, PV at MPPT and ultracapacitor as the slack terminal.

- **Mode II:** The battery regulating the bus voltage by drawing power from the microgrid following a droop profile while the PV operating at MPPT and the grid-tied inverter is at stand by. The bus voltage can be anywhere between $360\,V_{dc}$ and $380\,V_{dc}$, depending on the required power that battery has to store. Figure 4.6 shows the result from this operation mode.

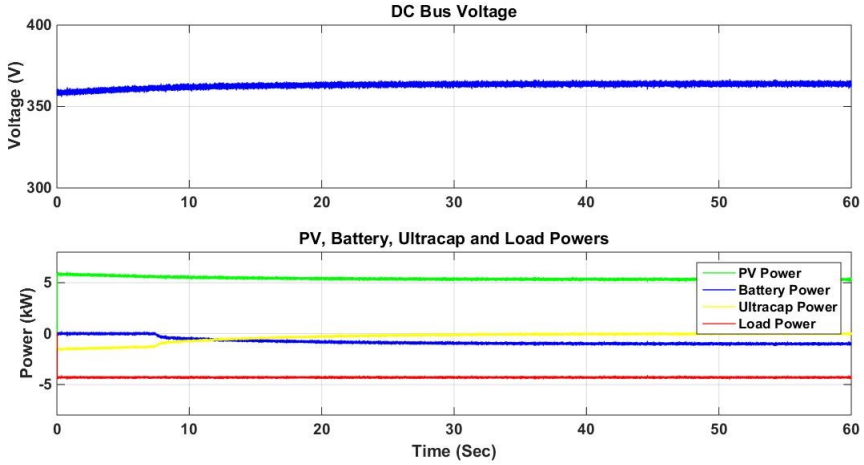

Figure 4.6 Operation Mode II: Battery regulates the bus voltage by drawing power from the microgrid and Grid-tied inverter at stand while PV is at MPPT.

- **Mode III:** The battery regulating the bus voltage by discharging to the microgrid following a droop profile while the PV operating at MPPT and the grid-tied inverter is at stand by. The bus voltage can be anywhere between $320\,V_{dc}$ and $340\,V_{dc}$, depending on the required power from the battery. Results from this operation mode is presented in Figure 4.7.

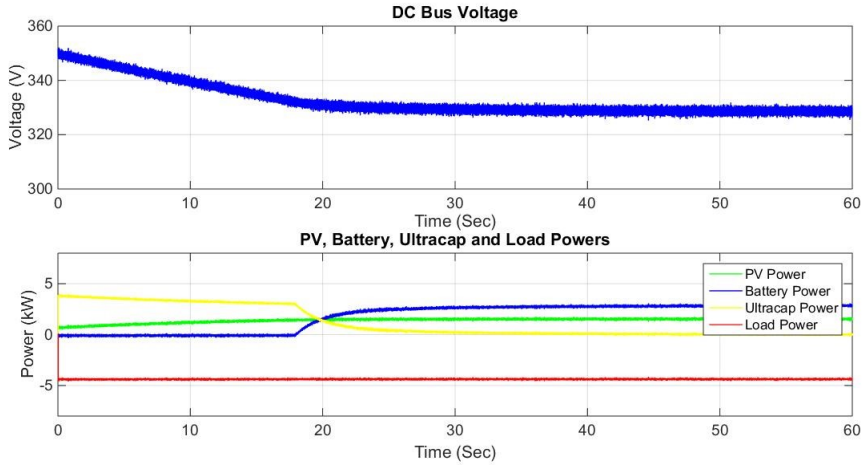

Figure 4.7 Operation Mode III: Battery regulates the bus voltage by importing power to the microgrid and the grid-tied inverter at stand by, while PV is at MPPT.

- **Mode IV:** In this mode, the battery cannot regulate the DC bus voltage. This can be due to high load or low PV generation or low SoC of the battery. Therefore, the grid-tied inverter keeps the voltage at $320\,V_{dc}$ by importing power form the main grid. Figure 4.8 Summarizes the results from this mode.

- **Mode V:** In this mode, the battery cannot regulate the DC bus voltage. This can be due to low load or high PV generation or high SoC of the battery. Therefore, the grid-tied inverter keeps the voltage at $380\,V_{dc}$ by exporting the excess power form the microgrid to the main grid as it is shown in Figure 4.9.

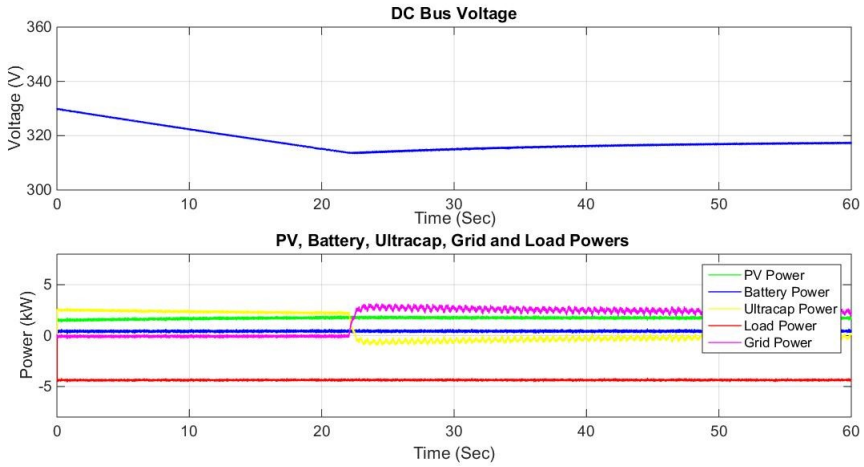

Figure 4.8 Operation Mode IV: Grid-tied inverter is the slack terminal and regulates the voltage by importing power to the microgrid from the main AC grid.

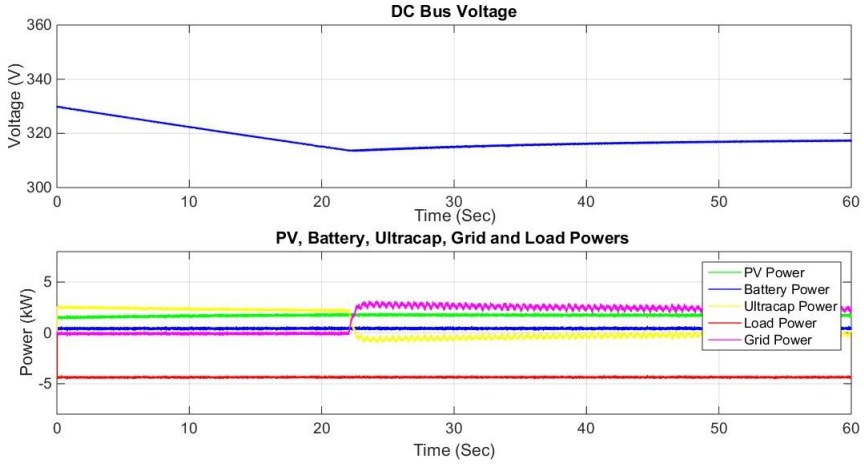

Figure 4.9 Operation Mode V: Grid-tied inverter is the slack terminal and regulates the voltage by exporting power to the main AC grid.

4.2 Distributed with Multiple Slack Terminals

The basis of the proposed control platform is to achieve stability by paralleling voltage sources on the DC bus. Each source is able to regulate the voltage at its output and is designed with the knowledge of its topology, switches, power source, and output capacitance such that it is stable under any external load fluctuations within the limits of its power

rating. In other words, each source is a "slack" terminal, similar to slack generators in power systems, in that it provides whatever power is necessary to ensure power balance and maintain the bus voltage. As a system expands to include multiple sources, the system is stable as long as each source is stable. This core structure enables microgrid advantages of redundancy, simple plug-and-play, modularity and expandability.

In this section, we first explain the control strategy in details as well as the controller design criteria of the different converters of the system. Then, C-HIL simulations are used for demonstrating the effectiveness and feasibility of the proposed platform and control algorithm in a typical PV plus BESS grid-interactive DC microgrid.

4.2.1 Control Algorithm

The basis of the proposed control platform is to achieve stability by paralleling voltage sources on the DC bus. The challenge that comes in paralleling voltage sources, is to control the amount of power each source contributes or absorbs. Without an additional control layer, sources may disproportionally source or sink power due to proximity and line impedances. Additionally, circulating currents can arise from slight differences in voltage feedback measurements, which is significant in microgrid systems with relatively small line impedances. To control and balance the power contribution among sources, a virtual resistance is added in the controller to dominate the effects of actual line resistance and feedback error. With multiple devices paralleled, their power contribution is proportional to their virtual resistances, allowing the system to achieve power sharing or alternatively prioritization of the sources. The virtual resistance control method is extended to defining a steady state voltage vs. current function for each converter, such that the operating power of each device is defined at the specific global voltage. This control falls under the category of droop control, a well-established method of distributed control, where devices react to locally measurable quantities and according to a common predefined relationship or

equation. The following equation shows that how the reference voltage of a typical converter in a DC microgrid is calculated based on its virtual resistance and its output current [74].

$$V_{ci}^{*} = V_{ni} - R_{di} I_{ci} \tag{4.6}$$

where V_{ci}^{*} is the reference output voltage for the i^{th} converter, V_{ni} is the nominal voltage of the i^{th} converter, R_{di} is the value of the virtual resistance (droop coefficient) and I_{ci} is the output current of the i^{th} converter.

In this dissertation, we are modifying equation (4.19) so that the reference voltage will be dependent not only on the output current and the droop coefficient, but also the DC bus voltage and the nominal voltage of the converter. In the other words, the proposed control algorithm is the combination of voltage droop control and DBS. The reason behind this modification is to enable features such as islanding, demand response, peak shaving, and redundancy in the microgrid.

Following equation shows which parameters are used for calculating the reference voltage of the system's converters.

$$V_{ci}^{*} = f(V_{ni}, V_{dc}, I_{ci}, R_{di}) \tag{4.7}$$

where V_{dc} is the DC bus voltage.

Fig. 4.10(a) shows the schematic of a typical DC microgrid consisting of a PV array, two BESSs and a grid-tied converter. Same figure shows the $I-V$ characteristics of the system's slack sources in two different cases and how the global voltage is determined by the balance of load and supply on the system. The distributed sources will share current according to the modified droop function discussed in Equation 4.7. In the first case, Figure 4.10(b), the BESSs (red and blue) will supply power only if the grid-tied converter and the PV cannot meet the demand, which happens if the voltage falls out of the dead-band. In the second

case, Figure 4.10(c), the grid-tied source (green) will supply power only if the two BESSs and the PV cannot meet the demand, which happens if the voltage falls out of the dead-band. In the other words, grid is a redundant backup source. In both cases, each slack source's outer control layer handles the energy management by the droop function, and the inner voltage control layer achieves instantaneous power balance and ensures stability.

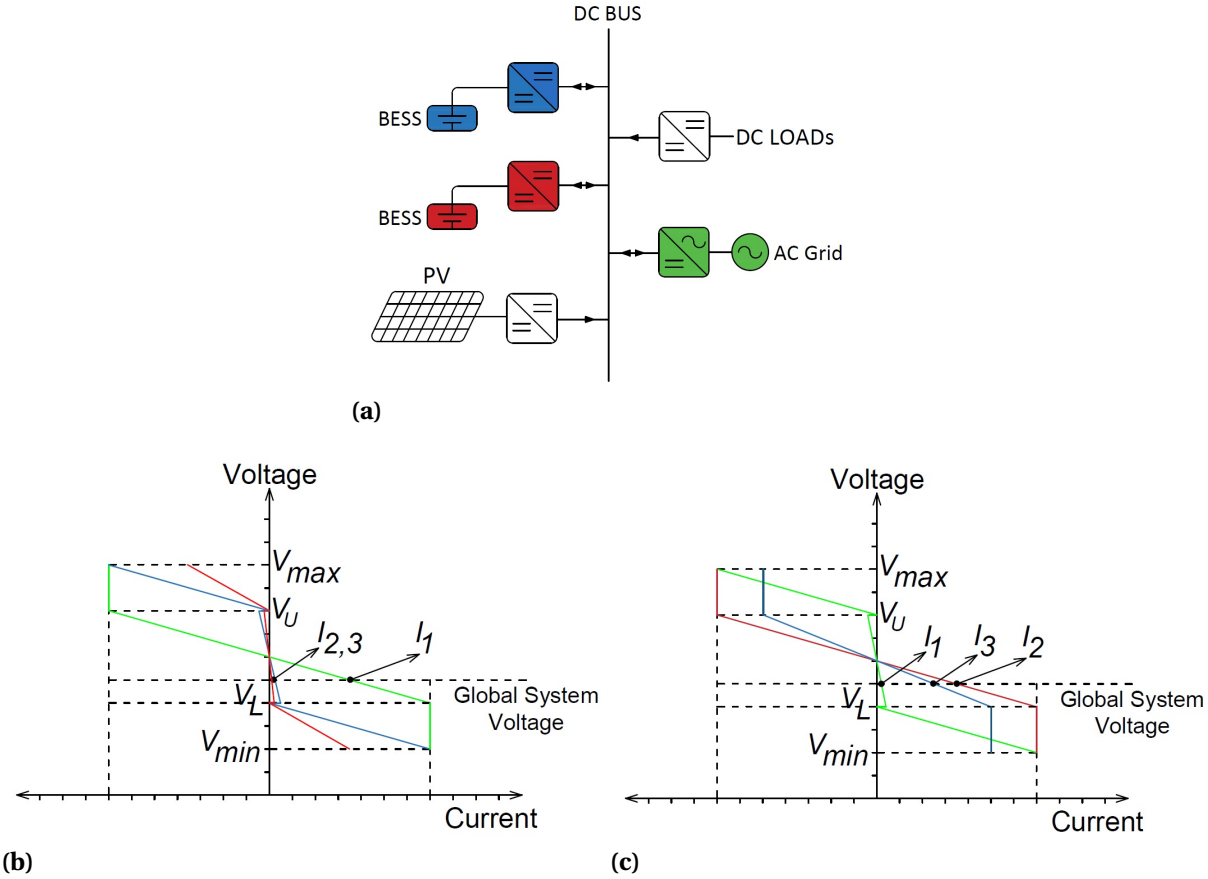

Figure 4.10 (a): Schematic of a typical DC microgrid. (b): I-V characteristics of the slack sources in case I. (c): I-V characteristics of the slack sources in case II.

In this study, the BESS converters assumed to be bidirectional buck converters. The grid-tied inveter is a voltage source inverter (VSI) in series with a bidirectional buck converter as shown in Figure 4.11. The first stage, VSI, is responsible to keep V_{in} at $1.3kV$, while the

second stage is responsible for energy management and regulating the microgrid's DC bus voltage.

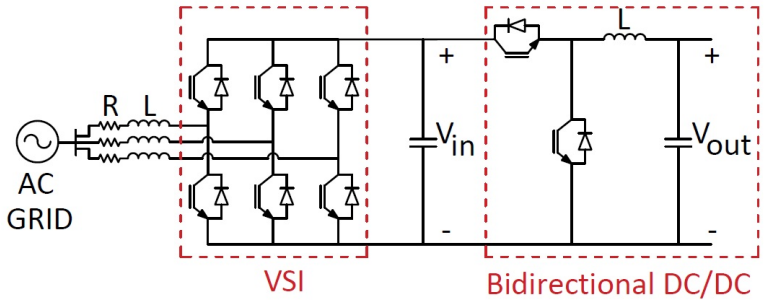

Figure 4.11 Topology of the grid-tied inverter.

Block diagram of the VSI and the DC/DC converters of the system including: the BESSs converter and the second stage of the grid-tied converter are shown in Figure 4.12(a) and (b), respectively.

4.2.2 Controller Design

As it was shown in Figure 4.10, the microgrid consists of a grid-tied converter, two BESS units, a PV array and DC loads. BESSs and the grid-tied converter are considered to be slack sources in this system and regulate the DC bus voltage following the modified droop-based controller discussed earlier. PV converter uses well-known perturb and observe algorithm to track the maximum power point and it can be considered as a variable current source, while loads are considered as a variable current sink. Therefore, controller design will be done for the slack sources of the system only. Table 4.1 shows the specifications of the DC microgrid which controller has been designed for.

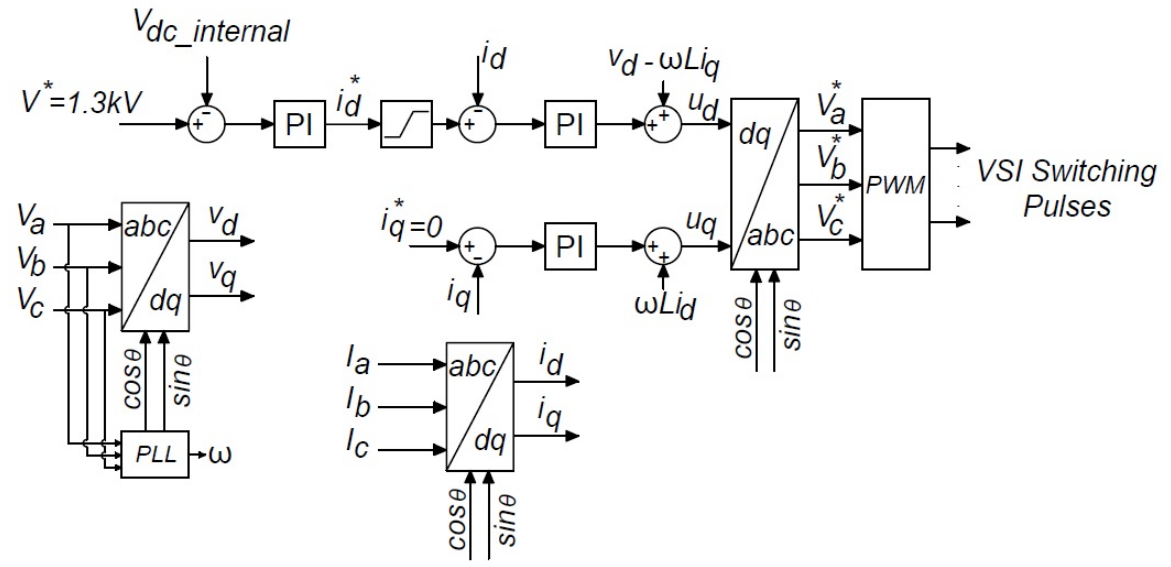

(a)

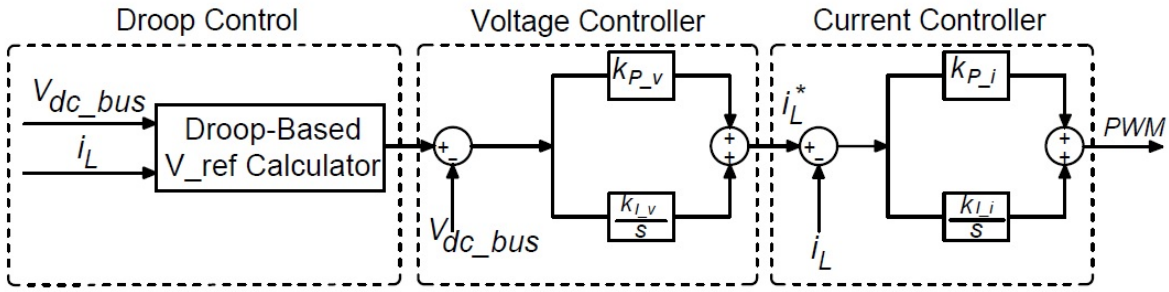

(b)

Figure 4.12 (a): Control block diagram of the VSI. (b): Control block diagram of the system's DC/DC converters including inner voltage control and current control layers and outer energy management layer.

4.2.2.1 Inner Current and Voltage Control Layers

The first step toward designing the controller is to design the inner current and voltage controller layers of each source with the knowledge of its topology, power rating and output filter such that it is stable under any external load fluctuations within the limits of its power rating. Then, the current controller is designed in such a way to be at least 5 times faster than the voltage controller so that the current controller does not affect the response time

Table 4.1 Specifications of the DC Microgrid.

Component	Power Rating	Max Current	Nominal Output Voltage	Output LC Filter	Switching Frequency
Grid-Tied Converter	$60kW$	$130(A)$	$380V_{dc}$	$L=5mH, C=500\mu F$	$20kHz$
BESS Units (each)	$30kW$	$65(A)$	$380V_{dc}$	$L=5mH, C=500\mu F$	$20kHz$
PV Optimizer	$80kW$	$220(A)$	$380V_{dc}$	$L=5mH, C=500\mu F$	$20kHz$
Load	$50kW$	$137(A)$	$380V_{dc}$	$L=5mH, C=500\mu F$	$20kHz$

and stability of the converter. It was mentioned earlier that, the battery converters of the system are bidirectional buck converters and we also assume that the first stage of the grid-tied converter, VSI, is fast enough so that the internal DC bus of the grid-tied inverter (the input voltage of the second stage) is always fixed at $1.3kV$. With these assumptions, the design of current and voltage controllers for all the system's slack converters, will be similar to the design of voltage controller for the buck converters and can be described as following

The first step toward designing a voltage regulator for a DC/DC converter is to derive its small signal model and the transfer functions. Then the compensator can be designed using the small signal model.

Output voltage of the open-loop converter can be expressed as

$$\hat{v}(s)=G_{vd}(s)\hat{d}(s)+G_{vg}(s)\hat{v_g}(s)-Z_{out}(s)\hat{i}_{load}(s) \tag{4.8}$$

where $\hat{v}(s)$ is the small signal variations of the output voltage, $\hat{d}(s)$ is the small signal variations of the duty cycle , $\hat{v}(g)$ is the small signal variations of the input voltage, $\hat{i}_{load}(s)$ is the small signal variations of the load current . and:

$G_{vd}(s) = \frac{\hat{v}(s)}{\hat{d}(s)}$, $G_{vg}(s) = \frac{\hat{v}(s)}{\hat{v}_g(s)}$, $Z_{out}(s) = \frac{\hat{v}(s)}{\hat{i}_{load}(s)}$.

Output voltage of the closed-loop converter (including sensor, compensator and pulse width modulation gains) can be expressed as

$$\hat{v} = \hat{v_{ref}} \frac{1}{H} \frac{T}{1+T} + \hat{v}_g \frac{G_{vg}}{1+T} - \hat{i}_{load} \frac{Z_{out}}{1+T} \tag{4.9}$$

with

$$T(s) = H(s) G_c(s) G_{vd}(s) \frac{1}{V_M} \tag{4.10}$$

where $H(s)$ is the sensor gain, $G_c(s)$ is the compensator transfer function and V_M is the pulse width modulator gain.

Also Equations 4.11, 4.12 show G_{vd} and G_{vg} of the buck converter.

$$G_{vd} = \frac{V_0}{D} * \frac{1}{LCS^2 + \frac{L}{R}S + 1} \tag{4.11}$$

$$G_{vg} = D * \frac{1}{LCS^2 + \frac{L}{R}S + 1} \tag{4.12}$$

Products of the gains around the negative feedback loop also known as loop gain for the buck converter is shown in equation 4.13. It should be noted that this the uncompensated loop gain.

$$T_U(S) = \frac{T_U(0)}{LCS^2 + \frac{L}{R}S + 1} \tag{4.13}$$

Where $T_U(0) = V_{in} * \frac{1}{V_M} * H$.

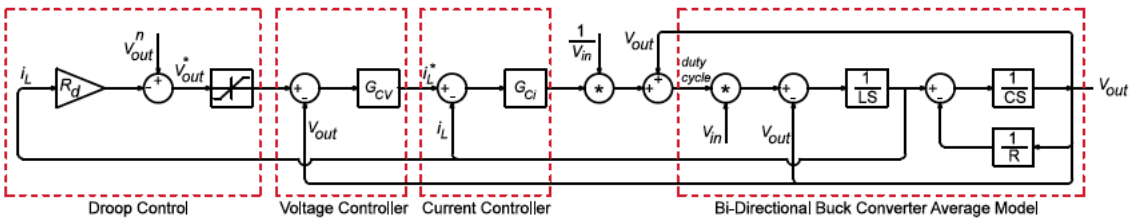

Figure 4.13 Block diagram of the bi-directional buck DC/DC converter average model and its controllers.

Also the compensator's gain can be written as

$$G_c(s) = K_p(1 + \frac{\frac{K_I}{K_P}}{S}) \tag{4.14}$$

where K_P and K_I are the proportional and integral gains of the voltage PI controller. Consequently, the compensated loop gain for the buck converter can be shown as the following equation

$$T(S) = (1 + \frac{\frac{K_I}{K_P}}{S}) \frac{T_U(0)K_P}{LCS^2 + \frac{L}{R}S + 1} \tag{4.15}$$

In this dissertation, the voltage controller of the converters were designed using the aforementioned approach to give us the desired bandwidth. Since the switching frequency considered to be $20kHz$ for all the converters, the compensator for the DC/DC converters of the system, i.e. battery converters and second stage of the grid-tied inverter, were designed to result in crossover frequency of $200Hz$.

Block diagram of the bidirectional buck DC/DC converter and its controllers including: droop controller, voltage and current controller is shown in Figure 4.13. Also the bode plot of the open loop compensated voltage controllers is shown in Figure 4.14. It can be seen in the bode plots that the desired crossover frequency is achieved and a phase margin test will show that the controllers are stable.

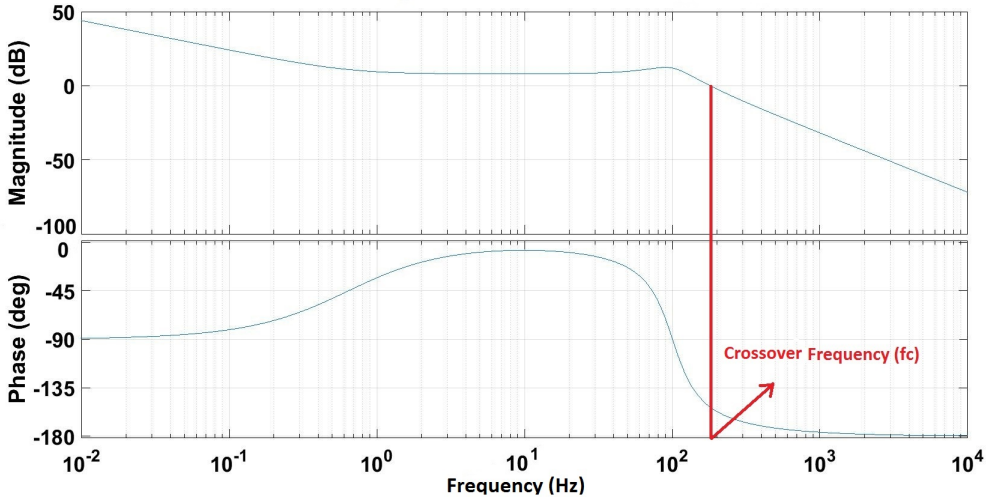

Figure 4.14 Bode plot of the voltage controllers of the converters of the system for illustrating the controllers bandwidth and stability.

4.2.2.2 Outer Energy Management Layer

The second step is to design the outer control layer which handles the energy management by the droop function. The outer layer can be designed in number of different ways to fit the requirements of the customer. In this section, design was done for two cases: **Case I:** where grid is the primary source responsible for regulating the DC bus voltage and BESS units are the backup to the grid. **Case II:** where BESS units are the primary sources responsible for regulating the DC bus voltage and grid is the backup to BESSs. The outcomes of these two design steps for the system shown in Figure 4.10 with the specifications shown in Table 4.1, are summarized as the following

In Both Cases:

$$\begin{cases} V_{min} = 365V \quad V_L = 372.5V \\ V_U = 387.5V \quad V_{max} = 395V \\ k_{P_{vG}} = 0.04 \quad k_{I_{vG}} = 2.5, k_{P_{cG}} = 1.5 \quad k_{I_{cG}} = 3.5 \\ k_{P_{vB}} = 0.25 \quad k_{I_{vB}} = 2, k_{P_{cB}} = 2.5 \quad k_{I_{cB}} = 5 \end{cases} \tag{4.16}$$

where k_P and k_I are proportional and integral gains of the PI controller. v and c subscripts stand for the voltage and current controllers respectively, while G and B stand for the grid-tied converter and BESS converter.

Case I: Grid is the Primary, BESSs are the Backup:

$$\begin{cases} V^*_{Grid} = 380 - R_{dG} * I_G \\ V_{dc} > V_U : V^*_{BESS} = 387.5 - R_{dB} * I_B \\ V_{dc} < V_L : V^*_{BESS} = 372.5 - R_{dB} * I_B \\ V_L < V_{dc} < V_U : V^*_{BESS} = 380 - 1.5 * I_B \\ R_{dG} = \frac{15}{260} \quad R_{dB} = \frac{7.5}{65} \end{cases} \tag{4.17}$$

where V^*_{Grid} is the calculated reference voltage of the grid-tied converter, R_{dG} is the droop slope of the grid-tied converter, I_G is the output current of the grid-tied converter, V_{dc} is the DC bus voltage, V^*_{BESS} is the calculated reference voltage of the BESS converters, R_{dB} is the droop slope of the BESS converters, I_B is the output current of the BESS converters.

Case II: BESSs are the Primary, Grid is the Backup:

$$\begin{cases} V^*_{BESS} = 380 - R_{dB} * I_B \\ V_{dc} > V_U : V^*_{Grid} = 387.5 - R_{dG} * I_G \\ V_{dc} < V_L : V^*_{Grid} = 372.5 - R_{dG} * I_G \\ V_L < V_{dc} < V_U : V^*_{Grid} = 380 - 1.5 * I_G \\ R_{dG} = \frac{7.5}{130} \quad R_{dB} = \frac{15}{130} \end{cases} \tag{4.18}$$

It should be mentioned that in all the above expressions, currents injected to the DC bus are considered as positive and the currents drawn from the microgrid are considered negative.

4.2.3 Control-HIL Platform and Results

Effectiveness and feasibility of the proposed control method were tested in a C-HIL platform as shown in Figure 4.15. PV, BESS, AC grid and all the power electronics converters of the system shown in Figure 4.10 are modeled in the Typhoon HIL 602 simulator. Three TI DSP f28335 controllers were used to control the switching converters of the system. First DSP controls the grid-tied inverte, second DSP controls the two battery charge controllers and the last DSP is responsible to control the PV MPPT converter. Finally, an interface board was used for interfacing the simulated model to the TI controllers.

Simulation results for case I (grid is the primary, BESSs are backup) and case II (BESSs are the primary, grid is backup) summarized in Figure 4.16 and 4.17.

For the reasons mentioned in Section 4.1.1.2, a communication network can be beneficial for the system. Also implementing a communication network will enable remote monitoring and control of the converters as well.

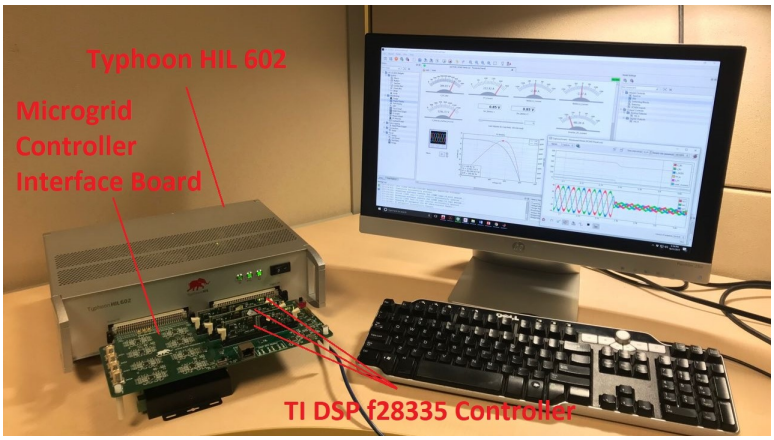

Figure 4.15 C-HIL setup of for testing the system's effectiveness and features.

Figure 4.18(a) shows the adopted scheme for the communication network. As it can be seen the Master collects data from slaves using MODBUS Queries and instructs to change parameters to control the DC Microgrid by writing to MODBUS registers. The Master exposes a web-interface to observe and visualize the Data. The web-interface provides users the ability to turn on/off or send instructions to slaves via user input. The operation of this scheme can be summarized as

The Master Polls for Data from slaves by making MODBUS Queries using a MODBUS TCP Client, MODBUS RTU messages are exchanged with a DSP on a RS232 line. Modbus messages that are not intended for DSP1 are encapsulated in a CAN message and broadcasted to other slaves on CAN Bus. Only the DSP whose slave ID matches the one in the request responds by encapsulating a MODSBUS response in a CAN message and sends it back to DSP1 which responds back to the request made by the master.

Figure 4.18(b) shows the hardware setup for the communication network. In Figure 4.19 a screenshot of the web-interface is shown. The web-interface can be used for only monitoring purposes as well as sending control commands. In this work, the master is programmed in such a way to enable remote monitoring, sending on/off commands to the system components and perform SoC balancing.

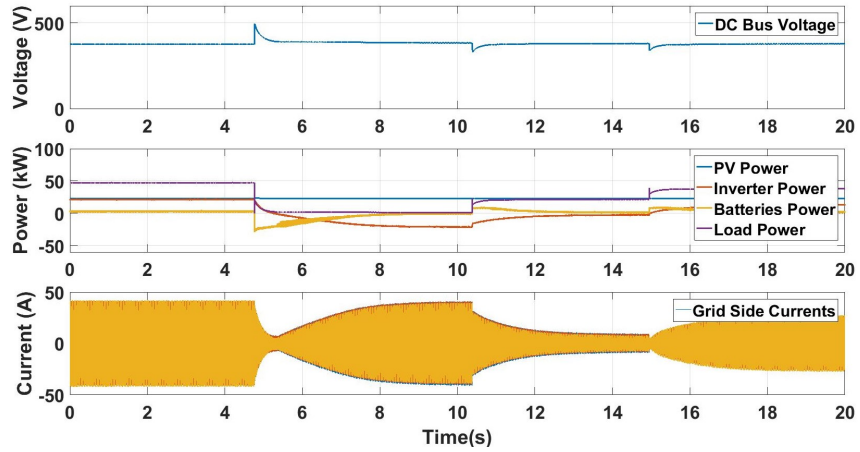

(a)

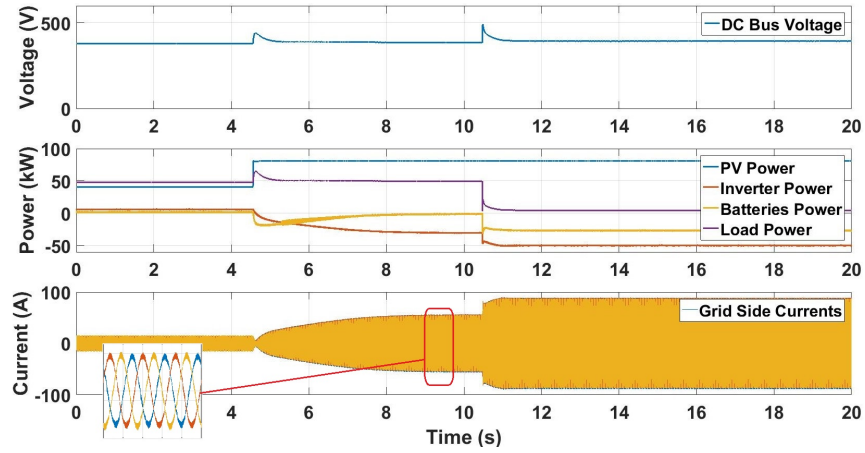

(b)

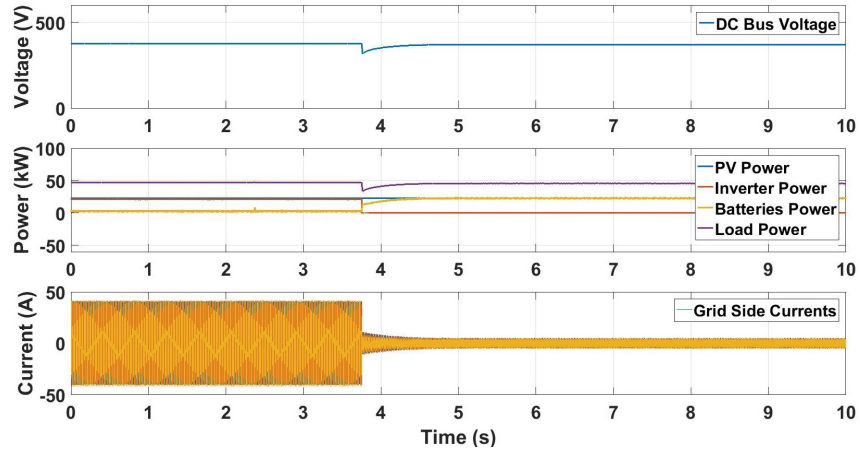

(c)

Figure 4.16 Simulation results for case I: grid is the primary, BESSs are backup. (a): Grid-tied converter regulating the bus voltage and BESSs are backup. (b): BESSs helping the grid to regulate the DC bus voltage. (c): Grid connection is lost and BESSs regulate the DC bus voltage (islanding).

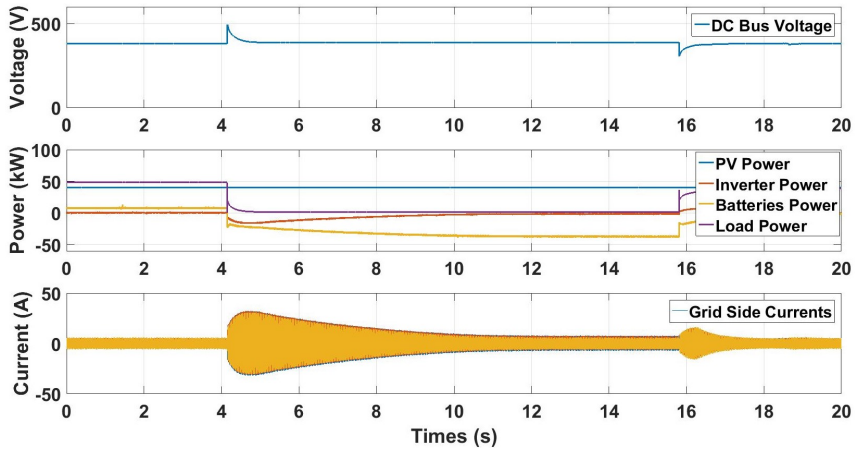

(a)

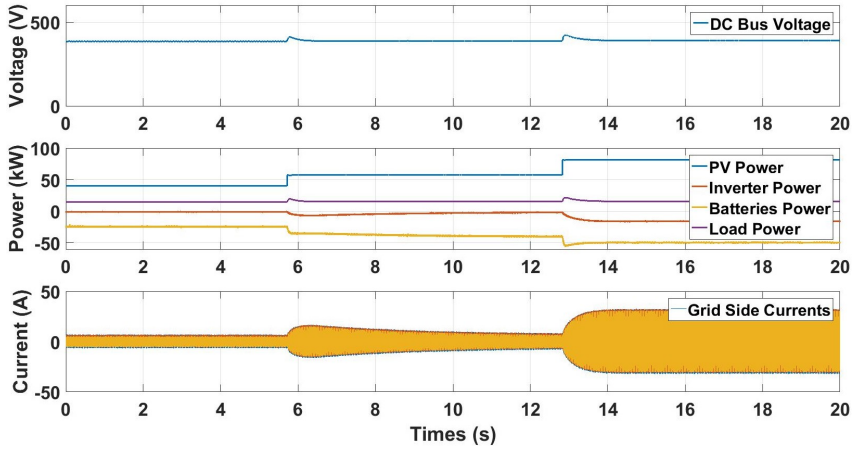

(b)

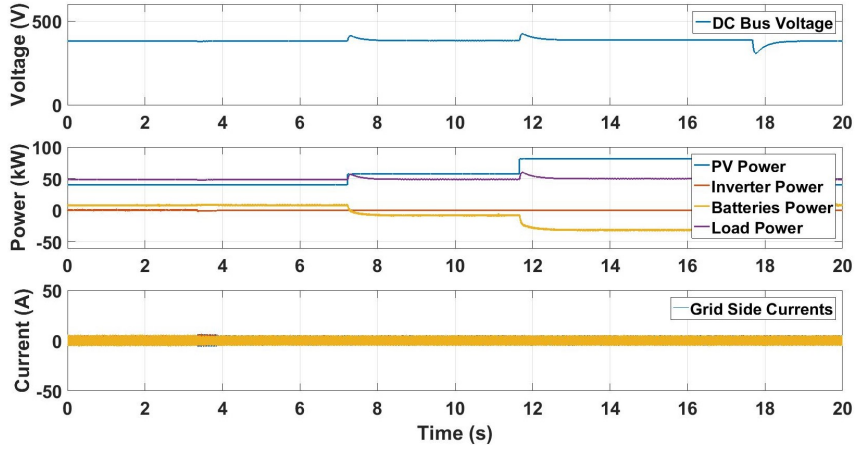

(c)

Figure 4.17 Simulation results for case II: BESSs are the primary, grid is backup. (a): BESSs are regulating the DC bus voltage and grid is the backup. (b): Grid-tied converter helps BESSs to regulate the DC bus voltage. (c): Grid connection is lost and BESSs regulate the DC bus voltage (islanding).

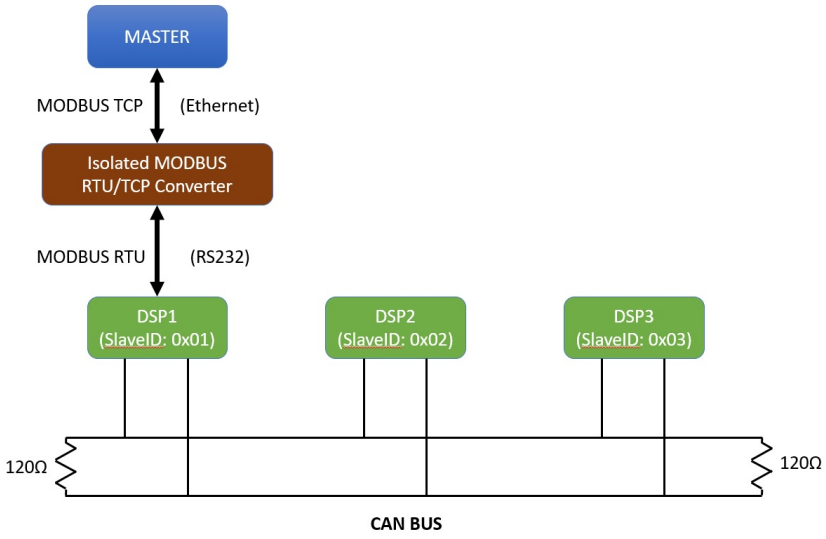

(a)

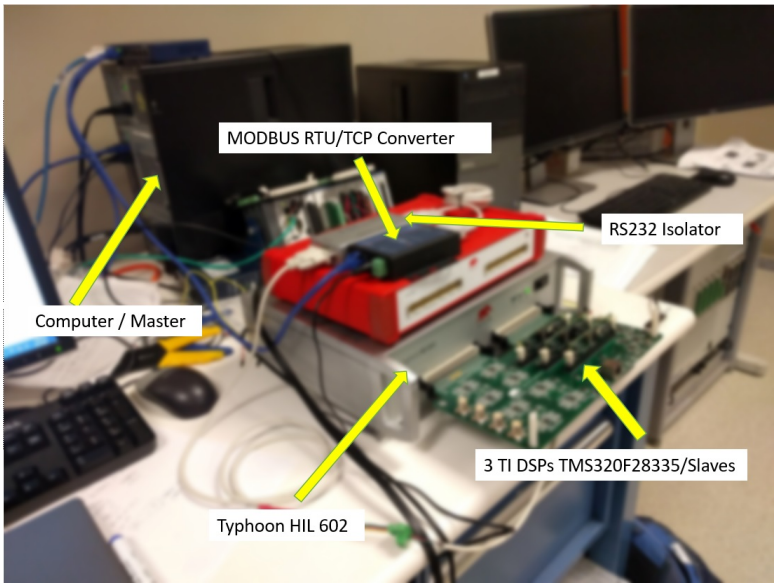

(b)

Figure 4.18 (a): Adopted scheme for the communication network. (b): Communication network hardware setup.

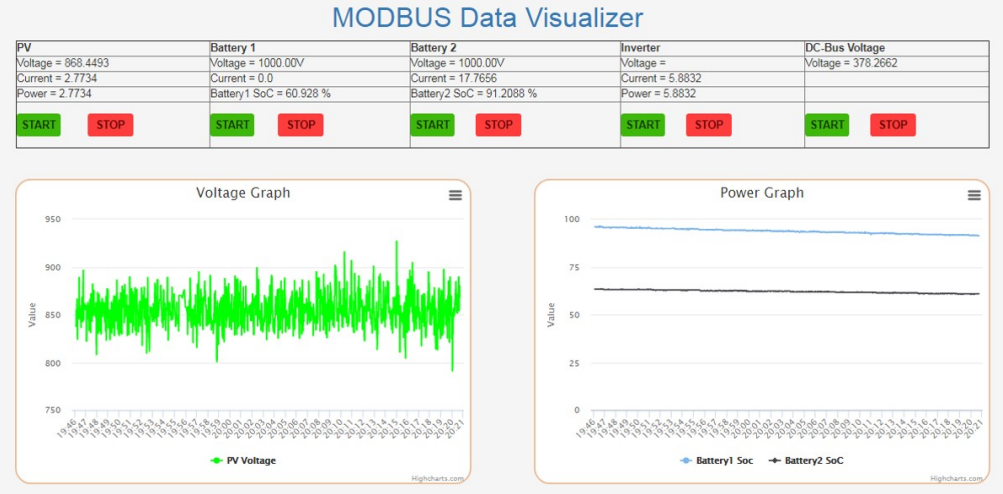

Figure 4.19 A screenshot of the webpage designed for remote monitoring and control of the system.

4.3 PV and Load Power Smoothing

Large-scale deployment of distributed renewable energy resources like solar in the micro-grids, has to provide utilities and grid operators the capability to safely and reliably mitigate the impact of solar and loads intermittency on the main AC power grid [75]. Therefore, the control algorithm should be able to reliably mitigate the impact of PV and load variations in the microgrid from transferring to the AC power grid, when the microgrid is operating in grid-tied mode.

The goal for the power smoothing algorithm is to be able to selectively choose one or more slack converters to handle power fluctuations by regulating the DC bus voltage, while other converters do not see the power fluctuations, but are available to regulate the DC bus if the primary converter were to fail or could not handle the fluctuation. In this section, four possible methods for PV and load power smoothing are proposed and two of the most promising methods are further studied.

4.3.1 Standby Mode

One approach to selectively control converters as to whether they are subject to power fluctuations is to use a standby mode. In this approach, the active converters, the ones that regulate the DC bus and handle power fluctuations, are controlled as voltage sources with the goal of maintaining their output voltage. These converters can utilize droop control, as in the aforementioned DC control platform, in order to control power sharing at steady-state. When a transient occurs, one or more of the active converters will act to regulate the voltage, while the standby converters remain in a constant state. The portion of power each active converter contributes to mitigating the fluctuation depends on the proximity to the fluctuation in terms of line resistance and on the speed of the voltage controller.

The standby mode would put the inactive converters into a current-control or power-control mode, where they can either remain idle or they could import/export a fixed quantity. These converters would monitor the bus voltage and if it falls outside of a specific range, they would switch control modes to voltage-control in order to maintain power balance and regulate the bus voltage.

The disadvantage of the standby mode approach is that when the controller changes from current-control mode to voltage-control mode, the integrator term in the voltage controller takes time to accumulate an error. This discrete change-over would cause an overshoot, which is difficult to predict and therefore difficult to account for in design. A predictive component or a derivative gain can be added to the controller to mitigate the overshoot term. Or an energy storage system such as ultracapacitor or battery can be connected to the DC bus directly to prevent voltage overshoot or undershoot in the mode changes.

4.3.2 Current Based Droop Control

As an alternate to the approach of having multiple voltage sources in parallel for redundancy, a current control based droop algorithm can be used to achieve both redundancy and selective power smoothing. In this type of droop control, the slack sources, like batteries or grid-tied converters, are current controlled where the setpoint or current command reference is a function of the DC bus voltage. Whenever the bus voltage drops, the sources sense the dropping voltage and increase their current to compensate. Likewise, when the bus voltage increases, they draw current from the bus to prevent an overvoltage. The current functions allow devices to share power at a steady state voltage as well as prioritize which devices take on the load fluctuations first. For example, a converter that is set to supply power to the bus when the voltage falls below $350 V_{dc}$ would handle fluctuations within its power before a converter that is set to supply power to the bus when the voltage falls below $340 V_{dc}$.

However, the downside of the current-based droop control approach is that the stability depends on many factors including the response time of each converter, the overall capacitance in the system, and the size of the overall generation and load. In medium sized systems around 100 kW, the sources have to be extremely fast to ensure stability.

4.3.3 Standby Mode with Direct Connection of Energy Storage

This approach is similar to the standby method, but the overshoot/undershoot concern is mitigated by attaching a large energy storage element directly to the DC bus. A battery or ultracapacitor could be used to regulate the DC bus voltage, and other connected sources could be controlled in constant power mode (current mode). In this scenario, the storage element would handle all power fluctuations and all other converters could be controlled to have constant or smooth power outputs.

4.3.3.1 Experimental Verification

Setup shown in Figure 4.4 was used to demonstrate the feasibility of the proposed PV smoothing method. Figure 4.20 shows how the PV output fluctuations are getting absorbed by the ultracapacitor when the microgrid is transferring power with the main AC grid. In this figure, the grid-tied is operating in constant power mode and the ultracapacitor is the slack terminal.

Figure 4.21 shows a case where grid-tied converter is operating in voltage control mode and whenever the voltage falls out of the dead band, tries to regulate the voltage. As it can be seen, the grid-tied converter is reacting to PV changes and solar output smoothing is not achieved.

There are several downsides of this approach. Ultracapacitors are expensive for this type of application. Direct connection of batteries may be a viable solution economically, but it inhibits the flexibility of the bus voltage. The bus voltage is fixed according to the battery, and cannot be easily used as a control variable for the system. Additionally, care must be taken such that the battery is not over charged or over discharged and that the charging and discharging rates do not damage the battery. Finally, both directly connected ultracapacitors and batteries would increase the available fault current on a system, making the system potentially less safe and the protection design more difficult.

4.3.4 Controller Bandwidth Adjustment

The proposed control method in this section achieves allows the user, or supervisor controller, to designate one or more converters to absorb power fluctuations while the other converters experience smoother power demands. The proposed method adjusts the bandwidth of the controllers to select the frequency of fluctuations to subject to each converter. This method fits nicely within the larger power control framework to achieve all of the

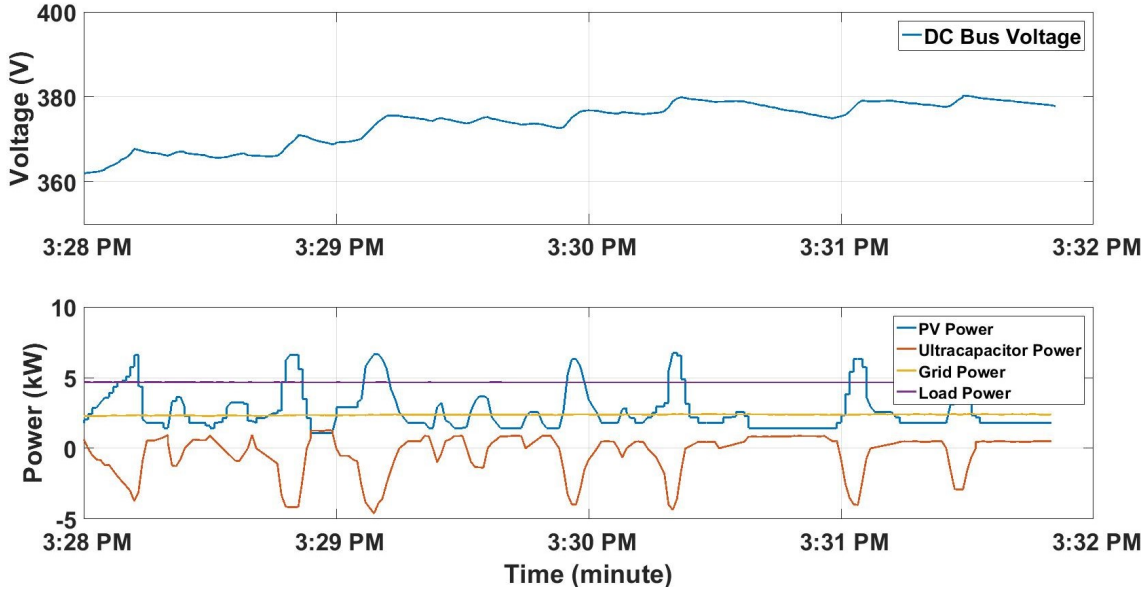

(a)

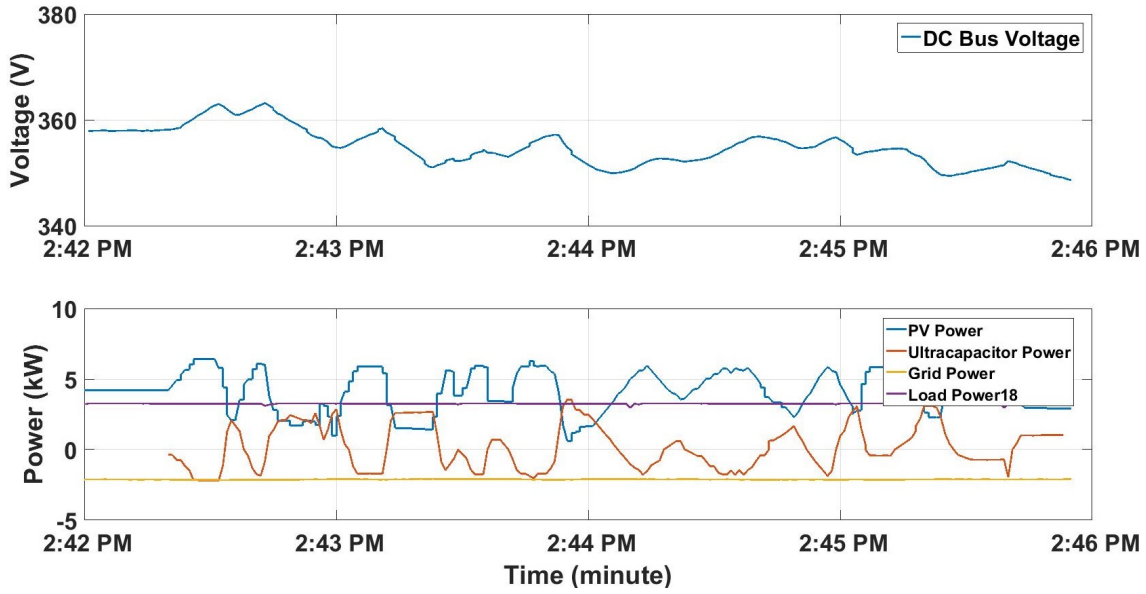

(b)

Figure 4.20 Solar output smoothing using standby mode with direct connection of energy storage method. (a): Microrgid imports power from the AC grid. (b): Microgrid exports power to the AC grid.

control objectives of instantaneous power balance, steady state power sharing, redundancy, expandability, and finally selective transient power smoothing [74]. Compared to previous

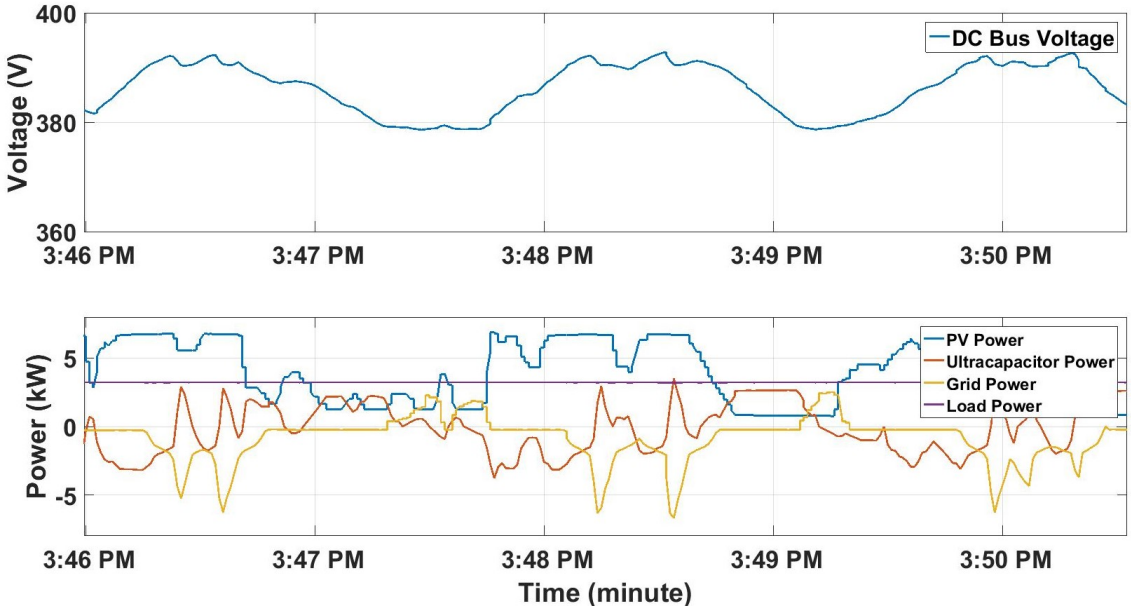

Figure 4.21 Grid-tied converter is reacting to PV changes and solar output smoothing is not achieved.

methods of power smoothing, the proposed method does not require a single slack terminal, DC bus signaling, or converter mode changes, which can lead to high overshoots or instability [76].

4.3.4.1 Overall Approach

The proposed approach works alongside the voltage-based droop control platform described in Section 4.2. In that platform, there are multiple voltage sources regulating the DC bus in parallel. To control and balance the power contribution among sources, a virtual resistance is added to the voltage controller to dominate the effects of actual line resistance and feedback error. With multiple devices paralleled, their power contribution is proportional to their virtual resistances, this method of power balancing and paralleling is known as droop control method also.

The following equations shows that how the reference voltage of each converter gets

updated based on its virtual resistance and output current.

$$V_{ci}^{*} = V_n - R_{di} I_{ci} \tag{4.19}$$

where V_{ci}^{*} is the updated reference voltage of the i^{th} converter, V_n is the nominal voltage, R_{di} is the virtual resistance(droop slope) of i^{th} converter and I_{ci} is the output current of the i^{th} converter.

Each voltage controller is designed such that it is stable in regulating its output voltage given the capacitance in the converter and given its power rating. For a given capacitance, and power rating, there is minimum speed, or bandwidth, at which the voltage controller must respond to ensure stability. If the converter speed exceeds the minimum requirement, it remains stable and will act faster in regulating the voltage.

We propose an adjustable controller bandwidth, or adjustable speed, such that specific voltage controllers can be designated to act more quickly or slowly than others. During adjustments, the slower controllers would remain above the stability threshold, so as to provide redundancy if the fast controllers are unable to regulate the DC bus voltage. The downside of this approach is that the converters may have to be overdesigned to operate at a speed faster than absolutely necessary.

4.3.4.2 System Specifications

Figure 4.22 shows the schematic of a generic DC micorgrid which we demonstrate the feasibility of our control algorithm on. As it can be seen in the figure, the microgrid consists of loads, sources, the local controllers, master controller and the communication network. The communication is used for higher level features only, whereas the power balancing algorithm is distributed and fast acting, since it responds to unexpected events such as a device failures, new devices coming online, and grid outages.

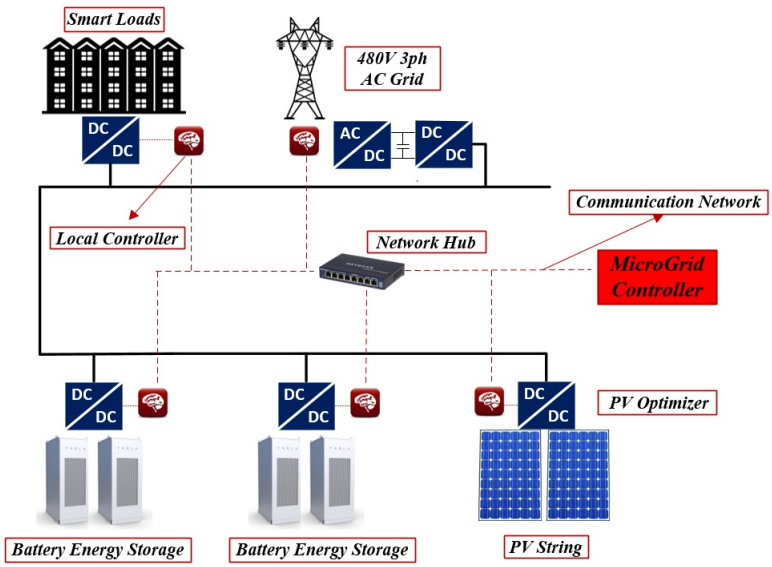

Figure 4.22 Schematic of a generic DC micorgrid which is used for demonstrating our control algorithm.

In this system, grid and two batteries are the slack terminals which are responsible for regulating the DC bus voltage. The power sharing between the slack terminals are achieved using droop control. The PV is always operating at the maximum power point and therefore, it is considered as a variable current source, while the load terminal is considered as a variable current sink. PV and load smoothing are realized by adjusting voltage controller speed for the slack terminals such that specific terminals, battery terminals in this case, act more quickly to absorb the fluctuations in PV and load. The controller design is discussed in the remainder of this section.

Topology of the grid-tied inverteras it was shown in Figure 4.11, it can be seen that it is a double stage converter where a three phase VSI is in series with a bidirectional buck DC/DC converter. All the other DC/DC converters of the system are bidirectional buck converters as well, the same as the second stage of the grid-tied inverter, except the PV DC/DC optimizer which is a unidirectional buck converter.

For designing the controllers, it is assumed that the nominal DC bus voltage is $380 V_{dc}$,

Table 4.2 Specifications of the DC system for testing PV and load smoothing functionalities.

Component	Power Rating	Max Current	Nominal Output Voltage	Output LC Filter	Switching Frequency
Grid-Tied Inverter	$30kW$	$30A$	$380V_{dc}$	$L=5mH, C=500\mu F$	$20kHz$
Battery DC/DC	$30kW$	$30A$	$380V_{dc}$	$L=5mH, C=500\mu F$	$20kHz$
PV Optimizer	$30kW$	$30A$	$380V_{dc}$	$L=5mH, C=500\mu F$	$20kHz$

power rating of all the converters of the system are $30kW$, and the voltage controller of the first stage of grid-tied inverter is fast enough so that the internal DC bus voltage of the double stage inverter is always fixed at $1.3kV_{dc}$. Table 4.2 summarizes the specs of the system.

4.3.4.3 Controller Design

The three voltage sources that operate in parallel and are responsible for power balancing in the mentioned DC microgrid, are two batteries and a grid-tied inverter. Therefore, to ensure stable operation of the microgrid as well as the power smoothing capability, their voltage controllers need to be designed carefully. It was mentioned earlier that, the battery converters of the system are bidirectional buck converters and it was also assumed that the first stage of grid-tied inverter is fast enough so that the internal DC bus of the inverter is always fixed at $1.3kV_{dc}$. With these assumptions, the design of voltage controllers for all the system's slack converters, will be similar to the design of voltage controller for the buck converters.

Design steps of the voltage controller were discussed in Section 4.2.2.1 and can be

summarized as following

Output voltage of the open-loop converter can be expressed as

$$\hat{v}(s) = G_{vd}(s)\hat{d}(s) + G_{vg}(s)\hat{v_g}(s) - Z_{out}(s)\hat{i}_{load}(s) \tag{4.20}$$

$G_{vd}(s) = \frac{\hat{v}(s)}{\hat{d}(s)}$, $G_{vg}(s) = \frac{\hat{v}(s)}{\hat{v}_g(s)}$, $Z_{out}(s) = \frac{\hat{v}(s)}{\hat{i}_{load}(s)}$.

Output voltage of the closed-loop converter (including sensor, compensator and pulse width modulation gains) can be expressed as

$$\hat{v} = \hat{v_{ref}}\frac{1}{H}\frac{T}{1+T} + \hat{v}_g\frac{G_{vg}}{1+T} - \hat{i}_{load}\frac{Z_{out}}{1+T} \tag{4.21}$$

with

$$T(s) = H(s)G_c(s)G_{vd}(s)\frac{1}{V_M} \tag{4.22}$$

Also equations 4.23, 4.24 show G_{vd} and G_{vg} of the buck converter.

$$G_{vd} = \frac{V_0}{D} * \frac{1}{LCS^2 + \frac{L}{R}S + 1} \tag{4.23}$$

$$G_{vg} = D * \frac{1}{LCS^2 + \frac{L}{R}S + 1} \tag{4.24}$$

Products of the gains around the negative feedback loop also known as loop gain for the buck converter is shown in equation 4.25. It should be noted that this the uncompensated loop gain.

$$T_U(S) = \frac{T_U(0)}{LCS^2 + \frac{L}{R}S + 1} \tag{4.25}$$

Where $T_U(0) = V_{in} * \frac{1}{V_M} * H$.

Also the compensator's gain can be written as

$$G_c(s) = K_p(1 + \frac{\frac{K_I}{K_P}}{S}) \tag{4.26}$$

Consequently, the compensated loop gain for the buck converter can be shown as the following equation

$$T(S) = (1 + \frac{\frac{K_I}{K_P}}{S}) \frac{T_U(0)K_P}{LCS^2 + \frac{L}{R}S + 1} \tag{4.27}$$

By following the discussed procedure, the voltage controller of different converters can be designed with different bandwidth. Since the switching frequency considered to be $20kHz$ for all the converters, the compensator for the fast acting converters of the system, i.e. battery converters, were designed to result in crossover frequency of $200Hz$ and the compensator for the slow acting converter of the system, i.e. the grid-tied inverter, were designed to result in crossover frequency of $0.1Hz$.

Block diagram of the bidirectional buck DC/DC converter and its controllers including: droop controller, voltage and current controller was shown in Figure 4.13. Also the bode plot of the fast acting and slow acting voltage controllers are shown in Figure 4.23(a) and (b), respectively. It can be seen in the bode plots that the desired crossover frequencies are achieved and a phase margin test will show that the controllers are stable.

4.3.5 Control-HIL Platform and Results

Feasibility and effectiveness of the proposed control algorithm were tested in a C-HIL platform. Figure 4.24 shows the test setup. In this setup, a Typhoon HIL602 were used for modeling the power stage of the converters of the system. A F28335 DSP from Texas Instruments was used for implementing the control algorithm as well as controlling the switches of the converters. Also a DSP interface board provides pin-to-pin connection

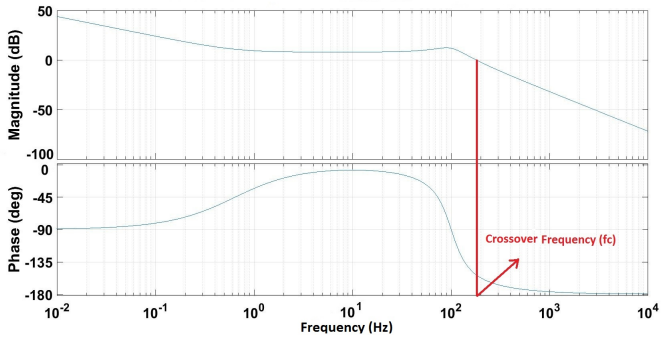

(a)

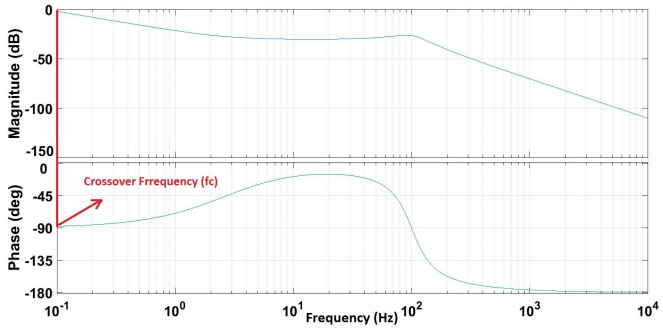

(b)

Figure 4.23 Bode plot of the voltage controllers of the converters of the system for illustrating the controllers bandwidth and stability. Fact acting slack terminals (battery converters)(a). Slow acting slack terminal (grid-tied inverter)(b).

between the Typhoon HIL602 and the DSP.

As it was mentioned earlier in the paper, the proposed architecture is a distributed DC system, connected to the 480V 3-phase AC grid through a double stage bidirectional inverter. Each source/load is connected to the distributed 380V_{dc} bus through a converter, which implements the DC control algorithm to ensure stable and optimal operation of the system. The devices are coordinated by a central microgrid controller and a low-bandwidth communication network to implement system features such as demand response and prioritization. The system architecture and specs are the same as Fig.4.22 and Table 4.1.

To illustrate the effectiveness of the control algorithm, the micorgrid was simulated

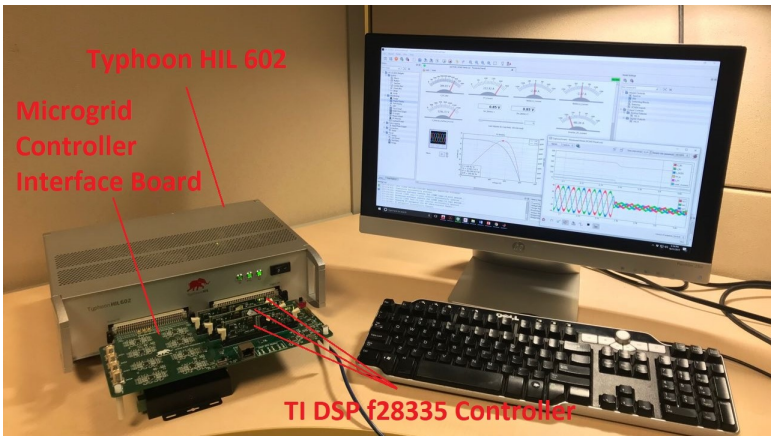

Figure 4.24 Control Hardware-in-the-Loop setup for demonstrating PV power and load smoothing functionalities.

under different conditions.

- **Case I:** PV kept constant at $5.5kW$ and the load is changing between $13.5kW$ and $27kW$ and grid is contributing to the voltage regulation.
- **Case II:** PV kept constant at $5.5kW$ and the load is changing between $13.5kW$ and $27kW$ and grid is not contributing to the voltage regulation.
- **Case III:** Load kept constant at $27.5kW$ and the PV is changing between $5.5kW$ and $11W$ and grid is contributing to the voltage regulation.
- **Case IV:**. Load kept constant at $27.5kW$ and the PV is changing between $5.5kW$ and $11W$ and grid is not contributing to the voltage regulation. It should be mentioned that all the cases were simulated once with power smoothing control enabled and once disabled.

Figure 4.25-4.28 shows the results for all the discussed cases. It can be seen that whenever the power smoothing is enabled, all the PV or load power fluctuations are absorbed by the batteries of the system and they don't get transferred to the AC grid.

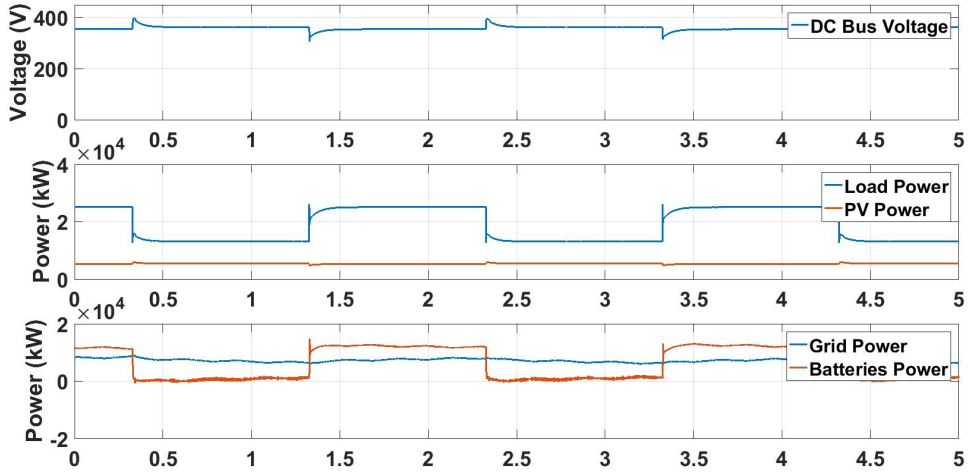

(a)

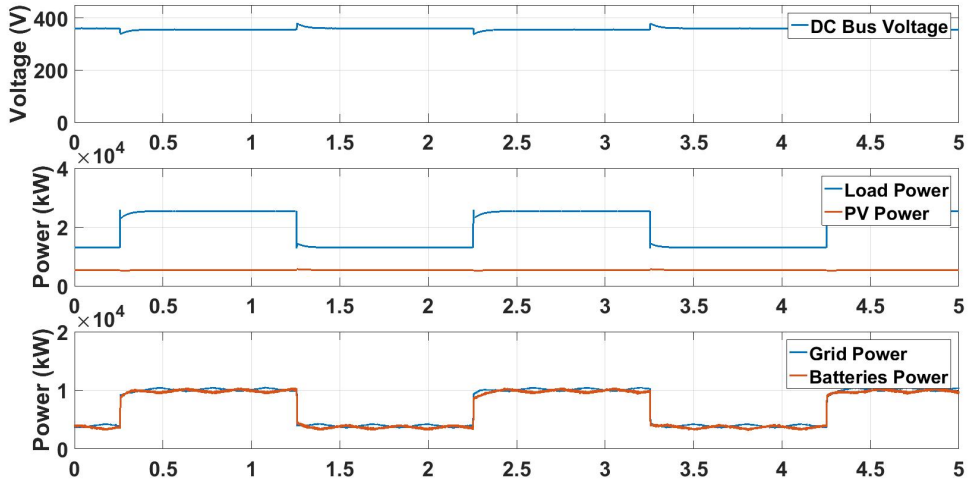

(b)

Figure 4.25 (a): Case I: DC bus voltage and the amount of power transferred between each converter and the microgrid for Case I: PV kept constant at $5.5kW$ and the load is changing between $13.5kW$ and $27kW$ and grid is contributing to the voltage regulation, power smoothing enabled. (b): no power smoothing.

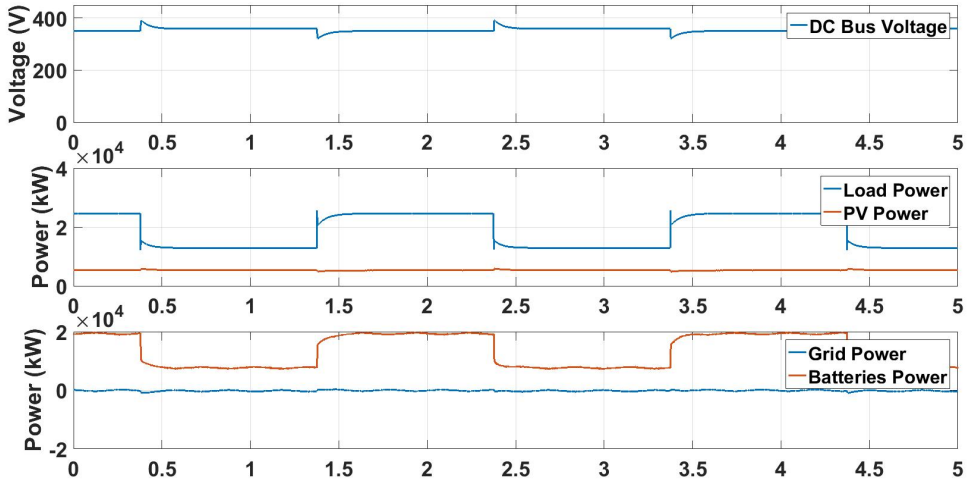

(a)

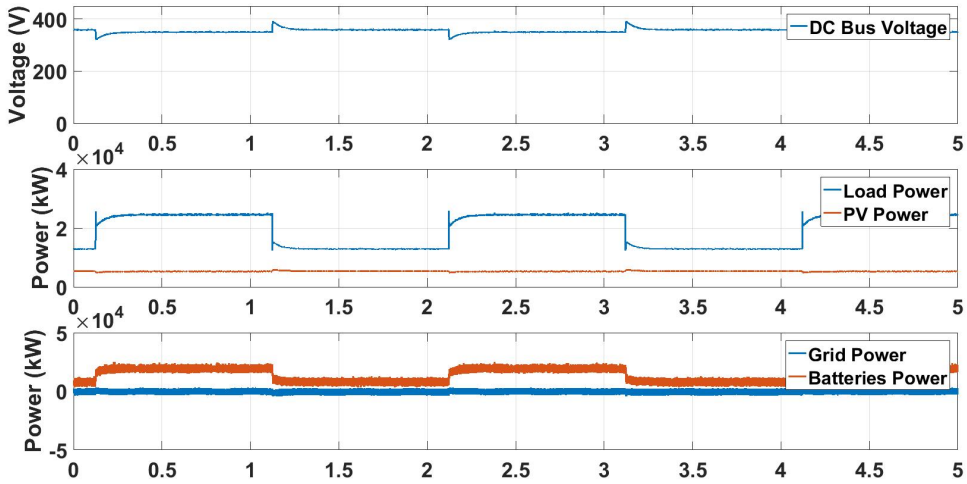

(b)

Figure 4.26 (a): Case II: PV kept constant at $5.5kW$ and the load is changing between $13.5kW$ and $27kW$ and grid is not contributing to the voltage regulation, power smoothing enabled. (b): no power smoothing.

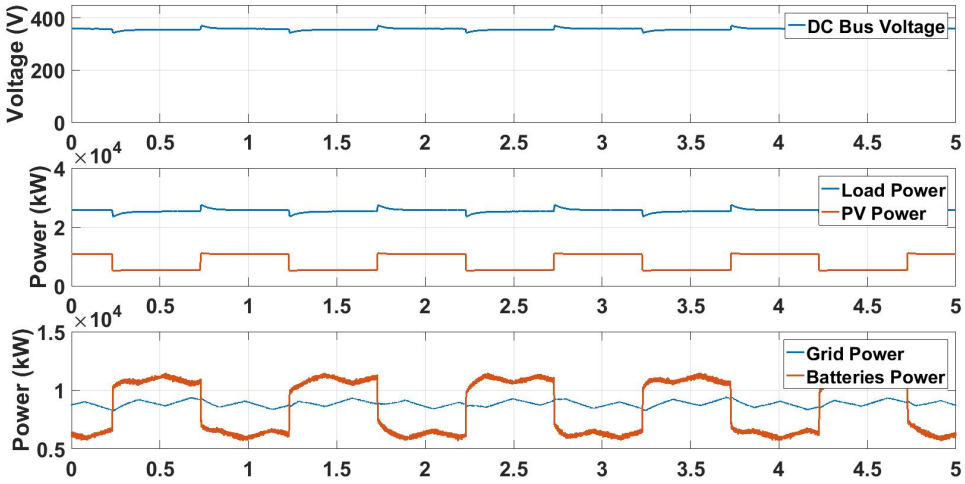

(a)

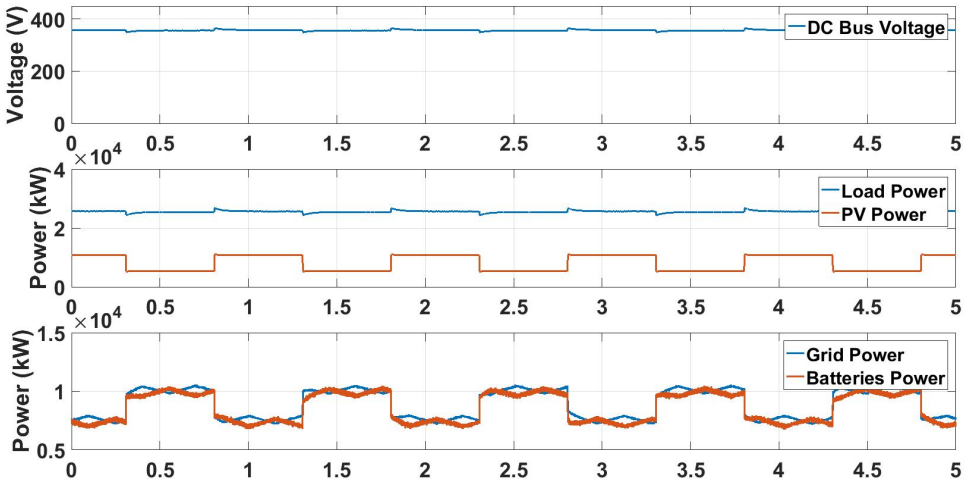

(b)

Figure 4.27 (a): Case III: Load kept constant at $27.5kW$ and the PV is changing between $5.5kW$ and $11W$ and grid is contributing to the voltage regulation, power smoothing enabled. (b): no power smoothing.

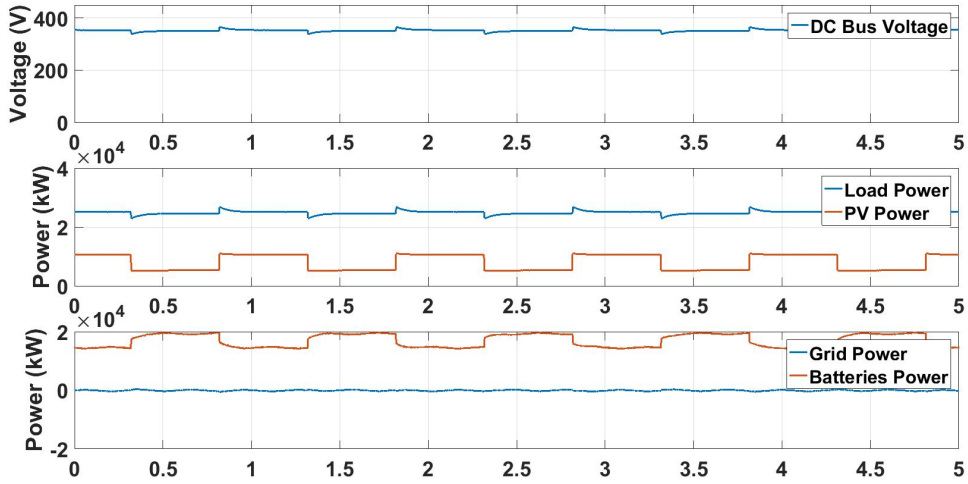

(a)

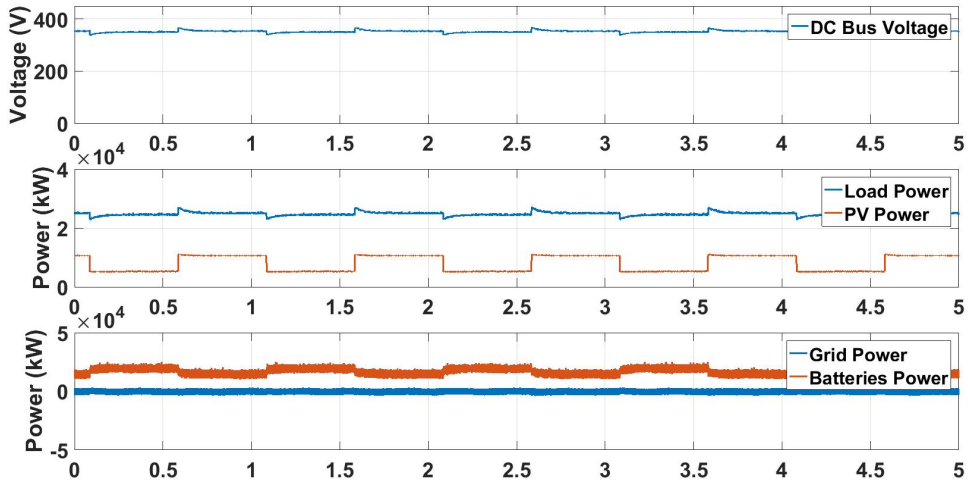

(b)

Figure 4.28 (a): Case IV: Load kept constant at $27.5kW$ and the PV is changing between $5.5kW$ and $11W$ and grid is not contributing to the voltage regulation, power smoothing enabled. (b): no power smoothing.

CHAPTER

5

SYSTEM MODEL

The purpose of this chapter is to quantitatively examine the stability and performance of the discussed DC system. For the mentioned purpose, the the DC system including: all the components and their controllers are described in terms of mathematical models. Then, the mathematical model will be used to properly set the response time of the components controller to ensure stability of the system in all different operation modes.

5.1 Model Development

In this section, we derive the mathematical model of the system shown in Figure 5.1. The model includes all the components and their controllers: including the inner current and

voltage controllers and outer energy management ayers.

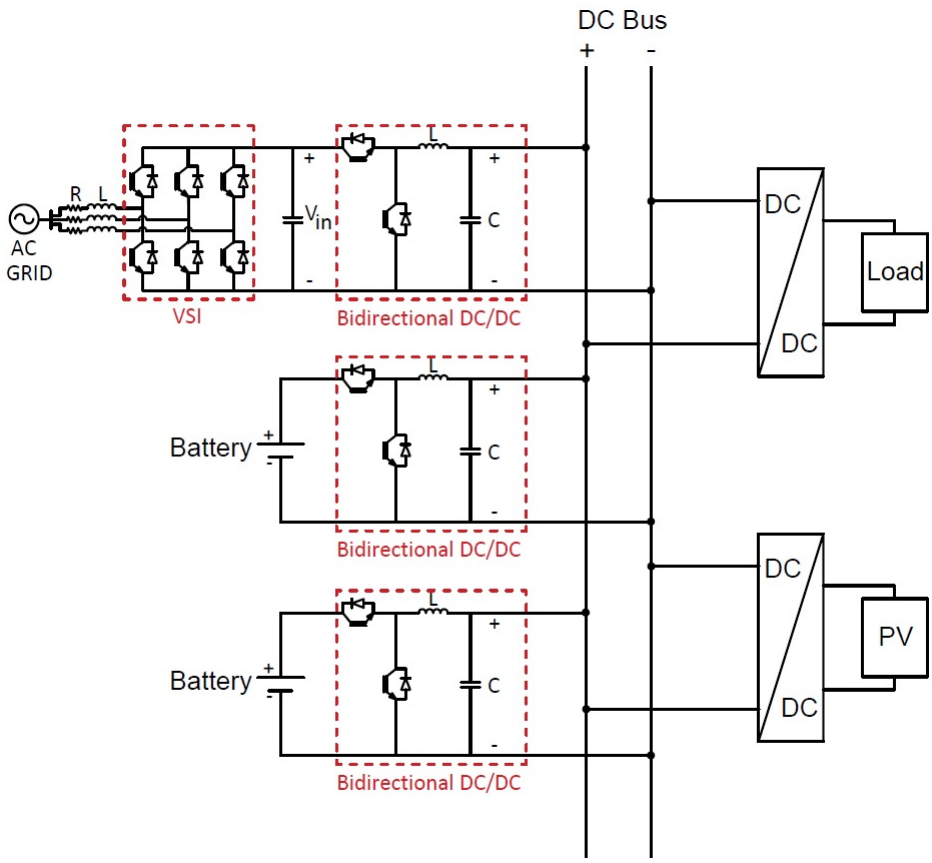

Figure 5.1 Schematic of the system used for mathematical model derivation.

The controller of the individual components of the system depends on the adopted power balancing strategies in that system. In this chapter, the system is modeled assuming that the power balancing strategy proposed in Section 4.2 is adopted for the system. Figure 5.2 shows the control block diagram of the system's components for the mentioned power balancing method.

The state space description is a method for describing a system in terms of mathematical model [77], [78]. For a linear network, the derivatives of the state variables are expressed as

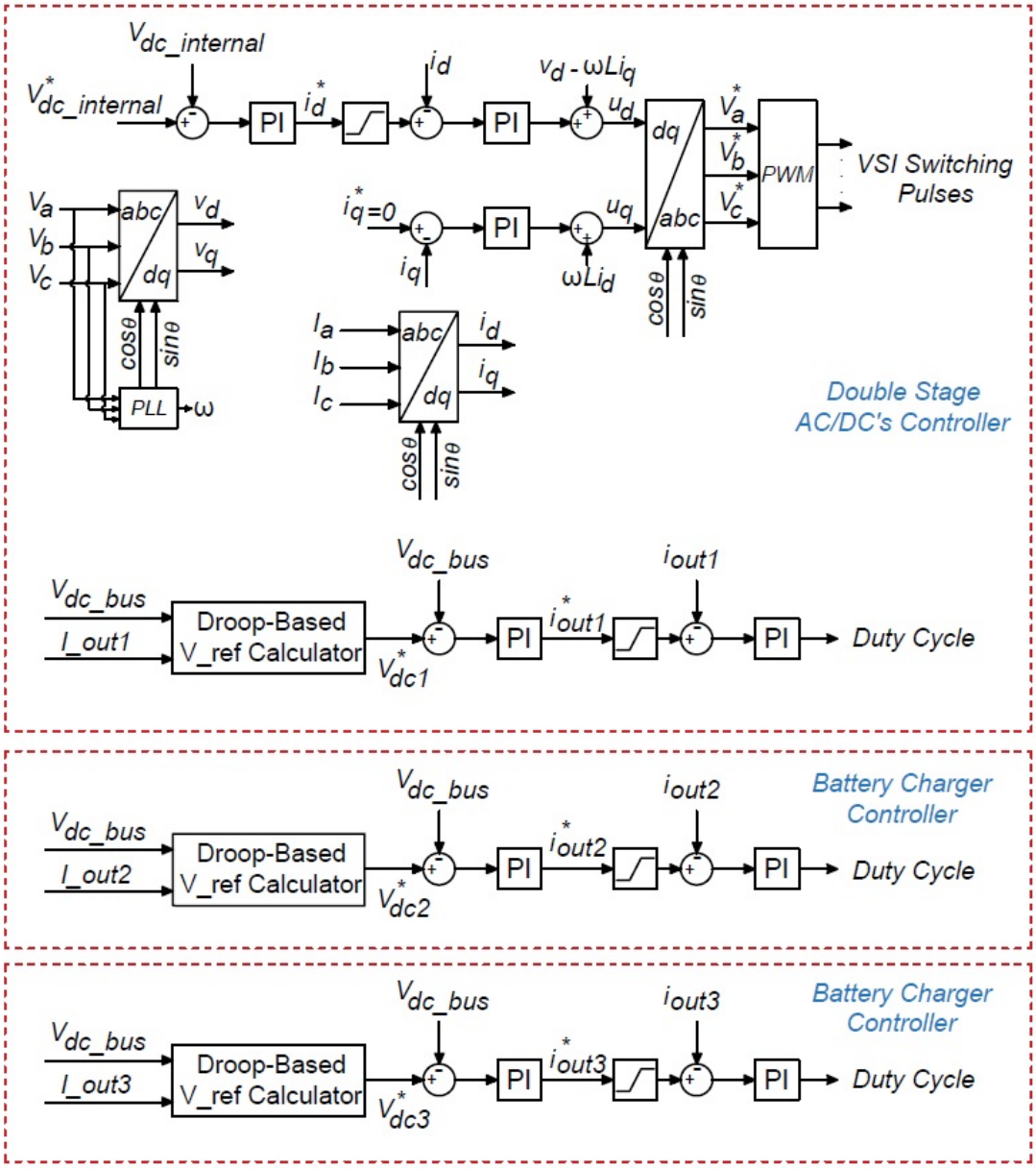

Figure 5.2 Control block diagram of the system's components.

linear combinations of the system's independent inputs and the state variables as shown in Equation 5.1 [79], [80]. For the stability analysis, only matrix A of the system is required [81]. Therefore, the focus of this chapter is on deriving matrix A and examining its eigenvalues for the stability analysis.

$$\begin{cases} \dot{X} = AX + BU \\ Y = CX + DU \end{cases} \tag{5.1}$$

where matrix X is the states of the system, matrix U, and Y are the inputs and outputs, respectively. And since our system is time invariant, A, B, C and D are constant matrices.

In order to develop the system model, first we need to model each components of the system individually. Then, these individual models can be added together to form the model of the whole system.

5.1.1 Assumption in Model Development

All the system's converters are bidirectional DC/DC converters except the grid-tied converter which is a double stage converter (Figure 5.1). As it can be seen in Figure 5.3, the grid-tied converter is a VSI in series with a bidirectional DC/DC converter. To simplify the modeling of the system, it is assumed that the voltage controller of VSI is fast enough so that the internal DC voltage of the converter or the input voltage of the DC/DC converter (V_{in}) is fixed at $1.3kV$ during load changes. If we can prove this assumption analytically, the grid-tied converter can be considered as a bidirectional DC/DC converter for modeling and stability analysis purposes. In the reminder of this section, this assumption is proved analytically.

From [82], the small signal model of VSI can be written as

$$\begin{bmatrix} \dot{\tilde{i}}_d \\ \dot{\tilde{i}}_q \\ \dot{\tilde{v}}_{dc} \end{bmatrix} = \underbrace{\begin{bmatrix} 0 & \omega & -\frac{D_d}{3L} \\ -\omega & 0 & -\frac{D_q}{3L} \\ \frac{D_d}{C} & \frac{D_q}{C} & -\frac{1}{RC} \end{bmatrix}}_{\mathbf{A}} \underbrace{\begin{bmatrix} \tilde{i}_d \\ \tilde{i}_q \\ \tilde{v}_{dc} \end{bmatrix}}_{\mathbf{x}} + \underbrace{\begin{bmatrix} -\frac{V_{dc}}{3L} & 0 \\ 0 & -\frac{V_{dc}}{3L} \\ \frac{I_d}{C} & \frac{I_q}{C} \end{bmatrix}}_{\mathbf{B}} \begin{bmatrix} \tilde{d}_d \\ \tilde{d}_q \end{bmatrix} + \underbrace{\mathbf{E}\tilde{v}}_{\text{Disturbances}} \tag{5.2}$$

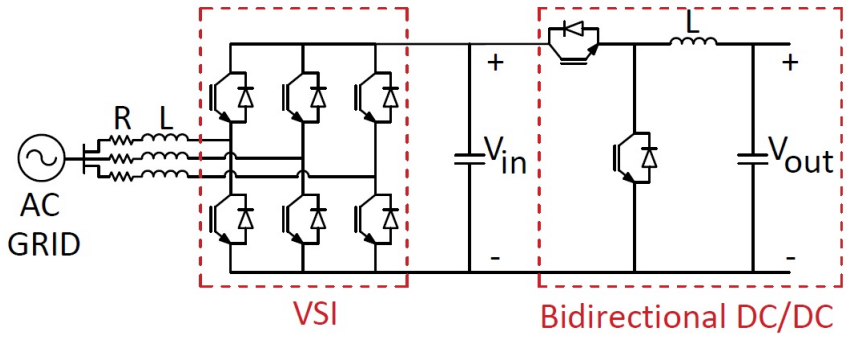

Figure 5.3 Topology of the double-stage grid-tied converter.

Table 5.1 Specification of the VSI.

$f = 60Hz$	$V_s = 277V$	$L = 1.5mH$
$P = 60kW$	$V_o = 1.3kV$	$C = 500\mu F$

where $\tilde{i_d}$ and $\tilde{i_q}$ are the small variations in the d and q components of the current. $\tilde{d_d}$ and $\tilde{d_q}$ are the small variations in d and q duty cycles. ω is the angular frequency. L, C, R are the inductance of the AC side, C is the capacitance of the DC link capacitor and R is the resistance of the load, respectively.

From Equation 5.2

$$\tilde{x}(s) = (sI - A)^{-1} B\tilde{d} \tag{5.3}$$

From Equations 5.2 and 5.3

$$\frac{\tilde{v_{dc}}}{\tilde{d_d}} = \frac{V_o^*}{2L} \frac{K_{vd}(\frac{s}{\omega_{vd_1}} - 1)(\frac{s}{\omega_{vd_2}} - 1)}{(\frac{s}{\omega_{pi}} + 1)(\frac{s^2}{\omega_p^2} + \frac{2\zeta}{\omega_p}s + 1)} \tag{5.4}$$

Using the given information in Table 5.1, the parameters of the transfer function can be calculates as

$$K_{vd} = -6.5e^{-4} \quad \omega_{vd_1} = 1750 \quad \omega_{vd_2} = 5.5$$

$$\omega_{pi} = 52 \quad \omega_p^2 = 580 \quad \zeta = 4.5E^{-3}$$

From above the bode plot of the uncompensated VSI can be drawn as Figure 5.4.

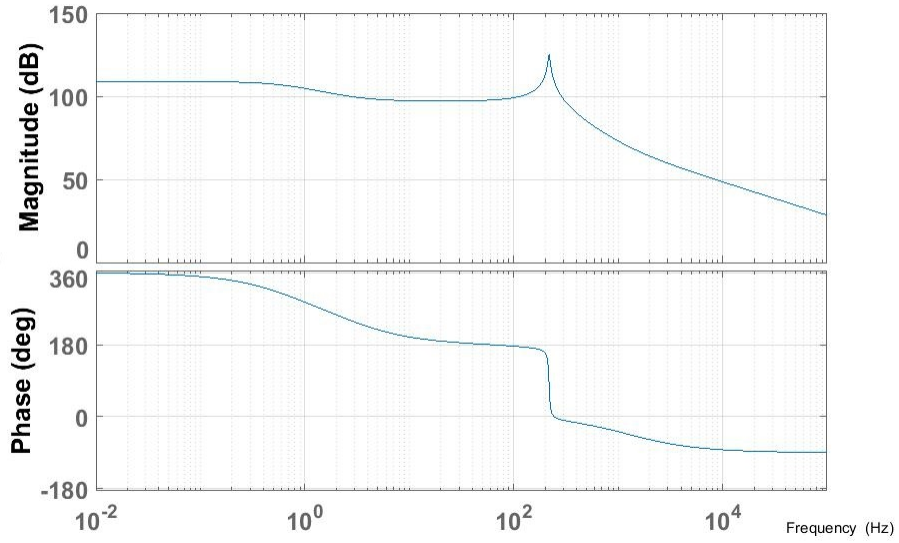

Figure 5.4 Bode plot of the uncompensated VSI.

By adding the PI controller designed in Section 4.2 to the uncompensated loop, the bode plot of the compensated VSI can be obtained. Figure 5.5 shows the bode plot of the compensated VSI.

As it can be seen in Figure 5.5, the cut off frequency of the VSI is much higher than the second stage of the converter ($10kHz$ vs. $100Hz$) meaning that the second stage does not see any voltage changes in its input.Therefore, the grid-tied converter can be considered as a bidirectional DC/DC converter in modeling of the DC system. This assumption is true as long as the voltage controller of the VSI part of the grid-tied converter is fast enough to

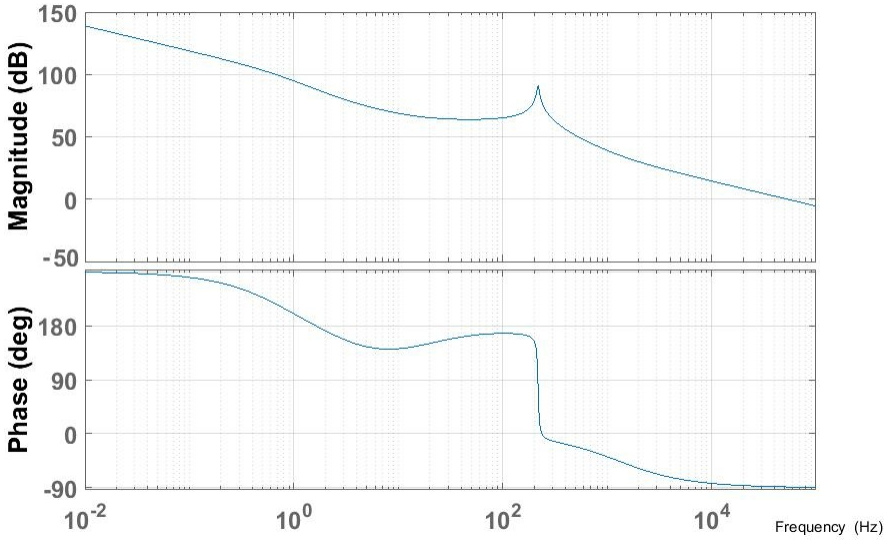

Figure 5.5 Bode plot of the compensated VSI.

keep the internal DC bus voltage at $1.3kV$ in the extreme load changing.

5.1.2 Model of the Compensated Bidirectional Buck Converter

State space description of an uncompensated bidirectional buck converters has been well-discussed in literature and can be written as following

$$\begin{bmatrix} \dot{x_1} \\ \dot{x_2} \end{bmatrix} = \begin{bmatrix} 0 & \frac{-1}{L} \\ \frac{1}{C} & \frac{-1}{RC} \end{bmatrix} \begin{bmatrix} x_1 \\ x_2 \end{bmatrix} + \begin{bmatrix} \frac{V_{in}}{L} \\ 0 \end{bmatrix} D \tag{5.5}$$

where states of the converter, x_1 and x_2, are the output inductor current and capacitor voltage. L, C are inductance and capacitance of the output filter. V_{in} is the input voltage of the converter. D is the duty cycle and R is the resistance of the load.

The next step is to add the all the control layers to the state space description of the uncompensated converter. Figure 5.6 shows the states and control block diagram of an

Table 5.2 Description of the system's states.

State	Description
x_{n1}	Output inductor current of n^{th} converter
x_{12}	DC bus voltage (common state among all the converters)
x_{n3}	Output of the integrator part of the n^{th} converter's PI voltage controller
x_{n4}	Output of the integrator part of the n^{th} converter's PI current controller

individual converter including: the inner voltage and current controllers as well as the outer energy management layer. As a rule of thumb, inductor current and capacitor voltage and the output of the integral part of the PI controllers are selected as the system's states. States of the system are described in Table 5.2.

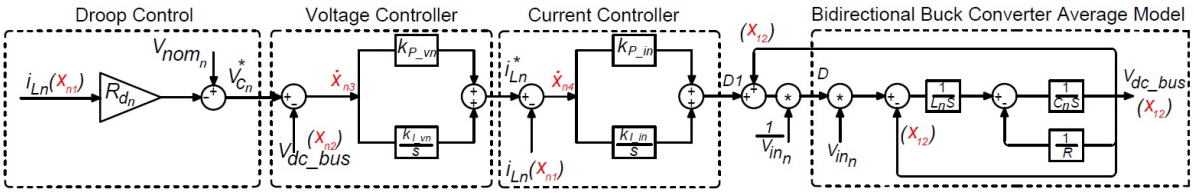

Figure 5.6 Control block diagram and state definition of an individual converter operating in droop control mode.

From Figure 5.6

$$\dot{x_{n3}} = V_{nom_n} - R_{d_n} x_{n1} - x_{12} \tag{5.6}$$

where V_{nom_n} is the nominal output voltage of the n^{th} converter and R_{d_n} is the droop coefficient of the n^{th} converter.

$$i_{L_n}^* = k_{P_{vn}}[V_{nom_n} - R_{d_n} x_{n1} - x_{12}] + k_{I_{vn}} x_{n3} \tag{5.7}$$

where i_{L_n} is the output inductor current of the n^{th} converter. $k_{P_{vn}}$ and $k_{I_{vn}}$ are the voltage controller gains of the n^{th} converter.

$$\begin{aligned} \dot{x_{n4}} &= k_{P_{vn}}[V_{nom_n} - R_{d_n} x_{n1} - x_{12}] + k_{I_{vn}} x_{n3} - x_{n1} \\ &= (-1 - k_{P_{vn}} R_{d_n}) x_{n1} - k_{P_{vn}} x_{12} + k_{I_{vn}} x_{n3} + k_{P_{vn}} V_{nom_n} \end{aligned} \tag{5.8}$$

$$\begin{aligned} D_1 &= k_{P_{in}}[k_{P_{vn}}[V_{nom_n} - R_{d_n} x_{n1} - x_{12}] + k_{I_{vn}} x_{n3} - x_{n1}] + k_{I_{in}} x_{n4} \\ &= (-k_{P_{in}} - k_{P_{in}} k_{P_{vn}} R_{d_n}) x_{n1} - k_{P_{in}} k_{P_{vn}} x_{12} + k_{P_{in}} k_{I_{vn}} x_{n3} + k_{I_{in}} x_{n4} + k_{P_{in}} k_{P_{vn}} V_{nom_n} \end{aligned} \tag{5.9}$$

where $k_{P_{in}}$ and $k_{I_{in}}$ are the current controller gains of the n^{th} converter.

$$D = \frac{D_1 + x_{12}}{V_{in_n}} \tag{5.10}$$

where V_{in_n} is the input voltage of the n^{th} converter.

From state space description of the buck converter , Equation 5.5, x_{n1} can be written as

$$\dot{x_{n1}} = -\frac{1}{L_n} x_{12} + \frac{V_{in_n}}{L_n} D \tag{5.11}$$

By putting Equation 5.10 in Equation 5.11, x_{n1} can be written as

$$\dot{x_{n1}} = -\frac{1}{L_n} x_{12} + \frac{D_1}{L_n} + \frac{1}{L_n} x_{12} = \frac{D_1}{L_n} \tag{5.12}$$

By combining Equations 5.12 and 5.9

$$\dot{x_{n1}} = \frac{-k_{P_{in}} - k_{P_{in}} k_{P_{vn}} R_{d_n}}{L_n} x_{n1} + \frac{-k_{P_{in}} k_{P_{vn}}}{L_n} x_{12} + \frac{k_{P_{in}} k_{I_{vn}}}{L_n} x_{n3} + \frac{k_{I_{in}}}{L_n} x_{n4} + \frac{k_{P_{in}} k_{P_{vn}}}{L_n} V_{nom_n} \quad (5.13)$$

Finally, State space description of the compensated converter can be written by using Equations 5.6, 5.8, 5.13. The result can be summarized as the following

$$\begin{bmatrix} \dot{x_{n1}} \\ \dot{x_{12}} \\ \dot{x_{n3}} \\ \dot{x_{n4}} \end{bmatrix} = \begin{bmatrix} \frac{-k_{P_{in}} - k_{P_{in}} k_{P_{vn}} R_{d_n}}{L_n} & \frac{-k_{P_{in}} k_{P_{vn}}}{L_n} & \frac{k_{P_{in}} k_{I_{vn}}}{L_n} & \frac{k_{I_{in}}}{L_n} \\ \frac{1}{C_n} & \frac{-1}{RC_n} & 0 & 0 \\ -R_{d_n} & -1 & 0 & 0 \\ -1 - k_{P_{vn}} R_{d_n} & -k_{P_{vn}} & k_{I_{vn}} & 0 \end{bmatrix} \begin{bmatrix} x_{n1} \\ x_{12} \\ x_{n3} \\ x_{n4} \end{bmatrix} + \begin{bmatrix} \frac{k_{P_{in}} k_{P_{vn}}}{L_n} \\ 0 \\ 1 \\ k_{P_{vn}} \end{bmatrix} V_{nom_n} \quad (5.14)$$

where L_n and C_n are inductance and capacitance of the the outout filter of n^{th} converter.

The above state space description can be modified for a system with a single converter and a PV array. In this dissertation, PV is considered as a variable current source. Figure 5.7 shows the Control block diagram and state definition of an individual converter in the DC microgrid connected to a PV array. I_{PV} is the output current of the PV array.

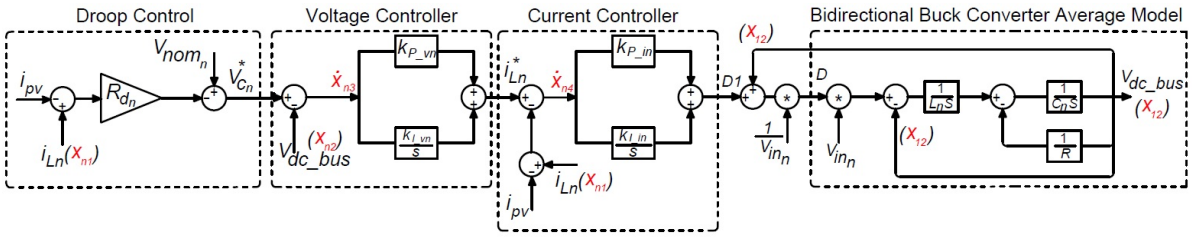

Figure 5.7 Control block diagram and state definition of an individual converter in the DC microgrid connected to a PV array.

From Figure 5.7

$$\dot{x_{n3}} = V_{nom_n} - R_{d_n}(x_{n1} - I_{pv}) - x_{12} \tag{5.15}$$

$$i^*_{L_n} = k_{P_{vn}}[V_{nom_n} - R_{d_n}(x_{n1} - I_{pv}) - x_{12}] + k_{I_{vn}} x_{n3} \tag{5.16}$$

$$\begin{aligned} \dot{x_{n4}} &= k_{P_{vn}}[V_{nom_n} - R_{d_n}(x_{n1} - I_{pv}) - x_{12}] + k_{I_{vn}} x_{n3} - x_{n1} + I_{pv} \\ &= (-1 - k_{P_{vn}} R_{d_n})(x_{n1} - I_{pv}) - k_{P_{vn}} x_{12} + k_{I_{vn}} x_{n3} + k_{P_{vn}} V_{nom_n} \end{aligned} \tag{5.17}$$

$$\begin{aligned} D_1 &= k_{P_{in}}[k_{P_{vn}}[V_{nom_n} - R_{d_n}(x_{n1} - I_{pv}) - x_{12}] + k_{I_{vn}} x_{n3} - (x_{n1} - I_{pv})] + k_{I_{in}} x_{n4} \\ &= (-k_{P_{in}} - k_{P_{in}} k_{P_{vn}} R_{d_n})(x_{n1} - I_{pv}) - k_{P_{in}} k_{P_{vn}} x_{12} + k_{P_{in}} k_{I_{vn}} x_{n3} + k_{I_{in}} x_{n4} + k_{P_{in}} k_{P_{vn}} V_{nom_n} \end{aligned} \tag{5.18}$$

From the above equations, state space description of the system can be written as following

$$\begin{bmatrix} \dot{x_{n1}} \\ \dot{x_{12}} \\ \dot{x_{n3}} \\ \dot{x_{n4}} \end{bmatrix} = \begin{bmatrix} \frac{-k_{P_{in}} - k_{P_{in}} k_{P_{vn}} R_{d_n}}{L_n} & \frac{-k_{P_{in}} k_{P_{vn}}}{L_n} & \frac{k_{P_{in}} k_{I_{vn}}}{L_n} & \frac{k_{I_{in}}}{L_n} \\ \frac{1}{C_n} & \frac{-1}{RC_n} & 0 & 0 \\ -R_{d_n} & -1 & 0 & 0 \\ -1 - k_{P_{vn}} R_{d_n} & -k_{P_{vn}} & k_{I_{vn}} & 0 \end{bmatrix} \begin{bmatrix} x_{n1} \\ x_{12} \\ x_{n3} \\ x_{n4} \end{bmatrix} + \begin{bmatrix} \frac{k_{P_{in}} k_{P_{vn}}}{L_n} \\ 0 \\ 1 \\ k_{P_{vn}} \end{bmatrix} V_{nom_n} - \begin{bmatrix} \frac{-k_{P_{in}} - k_{P_{in}} k_{P_{vn}} R_{d_n}}{L_n} \\ \frac{1}{C_n} \\ -R_{d_n} \\ -1 - k_{P_{vn}} R_{d_n} \end{bmatrix} I_{pv} \tag{5.19}$$

5.1.3 Model of the DC Microgrid

In this section, the model of DC microgrid shown in Figure 5.1 will be derived for both power balancing cases discussed in Section 4.2 of Chapter 4. As a reminde, the $V-I$ profiles of the slack terminal in two cases discussed in Section 4.2 of Chapter 4 are shown in Figure 5.8.

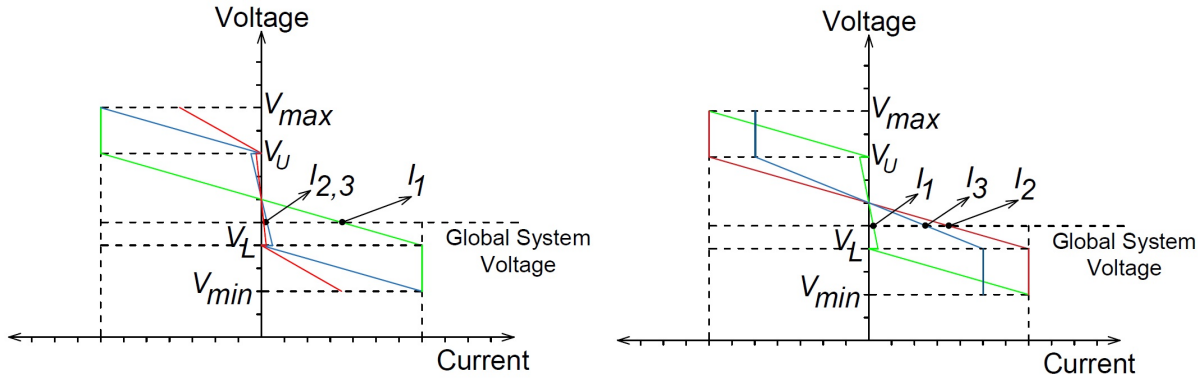

Figure 5.8 (a): $I-V$ profiles of the slack sources in case I. (c): $I-V$ profiles of the slack sources in case II.

5.1.3.1 Case I: Grid is the Primary, Batteries are Backup

As it can be seen in Figure 5.8(a), whenever the voltage is between V_L and V_U, all the three slack terminals of the system are operating in droop control mode. Whenever the voltage falls out of this window, grid converter becomes a current source and the batteries keep operating in droop control mode (with different droop coefficients.). The following shows the mathematical model of the system in these two modes

Mode I - All the Three Slack Terminals Operating in Droop Control Mode:

In this mode, three converters are operating in parallel and contribute to the voltage regulation. Therefore, the output voltage depends on the sum of the output currents of individual converters and the sum of output capacitance of the individual converters as it is shown in Equation 5.20.

$$\dot{x_{12}} = \frac{1}{C_1 + C_2 + C_3}(x_{11} + x_{21} + x_{31}) - \frac{1}{R(C_1 + C_2 + C_3)}x_{12} \tag{5.20}$$

The model of a single converter has been derived earlier, Equation 5.19. From Equations 5.19 and 5.20, the model of three converters working in droop control mode can be obtained as the following

$$
\begin{bmatrix} \dot{x_{11}} \\ \dot{x_{12}} \\ \dot{x_{13}} \\ \dot{x_{14}} \\ \dot{x_{21}} \\ \dot{x_{23}} \\ \dot{x_{24}} \\ \dot{x_{31}} \\ \dot{x_{33}} \\ \dot{x_{34}} \end{bmatrix} = \begin{bmatrix} a_{11} & a_{12} & a_{13} & a_{14} & 0 & 0 & 0 & 0 & 0 & 0 \\ a_{21} & a_{22} & 0 & 0 & a_{25} & 0 & 0 & a_{28} & 0 & 0 \\ -R_{d1} & -1 & 0 & 0 & 0 & 0 & 0 & 0 & 0 & 0 \\ a_{41} & a_{42} & a_{43} & 0 & 0 & 0 & 0 & 0 & 0 & 0 \\ 0 & a_{52} & 0 & 0 & a_{55} & a_{56} & a_{57} & 0 & 0 & 0 \\ 0 & -1 & 0 & 0 & -R_{d2} & 0 & 0 & 0 & 0 & 0 \\ 0 & a_{72} & 0 & 0 & a_{75} & a_{76} & 0 & 0 & 0 & 0 \\ 0 & a_{82} & 0 & 0 & 0 & 0 & 0 & a_{88} & a_{89} & a_{810} \\ 0 & -1 & 0 & 0 & 0 & 0 & 0 & -R_{d3} & 0 & 0 \\ 0 & a_{102} & 0 & 0 & 0 & 0 & 0 & a_{108} & a_{109} & 0 \end{bmatrix} \begin{bmatrix} x_{11} \\ x_{12} \\ x_{13} \\ x_{14} \\ x_{21} \\ x_{23} \\ x_{24} \\ x_{31} \\ x_{33} \\ x_{34} \end{bmatrix} \tag{5.21}
$$

$$
+ \begin{bmatrix} \frac{k_{P_{i1}} k_{P_{v1}}}{L_1} \\ 0 \\ 1 \\ k_{P_{v1}} \\ \frac{k_{P_{i2}} k_{P_{v2}}}{L_2} \\ 1 \\ k_{P_{v2}} \\ \frac{k_{P_{i3}} k_{P_{v3}}}{L_3} \\ 1 \\ k_{P_{v3}} \end{bmatrix} V_{nom} - \begin{bmatrix} \frac{-k_{P_{i1}} - k_{P_{i1}} k_{P_{v1}} R_{d1}}{L_1} \\ \frac{1}{C_1 + C_2} \\ -R_{d1} \\ -1 - k_{P_{v1}} R_{d1} \\ \frac{-k_{P_{i2}} - k_{P_{i2}} k_{P_{v2}} R_{d2}}{L_2} \\ -R_{d2} \\ -1 - k_{P_{v2}} R_{d2} \\ \frac{-k_{P_{i3}} - k_{P_{i3}} k_{P_{v3}} R_{d3}}{L_3} \\ -R_{d3} \\ -1 - k_{P_{v3}} R_{d3} \end{bmatrix} I_{pv}
$$

where

$$a_{11}=\frac{-k_{P_{i1}}-k_{P_{i1}}k_{P_{v1}}R_{d1}}{L_1} \qquad a_{12}=\frac{-k_{P_{i1}}k_{P_{v1}}}{L_1} \qquad a_{13}=\frac{k_{P_{i1}}k_{I_{v1}}}{L_1}$$

$$a_{14}=\frac{k_{I_{i1}}}{L_1} \qquad a_{21}=\frac{1}{C_1+C_2+C_3} \qquad a_{22}=\frac{-1}{R(C_1+C_2+C_3)}$$

$$a_{25}=\frac{1}{C_1+C_2+C_3} \qquad a_{28}=\frac{1}{C_1+C_2+C_3} \qquad a_{41}=-1-k_{P_{v1}}R_{d1}$$

$$a_{42}=-k_{P_{v1}} \qquad a_{43}=k_{I_{v1}} \qquad a_{52}=\frac{-k_{P_{i2}}k_{P_{v2}}}{L_2}$$

$$a_{55}=\frac{-k_{P_{i2}}-k_{P_{i2}}k_{P_{v2}}R_{d2}}{L_2} \qquad a_{56}=\frac{k_{P_{i2}}k_{I_{v2}}}{L_2} \qquad a_{57}=\frac{k_{I_{i2}}}{L_2}$$

$$a_{72}=-k_{P_{v2}} \qquad a_{75}=-1-k_{P_{v2}}R_{d2} \qquad a_{76}=k_{I_{v2}}$$

$$a_{82}=\frac{-k_{P_{i3}}k_{P_{v3}}}{L_3} \qquad a_{88}=\frac{-k_{P_{i3}}-k_{P_{i3}}k_{P_{v3}}R_{d3}}{L_3} \qquad a_{89}=\frac{k_{P_{i3}}k_{I_{v3}}}{L_3}$$

$$a_{810}=\frac{k_{I_{i3}}}{L_3} \qquad a_{102}=-k_{P_{v3}} \qquad a_{108}=-1-k_{P_{v3}}R_{d3}$$

$$a_{109}=k_{I_{v3}}$$

Mode II: Batteries operating in droop control mode and grid is a current source:

In this case, batteries operate in droop control mode and the grid-tied converter is in current control mode. In order to be able to derive the system's model for this case, first the model of single converter with in current control mode is required. Figure 5.9 shows the control block diagram and state definition of an individual converter operating in current control mode in parallel with a PV array.

From Figure 5.9

$$\dot{x_{n4}}=i^*_{L_n}-x_{n1}+I_{pv} \tag{5.22}$$

where i^*_L is the reference current of the current control loop of the n^{th} converter.

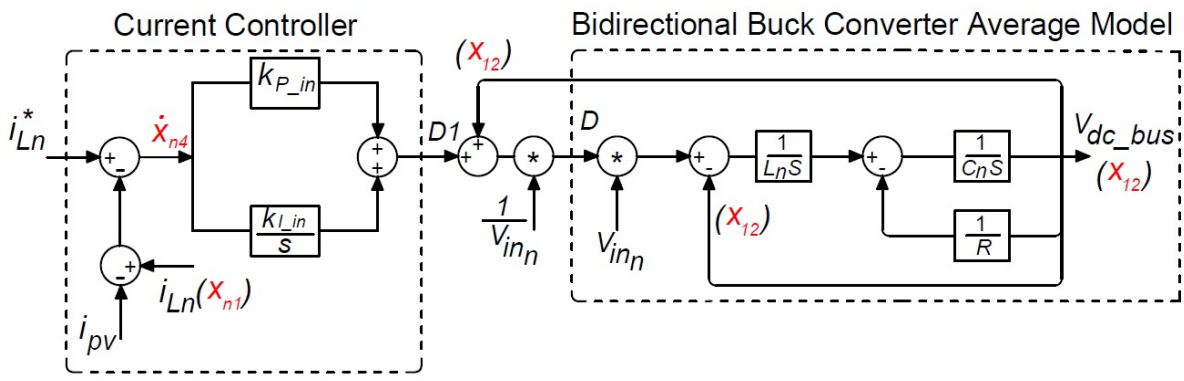

Figure 5.9 Control block diagram and state definition of an individual converter operating in current control mode.

$$D_1 = K_{I_{in}} x_{n4} + K_{P_{in}}(i^*_{L_n} - x_{n1} + I_{pv}) \tag{5.23}$$

$$\dot{x_{n1}} = -\frac{1}{L_n} x_{12} + \frac{D_1}{L_n} + \frac{1}{L_n} x_{12} = \frac{D_1}{L_n} = -\frac{K_{P_{in}}}{L_n} x_{n1} + \frac{K_{I_{in}}}{L_n} x_{n4} + \frac{K_{P_{in}}}{L_n} i^*_{L_n} + \frac{K_{P_{in}}}{L_n} I_{pv} \tag{5.24}$$

$$\dot{x_{12}} = \frac{1}{C_n}(x_{n1} - I_{pv}) - \frac{1}{RC_n} x_{12} \tag{5.25}$$

From the above equations, state space model of the converter operating in current control mode in parallel with a PV array can be written as following

$$\begin{bmatrix} \dot{x_{n1}} \\ \dot{x_{12}} \\ \dot{x_{n4}} \end{bmatrix} = \begin{bmatrix} -\frac{K_{P_{in}}}{L_n} & 0 & \frac{K_{I_{in}}}{L_n} \\ \frac{1}{C} & \frac{-1}{RC} & 0 \\ -1 & 0 & 0 \end{bmatrix} \begin{bmatrix} x_{n1} \\ x_{12} \\ x_{n4} \end{bmatrix} + \begin{bmatrix} \frac{k_{P_{in}}}{L_n} \\ 0 \\ 1 \end{bmatrix} i^*_{L_n} - \begin{bmatrix} -\frac{K_{P_{in}}}{L_n} \\ \frac{1}{C_n} \\ -1 \end{bmatrix} I_{pv} \tag{5.26}$$

From Equation 5.26, and the model of converter operating in droop control mode,

Equation 5.14, the system model can be written as

$$\begin{bmatrix} \dot{x_{11}} \\ \dot{x_{12}} \\ \dot{x_{14}} \\ \dot{x_{21}} \\ \dot{x_{23}} \\ \dot{x_{24}} \\ \dot{x_{31}} \\ \dot{x_{33}} \\ \dot{x_{34}} \end{bmatrix} = \begin{bmatrix} a_{11} & a_{12} & a_{13} & 0 & 0 & 0 & 0 & 0 & 0 \\ a_{21} & a_{22} & 0 & a_{24} & 0 & 0 & a_{27} & 0 & 0 \\ -1 & 0 & 0 & 0 & 0 & 0 & 0 & 0 & 0 \\ 0 & a_{42} & 0 & a_{44} & a_{45} & a_{46} & 0 & 0 & 0 \\ 0 & -1 & 0 & -R_{d2} & 0 & 0 & 0 & 0 & 0 \\ 0 & a_{62} & 0 & a_{64} & a_{65} & 0 & 0 & 0 & 0 \\ 0 & a_{72} & 0 & 0 & 0 & 0 & a_{77} & a_{78} & a_{79} \\ 0 & -1 & 0 & 0 & 0 & 0 & -R_{d3} & 0 & 0 \\ 0 & a_{92} & 0 & 0 & 0 & 0 & a_{97} & a_{98} & 0 \end{bmatrix} \begin{bmatrix} x_{11} \\ x_{12} \\ x_{14} \\ x_{21} \\ x_{23} \\ x_{24} \\ x_{31} \\ x_{33} \\ x_{34} \end{bmatrix} + \begin{bmatrix} 0 \\ 0 \\ 0 \\ \frac{k_{P_{i2}} k_{P_{v2}}}{L_2} \\ 1 \\ k_{P_{v2}} \\ \frac{k_{P_{i3}} k_{P_{v3}}}{L_3} \\ 1 \\ k_{P_{v3}} \end{bmatrix} V_{nom} + \begin{bmatrix} \frac{k_{P_{i1}}}{L_1} \\ 0 \\ 1 \\ 0 \\ 0 \\ 0 \\ 0 \\ 0 \\ 0 \end{bmatrix} i_L^* - \begin{bmatrix} -\frac{k_{P_{i1}}}{L_1} \\ \frac{1}{C_1+C_2+C_3} \\ -1 \\ \frac{-k_{P_{i2}} - k_{P_{i2}} k_{P_{v2}} R_{d2}}{L_2} \\ -R_{d2} \\ -1 - k_{P_{v2}} R_{d2} \\ \frac{-k_{P_{i3}} - k_{P_{i3}} k_{P_{v3}} R_{d3}}{L_3} \\ -R_{d3} \\ -1 - k_{P_{v3}} R_{d3} \end{bmatrix} I_{pv} \tag{5.27}$$

where

$$
\begin{aligned}
a_{11} &= -\frac{k_{P_{i1}}}{L_1} & a_{12} &= 0 & a_{13} &= \frac{k_{I_{i1}}}{L_1} \\
a_{21} &= \frac{1}{C_1+C_2+C_3} & a_{22} &= \frac{-1}{R(C_1+C_2+C_3)} & a_{24} &= \frac{1}{C_1+C_2+C_3} \\
a_{27} &= \frac{1}{C_1+C_2+C_3} & a_{42} &= \frac{-k_{P_{i2}}k_{P_{v2}}}{L_2} & a_{44} &= \frac{-k_{P_{i2}}-k_{P_{i2}}k_{P_{v2}}R_{d2}}{L_2} \\
a_{45} &= \frac{k_{P_{i2}}k_{I_{v2}}}{L_2} & a_{46} &= \frac{k_{I_{i2}}}{L_2} & a_{62} &= -k_{P_{v2}} \\
a_{64} &= -1-k_{P_{v2}}R_{d2} & a_{65} &= k_{I_{v2}} & a_{72} &= \frac{-k_{P_{i3}}k_{P_{v3}}}{L_3} \\
a_{77} &= \frac{-k_{P_{i3}}-k_{P_{i3}}k_{P_{v3}}R_{d3}}{L_3} & a_{78} &= \frac{k_{P_{i3}}k_{I_{v3}}}{L_3} & a_{79} &= \frac{k_{I_{i3}}}{L_3} \\
a_{92} &= -k_{P_{v3}} & a_{97} &= -1-k_{P_{v3}}R_{d3} & a_{98} &= k_{I_{v3}}
\end{aligned}
$$

5.1.3.2 Case II: Batteries are the Primary, Grid is the Backup

As it can be seen in Figure 5.8(b), whenever the voltage is between V_L and V_U, all the three slack terminal of the system are operating in droop control mode. Whenever the voltage falls out of this window, batteries become current sources and the grid-tied converter keep operating in droop control mode (with different droop coefficients.). The following shows the mathematical model of the system in these two modes

Mode I - All the three slack terminals operating in droop control mode:

This mode is similar to mode I in Case I and the only difference is the value of droop coefficients. Therefore, model presented in Equation 5.21 can be used for stability analysis of this mode.

Mode II - Grid operating in droop control mode and batteries are current sources:

This mode is similar to mode II of the case I. However, in this mode, there are two converters in current control mode and one converter in droop control mode.

From the model of converter operating in current control mode, Equation 5.26, and the

model of converter operating in droop control mode, Equation 5.14, the system model in this mode can be written as

$$\begin{bmatrix} \dot{x_{11}} \\ \dot{x_{12}} \\ \dot{x_{14}} \\ \dot{x_{21}} \\ \dot{x_{23}} \\ \dot{x_{31}} \\ \dot{x_{33}} \\ \dot{x_{34}} \end{bmatrix} = \begin{bmatrix} a_{11} & a_{12} & a_{13} & 0 & 0 & 0 & 0 & 0 \\ a_{21} & a_{22} & 0 & a_{24} & 0 & a_{26} & 0 & 0 \\ -1 & 0 & 0 & 0 & 0 & 0 & 0 & 0 \\ 0 & a_{42} & 0 & a_{44} & a_{45} & 0 & 0 & 0 \\ 0 & 0 & 0 & -1 & 0 & 0 & 0 & 0 \\ 0 & a_{62} & 0 & 0 & 0 & a_{66} & a_{67} & a_{68} \\ 0 & -1 & 0 & 0 & 0 & -R_{d3} & 0 & 0 \\ 0 & a_{82} & 0 & 0 & 0 & a_{86} & a_{87} & 0 \end{bmatrix} \begin{bmatrix} x_{11} \\ x_{12} \\ x_{14} \\ x_{21} \\ x_{23} \\ x_{31} \\ x_{33} \\ x_{34} \end{bmatrix} + \begin{bmatrix} 0 \\ 0 \\ 0 \\ 0 \\ 0 \\ \frac{k_{P_{i3}} k_{P_{v3}}}{L_3} \\ 1 \\ k_{P_{v3}} \end{bmatrix} V_{nom} + \begin{bmatrix} \frac{k_{P_{i1}}}{L_1} \\ 0 \\ 1 \\ \frac{k_{P_{i2}}}{L_2} \\ 1 \\ 0 \\ 0 \\ 0 \end{bmatrix} i_L^* - \begin{bmatrix} -\frac{k_{P_{i1}}}{L_1} \\ \frac{1}{C_1+C_2+C_3} \\ -1 \\ -\frac{k_{P_{i2}}}{L_2} \\ -1 \\ \frac{-k_{P_{i3}} - k_{P_{i3}} k_{P_{v3}} R_{d3}}{L_3} \\ -R_{d3} \\ -1 - k_{P_{v3}} R_{d3} \end{bmatrix} I_{pv} \tag{5.28}$$

$$a_{11} = \frac{-k_{P_{i1}}}{L_1} \qquad a_{12} = 0 \qquad a_{13} = \frac{k_{I_{i1}}}{L_1}$$

$$a_{21} = \frac{1}{C_1 + C_2 + C_3} \qquad a_{22} = \frac{-1}{R(C_1 + C_2 + C_3)} \qquad a_{24} = \frac{1}{C_1 + C_2 + C_3}$$

$$a_{26} = \frac{1}{C_1 + C_2 + C_3} \qquad a_{42} = 0 \qquad a_{44} = \frac{-k_{P_{i2}}}{L_2}$$

$$a_{45} = \frac{k_{I_{i2}}}{L_2} \qquad a_{62} = \frac{-k_{P_{i3}} k_{P_{v3}}}{L_3} \qquad a_{66} = \frac{-k_{P_{i3}} - k_{P_{i3}} k_{P_{v3}} R_{d3}}{L_3}$$

$$a_{67} = \frac{k_{P_{i3}} k_{I_{v3}}}{L_3} \qquad a_{68} = \frac{k_{I_{i3}}}{L_3} \qquad a_{82} = -k_{P_{v3}}$$

$$a_{86} = -1 - k_{P_{v3}} R_{d3} \qquad a_{87} = k_{I_{v3}}$$

5.2 Stability and Performance Analysis

The system stability can be determined by examining the eigenvalues of the state transition matrix (A matrix). The system is asymptotically stable if all the eigenvalues of the transition matrix are negative. In an asymptotically stable system, the system will always return to an equilibrium. The models developed for the DC system in different operation modes will be used for stability analysis and the results are summarized as following

5.2.1 Case I: Grid is the Primary, Batteries are Backup

Figure 5.10(a) and (b) shows the dominant eigenvalues when the system operates in Mode I & II. The parameters and system specifications considered for this analysis is similar to the parameters and specs derived in Chapter 4 (Equations 4.16, 4.17 and 4.18).

Figure 5.11 shows the stable/unstable operating points of the system for different loading conditions and PI voltage controller response times. Blue is used for the stable region and red for unstable region.

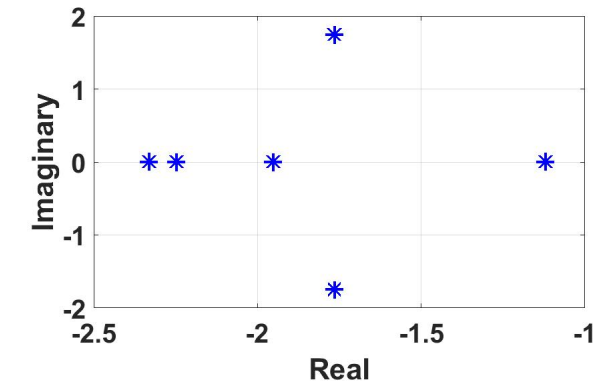

(a)

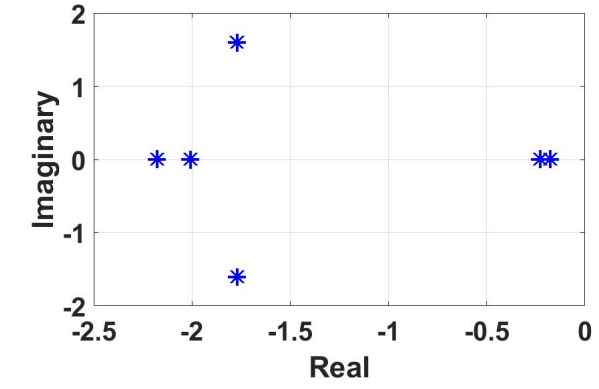

(b)

Figure 5.10 (a): Eigenvalues of the system in Case I - Mode I. (b): Eigenvalues of the system in Case I - Mode II.

5.2.2 Case II: Batteries are the Primary, Grid is the Backup

Figure 5.12(a) and (b) shows the dominant eigenvalues when the system operates in Mode I & II. The parameters and system specifications considered for this analysis is similar to the parameters and specs derived in Chapter 4 (Equations 4.16, 4.17 and 4.18).

Figure 5.13 shows the stable/unstable operating points of the system for different loading conditions and PI voltage controller response times. Blue is used for the stable region and red for unstable region.

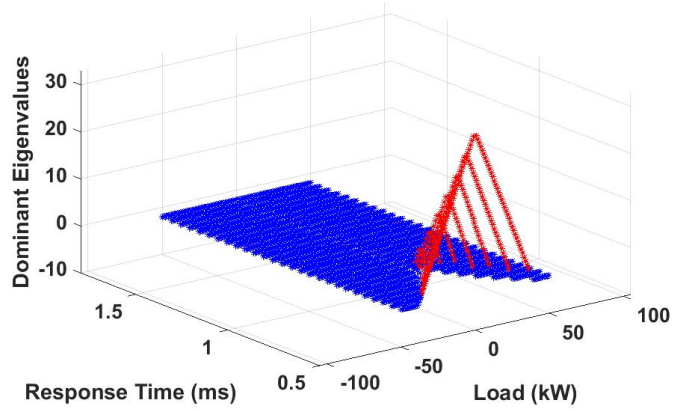

(a)

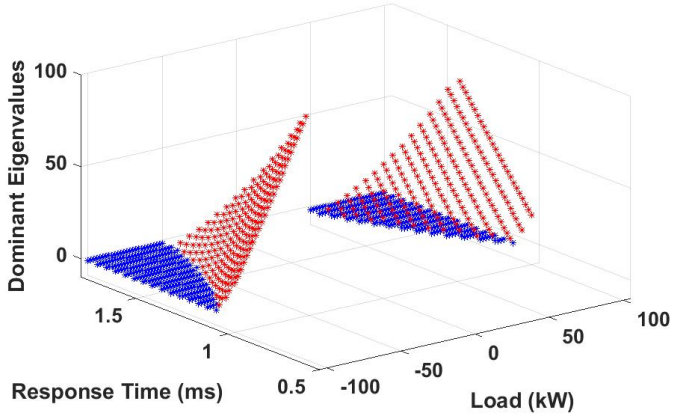

(b)

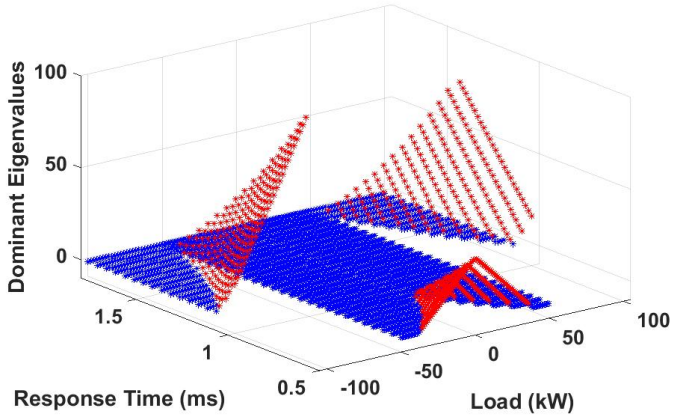

(c)

Figure 5.11 Stable (blue)/unstable (red) operating points of the system for different loading conditions and PI voltage controller response time. (a): Case I-Mode I. (b): Case I-Mode II (c): Case I-Both Modes.

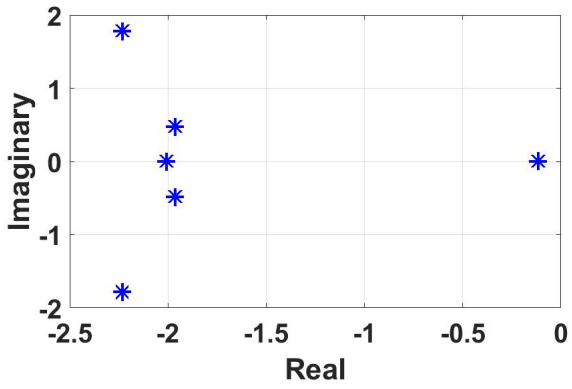

(a)

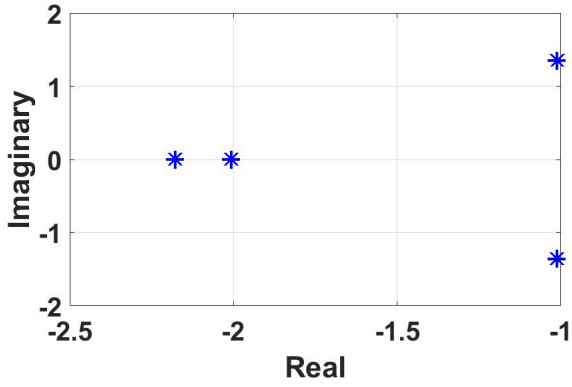

(b)

Figure 5.12 (a): Eigenvalues of the system in Case II - Mode I. (b): Eigenvalues of the system in Case II - Mode II.

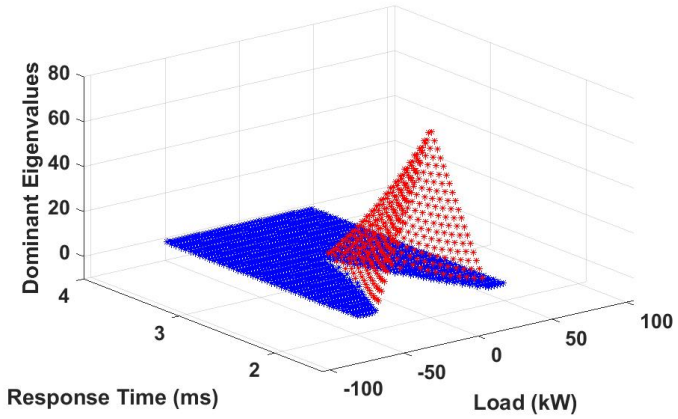

(a)

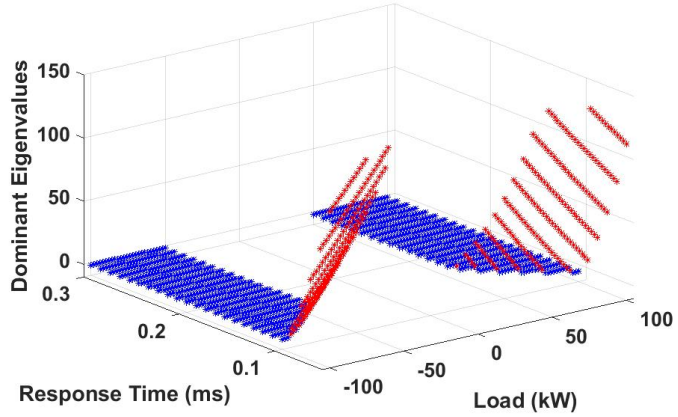

(b)

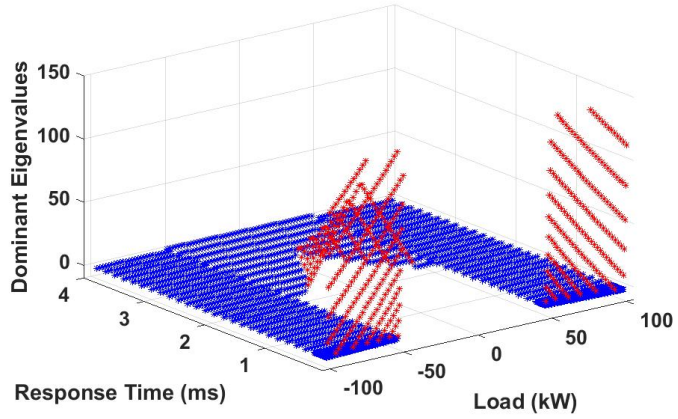

(c)

Figure 5.13 Stable/unstable operating points of the system for different loading conditions and PI voltage controller response time. (a): Case II-Mode I. (b): Case II-Mode II (c): Case II-Both Modes.

CHAPTER

6

PROTECTION OF DC SYSTEMS

6.1 Introduction

In the previous chapters, benefits of the DC microgrids over their equivalent AC systems have been discussed in great detail. It was shown that employing distributed generation, and DC microgrids specifically, in the power grid will result in considerable efficiency improvement and increase in reliability and stability of the grid. However, realization of DC microgrids requires that all the technical issues such as power balance, power quality and protection, are resolved. Although DC microgrids have clear advantages over the AC microgrids, but when it comes to protection, the AC systems enjoy the 100 years of experience, well-defined standards and mature protection devices. On the other hand,

there is no standard for protection of DC systems. And since the AC overcurrent protection devices rely on natural zero current crossing, they cannot be used in a DC system where zero crossing for the current does not exist.

A microgrid consists of multiple sources and loads connecting to the DC bus through VSCs. When a short circuit fault happens on the DC bus, the semiconductor switches in the VSCs lose control and depending on the topology of the VSC, either the freewheeling diodes of the converter behave as a diode rectifier feeding the fault. Or the energy stored in the capacitors and inductors of the system discharges through the freewheeling diodes of the converter. In both cases fast fault detection and interruption is required to prevent the VSC from serious damage.

DC circuit breakers and disconnectors for application up to $1.5kV$ are commercially available [83]. However, they rely on mechanical separation of the contacts in the current path. Therefore, they are not suitable for the circuits that require fast current interruption. Although the mechanical DC breakers are effective in protection of the conductors of the system, but they do not provide protection for the converters of the system. On the other hand, the cost associate with the mechanical DC circuit breakers are higher compared to the AC counterpart which is in contrast with the lower initial investment of the DC systems. According to the mentioned reasons, the need for a fast, cost-effective with smaller footprint DC circuit breakers is unquestionable.

In the remainder of this chapter, the protection of DC microgrid with the focus on overcurrent protection devices and methods is presented [84], [85]. Then, we examine the different grounding methods and system architectures and discusss the design trade-offs in terms of safety, reliability, detection, mitigation, noise, and cost. Moreover, impedance grounding, isolation, and bi-polar architectures are examined and their benefits with respect to these criteria are discussed [86].

6.2 Fault Types

In general, faults in a DC microgrid can be divided into line to line faults and one line to ground faults. The line to line fault happens when the positive and negative poles of the system get shorted, this type of fault often has low fault impedance. The line to ground fault happens when the positive or negative pole of the systems touches the ground, this fault can have either low fault impedance or high fault impedance. These faults can happen anywhere in the system including on the main bus, feeders, close to the converters, close to the main bus. Figure 6.1 shows possible faults in different locations in a typical DC microgrid. F1 and F4 are line to line faults at the converter terminals while F2 and F3 show line to line faults closer to the main bus. F6 is a negative to ground fault on the main bus.

It can be seen that the DC microgrid shown in Figure 6.1 consists of two grid connected bidirectional AC/DC converters and one battery with DC/DC charge controller and a DC load connected to the main bus through a DC/DC converter. Cables connecting each converter to the main bus are modeled with series resistance and inductance in parallel with capacitors, as an example cable 1 is modeled with R_{L1} L_{L1} C_{L1} in the figure.

6.3 Remarks on Interruption of DC Current

There is a structural difference between the AC and DC circuit breakers and this is because of the absence of natural zero crossing of the current in a DC system. Therefore, DC breakers need to create an artificial current zero crossing by some extra means and then open the switch or they should employ the solid state devices to interrupt the DC current.

From Figure 6.2

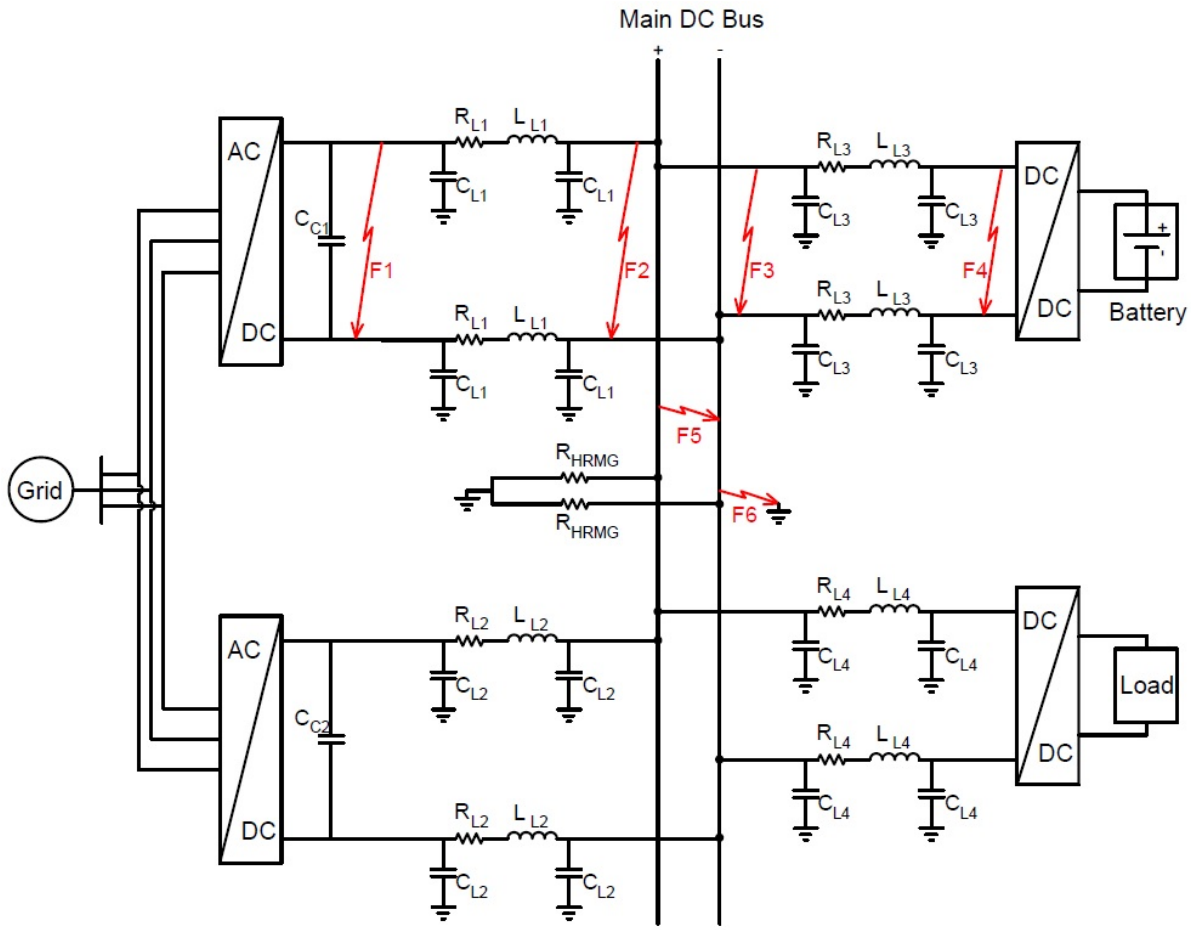

Figure 6.1 Possible faults in a typical DC microgrid with star configuration.

$$U = L\frac{di}{dt} + Ri + U_a \tag{6.1}$$

where U is the rated voltage of the system, L is the inductance of the circuit, R is the resistance of the circuit and U_a is the arc voltage. The formula can be rearranged as the following

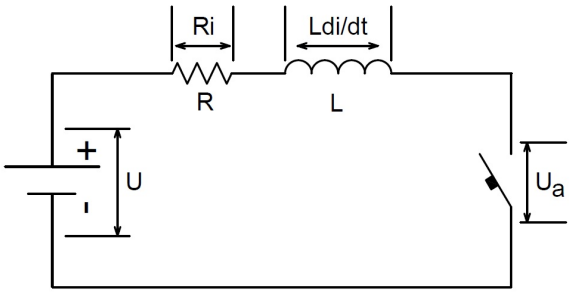

Figure 6.2 Simplified circuit of a DC system with DC circuit breaker.

$$L\frac{di}{dt} = U - Ri - U_a \tag{6.2}$$

To achieve the zero current crossing, $\frac{di}{dt}$ should become negative. This will be achieved when U_a is high enough that the right side of Equation 6.2 becomes negative. Besides the mathematical considerations, it can be concluded from Equation 6.2 that, the dying rate of the current is proportional to the time constant of the circuit ($\tau = \frac{L}{R}$) and the extinction constant which itself depends on the arc characteristic and the supply voltage [83]. Figure 6.3 shows the result from a short-circuit test carried out at ABB SACE power testing laboratories.

where I_p is short circuit current , I_{cn} is prospective short circuit current, U_a is maximum arc voltage, U_n is network voltage, T is time constant, t_0 is beginning of the short circuit, t_s is beginning of the contact opening, t_a is instant of current interruption.

When a fault/short circuit happens in the system at t_0, the current starts increasing with respect to the time constant of the system, at t_s the contacts of the breaker start separating and an arc generates in the breaker. The short circuit current keeps increasing even after the contact separation, and then starts to decrease depending on the arc voltage. As it is shown in Figure 6.3, during the current interruption, the arc voltage is higher than the

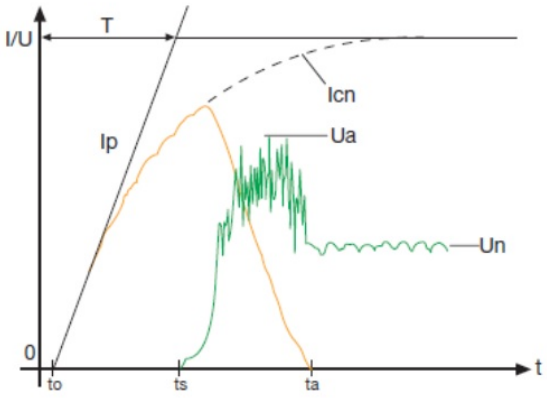

Figure 6.3 Short circuit current interruption test carried out at ABB SACE [83].

system voltage. Eventually at t_a the current is completely quenched. As the graph shows, the short circuit current is interrupted without sudden interruption which can cause high voltage peaks. Consequently, to achieve gradual extinction, it is necessary to cool the arc and increase the arc resistance and consequently the arc voltage. This is an energetic phenomena which depends on the system voltage, U_n, and can be obtained by inserting more and more opening contacts in series in a breaker. This means that, when the voltage level increases, it is necessary to increase the number of current interruptions (poles) to increase the arc voltage. However, the mentioned procedure for interrupting DC current cannot be used for the systems with high voltage ratings and for the systems that require fast current interruption. Therefore, different techniques of interrupting DC current need to be used.

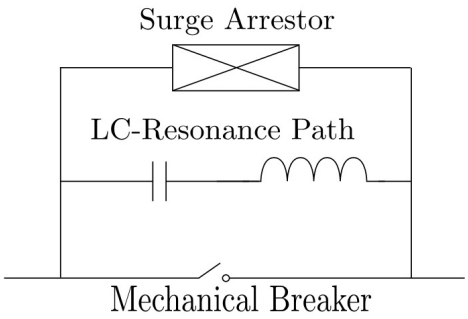

Figure 6.4 Mechanical DC circuit breaker with parallel LC resonance path.

6.4 Possible DC Circuit Breaker Topologies

6.4.1 Mechanical DC Circuit Breaker with Parallel LC Resonance Path

Figure 6.4 shows the schematic of the mechanical DC circuit breaker with parallel LC resonance path. When the fault is detected, the mechanical breaker is opened and an arc is established between the terminals. The arc voltage causes an oscillation in the main current path. At a certain instant, oscillation forces the current to cross zero and the breaker will interrupt the current. The short circuit current starts flowing through the resonating circuit charging the capacitor. At a particular voltage level, the surge arrester starts conducting and the current slowly ceases.

Table 6.1 below shows the typical ratings and present status of development of this resonance circuit breaker.

6.4.2 Full Solid State DC Circuit Breaker

Figure 6.5 shows the circuit breaker using fully solid state devices. Here no artificial zero crossing arrangement is used as discussed earlier. The solid state devices are turned off as soon as any fault is detected. Therefore, the current has to find path through the surge

Table 6.1 Typical ratings and present development status of the resonance circuit breaker.

Expected total interruption time	$< 60ms$
Required time for 1. Commutation and 2. Energy absorption	 $<\sim 20ms$ for contact separation and current zero creation $<\sim 30ms$ for passive resonance $<\sim 2ms$ for active resonance
Maximum rated voltage	$< 500kV$
Maximum DC breaking current	< up to $4kA$ proven in operation (up to $8kA$ possible with active resonance) Possible to survive transient over-currents
Expected power loss compared to the protected VSC	0.001% (metal contacts)
Current state of development	Applied in CSC HVDC Used as Metallic Return Transfer Breaker (MRTB)
Further development steps	Optimization of DC arc chamber for passive resonance to achieve higher current rating and to minimize time for current zero creation

arresters and hence the current dies down to zero after few microseconds. The energy stored in the system inductances is dissipated in the surge arresters or the snubber circuit.

Table 6.2 shows the typical ratings and present development status of this solid state circuit breaker.

6.4.3 Hybrid Solid State DC Circuit Breaker with Mech Disconnector

Fig 6.6 shows the structure of the hybrid solid state circuit breaker with mechanical disconnector. Here also no artificial zero crossing arrangement is used as discussed earlier. In

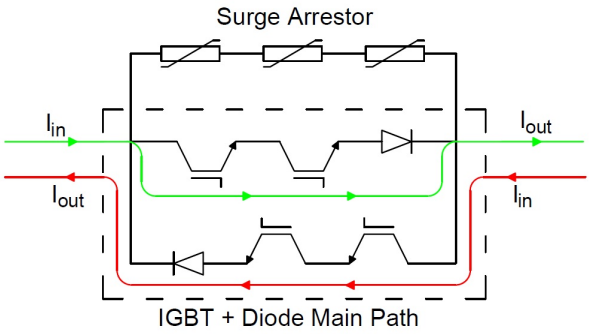

Figure 6.5 Full solid state DC circuit breaker.

Table 6.2 Typical ratings and present development status of the full solid state DC circuit breaker.

Expected total interruption time	$<1ms$
Required time for 1. Commutation and 2. Energy absorption	 $<0.1ms$ $<1ms$
Maximum rated voltage	$<800kV$
Maximum DC breaking current	$5kA$ expected
Expected power loss compared to the protected VSC	<30% (large forward voltage drop)
Current state of development	Available for low voltage
Further development steps	Development in solid state devices technology to reduce on-state forward voltage and number of modules in series for high voltage applications

the main path only a few semiconductor switches such as IGBTs in are placed in series to have low conduction loss. In the commutation path more number of IGBTs are connected in series to block the voltage. As the fault is detected, the IGBTs in the main path are turned off and that of commutation path are turned on. The fault current starts flowing through the commutation path IGBTs. Eventually, the mechanical switch in the main path is opened

and the commutation circuit IGBTs are opened after that. The current is then forced to flow thorough the surge arresters and hence the short circuit current dies down to zero after a few milliseconds.

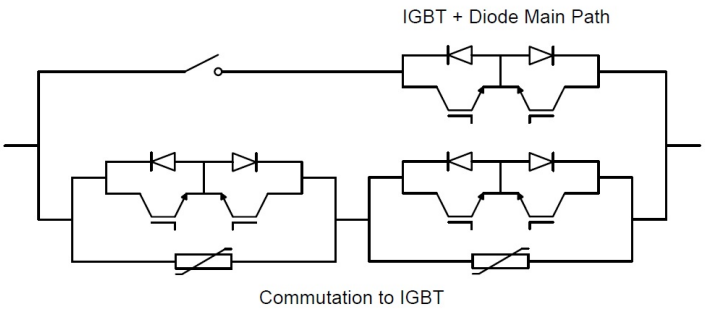

Figure 6.6 Hybrid solid state circuit breaker with mechanical dis-connector.

Table 6.3 shows the typical ratings and present status of development of this solid state circuit breaker.

6.4.4 Hybrid Solid State DC Circuit Breaker with Fast Mechanical Switch

Schematic of this circuit breaker is shown in Figure 6.7. This configuration is slightly slower compared to the other solid state breakers. The solid state switches are chosen to block the full voltage and have high on state resistance. Therefore, during normal operation, they are kept OFF and they only come into picture as any fault is detected in the line. The mechanical switch is turned off and the short circuit current starts flowing through the solid state switches. After a few milliseconds the solid state switches are also turned OFF and the current is forced to flow through the surge arrestors. Hence the short circuit current slowly becomes zero after few milliseconds.

Table 6.4 shows the typical ratings and present status of development of this hybrid

Table 6.3 Typical ratings and present development status of the hybrid solid state DC circuit breaker with mechanical dis-connector.

Expected total interruption time	$<2ms$
Required time for 1. Commutation and 2. Energy absorption	 $<0.2ms$ for commutation <1ms for dis-connector opening $<1ms$
Maximum rated voltage	$<120kV$ verified by test (up to $320kV$ achievable)
Maximum DC breaking current	$9kA$ experimentally proven (up to $16kA$ expected)
Expected power loss compared to the protected VSC	<1% (only few IGBTs in series in the main path)
Current state of development	Working principle proven type test and interruption test with downscaled breaker passes
Further development steps	Field experience with prototype in a test grid and reduction of IGBT costs

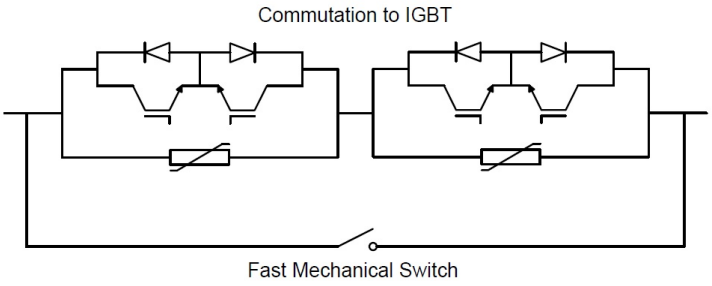

Figure 6.7 Hybrid solid state circuit breaker with fast mechanical switch.

solid state circuit breaker.

Table 6.4 Typical ratings and present development status of the hybrid solid state DC circuit breaker with fast mechanical switch.

Expected total interruption time	$<5-30ms$
Required time for 1. Commutation and 2. Energy absorption	 $<20ms$ for contact separation (conventional AC circuit breaker) $<1-5ms$ for magnetically driven ultra-fast switch with opening speed $>20m/s$
Maximum rated voltage	AC circuit breakers>$500kV$ Ultra-Fast Switches>$12kV$
Maximum DC breaking current	$6-12kA$ (estimated)
Expected power loss compared to the protected VSC	<0.001% (metal contacts)
Current state of development	Not yet available Slow AC breakers are available Ultra-Fast Switches not yet available
Further development steps	Development of ultra-fast mechanical drives to reduce commutation time

6.4.5 Hybrid Fault Current Limiting Circuit Breaker

As of today, several approaches have been introduced for the fault current limiters (FCL) which their key elements are semiconductor switches, ultra-fast switches and pure nickel wire resistor (PTC) [87], [88]. The hybrid limiter that is discussed in this thesis does not have any semiconductor devices in it and its key elements are ultra-fast switches and PTC. A FCL is required to be able to 1) carry the load current in the normal operation condition, 2) increase the impedance quickly in the case of fault and 3) dissipate the energy stored in the system inductances. To fulfill these requirements, a hybrid system will be used as it is

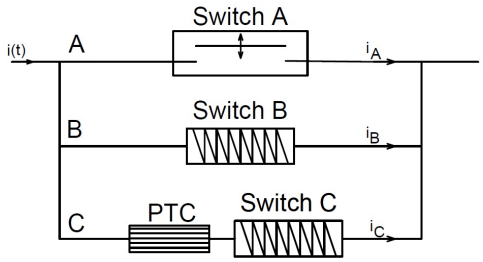

Figure 6.8 Schematic of the hybrid FCL.

shown in Figure 6.8. For the current limitation purpose, the voltage drop across the limiter should be as high as the system voltage. Based on this, the impedance in path A should increase rapidly. Consider a DC system with voltage of $20kV$. Assume the arc voltage in switch A after opening is $100V$. Therefore, the impedance needs to be increased by the ratio of 200. Moreover, the limiter should be able to dissipate huge amount of energy, if the current needs to be limited by $5kA$ in the above system, the dissipated power would be $100MW$ and an energy of several $100kJ$ [87].

6.4.5.1 Operation Principle of the Hybrid Fault Current Limiter

In the normal operation condition, the load current flows through path A. Whenever a fault is detected, the current will be commuted to path B at t_1. Switch A is an ultra-fast switch with a very low moving mass which can be opened in the order of $100\mu s$. The arc voltage of $10-100V$ between switch A contact will force the current to flow through switch B which is closed. Switch B consists of several ultra-fast switches in series which are driven by a common repulsion drive. Switch B opens at t_2, since switch B consists of several ultra-fast switches, when it opens the arc voltage across the switch would be equal to the summation of the arc voltage over the each ultra-fast switch. Therefore, the overall arc voltage would be high enough to commute the fault current, which is still rising, to the path C. Path C consists of several nickel wire resistors in series, the resistance of these resistors are increased when

the current flows through them and heats them up. Therefore, the large voltage drop over these resistors can limit the fault current [87], [88].

6.4.5.2 Requirements for the Fast Switches Used in the Hybrid Fault Current Limiter

The hybrid FCL that was discussed in this chapter has three current paths with ultra-fast switches in each. In this section, the requirements for each of these switches are discussed. The ultra-fast switch in path A needs to be designed in such a way to carry the load current continuously, and also to withstand system voltage when it is opening. Moreover, it needs to commute the fault current in $10-100\mu s$ to path B. Therefore, allowable commutation time, maximum current and resistance of switch B needs to be take into account in selecting switch A. The current is flowing in switch B for less than $1ms$ during the limitation process. The resistance of switch B in closed position is very important for current commutation. The most important thing that influences in the resistance of switch B is the number of ultra-fast switches that are put in series. The following equation can be used to calculate the minimum number of series modules.

$$n_m > \frac{U_n(I_{pros}.W_n t_{com,B} + \sqrt{2}I_n)}{\sqrt{2}U_{arc,B} I_n K_{PTC} K_{lim}} \tag{6.3}$$

Where U_n is the rated voltage, I_n is the rated current, W_n is the frequency, $U_{arc,B}$ is the arc voltage, $t_{com,B}$ is the the commutation time, K_{PTC} is the increase of resistance of PTC, and K_{lim} is the limitation factor [87]. As it was mentioned earlier, one of the components in the hybrid FCL is the fast/ultra-fast mechanical switch. There are three different mechanisms that are used in these switches including: ultra-fast switches using Thompson effect, ultra-fast switches with linear acceleration design and ultra-fast switches with rotational acceleration design [87],[88],[89], [90].

1. **Ultra-Fast Switch based on Thompson Effect:** Thompson coil based operating mechanism for ultra-fast switches have been discussed in detail in [89], [90] and [91]. The main limiting factor of the opening speed, is the generation and transmission to the moving parts of a large actuating force. The ironless Thomson actuator can make the opening delay as short as possible [89]. There are different methods of opening and closing for the fast mechanical switch. In one of these methods which is presented by [89], the main forces are applied to the moving contact. The closing force is produced by a combination of an electromagnet/permanent magnet. Figuref 6.9(a) shows how the closing force, f_s, mechanism works. The closing force is produced by a combination of an electromagnet/permanent magnet. When the electromagnet energizes, the iron core is attracted to it and this magnetizes the permanent magnet and keeps the moving contact in the closing position. The opening procedure is completely different from the closing. Thomson effect is the base for the opening mechanism. In this method, two windings, primary (fixed) winding and secondary (moving) winding, are producing the opening force. The primary winding is made from an extremely thin and compact planar coil while the secondary winding, consists of a massive copper disk. These two windings are placed in a coaxial configuration. A capacitor is discharged in the primary winding, this generates a current in the primary winding and consequently a strong current is induced in the secondary winding. The currents in the primary and secondary are in opposite directions, which creates a strong force to the moving contacts [89].

2. **Ultra-Fast Switch with Linear Design:** This mechanism is considered as a basic method to design such fast switches. In this design, a repulsion drive is used to open and close the switch. A ring of aluminum is used as the moving contact. This ring connects two fixed contacts of the switch in the closed position. The fixed contacts

are shown as FC1 and FC2 in Figure 6.9(b). When the switch is in the on position, the load current flows from the inner FC1 to outer FC2 in the radial direction. Drive coil 1 and 2 which have several turns are used to open and close the switch respectively. Capacitor C_d is connected in series switch T1, by closing T1 the capacitor discharges into the drive coil which results in high current i_d. i_d induces eddy current called i_E in the aluminum ring. These two currents, i_d and i_E, produce a repulsion force which moves the ring to the upward direction and opens the switch The closing procedure is the same as opening, however for the closing the drive coil 2 is used [87], [88].

3. **Ultra-Fast Switch with Rotational Design:** Figuref 6.9(c) shows the sketch of the ultra-fast switch using rotational design. The same as the switch with linear design, repulsion force is used to open and close this switch. However, the moving contact has rotational movement and the shape of the moving contact is cuboidal. In the normal operating condition, the load current flows from FC1 to the FC2. The drive coil 1 and 2 are used for opening and closing the switch respectively. Capacitor C_d is connected in series with switch T1, by closing T1 the capacitor discharges into the drive coil which results in high current i_d. id induces eddy current called i_E in the moving contact. These two currents, i_d and i_E, produce a repulsion force which rotates the moving contact to the upward direction and opens the switch. The closing procedure is the same as opening, however for closing the drive coil 2 is used [87], [88].

6.5 Performance Evaluation of the DC Circuit Breakers

When it comes to selecting a DC circuit breaker, parameters like efficiency, size, costs and the time required by the breaker to interrupt the current should be taken into consideration. In order to make our four depicted topologies comparable, these topologies are modeled

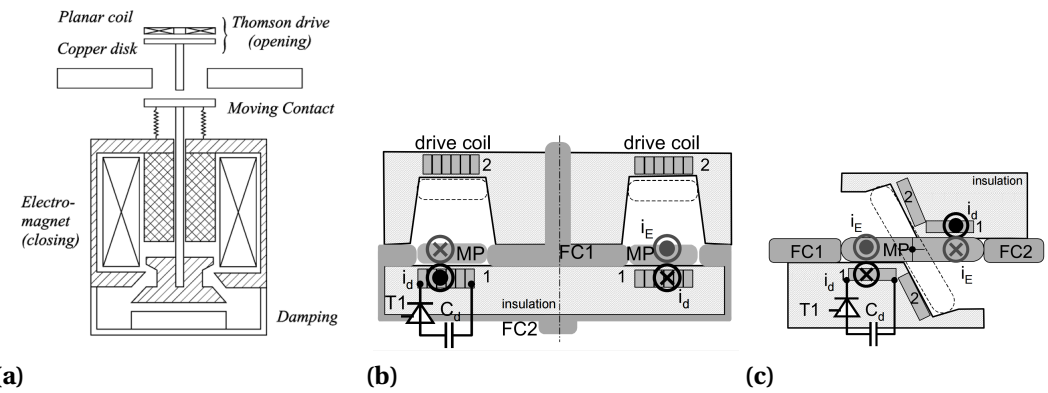

Figure 6.9 (a): Mechanism used for opening and closing the breaker [92]. (b) Linear operation design for the fast switch. (c): Rotational operation design for the fast switch [87].

in PSCAD and the performance of them are evaluated under the DC fault condition. In this section, the model of DC circuit breakers in PSCAD and their performance under fault is presented.

6.5.1 Mechanical DC Circuit Breaker with Parallel LC Resonance Path

The first circuit breaker selected for evaluation is the mechanical circuit breaker with parallel LC resonance path, the configuration of this breaker was shown in Figure 6.4. Under normal operation the entire load current flows through the mechanical switch. Under steady state condition, the LC path stays inactive. When a fault is detected in the system, the mechanical switch is opened and as a consequence arcing occurs between the contacts. For a conceptual study, the arcing characteristics were developed as per the model developed for LV DC breakers. The arcing voltage developed has an important characteristic; the $I-V$ characteristic of the arc has a negative gradient as a result of which the LC circuit is activated. Owing to this, the current begins to oscillate and at the zero crossing, the mechanical breaker is fully opened. The equation for the circuit under oscillation can be written as

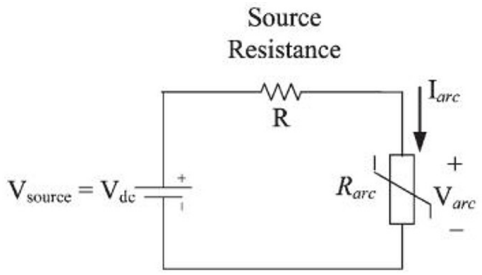

Figure 6.10 Simplified equivalent circuit for representing DC arc [93].

$$LD^2 I_{\text{Breaker}} + \frac{DV_{\text{arc}}}{DI_{\text{Breaker}}} + \frac{I_{\text{Breaker}}}{C} = \frac{I_0}{C} \tag{6.4}$$

where, $D = \frac{d}{dt}$, I_0=line current, L, C are the inductance and capacitance of the resonant circuit. The equation for the breaker current is thus obtained as

$$I_{\text{Breaker}} = I_0[1 + e^{\frac{1}{2L}\frac{dV_{\text{arc}}}{DI_{\text{Breaker}}}t} sin(W_C t)] \tag{6.5}$$

where W_C is determined by C and L.

In order to be able to simulate this DC circuit breaker in PSCAD, model of high-current DC arc is required. It is very complicated if not impossible to develop a theoretical arc model based on arc's physics. So, a simplified equivalent circuit can represent arc when only objectives are to determine arc current and voltage. This simplified equivalent circuit is shown in Figure 6.10.

6.5.1.1 High-Current DC Arc Modeling

DC arc model is needed to model different situations in the DC power systems. The discussed mechanical DC circuit breaker is a good example. However, there are limited scien-

tific literature in modeling high-current DC arcs [93]. In this part, the process of finding a good model and implementing that model in PSCAD will be discussed. There are three different methods that can be used to develop a model for arc [94]

- Physics-based models: arcs are very chaotic in nature and complex, so developing a theoretical model based on arc physics is very complicated.
- Equivalent circuit models: this model focuses on either V-I characteristic of the arc or its apparent impedance. So whenever the effect of the arc on an electric circuit is desired, this model can be considered.
- Heuristic model: experimental data is used along with mathematical macroscopic mathematical model to model the arc [95].

Since we need to see the effects of arc on the electric circuit shown in Figure 6.10, the **Equivalent Circuit Model** will be used in our modeling. From early 1900s to present, scientists have tried to obtain the $V-I$ characteristics and equations of DC arcs. Results from these efforts are presented in the remainder of this chapter. It should be noticed that the earlier research was mostly focused on low-current DC arcs. However, the most recent ones cover the high-current DC arcs also.

6.5.1.2 V-I Characteristics and Equations of DC Arc

(a) **Ayrton Equation**: Ayrton formulated the first steady-state arc which goes back to 1902. The electrodes (anode and cathode) are from carbon and are separated by a few millimeters. The following equation shows the $V-I$ relation of the arc.

$$V_{arc} = A + BL + \frac{C + DL}{I_{arc}} \tag{6.6}$$

where A is the electrode voltage drop, B is the voltage gradient. C and D are constants to model the non-linear characteristic of the arc. L represents the arc length (which is difficult to specify).

(b) **Steinmetz Equation**:The semi-empirical equation in the following relates to the voltage and current of the arc based on Charles Steinmetz findings in 1906.

$$V_{arc} = A + BL + \frac{C + DL}{I_{arc}} \tag{6.7}$$

where A and C and D are constants that depend on arc length and electrodes material. And L is the arc length.

(c) **Nottingham Equation**

The last two models show an inverse characteristics of the arc current and voltage. In 1920 Nottingham came to the same conclusion.

$$V_{arc} = A + \frac{B}{I_{arc}^{n}} \tag{6.8}$$

where A and B are constants which depend on the electrode materials and the arc length. Also n is the function of the electrode material. Figure 6.11 shows the $V-I$ characteristic of the DCarc based on Nottingham model.

These early studies are based on limited tests and low currents; and the test procedure does not follow standard procedure. Therefore, many of these data cannot be considered as precise and reliable. Other scientists have done research on DC arc modeling which have been discussed in detail in [93]. In the following they are mentioned by name.

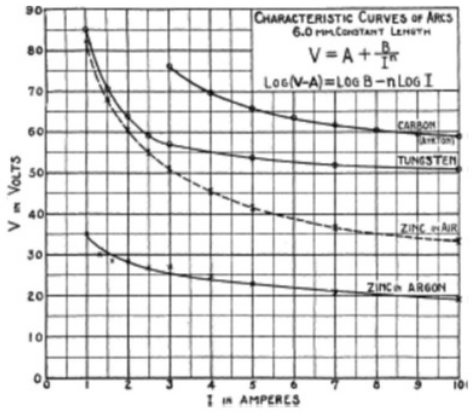

Figure 6.11 sample of $V-I$ characteristic of dc arc, arc length is $6mm$ [96].

(d) **Van and Warrington Equation**

(e) **Miller and Hilderbrand**

(f) **Hall, Myers and Vilicheck**

(g) **Stokes and Openlander Model**

(h) **Paukert's Compilation of LV Arcing-Fault Data Solver**

6.5.1.3 Selected DC Arc Model

The model developed by **Stokes & Oppenlander** seems to be the closest model of a DC arc which can be used in our case. This model covers the free-burning vertical and horizontal arcs between series electrodes with high DC current in order of kA as well as gap lengths from $5mm$ to $500mm$ [97]. The following equations show the $V-I$ relation of the DC arc and its apparent resistance for currents greater than transition current.

$$V_{\text{arc}} = (20 + 0.534 Z_g) I_{arc}^{0.12} \tag{6.9}$$

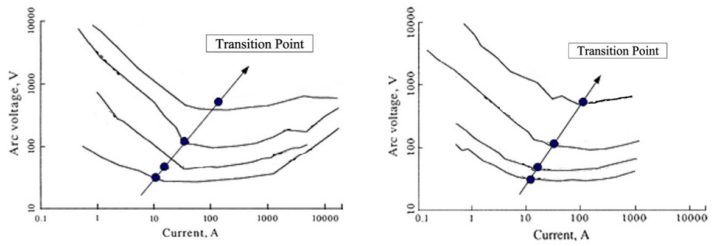

(a) (b)

Figure 6.12 (a): Minimum arc voltage for horizontal arcs. (b): Minimum voltage arc for vertical arcs. For both cases the gap lengths from bottom to top are: 5, 20, 100 and 500mm.

$$R_{\text{arc}} = \frac{20 + 0.534 Z_g}{I_{arc}^{0.88}} \tag{6.10}$$

where Z_g is the length of the gap in millimeters.

$I_t = 10 + 0.2 Z_g$ Specifies the transition current for different gap lengths. These transition points have been shown in Figure 6.12. The curves show inverse $V - I$ characteristics for currents less than transition current. However, for currents greater than the transition currents, the voltage increases slightly by increasing in current. Stokes and Oppenlander model also shows a good agreement with Paukert's finding especially for the currents above $100A$ [93].

6.5.1.4 Gap Length Change in a Real Breaker

As it can be seen in Equation 6.10, arc resistance varies by change in the gap length between the electrodes. Therefore, gap length change in a real circuit breaker over time needs to be known to have a realistic model. In the following an estimation was done based on some assumptions. Firstly, it is not necessary to consider acceleration of the moving of the breaker. The Moment of Inertia of the moving arm is very small when compared to the amount of torque that will be applied. Secondly, the arc path: The path is determined

by the geometry of the contact arrangement. If a flat bar type arrangement is considered, then the minimum distance is the perpendicular distance between the arm and the fixed contact at any point of time. This turns out to be a sine function of the angle of the arm. If the contact is arranged so that it is not possible for an arc to form from the moving arm then the relationship is linear with the angle of the arm. This appears to be the way that most breakers are arranged based on typical size breakers that are presently available. If the maximum contact opening distance is assumed around $5cm$, probably fairly accurate for a $1200A$ frame circuit breaker. And a maximum clearing time of 5 cycles at $60Hz$, we should be able to come up with a relationship between arc length and time. It will look like the following equation

$$L = \frac{5cm\frac{1m}{100cm}}{\frac{5\text{cycles}}{60\frac{\text{cycles}}{s}}} = \frac{0.05m}{0.0833s} = 0.6\frac{m}{s} \tag{6.11}$$

So a good relationship between the gap length and time can be presented as

$$Z_g = 600t \qquad 0 < t < 0.083s \tag{6.12}$$

where Zg is in millimeter.

6.5.1.5 Steady State DC Arc Model in PSCAD

The steady state DC arc has been modeled using the variable resistor component in PSCAD. Equations 6.10,6.12 were used to calculate the value of arc resistance. In our case, while a $380V_{dc}$ source is supplying total load of $170kW$ through a DC cable with $R = 0.128\Omega$ and $L = 1.11mH$, a normal AC breaker opens the circuit and since there is no zero crossing in

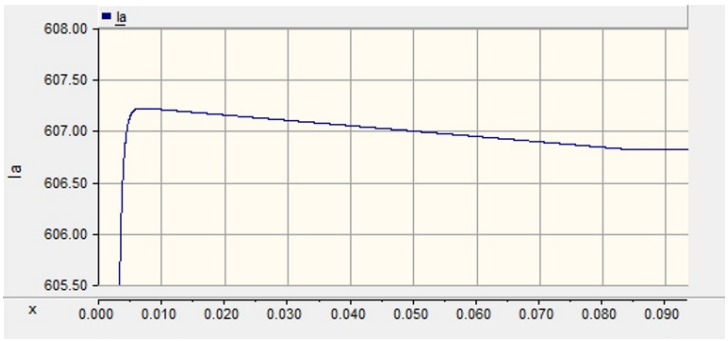

(a)

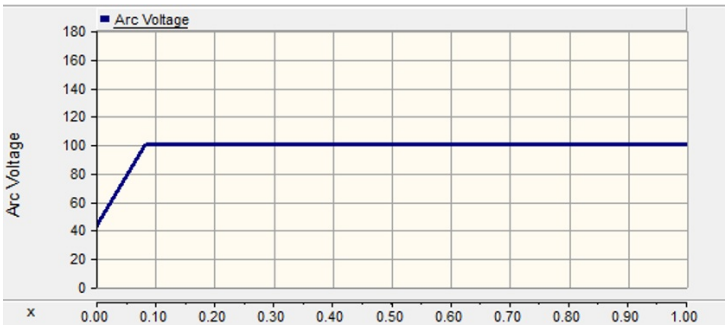

(b)

Figure 6.13 Steady state DC arc current (a). Steady state DC arc voltage (b).

current, the DC arc will be achieved. Figure6.13 the arc voltage and current in the above circuit.

6.5.1.6 Mechanical Resonance DC Circuit Breaker Requirements

The discussed mechanical resonance DC circuit breaker produces artificial zero current by superposing an oscillating current on the DC current. To achieve the artificial zero current crossing, an LC series resonance circuit is put in parallel with the interrupter (can be a conventional AC breaker). By appropriate selection of L and C, the oscillating current will be greater than the DC current passing through the interrupter and accordingly, a superposed current, which is the summation of oscillating current and the DC current can produce zero current in the interrupter. So, the DC arc in the breaker can be extinguished.

This method of arc extinguishing can be divided into two different methods with respect to the electrical charge of the capacitor before its connection to the interrupter [98]. The two methods are

1. Pre-charging method.

2. Non-charging method.

In the pre-charging method, the capacitor can be connected to the interrupter just before or just after the interrupter is opened. The oscillating current in this method can be described as

$$I_{oscillating} = E_c \sqrt{\frac{C}{L}} e^{-\alpha t} sin \frac{t}{\sqrt{LC}} \tag{6.13}$$

where: E_c is the initial voltage of the capacitor, C is the capacitance of the capacitor, L is the inductance of the inductor, t is time, α is a constant.

In order to interrupt the DC current with pre-charging method, the following two requirements need to be fulfilled.

$$I_{max} = E_c \sqrt{\frac{C}{L}} \tag{6.14}$$

$$\frac{di}{dt} < \beta \tag{6.15}$$

where I_{max} is the maximum DC current that can be interrupted by the breaker. β depends on the interrupter, if the current slope exceeds from that value failure can occur The current

slope can be determined using

$$\frac{di}{dt} \sim (0.6-0.7)\frac{E_c}{L} \tag{6.16}$$

Equation 6.14 shows that increasing the initial voltage of the capacitor, will increase the capability of the breaker in interrupting higher DC currents. However, increasing E_c will increase the current slope. In order to keep the current slope constant, L needs to be increased. On the other hand, increase in L, reduces the oscillating frequency which means that higher time will be needed for the breaker to interrupt the current. So it can be concluded that the higher the breakable current, the slower the breaker in interrupting the current. In the non-charging method, the capacitor is connected in parallel with the interrupter through a switch. Whenever the arc voltage of the interrupter reaches to a certain value, the switch will be closed. The maximum DC current that can be interrupted with this method is shown in the following equation.

$$I_{max} < V_a\sqrt{\frac{C}{L}} \tag{6.17}$$

where V_a is the arc voltage at the time of connecting the capacitor.

In this method, the increase in maximum breakable current can be achieved by choosing a small inductance. Therefore, the oscillating frequency will also increase by increase in the maximum breakable current. This characteristic, makes the non-charging method the superior method for interrupting high DC currents.

6.5.1.7 Mechanical Resonance DC Circuit Breaker Evaluation in PSCAD

The model system in PSCAD is a $380 V_{dc}$ voltage source that supplies a $380 kW$ load through a cable with resistance of 0.128Ω and inductance of $1.11 mH$. A line to line DC fault happens at $0.1 s$ as soon as the current reaches to two times of the rated current, $2 kA$ in this case, a fault is detected and the interrupter will be opened. Whenever the arc voltage reaches to a certain value, $50 V$ in our case, the series resonance LC circuit connects in parallel with the interrupter to extinguish the arc by creating zero current crossing. The values of C and L have been calculated based on the explanations in the previous section. $L = 0.05 \mu H$ $C = 0.1 F$

DC current in the main path, oscillating current, arc voltage are shown in Figure6.14 (a), (b) and (C), respectively.

As it can be seen in Figure 6.14, at $0.1 s$ the breaker opens and the arc is extinguished in $0.145 s$. It means that it takes less than 50ms for the breaker to interrupt the fault current. The zero arc voltage before $0.1 s$ means that the interrupter has not been opened yet and there is arc doesn't exist.

6.5.2 Full Solid State DC Circuit Breaker

The second evaluated topology is full solid state DC circuit breaker, configuration of this topology was shown in Figure6.5. The model system in PSCAD is an $380 V_{dc}$ voltage source that supplies a $380 kW$ load through a cable with resistance of 0.128Ω and inductance of $1.11 mH$. Under normal operation the entire load current flows through the semiconductor devices (diodes and IGBTs in series). The line current is to be continuously sensed and when a fault is detected the gating pulse is made low to turn off the IGBTs. Thus the IGBT switches are subjected to a blocking voltage the same as system voltage, $380 V_{dc}$ in this case. On state resistance of IGBTs and diodes result in high conduction losses which affects

(a)

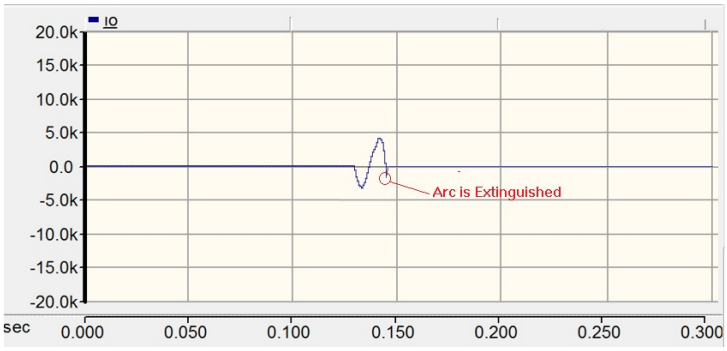

(b)

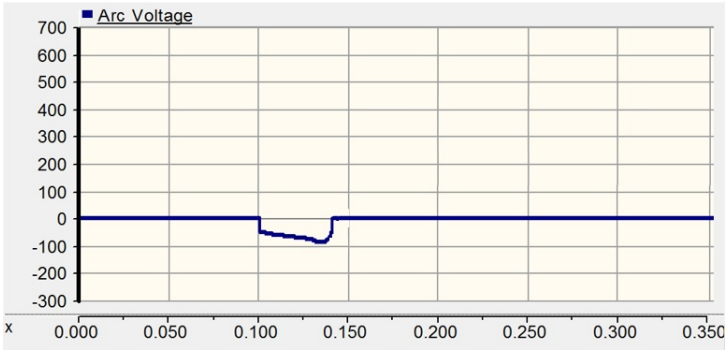

(c)

Figure 6.14 (a): Current in the main path. (b): Oscillating current. (c): Arc voltage.

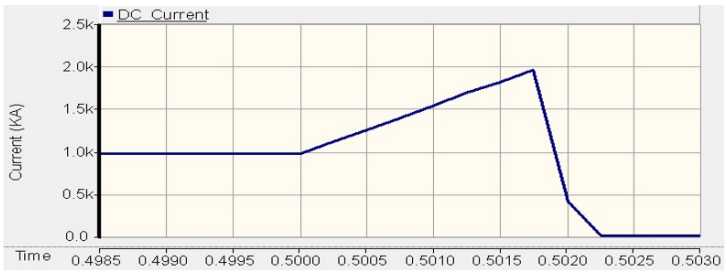

Figure 6.15 Line current waveform of full solid state DC circuit breaker under line to line DC fault.

the efficiency of this configuration. For the test system, the current limit is set at $2kA$. The response time with this topology in order to cut off the fault is under $1ms$ as shown in Figure 6.16.

6.5.3 Hybrid Solid State DC Circuit Breaker with Mech Disconnector

The third topology is as shown in the Figure 6.6. The model system in PSCAD is a $380V_{dc}$ voltage source that supplies a $380kW$ load through a cable with resistance of 0.128Ω and inductance of $1.11mH$. Under normal operation the entire load current flows through the semiconductor devices in series with the mechanical switch, while the lower devices stay off. When a fault occurs, the mechanical switch is opened and the lower devices are turned on simultaneously, followed by the switching of the upper devices. Thus the lower IGBT switches and diodes are subjected to a blocking voltage, while the upper switches that carry the load current under normal conditions are protected from the voltage surge owing to the opening of the mechanical switch. Thereby in comparison with the full solid state circuit breaker, this topology results in a more efficient DC circuit breaker. This topology is suitable for the applications that require high voltage blocking.

For the test system, the current limit is set at $2kA$. The response time with this topology in order to cut off the fault is about $3ms$ as shown in Figure 6.16.

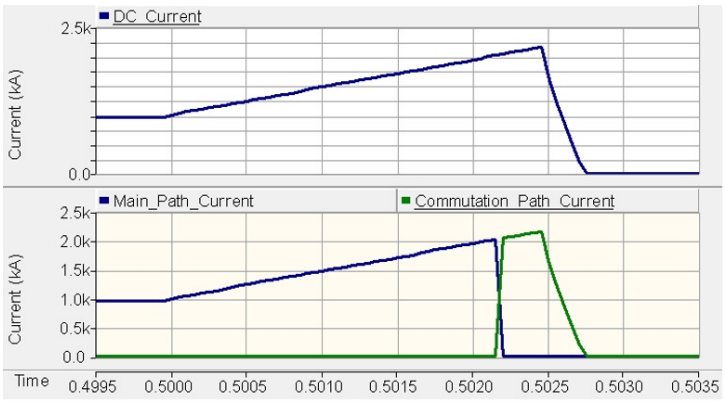

Figure 6.16 Line current wavegorm of hybrid solid state DC circuit breaker with mechanical dis-connector under line to line DC fault.

6.5.4 Hybrid Solid State DC Circuit Breaker with Fast Mechanical Switch

The configuration of fourth evaluated topology was shown in figure6.7. The model system in PSCAD is a $380V_{dc}$ voltage source that supplies a $380kW$ load through a cable with resistance of 0.128Ω and inductance of $1.11mH$. Under normal operation the entire load current flows through the mechanical switch, while the upper devices stay off. When a fault occurs, the mechanical switch is opened and the lower devices are turned on simultaneously. This configuration is identical to the previous topology, but without the solid state devices in series with the mechanical switch. Thus the lower IGBT switches and diodes are subjected to a very high blocking voltage, while the mechanical switch with negligible contact resistance carries the load current under normal conditions. Therefore, the breaker's efficiency doesn't get affected by semiconductor switches.

For the test system, the current limit is set at $2kA$. The response time with this topology in order to cut off the fault is about $40ms$ as shown in Figure 6.17.

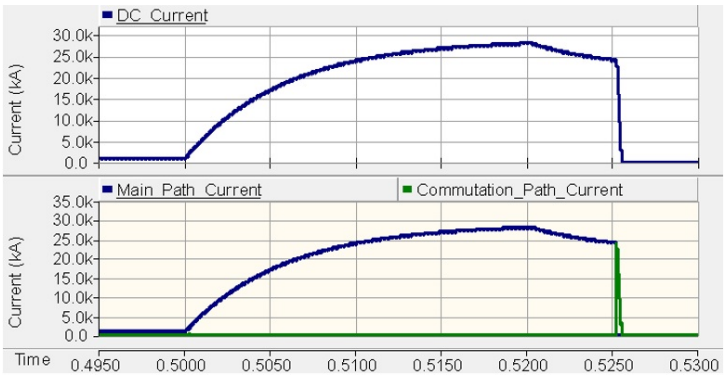

Figure 6.17 Line current wavegorm of hybrid solid state DC circuit breaker with mechanical dis-connector under line to line DC fault.

6.5.5 Hybrid Fault Current Limiting Circuit Breaker

In this section, the mentioned hybrid FCL is modeled in PSCAD and the operation of the limiter when a line to line DC fault occurs is studied. The test system is a $380 V_{dc}$ voltage source that supplies a $380 W$ load through a cable with resistance of 0.128Ω and inductance of $1.11 mH$. A line to line dc fault occurs at $0.2 s$, as soon as the DC current reaches to two times of the rated current, $2 kA$ in this case, fault is detected and the interrupter will be opened. Configuration of this hybrid FCL was shown in Figure 6.8.

As it was mentioned earlier, in the normal operating condition, current flows through the path A, and whenever a fault is detected, breaker in path B will be closed and the breaker in path A is opened. The arc voltage over the breaker A, forces the fault current to flow through the path B. When the current transfers to path B, the arc generated earlier in the breaker of path A will cool down and will be extinguished. In order to be able to model this behavior in PSCAD, two sets of breakers are used in each path, one of them has an open resistance in the order of $10-50\Omega$ to model the arc, and another one has infinite resistance to model the open breaker after the arc has been extinguished. It should be noted that, in reality only one breaker is used. It was discussed earlier that path C consists

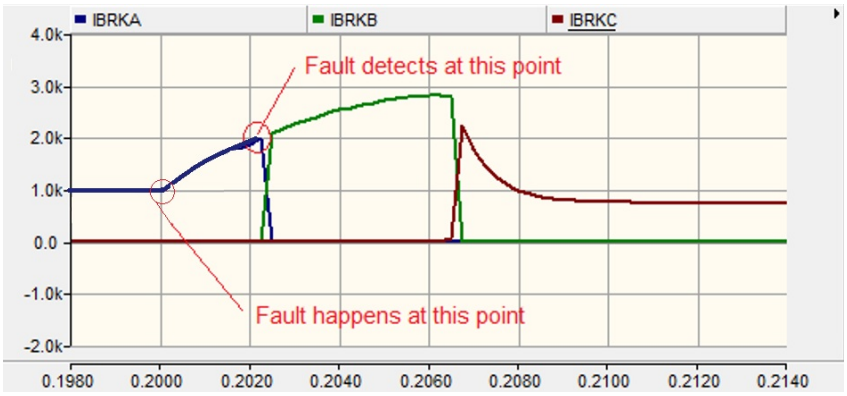

Figure 6.18 Current through the different paths of the hybrid FCLCB during fault limiting.

of an ultra-fast switch and several nickel wire resistors in series, the resistance of these resistors are increased when the current flows through them and heat them up. These two elements, the ultra-fast switch and PTC were modeled with two breakers in PSCAD one with lower open resistance to simulate the ultra-fast switch, and another one with a higher open resistance to model the PTC. The values of the resistances that are used in each breaker were selected based on the DC arc model derived earlier in this chapter.

The hybrid FCLCB with the specification mentioned earlier has been modeled in PSCAD. Figure 6.18 shows the current through each path during the current limiting sequences. The blue curve corresponds to current through path A, green curve and the red curve correspond to currents flow through path B and path C, respectively.

From Figure 6.18, it can be seen that at $0.2s$ a line to line DC fault occurs in the system, and the current starts increasing, whenever the current reaches to $2kA$, fault will be detected in the system. After that, an on command will be sent to the breaker in path B and at the same time an off command will be sent to the breaker in path A. As soon as the voltage over the generated arc of the breaker A reaches to a certain value, the current is transferred to path B and the arc of the breaker in path A will be extinguished. When the current transferred completely to the path B, an off command and on command will be sent to

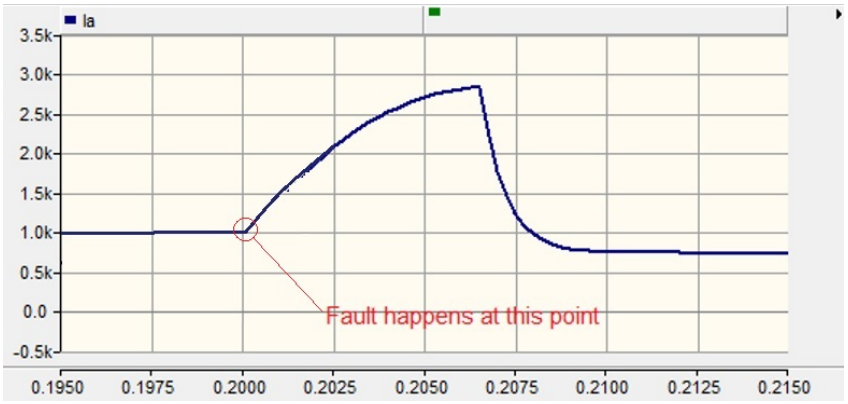

Figure 6.19 The main current of the DC system when a fault happens and limited by the hybrid FCL.

the breakers in path B and C, respectively. Whenever the arc voltage over the breaker in path B (which consists of several breakers in series) reaches to a certain value, the current is transferred to path C, which consists of several pure nickel wire resistors in series and an ultra-fast switch. The resistance of the pure nickel wire resistor increases when current flows through them and heats them up. Therefore, the fault current can be limited. Figure 6.19 shows the main current of the DC system when a line to line DC fault happens and limits by the hybrid FCLCB.

6.6 Summary and Comments on the Evaluated DC Circuit Breakers

The discussed DC breakers can be divided into three main groups. These three groups and their basic characteristics are shown in the following

1. Mechanical DC Circuit Breaker.
    - Response time $20-60ms$.
    - Full voltage/current range.

- Arc generated.
- Maintenance required.
- Low loss.

2. Hybrid DC Circuit Breaker.
    - Response time $1-10ms$.
    - Limited voltage/current range.
    - No arc.
    - Maintenance-free.
    - Low conduction loss.
3. Solid-State DC Circuit Breaker
    - Response time $5-1000\mu s$.
    - Limited voltage/current range.
    - No arc.
    - Maintenance-free.
    - High conduction loss.

- **Solid state DC breakers**: These breakers have the ability to interrupt the current as low as a few microseconds. However, costs of these breakers and the on resistance are much higher in comparison with the mechanical switches. The conduction losses of the solid state devices have been estimated in the order of $0.1-0.4\%$ of the transmitted power. This characteristic of the solid state DC breakers limits its applications to where the minimum interrupting times are required. However, it should be considered that the performance of a solid state circuit breaker depends mainly on the semiconductor

devices which are used in the breaker. The performance of these semiconductor devices are improving continuously and devices with high blocking voltages and high current ratings such as SiC MOSFETs and IGBTs are becoming commercially available. Therefore, these breakers are expected to become popular in the near future.

- **Hybrid Solid state DC breakers**: These breakers have been proposed to reduce the losses of the solid state DC circuit breakers. In this scheme, current in normal condition passes through a fast mechanical switch, whenever a fault occurs, the mechanical switch is open and causes the current to commutate to a parallel path where the semiconductor devices exist to interrupt the fault current. However, these breakers are not as fast as the full solid state breakers. Moreover, the interaction of mechanical switch and semiconductor devices makes these schemes complex.

- **Mechanical DC breakers**: These type of breaker need longer time to interrupt the current. Moreover, evaluating these breakers is always accompanied with arc modeling which adds complexity to the evaluation..

6.7 Protection of VSCs of a DC System without DC Circuit Breaker

Among the DC circuit breakers discussed in the previous section, hybrid solid state breaker with mechanical dis-connector and the circuit breaker with pre-charged capacitor are able to interrupt the dc current in less than 5ms with high efficiency. However, they are not commercially available yet and if they come to market they will suffer from high price tag initially. When a short circuit fault happens on the DC bus, the semiconductor switches in a VSC lose control and depending on the topology of the VSC, either the freewheeling diodes of the converter behave as a diode rectifier feeding the fault or the energy stored in

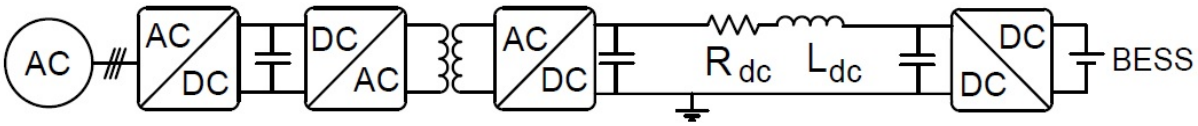

Figure 6.20 DC coupled BESS and isolated grid-tied converter.

the capacitors and inductors of the system discharges through the freewheeling diodes of the converter. In both cases, fast fault detection and interruption are required to prevent the VSC from serious damage. Although the commercially available DC circuit breakers are effective in protection of the cables and wires of the system, but they do not provide protection for the converters of the system since they rely on slow mechanical separation of the contacts in the current path. In this section, a control method is proposed which protects the VSCs and enables them to interrupt the DC side fault current without the need for circuit breaker.

Figure 6.20 shows a typical DC system where a BESS is connected to an isolated inverter. In this system, when a line to line fault happens on the DC side, the current starts increasing, whenever, the current becomes twice the rated current, fault is detected. In this control algorithm, as soon as the fault is detected, the reference power value is set to zero and all the switches of the DAB DC/DC converter are turned off. Consequently, the energy stored in the DC side capacitor is discharged through the DC side inductor and cable resistors (Mode I). The equivalent circuit of the VSC during mode I is shown in Figure 6.21 and the DC side current and voltage can be described as following, if $R < 2\sqrt{\frac{L}{C}}$

$$i_{dc}(t) = I_0 e^{-\alpha t} cos(\sqrt{\omega_0^2 - \alpha^2}\, t) + [\frac{\frac{V_0}{L} - I_0\alpha}{\sqrt{\omega_0^2 - \alpha^2}}] e^{-\alpha t} sin(\sqrt{\omega_0^2 - \alpha^2}\, t) \qquad (6.18)$$

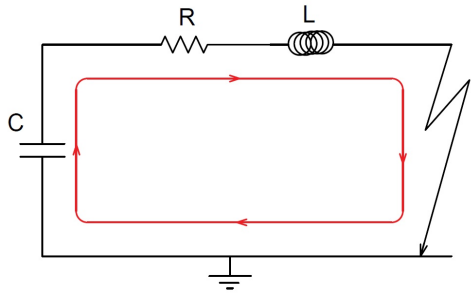

Figure 6.21 Equivalent circuit of the VSC under the dc fault in Mode I.

$$V_c(t) = V_0 e^{-\alpha t} cos(\sqrt{\omega_0^2-\alpha^2}\,t)+[\frac{V_0\alpha-\frac{I_0}{C}}{\sqrt{\omega_0^2-\alpha^2}}]e^{-\alpha t} sin(\sqrt{\omega_0^2-\alpha^2}\,t) \tag{6.19}$$

where $\alpha=\frac{R}{2L}$, $\omega_0=\frac{1}{\sqrt{LC}}$ In addition, the time required for the capacitor voltage to become zero can be calculated using the following equation

$$t_1 = t_0 + \frac{arctan[\frac{V_0 C\sqrt{\omega_0^2-\alpha^2}}{I_0-V_0\alpha C}]}{\sqrt{\omega_0^2-\alpha^2}} \tag{6.20}$$

where t_0 is the time that fault is detected and t_1 is the time that the voltage of the capacitor reaches to zero.

When at t_1 the DC bus voltage becomes zero, the energy stored in the DC side inductor is discharged through the system resistors and anti-parallel diodes of the VSC (Mode II). The equivalent circuit of the VSC during mode II is shown in Figure 6.22. The DC side current in mode II can be described as

$$i_{dc}(t)=I_1 e^{-\frac{R}{L}t}; T=\frac{L}{R} \tag{6.21}$$

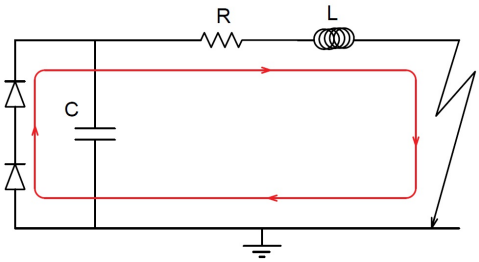

Figure 6.22 Equivalent circuit of the VSC under the dc fault in Mode II.

where I_1 is the initial current of the dc side inductor and T is the time constant of the mode II. Also the time required for the capacitor voltage to become zero can be calculated using

$$t_2 = t_1 + \frac{5L}{R} \tag{6.22}$$

where t_1 is the beginning of the mode II and t_2 is the moment that the dc current becomes zero [99], [85].

When the DC current becomes zero at t_2, the fast switches can be opened to isolate the fault from the rest of the system. When the fault is cleared, the recovery procedure starts with enabling all the switching signals of the DAB converter, when the voltage of the converter reaches its reference value, two DC terminals are connected and the reference power will set to the value before the fault [100]. In the discussed control algorithm, two discharge modes were studied. In the first discharge mode, the fault current starts increasing when the energy stored in the capacitor is discharged through the system resistor and the inductor, at the end of this mode the fault current reaches its maximum level. When the DC bus voltage becomes zero, the energy stored in the inductor is discharged through the anti-parallel diodes and the system resistors, in this mode the current decreases and becomes zero eventually. In the second mode, the fault current decreases as it is shown in equation 6.22. It can be seen that the rate of decrease, depends on the time constant, $T = \frac{L}{R}$.

In the worst case, when the fault happens very close to the converter in fact at the converter DC link, R is small compared to L and the time constant is high consequently. This means that a high current is passing through the anti-parallel diodes for a long time, which causes serious damage to the converter. Therefore, the control algorithm itself would not be able to protect the converter station during the worst situation. The performance of the control algorithm when the DC fault occurs 200m away from the converter and when it happens very close to the converter station are shown in Figure 6.23. It can be seen that when the fault happens far enough from the converter, the time constant, $T = \frac{L}{R}$, is small and the fault current decreases fast enough before damaging the converter. However, when the fault happens at the converter DC link, the time constant is large and the high fault current flows through the anti-parallel diodes for a long time, which will result in a serious converter damage. As it was mentioned and shown in the simulations, the control algorithm itself cannot protect the converter in the worst case scenario. In the next section, a novel method which employs a Hybrid FCL discussed earlier with the mentioned control algorithm is proposed to solve the discussed issue. This method works based on adding an additional resistance whenever the fault is close to the converter. The resistance should be added to the line whenever it is needed and should have no impact on the system in the normal operation. To overcome the discussed challenges, the hybrid FCL discussed in Section 6.4.5 will be used.

6.7.1 Protection of VSCs of a DC System in the Worst Case Scenario

It was shown that the control method discussed in section 6.7, is not capable of protecting the converter station in the worst-case condition, when the fault happens at the converter DC link. In this section, a new control method is proposed to overcome the mentioned issue. The proposed method, works based on employing the hybrid FCL discussed in section 6.4.5 to reduce the time constant of the inductor discharge. Therefore, the discharge current does

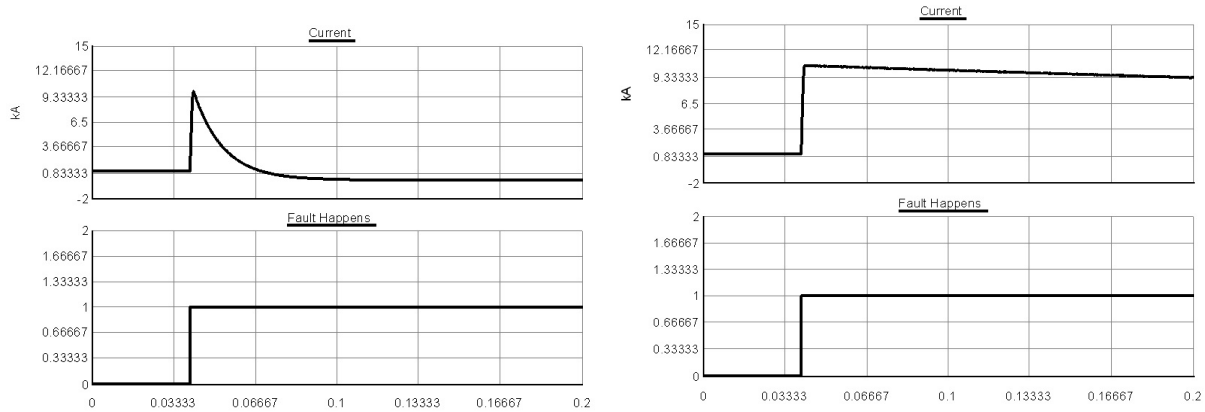

(a) **(b)**

Figure 6.23 (a): Performance of the control algorithm when the DC fault happens 200m away from the converter $L = 1.11mH, R = 0.128, T = 8.7ms$. (b): When it happens very close to the converter stations $L = 1.11mH, R = 0.5m, T = 2s$.

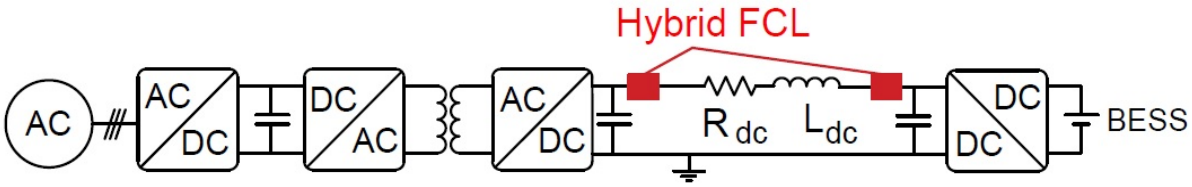

Figure 6.24 DC coupled BESS and isolated inverter employing hybrid FCL.

not cause damage to the converter. The hybrid FCL needs to be located at the converter DC link to ensure protection at the worst case scenario. Figure 6.24 shows a typical an interconnected BESS and an isolated inverter system employing hybrid FCL for protection.

When the fault happens close to the converter, a turn off command will be sent to the hybrid FCL. At the same time, the reference power value on the converter is set to zero and all the switches of the DAB DC/DC converter are turned off. In the first discharge mode, the fault current starts increasing when the energy stored in the capacitor is discharged through the system resistor and the inductor, at the end of this mode the fault current reaches its maximum level. When the dc bus voltage becomes zero, the energy stored in the inductor is discharged through the anti-parallel diodes and the line resistor, in this mode the current

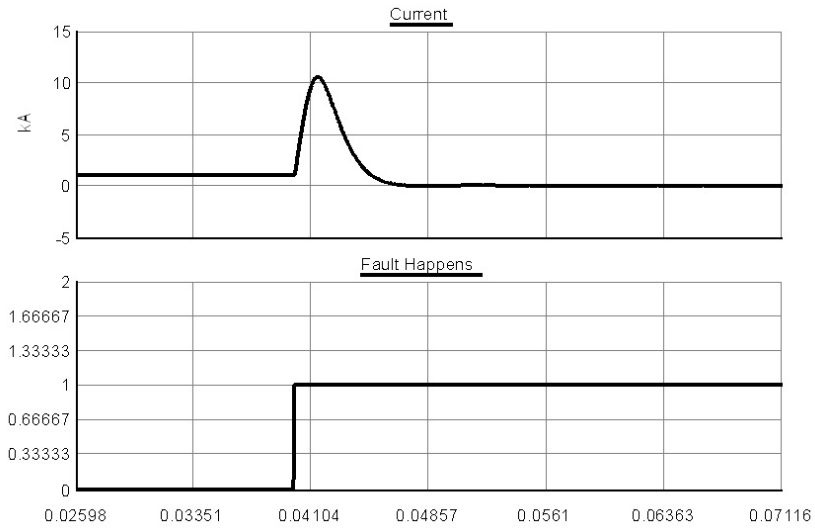

Figure 6.25 Performance of the proposed control method (control + hybrid FCL) when the DC fault happens very close to the converter.

decreases and becomes zero eventually, the rate of decrease depends on the time constant, $T = \frac{L}{R}$. Normally, the resistor is so small compared to the inductor and therefore the time constant is high. However, in this control method, the hybrid FCL adds resistance to the line resistance and reduces the time constant which causes the inductor discharge current to reach zero faster and protecting the VSC. Performance of the proposed control method when the DC fault happens at the converter DC link was evaluated in RTDS and the fault current before and during the fault is shown in Figure 6.25. It can be seen that with this approach the fault current decays to zero in 8.5ms from the point which fault occurs.

6.8 Grounding of DC Systems

6.8.1 Introduction

Although DC microgrids have clear advantages over the AC microgrids, but grounding of DC microgrids has not been fully explored in literature and there are still concerns about the

safety of the DC systems vs. the conventional AC systems [76]. Grounding is a complex topic involving many design considerations and trade-offs and it is needed to ensure the safety of personnel and equipment as well as detection of ground fault in the system. Grounding of DC power system should be designed to

1. During the normal operation, the grounding should minimize the DC leakage current.
2. During the emergency condition, the grounding should maximize the safety of personnel and equipment.

Therefore, it is necessary to address the grounding issue and discuss the grounding architectures that result in safer and more reliable operation of DC systems. DC systems are capable of having higher safety than traditional AC systems through high resistance grounding techniques. Additionally, with specific grounding and converter architectures features such as ground-fault ride through can be achieved. This work helps explain why the advantages of the DC systems are not limited to the higher efficiency, and lower cost, but also higher reliability and safety than AC systems as well.

In this section, we will first examine the design considerations for evaluating grounding techniques. Next, the different grounding options will be explained and the design trade-offs will be examined. Then, we will examine the impacts of bi-polar versus uni-polar architectures, discuss isolation, and describe some ground fault detection methods. Later, two system architectures that enable ground fault ride-through are discussed and their ground fault ride-through capability is proved using C-HIL simulations. Finally, a summary is presented of the strengths/weaknesses of the various grounding options in terms of the design criteria [86].

6.8.2 Design Criteria

The two types of faults to consider are line faults and ground faults. Ground faults are much more common than line faults as they occur whenever a conductive path exists from either positive or negative to ground. Ground faults can occur as insulation wears out or is damaged and an exposed conductor touches a conduit, which is grounded. Ground faults can also occur inside devices like motors, LED fixtures, or PV panels if the insulation between a conductor and the frame of the device breaks down. In PV systems, ground faults are common since there are many exposed wires in harsh environments, exposed to temperature swings, rain, sun, and wind. Installing wires in conduit is a way to protect them and to protect people, however it is cost prohibitive in PV systems to cover all of the wires in conduit.

Line faults occur when a conductive path exists between the positive and negative poles of a system. Line faults are far less common, but they are potentially more dangerous than ground faults and can be more difficult to detect. From the protection and control perspective, line faults may look just like loads on the system. This makes detection difficult. Additionally, the full power behind the system is available to feed the fault. Grounding methods are able to limit the available current to ground faults, but for line faults it is difficult to limit the available fault current since loads on the system must be served. The protection methods against line faults were discussed earlier in this chapter.

Safety is the first factor to consider when evaluating grounding methods. Safety of both personnel and equipment is important. The factors that are important for safety include fault current magnitude and susceptibility to faults, surges, electromagnetic interference, or other events that can cause damage.

The operational criteria to be considered are weighed according to the specific application. The type of grounding can impact whether the system has the ability to continue

operation in the presence of a fault. Likewise, grounding impacts whether the system is able to mitigate, or even detect a ground fault at all. Undetected ground faults make a system mores susceptible to dangerous line faults. Grounding can impact the reliability of a system by helping the system to filter noise and disturbances such that the equipment is not impacted and protection devices are not unnecessarily tripped.

Finally, there are practical constraints to consider for evaluating different grounding techniques. A system designer must consider the cost and size of converters, protection equipment, and extra wiring if it is necessary. There is a substantial difference in the size, weight, and cost of protection equipment across voltage classes and ranges of interrupting capability. Additionally, codes specify the protection necessary, the allowable voltage with respect to ground, and the allowable grounding and ground fault detection methods for specific applications.

6.8.3 Grounding Schemes

The standard method of grounding in AC systems is solid negative point grounding. At one or more locations in a building, the negative conductor is tied to earth ground such that it is at zero potential energy. A ground wire is typically run in parallel with the positive and negative conductors and is used for tying conduit and equipment to ground. When a fault from positive to ground occurs, the ground wire carries current in parallel to the negative wire, and is used to divert current away from sensitive equipment. In these systems, a single fault from positive to ground or from positive to negative has the same result. Either type of fault creates a high current and can harm people or equipment. Overcurrent protection is placed on the positive wires to protect wires from overheating and causing fires. Equipment may have internal protection that is even more selective in order to prevent faults from damaging personnel or equipment. In AC systems, negative to ground faults do not cause high currents, however they are monitored because they could cause low currents to flow

through ground which can cause harm to equipment.

DC systems can be solidly negative point grounded just like AC systems. The same results occur from positive to ground faults and negative to ground faults as in AC systems, except DC faults are potentially more dangerous due to their arcing ability. Since there is no natural zero crossing, DC faults are also more difficult to interrupt causing traditional protection equipment to be larger and more expensive than an AC equivalent [84]. An emerging technology to make DC systems safer and protection more compact is the use of solid state breakers, which can interrupt DC current without causing an arc. One advantage of negative point grounded DC systems over other types of grounded DC systems is that protection is only needed on the positive pole, and not on both poles. Alternatively, positive point grounded DC systems behave just like negative point grounded DC systems, offering the same advantages and disadvantages [83].

Aside from solid grounding, other grounding techniques use a resistive path, or another combination of impedances, to connect the system to ground. This ranges from low impedance to high impedance grounding, with a floating system being the most extreme. In separating the system from ground using an impedance, the system becomes safer in that a ground fault does not result in a high current. In solidly grounded system a fault from positive to ground has a return path to the source through the grounding point in the building where the negative is tied to earth. In a high impedance grounded system, there is no low impedance return path. If either positive or negative are faulted to ground, the only return path from ground to the opposite pole is through the high impedance. The reduction in ground fault magnitude, leading to greater safety for equipment and personnel, is the primary reason for high impedance grounding. In selecting the magnitude of impedance to use to ground the system, the trade-off is safety and ground fault ride-through capability versus ease of detection and immunity to noise. In a low-impedance grounded system, a ground fault causes a modest current to flow, typically somewhere around $100mA$. It is

important for safety to be able to detect a ground fault primarily because if the ground fault remains and another ground fault occurs on the opposite pole, a high current path through ground exists. This high current fault will flow outside of the conductors and can easily bypass proper operation of protection equipment. Ground currents in the order of $100mA$ are relatively easy to detect with inexpensive current transformers (CTs). Upon detection, either removal of the fault, shutdown of part of the system, or precautionary steps can be taken to increase safety.

In addition to ease of detection, low impedance grounded systems, like solidly grounded systems, are able to absorb and filter disturbances more easily than high impedance grounded systems. Disturbances such as switching harmonics, non-linear loads, and electromagnetic interference can inject currents into the system. With a high impedance path to ground, a small current can cause a large voltage spike with respect to ground. Solid and low impedance grounds mitigate voltage spikes from such disturbances.

The benefits of high impedance grounding are increased safety and ability to ride through ground faults in particular applications. Taken to the most extreme on the scale of high impedance grounding is a floating system. High impedance grounded and floating systems have many of the same characteristics. High impedance grounded and floating systems have little or no ground fault current in the case of a first ground fault. They are able to ride through these ground faults and continue operation. However, it can be more difficult to detect such a ground fault, since simple CT based solutions are not sensitive enough. The downside of such systems is that they are very susceptible to noise. A particularly good application of floating systems is a data center, where the environment is controlled such that no loads or sources are added to the system without careful consideration. The reliability of such systems is of the highest importance.

Finally, in impedance grounded systems, the designer has the option of placing the ground connection on the positive or negative pole or at a midpoint. The midpoint can

be created by capacitively or resistively dividing the two poles. The advantage of midpoint grounding is that the potential of each pole with respect to ground is half of the line to line potential. Mid-point grounding can reduce voltage insulation requirements if the positive and negative lines are in separate conduits. A disadvantage of midpoint grounding is that protection is required on both legs since both have potential with respect to ground. The grounding architectures discussed in this section are shown in Figure 6.26. Also the Figure 6.29 shows the current path in one line to ground fault condition.

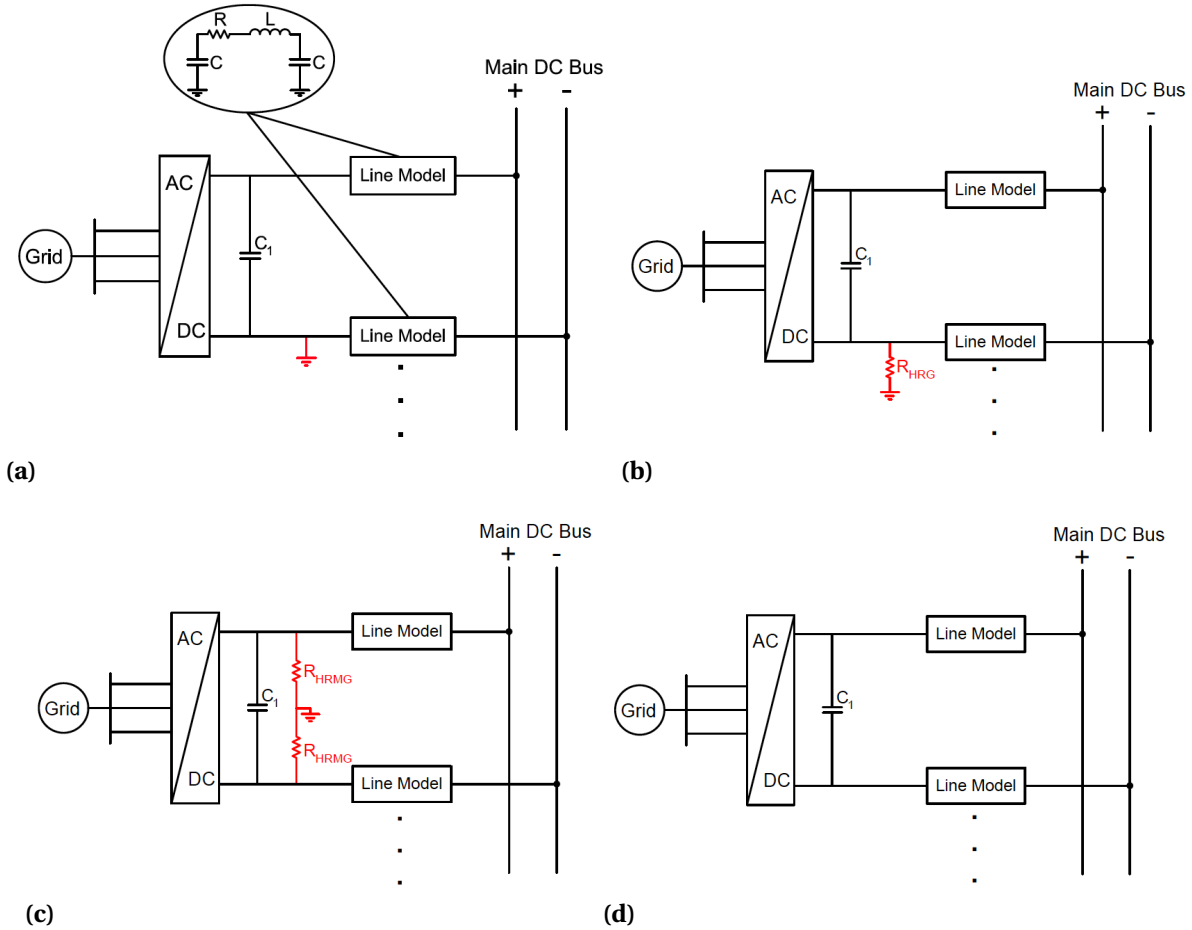

Figure 6.26 Possible grounding architectures for uni-polar DC systems. (a): Negative point solidly grounded system . (b): High resistance negative point grounded system . (c): High resistance midpoint grounded system .(d): Ungrounded (floating) system .

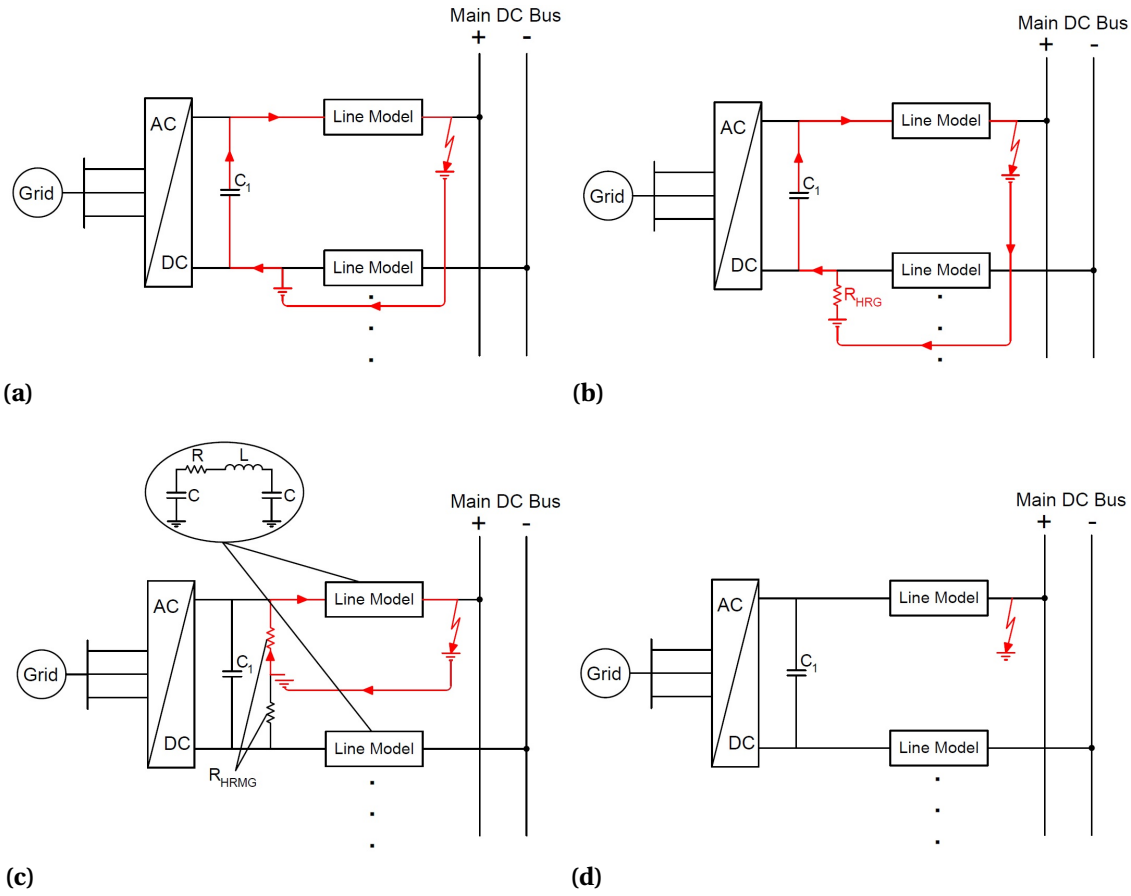

Figure 6.27 Current path when one line to ground fault occurs in the system. (a): Negative point solidly grounded system . (b): High resistance negative point grounded system . (c): High resistance midpoint grounded system .(d): Ungrounded (floating) system .

6.8.4 Isolation vs. Non-isolation

In addition to grounding, the isolation of a system impacts the aforementioned design criteria. Isolation also impacts which types of grounding are possible for a given system. In this dissertation, isolation refers to galvanic isolation through either a low-frequency transformer or a high frequency, power electronics integrated transformer.

Isolation gives the system designer the greatest flexibility in selecting a grounding

configuration. With a completely isolated DC system, meaning that all sources and loads are galvanically isolated from ground, the designer is free to select any grounding configuration, from solidly grounded to floating. In addition to grounding flexibility, galvanic isolation has the added safety and reliability factor from being electrically independent from the AC grid. Any unusual disturbances will not electrically pass through to the DC system. The galvanic isolation also limits the magnitude of fault current available on the DC side.

Non-isolated systems are commonly referred to as transformerless, because of the nature of the grid-tied converters that are used. In transformerless systems, the DC voltage is generated with respect to the AC voltages and ground. The DC voltage is already ground referenced and is not floating as in an isolated system, so the designer is not free to ground using any configuration. Through bi-polar topologies, some transformerless converters are able to achieve virtual isolation, which presents a high impedance path between the AC and DC sides, though not a galvanically isolated path. Virtual isolation allows the DC side to be floating or high impedance grounded. Bi-polar configurations allow for some of the advantages of isolated systems. They are explored in more detail in the next section.

The advantages of a non-isolated system are simply the gains in not having to use a transformer. In avoiding a high-frequency isolation stage, the converters can be made much simpler, smaller, lighter, efficient, and less expensive. In many applications, these factors are very important in adopting DC technology, since competing AC technology already has many of these qualities.

6.8.5 Unipolar vs. Bipolar

By using bi-polar converters for sources in a DC system, many of the advantages of isolated systems can be realized with a transformerless system. In a bi-polar converter, both the positive and negative poles are controlled through switches. The result is two independent voltage sources with respect to the DC side neutral, which is a third pole. Typically, the DC

neutral is a zero-potential pole and the positive and negative legs are centered around zero potential. By controlling both poles, the converter is able to limit current on the DC side and achieve virtual isolation. If a fault occurs on either pole, current is drawn through one of the converter legs, thus it can be regulated and limited. Figure 6.28. shows a bipolar high resistance midpoint grounded DC system and the topology of its converter.

For comparison, a uni-polar DC source controls the current and voltage on one pole, thus the other pole is tied to a DC voltage directly fed from an AC source. This uncontrolled pole has a voltage that is fixed and is subject to high fault current. Unipolar systems are ground referenced by default through the uncontrolled pole.

In a bi-polar configuration, if the DC side neutral is virtually isolated from the AC side neutral through control, the DC side is able to be high impedance grounded or floating. Therefore, a bi-polar configuration can achieve limited fault current and ground fault ride through just like an isolated system In addition to providing virtual isolation, bi-polar configurations provide greater flexibility in that there are two independent DC voltage sources. Loads or batteries can be connected across either source, from positive or negative to neutral, or from positive to negative. There is redundancy in that if one pole is faulted, the other pole can continue operation. Loads connected across both poles can continue operation at half of the maximum operating voltage in the case that one pole is faulted.

The disadvantage of bi-polar systems is simply that the converter will have additional switch when compared to a uni-polar source, adding to the cost, size, weight, and efficiency of the converter. However, the difference in these factors in going from uni-polar to bi-polar is not as great as the difference in going from transformerless to isolated.

6.8.6 Ground Fault Detection Methods

Ground fault detection is important because ground-faulted systems are vulnerable to high current faults in the occurrence of a second ground fault.

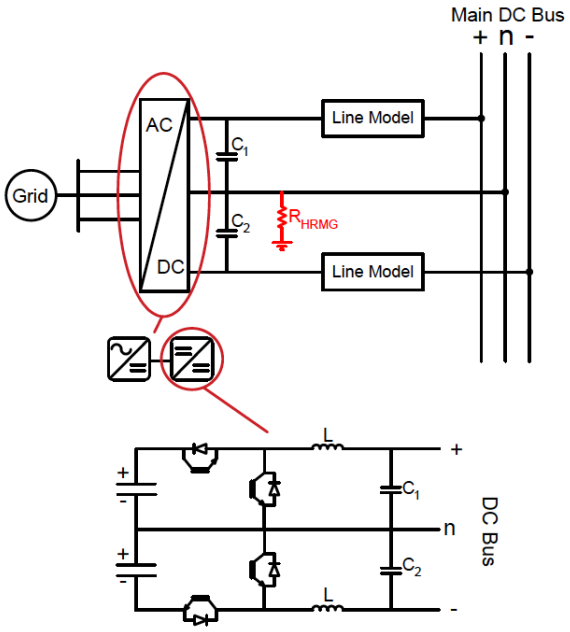

Figure 6.28 Bipolar high resistance midpoint grounded DC system (top). Bipolar DC/DC converter for enabling ground fault ride-through in the bipolar HRMG DC system (bottom).

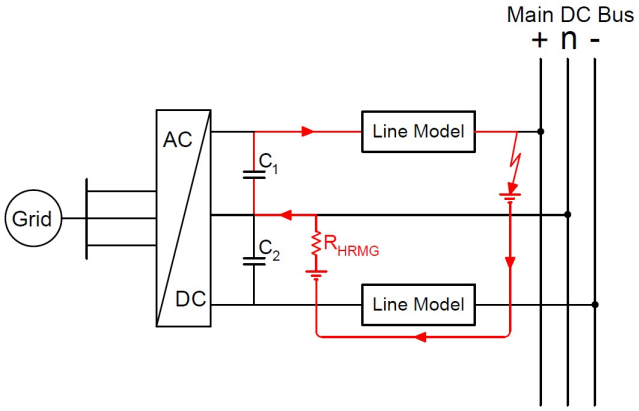

Figure 6.29 Current path when one line to ground fault occurs in a bipolar DC system.

The simplest method of ground fault detection is voltage measurement. In a mid-point grounded system, where the impedance to ground is relatively high, a ground fault will cause a shift in voltage. The pole that is faulted will move towards ground potential. This voltage shift is simply measurable and indicates that a ground fault has occurred. This approach does not work if the ground fault is not solid enough or if the system is not isolated

enough such that a ground fault moves the potential. Additionally, a balanced ground fault would not cause a shift in potential with respect to ground. Lastly, if one pole is already at zero potential, this method will not detect a ground fault. Approaches that measure current are applicable to many systems. These approaches use current transformers (CTs) to detect ground faults by measuring the current through a ground path, usually the grounding resistor, or by measuring differential current passing through the branch of a circuit. The differential current is measured by passing both positive and negative poles through a core. Any difference in current, indicating a leakage path back to the source, is detected by a highly sensitive core.

CT based ground fault detection works as long as the core is sensitive enough to detect the current present in a ground fault for a particular system. In high-resistance grounded or floating systems, the ground fault current is very small. Detectors in these types of systems are basically isolation monitors. Detectors inject currents, voltages, or low impedance paths between the poles and ground and measure the response of the system.

Ground fault location is of high value in many systems, since it allows the controller or user to isolate the ground fault to a particular branch in order to return the rest of the system to normal operation and to identify the faulted circuit so it can be fixed. CT based approaches allow for ground fault location when the CTs are placed on branches of the system. Current or voltage injection can be used along with CTs to locate ground faults in high-impedance or floating systems.

6.8.7 Ground Fault Ride-Through

As it was mentioned earlier in this section, it is generally safer to separate the ground from the system by using an impedance as the ground fault doesn't result in dangerous high currents. Also isolation is necessary for the uni-polar systems in order to be able to ride-through the ground fault. In order for a non-isolated system to be able to ride through a

ground fault, the system configuration has to be bi-polar. Bi-polar converters are able to limit current on the DC side and achieve virtual isolation. And if a fault occurs on either poles, current is drawn through one of the legs, thus it can be regulated and limited.

Among all the different grounding schemes and system configurations discussed, the two candidates for the ground fault ride-through are *Isolated Uni-polar HRMG* and *Non-Isolated Resistance Midpoint Grounded Bi-polar* systems. Obviously there are other configurations for ground fault ride-through such as isolated bi-polar HRMG, but the two mentioned candidates achieve the ground fault ride-through capability with the minimum number of components and with the lowest cost.

Matlab/Simulink was used for demonstrating the ground fault ride-through capability of the mentioned grounding architectures. Figure 6.30(a) shows the DC bus voltage and the ground fault current when a negative to ground fault happens at $1s$ in a non-isolated resistance midpoint grounded bi-polar system. The system architecture is similat to Figure 6.28. In this system, it is assumed that the converters of the system are regulating the DC bus voltage at $380V_{dc}$ and the neutral of the system is grounded through a 10Ω resistor, the reason for using smaller resistance is to reduce the noise. A ground fault applied to the negative pole at $1s$ and immediately the ground current increases and the CT-based ground fault detector of the system realizes that a ground fault occurred in the system. This process takes about $20ms$. After the fault is detected, the converter turns off the switches of the affected leg and doubles the reference voltage of the other leg. As it can be seen in the figure, the system keeps working and DC bus voltage does not change before and after the fault. It should be noted that, the bi-polar system is operating as a uni-polar system after the fault occurs and a second ground fault will result in dangerous high current. Therefore, it is necessary to locate and isolate the ground fault immediately after the first ground fault.

Figure 6.30(b) shows the DC bus voltage and the ground fault current when a negative to ground fault happens at $1s$ in an isolated uni-polar HRMG DC system. The grounding

architecture of this system is similar to Figure 6.30(c). In this system, it is assumed that the converters of the system are regulating the DC bus voltage at $380 V_{dc}$ and the positive and negative buses are grounded through a $80 k\Omega$ resistors. Since this is an isolated system, noise is not an issue and higher resistors can be used to limit the fault current. A ground fault applied to the negative pole at $1 s$ and immediately the negative bus voltage with respect to the ground goes to zero and the positive bus voltage with respect to the ground gets double, these happen automatically and without the need for a controller. It is shown the system keep working after the fault and the DC bus voltage does not get affected by the fault. Again it should be noted that, a second ground fault will result in dangerous high current. Therefore, it is necessary to locate and isolate the ground fault immediately after the first ground fault.

6.8.8 Summary

In this section, we've provided information on different grounding techniques and showed how polarity and isolation impact the system grounding, safety, reliability and detection of the ground fault. In this section, all the information provided earlier are summarized and presented. Table 6.5 summarizes the advantages and disadvantages of different grounding schemes while Table 6.6 shows the impact of different system configurations such as polarity and isolation on the system performance and grounding.

It is necessary to emphasis that although we separated the grounding and system architecture in this section, but these two concepts go hand in hand and the grounding has to be selected based on the system architecture and vice versa.

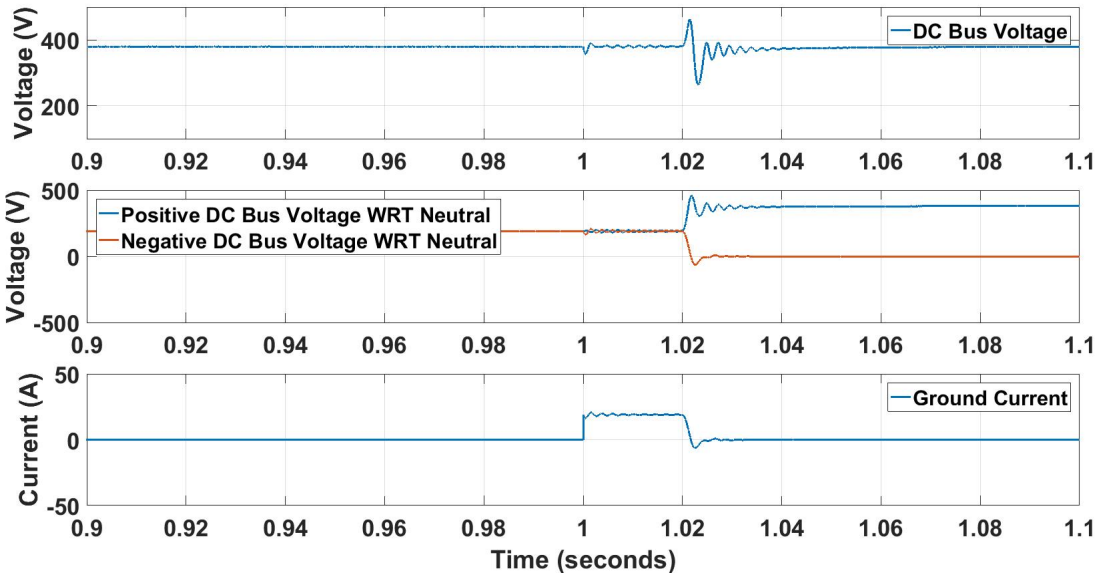

(a)

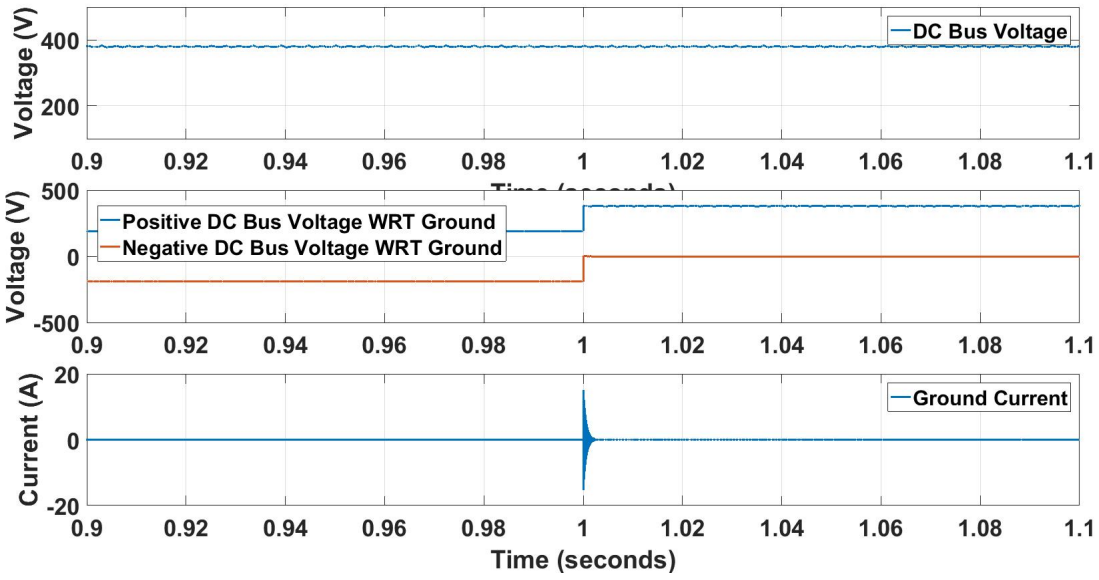

(b)

Figure 6.30 (a): Voltage and fault current waveform when a negative to ground fault happens at 1s in a non-isolated resistance midpoint grounded bi-polar system. (b): isolated uni-polar HRMG DC system.

Table 6.5 Summary of advantages and disadvantages of different grounding techniques [86].

Grounding	**Pros**	**Cons**
+/- Solidly grounded	- Overcurrrent protection needed only on the ungrounded pole. - Absorbs and filters disturbances. - Easy to detect ground fault	- Ground fault on the ungrounded pole results in high dangerous currents). - Not capable of ground fault ride-through.
+/- Impedance grounded	- Limited fault current under ground fault. - Better safety for equipment and personnel. - Ground fault ride-through capability. - Easy to detect ground fault.	- Susceptible to the noise and disturbances.
High resistance midpoint grounded	- Limited fault current under ground fault. - The potential of each bus with respect to the ground is half the system voltage (can reduce voltage insulation requirements) - Ground fault ride-through capability	- Both poles require overcurrent protection. - Susceptible to the noise and disturbances.
Floating	- Limited fault current under ground fault. - Ground fault ride-through capability	- Both poles require overcurrent protection. - Very susceptible to the noise and disturbances. - The potential of each poles with respect to the ground can float away to dangerous voltages. - Difficult to detect ground fault.

Table 6.6 Summary of advantages and disadvantages of different system architectures [86].

Architecture	Pros	Cons
Isolated	- Flexible in choosing grounding scheme. - Higher safety due to isolation from the AC grid. - Disturbances do not pass through to the DC grid. - Limits the magnitude of the fault current.	- Lower efficiency, higher costs and larger converter than the non-isolated systems. - Voltage might float away in some grounding schemes due to lack of reference.
Non-Isolated (Transformerless)	- Voltage does not float away. - Simpler control - More efficient, lighter, smaller and lower costs compared to the isolated systems.	- Less options for grounding. - Disturbances in AC grid can pass through the DC grid. - Might suffer from common mode voltage and current if not well-designed.
Uni-Polar	- High efficiency and lower costs compared to bi-polar systems. - Simple design and control of converters. - Ground fault ride-through capability. - Easy to detect ground fault.	- Cannot achieve ground fault ride-through in tranformerless systems. - Limited grounding options. - Can provide one voltage level.
Bi-Polar	- Can create virtual isolation in the non-isolated systems. - Can achieve limited fault current in transformerless systems. - Can provide two levels of voltage.	- Complicated converters and controllers. - Higher costs, lower efficiency compared to the unipolar systems.

CHAPTER

7

FUTURE WORK AND CONCLUSION

This chapter draws the conclusions of the present work and identifies the future work and research path.

7.1 Conclusions

Climate change is one of the most urgent and complex challenges we face today [1], and most of the climate scientists agree that greenhouse gas emissions from human activities is the main cause of global warming [2]. The primary greenhouse gas emitted through human activities is carbon dioxide (CO_2). One of the main activities that emits CO_2 is the combustion of fossil fuels to generate electricity. Based on the data from United States

Environmental Protection Agency (EPA), electricity accounts for about 37% of total U.S. CO_2 emissions and almost 31% of total U.S. greenhouse gas emissions in 2013 [4]. Therefore, U.S. has started to take aggressive actions, like net-zero energy building, to cut its greenhouse gas emissions to stabilize earth's climate. Residential and commercial buildings consume almost 40% of primary energy and approximately 70% of the electricity in the U.S [52]. To achieve net zero energy in these buildings, the adoption of energy efficient loads will reduce the building energy usage by 60 to 70% [53]. And the remaining 30 to 40% must come from on-site renewable energy sources like wind and solar.

In existing AC PV systems, PV generates DC voltage, this DC voltage is inverted to AC through a grid-tied inverter and on the load side the AC voltage is converted to DC once again. This AC power system requires to energy conversion steps, DC/AC conversion at the PV side and AC/DC conversion at the DC load side. Approximately 10% of PV generation is lost in these conversion steps [54]. Renewable energy resources like sola r and fuel cells generate DC power, on the other hand a large and increasing portion of loads use DC voltage internally such as LED lights, VFDs, battery chargers, and power supplies. There is a possibility to eliminate the costly and inefficient power inverters and install a DC network linking DC loads to the DC sources. DC microgrids and DC distribution power systems offer efficiency improvement, higher reliability better expandability and stability over their equivalent AC systems. The aim of this work is to accelerate the deployment of DC systems by quantifying the benefits of DC systems compared to AC ,removing the technical barriers and addressing the issues related to safety and protection. The list of achieved goals can be summarized as following:

1. **Investigate the existing and emerging PV plus storage DC microgrid architectures.**

2. **Conduct a comparative study between DC and AC distribution systems.**

3. **Demonstrate improvement in electrical system efficiency in the DC system over a**

conventional AC design.

4. **Identify and quantify the economic value of DC microgrids for different types of facilities in various locations.**

5. **Design, modeling and control of a functional, scalable, DC distribution system that incorporates energy storage and solar generation.**

6. **Control Hardware-in-the-Loop demonstration of a decentralized power and energy management scheme for DC microgrids to facilitate deployment of DC microgrids.**

7. **Develop mathematical model of the DC distribution system for stability and performance analysis purposes.**

8. **Explore overcurrent protection methods including: mechanical, solid state and hybrid DC circuit breakers and hybrid fault current limiter.**

9. **Design and selection of appropriate grounding schemes in terms of safety of personnel and equipment as well as detection of ground fault in the DC system.**

7.2 Future Work

The DC system discussed in this dissertation supports the AC system by maximizing the local consumption of solar generation, preventing the load and PV power fluctuations from transferring to the AC grid. Also the DC system is able to perform demand response and peak shaving and support the Ac grid in that manner as well. However, the DC microgrids can be considered as controllable entities and will be able to support the grid by performing voltage and frequency regulation. As an example, another control layer can be added to the grid-tied converter of the system to perform advances control techniques such as volt-var

and volt-watt [101]. An interesting research topic would be to investigate how multiple DC microgrids in a high PV penetrated AC feeder can help the feeder with voltage and frequency regulation.

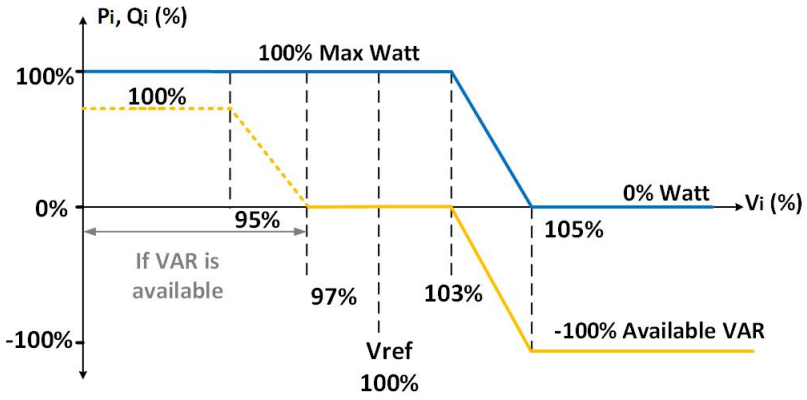

Figure 7.1 Possible volt-var and volt-watt profiles that can be built into the grid-tied converter of the system to support feeders with high PV penetrated systems [102], [103].

Solid State Transformers (SST) and the DC system discussed in this dissertation can be core structure for different possible modular multi-port hybrid inverter architectures for combined PV, BESSs, and other DERs. The term hybrid means that the these inverters are able to support both AC and DC loads, which unlocks the benefit of DC microgrids as well as the AC. Figure 7.2 shows a possible hybrid PV inverter with the ability to support AC and DC loads. The philosophy behind this inverter topology is to maximize the local PV generation and consumption (DC coupled PV, battery, load) while supporting the low voltage and high voltage AC grids with high PV penetration. Further research on the mentioned hybrid inverters would add value to the renewable energy owners and the utilities.

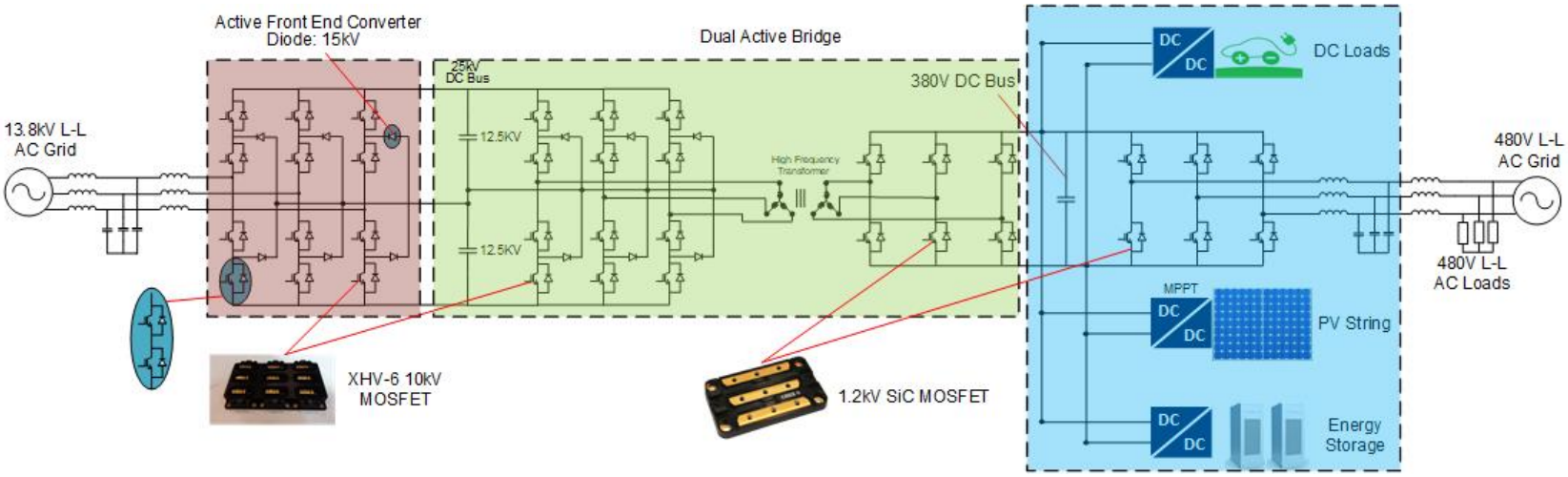

Figure 7.2 Possible modular multi-port hybrid inverter architectures for combined PV, BESSs, and other DERs.

BIBLIOGRAPHY

[1] J. F. Kerry. United States Department of State. 2014. URL: {http://www.state.gov/documents/organization/219040.pdf}.

[2] R.K. Pachauri & A. Reisinger. "Contribution of Working Groups I, II and III to the Fourth Assessment Report of the Intergovernmental Panel on Climate Change". *IPCC* (2007), p. 104.

[3] H. Riebeek. NASA Earth Observatory. 2014. URL: {http://climate.nasa.gov/causes/}.

[4] United States Environmental Protection Agency. 2015. URL: {http://www3.epa.gov/climatechange/ghgemissions/sources.html}.

[5] A. Borghetti, M. Bosseti, S. Grillo, S. Massaucco, C. Nucci, M. Paolone & F. Silvestro. "Short-term scheduling and control of active distribution systems with high penetration of renewable resources". *IEEE Syst* **4** (2010), pp. 313–322.

[6] S. Teleke, M. Baran, A. Huang, S. Bhattacharya & L. Anderson. "Control Strategies for Battery Energy Storage for Wind Farm Dispatching". *IEEE TRANSACTIONS ON ENERGY CONVERSION* **24** (2009), pp. 725–732.

[7] S. Teleke, M. Baran, S. Bhattacharya & A. Huang. "Optimal Control of Battery Energy Storage for Wind Farm Dispatching". *IEEE TRANSACTIONS ON ENERGY CONVERSION* **24** (2009), pp. 725–732.

[8] A. Hoke, R. B. J. Hambrick & B. Kroposki. "Maximum Photovoltaic Penetration Levels on Typical Distribution Feeders" (2010).

[9] B. Parkhideh & S. Bhattacharya. "Towards smart transmission substations with Modular Transformer Converter systems". *IEEE Power and Energy Society General Meeting* **1** (2011), pp. 24–29.

[10] C. L. Stiegemeier & R. Girgis. "Rapidly deployable recovery transformers". *IEEE Power and Energy Magazine* (2006), pp. 38–45.

[11] A. Kenward & U. Raja. "Blackout: Extreme weather, climate change and power outages". *Climate Central* (2014).

[12] U.S. Department of Energy. *Economic Benefits of Increasing Electric Grid Resilience to Weather Outages*. 2012. URL: {http://energy.gov/sites/prod/files/2013/08/f2/Grid%20Resiliency%20Report_FINAL.pdf}.

[13] J. M. Guerrero, J. C. Vasquez, J. Matas, L. G. de Vincuna & M. Castilla. "Hierarchical control of droop-controlled AC and DC microgrids - A general approach

toward standardization". *IEEE Transactions on Industrial Electronics* **58** (2011), pp. 158–172.

[14] R. Majumder, B. Chaudhuri, A. Ghosh, G. Ledwich & F. Zare. "Improvement of stability and load sharing in an autonomous microgrid using supplementary droop control loop". *IEEE Transactions on Power Systems* **25** (2010), pp. 796–808.

[15] H. Kakigano, Y. Miura & T. Ise. "Distribution voltage control for DC microgrids using fuzzy control and gain-scheduling technique". *IEEE Transactions on Power Electronics* **28** (2013), pp. 2246–2258.

[16] US Department of Energy Office of Electricity Delivery and Energy Reliability. 2014. URL: {http://energy.gov/oe/services/technology-development/smart-grid/role-microgrids-helping-advance-nation-s-energy-syst-0}.

[17] CIGRE. Working Group C6.22 Microgrids Evolution Roadmap. "Microgrids 1: Engineering, Economics, & Experience, forthcoming" (2010).

[18] U.S. Department of Energy, Office of Electricity Delivery and Energy Reliability. *Smart Grid Research & Development Multi-Year Program Plan (2010-2014)*. 2012. URL: {http://energy.gov/sites/prod/files/SG_MYPP_2012%20Update.pdf}.

[19] F. Katiraei, R. Iravani, N. Hatziargyriou & A. Dimeas. "Microgrids management". *IEEE Power Energy Mag* **6** (2008), pp. 54–65.

[20] N. Eghtedarpour & E. Farjah. "Power control and management in a hybrid AC/DC microgrid". *IEEE Trans. Smart Grid* **5** (2014), pp. 1494–1505.

[21] S. Bahramirad, A. Khodaei, J. Svachula & J. R. Aguero. "Building resilient integrated grids: One neighborhood at a time". *IEEE Electrific.Mag.* **28** (2015), pp. 48–55.

[22] H. Jiayi, J. Chuanwen & X. Rong. "A review on distributed energy resources and MicroGrid". *Renew. Sustain. Energy Re.* **12** (2008), pp. 2472–2483.

[23] A. M. Giacomoni, S. Y. Goldsmith, S. M. Amin & B. F. Wollenberg. "Analysis, modeling, and simulation of autonomous microgrids with a high penetration of renewables". *IEEE Power Energy Soc. General Meeting* (2012), pp. 1–6.

[24] A. Khodaei. "Provisional microgrids". *IEEE Trans. Smart Grid* **6** (2015), pp. 1–6.

[25] S. Wang, Z. Li, L. Wu & M. Shahidehpour. “New metrics for assessing the reliability and economics of microgrids in distribution system”. *IEEE Trans. Power Syst.* **28** (2013), pp. 2852–2861.

[26] A. Kwasinski, V. Krishnamurthy, J. Song & R. Sharma. “Availability evaluation of micro-grids for resistant power supply during natural disasters”. *IEEE Trans. Smart Grid* **3** (2012), pp. 2007–2018.

[27] J. He, Y. W. Li & F. Blaabjerg. “An accurate atonomous islanding microgrid reactive power, imbalance power and harmonic power sharing scheme”. *IEEE Energy Convers. Congr. Expo* (2013), pp. 1337–1343.

[28] S. V. Iyer, M. N. Belr & M. C. Chandorka. “A generalized computational method to determine stability of a multi-inverter microgrid”. *IEEE Trans. Power Electron* **25** (2010), pp. 2420–2432.

[29] N. Cai & J. Mitra. “A decentralized control architecture for a microgrid with power electronic interfaces,” *Proc. North Amer. Power Symp* (2010), pp. 1–8.

[30] W. Li, W. Li, Y. Deng & X. He. “Single-stage single-phase high-step up ZVT boost converter for fuel-cell microgrid system”. *IEEE Transansactions on Power Electronics* **25** (2010), pp. 3057–3065.

[31] T. Som & N. Chakraborty. “Studies on economic feasibility of an autonomous power delivery system utilizing alternative hybrid distributed energy resources”. *IEEE Transactions on Power Systems* **29** (2014), pp. 172–181.

[32] I. U. Nutkani, P. C. Loh, & F. Blaabjerg. “Droop scheme with consideration of operating costs”. *IEEE Transactions on Power Electronics* **29** (2014), pp. 1047–1052.

[33] I. C. Paschalidis, B. Li, & M. C. Caramanis. “Demand-side management for regulation service provisioning through internal pricing”. *IEEE Transactions on Power Systems* **27** (2012), pp. 1531–1539.

[34] A. Mehrizi-Sani & R. Iravani. “Potential-function based control of a microgrid in islanded and grid-connected modes”. *IEEE Transactions on Power Systems* **25** (2010), pp. 1883–1891.

[35] N. Pogaku, M. Prodanovic, & T. C. Green. “Modeling, analysis and testing of autonomous operation of an inverter-based microgrid”. *IEEE Transactions on Power Electronics* **22** (2007), pp. 613–625.

[36] J. M. Bloemink & M. R. Iravani. “Control of a multiple source microgrid with built-in islanding detection and current limiting,” *IEEE Transactions on Power Delivery* **27** (2012), pp. 2122–2132.

[37] A. G. Anastasiadis, A. G. Tsikalakis, & N. D. Hatziargyriou. “Operational and environmental benefits due to significant penetration of microgrids and topology sensitivity”. *IEEE PES General Meeting* (2010), pp. 1–8.

[38] J. Vasiljevska, J. A. P. Lopes, & M. A. Matos. “Integrated microgeneration, load and energy storage control functionality under the multi micro-grid concept”. *Electr. Power Syst. Res.* **95** (2013), pp. 292–301.

[39] G. N. Korres, N. D. Hatziargyriou, & P. J. Katsikas. “State estimation in multi-microgrids”. *Eur. Trans. Elect. Power* **21** (2011), pp. 1178–1199.

[40] S. D. A. Fletcher, P. J. Norman, S. J. Galloway, P. Crolla, & G. M. Burt. “Optimizing the roles of unit and non-unit protection methods within DC microgrids”. *IEEE Transactions on Smart Grids* **3** (2012), pp. 2079–2087.

[41] D. Salomonsson, L. Soder, & A. Sannino. “Protection of low-voltage DC microgrids”. *IEEE Transactions on Power Delivery* **24** (2010), pp. 1045–1053.

[42] J.-D. Park, J. Candelaria, L. Ma, & K. Dunn. “DC ring-bus microgrid fault protection and identification of fault location”. *IEEE Trans, Power Del* **28** (2013), pp. 2574–2584.

[43] H. Kakigano, Y. Miura & T. Ise. “Low-voltage bipolar-type DC microgrid for super high quality distribution”. *IEEE Transactions on Power Electronics* **25** (2010), pp. 3066–3075.

[44] Y. K. Chen, Y. C. Wu, C. C. Song & Y. S. Chen. “Design and implementation of energy management system with fuzzy control for DC microgrid systems”. *IEEE Transactions on Power Electronics* **28** (2013), pp. 1563–1570.

[45] D. Salomonsson, L. Soder & A. Sannino. “An adaptive control system for a DC microgrid for data centers”. *IEEE Transactions on Industrial Applications* **44** (2008), pp. 1910–1917.

[46] A. Kwasinski. “Quantitative evaluation of DC microgrids availability: Effects of system architecture and converter topology design choices”. *IEEE Transactions on Power Electronics* **26** (2011), pp. 835–851.

[47] Y. C. Chang & C. M. Liaw. “Establishment of a switched-reluctance generator-based common DC microgrid system”. *IEEE Transactions on Power Electronics* **26** (2011), pp. 2512–2527.

[48] Y. Gu, X. Xiang, W. Li & X. He. “Mode-adaptive decentralized control for renewable DC microgrid with enhanced reliability and flexibility”. *IEEE Transactions on Power Electronics* **29** (2014), pp. 5072–5080.

[49] P. C. Loh, D. Li, Y. K. Chai & F. Blaabjerg. “Autonomous operation of hybrid microgrid with AC and DC subgrids”. *IEEE Transactions on Power Electronics* **28** (2013), pp. 2214–2223.

[50] S. R. Huddy & J. D. Skufca. “Amplitude death solutions for stabilization of DC microgrids with instantaneous constant-power loads”. *IEEE Transactions on Power Electronics* **28** (2013), pp. 247–253.

[51] N. Bottrell, M. Prodanovic & T. C. Green. “Dynamic stability of a microgrid with an active load”. *IEEE Transactions on Power Electronics* **28** (2013), pp. 5107–5119.

[52] US Department of Energy. *Annual Energy Review 2006*. 2007. URL: {http://www.eia.doe.gov/emeu/aer/contents.html}.

[53] National Institute of Science and Technology. *Net Zero Energy report*. 2014. URL: {http://www.nist.gov/el/building_environment/netzero-070114.cfm}.

[54] D. Fregosi, S. Ravula, D. Brhlik, J. Saussele, S. Frank, E. Bonnema, J. Scheib & E. Wilson. “A Comparative study of DC and AC microgrids in commericial buildings across different climates and operating profiles”. *ICDCM IEEE First Int. Conf* (2015), pp. 159–164.

[55] D. J. Hammerstorm. “AC versus DC distribution systems-Did we get it right?” *Proc. IEEE Power Eng. Soc. Gen. Meet.* (2007), pp. 1–5.

[56] D. Salomonsson & A. Sannino. “Low-voltage dc distribution system for commercial power systems with sensitive electronic loads,” *IEEE Trans. Power Del.* **22** (2007), pp. 1620–1627.

[57] A. Kwasinski & C. N. Onwuchekwa. “Dynamic behavior and stabilization of dc microgrids with instantaneous constant-power loads”. *IEEE Trans. Power Electron* **26** (2011), pp. 822–834.

[58] F. Xiaogang & L. Jinjun. “Impedance specifications for stable dc distributed power systems”. *IEEE Trans. Power Electron* **17** (2002), pp. 157–162.

[59] Jae-Do Park & J. Candelaria. “Fault Detection and Isolation in Low-Voltage DC-Bus Microgrid System”. *IEEE Trans. on Power Del* **28** (2013), pp. 779–787.

[60] M. Mobarrez, M. Fazlali, M. A. Bahmani & T. Thiringer. “Performance and loss evaluation of a hard and soft switched 2.4 MW, 4 kV to 6 kV isolated DC-DC converter for a wind energy application”. *38th Annual Conference on IEEE Industrial Electronics Society (IECON)* (2012), pp. 5086–5091.

[61] M. Mobarrez, M. F. *Design, simulation and evaluation of two different topologies for the 2.4 MW 4/6 kV DC-DC fullbridge converter*. Chalmers University of Technology, 2012.

[62] M. A. Bahmani, K. Vechalapu, M. Mobarrez & S. Bhattacharya. "Flexible HF distribution transformers for inter-connection between MVAC and LVDC connected to DC microgrids: Main challenges". *IEEE Second International Conference on DC Microgrids (ICDCM)* (2017), pp. 53–60.

[63] X. Cao, J. Chen, Y. Xiao & Y. Sun. "Building-Environment Control With Wireless Sensor and Actuator Networks: Centralized Versus Distributed". *IEEE Trans. on Industrial Electronics* **57** (2010), pp. 3596–3605.

[64] S. K. Mazumder, M. Tahir & K. Acharya. "Master-Slave Current-Sharing Control of a Parallel DCâĂŞDC Converter System Over an RF Communication Interface". *IEEE Trans. on Industrial Electronics* **55** (2008), pp. 59–66.

[65] S. Anand, B. G. Fernandes & J. M. Guerrero. "Distributed Control to Ensure Proportional Load Sharing and Improve Voltage Regulation in Low-Voltage DC Microgrids". *IEEE Trans. on Power Electronics* **53** (2013), pp. 1900–1913.

[66] J. Schonberger, R. Duke & S. D. Round. "DC-bus signaling: A distributed control strategy for a hybrid renewable nanogrid". *IEEE Trans. on Industrial Electronics* **53** (2006), pp. 1453–1460.

[67] S. Backhaus & G. W. Swift. "DOE DC Microgrid Scoping Study-Opportunities and Challenges," *DC Microgrids (ICDCM), 2015 IEEE First Int. Conf.* (2015), pp. 43–44.

[68] S. Ravula. "Benefits of Using Direct Current Based Power Distribution Architectures for Commercial Buildings for Improved Utilization of On-Site Renewable Energy". *PITT EPIC Conference* (2015).

[69] Advanced Energy Industried, Inc. *Choosing 600 or 1000 VDC in Photovoltaics Projects*. 2014. URL: {http://solarenergy.advanced-energy.com/upload/File/Application%20Notes/ENG-600vor1000V-260-02.pdf}.

[70] Jim Morgenson. "The Commercial Promiseof 1000 VDC PV Design". *SMA America, LLC* ().

[71] K. Vechalapu, S. Hazra, U. Raheja, A. Negi & S. Bhattacharya. "High-speed medium voltage (MV) drive applications enabled by series connection of 1.7 kV SiC MOSFET devices". *Energy Conversion Congress and Exposition (ECCE), IEEE* (2017), pp. 808–815.

[72] M. Mobarrez, S. Bhattacharya & D. Fregosi. “Implementation of distributed power balancing strategy with a layer of supervision in a low-voltage DC microgrid”. *Applied Power Electronics Conference and Exposition (APEC)* (2017), pp. 1248–1254.

[73] C. Jin, P. Wang, J. Xiao, Y. Tang & F. H. Choo. “Implementation of Hierarchical Control in DC Microgrids”. *IEEE Transactions on Industrial Electronics* **61** (2014), pp. 4032–4042.

[74] M. Mobarrez, D. Fregosi, Gh. Jalali, S. Bhattacharya, & M.A. Bahmani. “A novel control method for preventing the PV and load fluctuations in a DC microgrid from transferring to the AC power grid”. *IEEE Second International Conference on DC Microgrids (ICDCM)* (2017), pp. 352–359.

[75] A. Hoke, R. B. J. Hambrick & B. Kroposki. “Maximum Photovoltaic Penetration Levels on Typical Distribution Feeders” (2010).

[76] S. Parhizi, H. Lotfi, A. Khodaei & SH. Bahramirad. “State of the Art in Research on Microgrids: A Review”. *IEEE Access* **3** (2015), pp. 890–925.

[77] M. T. A. Khan, A. A. Milani, A. Chakrabortty, & I. Husain. “Comprehensive dynamic modeling of a solid-state transformer based power distribution system”. *Energy Conversion Congress and Exposition (ECCE), Milwaukee* (2016).

[78] A. A. Milani, M. T. A. Khan, A. Chakrabortty, & I. Husaini. “Equilibrium Point Analysis and Power Sharing Methods for Distribution Systems Driven by Solid-State Transformers”. *IEEE Transactions on Power Systems* (2017).

[79] A. Singh, A. A. Milani, & B. Mirfazl. “Voltage regulation in single-stage boost inverter for stand-alone applications”. *Applied Power Electronics Conference and Exposition (APEC)* (2014), pp. 3011–3016.

[80] A. Singh, A. A. Milani, & B. Mirfazl. “Modified phasor pulse width modulation method for three-phase single-stage boost inverter”. *Applied Power Electronics Conference and Exposition (APEC)* (2014), pp. 1276–1280.

[81] M. T. A. Khan, A. A. Milani, A. Chakrabortty, & I. Husain. “Dynamic Modeling and Feasibility Analysis of a Solid-state Transformer Based Power Distribution System”. *IEEE Transactions on Industry Applications* **PP** (2017).

[82] R. W. Erickson, D. Maksimovic. “Fundamentals of Power Electronics”. *MA, Norwell:Kluwer* (2001).

[83] ABB Technical Application Papers. *ABB circuit-breakers for direct current applications*. 2007. URL: {http://www04.abb.com/global/seitp/seitp202.nsf/0/6b16aa3f34983211c125761f004fd7f9/$file/vol.5.pdf}.

[84] M. Mobarrez, M. G. Kashani, S. Bhattacharya & R. Adapa. “Comparative study of DC circuit breakers using realtime simulations”. *40th Annual Conference on IEEE Industrial Electronics Society (IECON)* (2014), pp. 3736–3742.

[85] M. Mobarrez, M. G. Kashani & S. Bhattacharya. “A Novel Control Approach for Protection of Multiterminal VSC-Based HVDC Transmission System Against DC Faults”. *IEEE Transactions on Industry Applications* **52** (2016), pp. 4108–4116.

[86] M. Mobarrez, D. Fregosi, S. Bhattacharya & M. A. Bahmani. “Grounding architectures for enabling ground fault ride-through capability in DC microgrids”. *IEEE Second International Conference on DC Microgrids (ICDCM)* (2017), pp. 81–87.

[87] W. Holaus & K. Frohlich. “Ultra-fast switches-A new element for medium voltage fault current limiting switchgear”. *IEEE Power Eng. Soc. Winter Meeting* (2002), pp. 299–304.

[88] M. Steurer, K. Frohlich, W. Holaus & K. Kaltenegger. “A novel hybrid current-limiting circuit breaker for medium voltage: principle and test results”. *IEEE Trans. Power Del.* **18** (2003), pp. 460–467.

[89] JM Meyer & A. Rufer. “A DC hybrid circuit breaker with ultra-fast contact opening and Integrated Gate-Commutated Thyristors (IGCTs)”. *IEEE Trans on Power Del* **21** (2006), pp. 646–651.

[90] C. Peng, I. Husain & A. Huang. “Evaluation of Design Variables in Thompson Coil based Operating Mechanisms for Ultra-Fast Opening in Hybrid AC and DC Circuit Breakers”. *Applied Power Electronics Conference and Exposition* (2014).

[91] C. Peng, I. Husain, A. Huang, B. Lequesne, & R. Briggs. “A fast mechanical switch for medium voltage hybrid DC and AC circuit breakers”. *IEEE Energy Convers. Congr. Expo., Montreal, QC, Canada* (2015).

[92] C. Meyer, M. Kowal, & R. W. De Doncker. “Circuit breaker concepts for future high-power DC-applications”. *Proc. 40th Conf. Rec. IEEE IAS Annu. Meeting, Hong Kong* (2005), 860âĂŞ866.

[93] R.F. Ammerman, T. Gammon, P.K. Sen & J.P. Nelson. “DC arc models and incident energy calculations”. *IEEE Trans. on Industry Applications* **46** (2010), pp. 1810–1819.

[94] Fabian M. Uriarte, A. L. Gattozzi, John D. Herbst, Hunter B. Estes, Thomas J. Hotz, Alexis Kwasinski, & Robert E. Hebner. “A DC Arc Model for Series Faults in Low Voltage Microgrids”. *IEEE Trans. on Smart Grids* **3** (2012), pp. 2063–2070.

[95] J. Andrea et al. “A new DC and AC arc fault electrical model”. *56th IEEE Holm Conf. Electr. Contacts, Charleston, SC* (2010), pp. 1–6.

[96] W. B. Nottinghahm. “Normal arc characteristic curves: Dependence on absolute temperature of anode”. *Phys. Rev* **28** (1926), pp. 764–768.

[97] A. D. Stokes & W. T. Oppenlander. “Electric arc in open air,” *J. Phys. D, Appl. Phys.* **24** (1991), pp. 26–35.

[98] S. Tokuyama & H. Sugawara. “4,216,513”. *US Patent* (1980).

[99] N. Yousefpoor, S. Kim & S. Bhattacharya. “Control of voltage source converter based multi-terminal DC grid under DC fault operating condition”. *Energy Conversion Congress and Exposition (ECCE)* (2014).

[100] M. Alharbi, M. Mobarrez & S. Bhattacharya. “Control and performance analysis methodology for scale-up of MMC submodules for back-to-back HVDC applications”. *Applied Power Electronics Conference and Exposition (APEC)* (2017), pp. 440–447.

[101] M. G. Kashani, Y. Cho & S. Bhattacharya. “Design consideration of volt-var controllers in distribution systems with multiple pv inverters”. *IEEE Energy Conversion Congress and Exposition (ECCE)* (2016).

[102] M. G. Kashani, M. Mobarrez & S. Bhattacharya. “Smart inverter volt-watt control design in high PV penetrated distribution systems”. *IEEE Energy Conversion Congress and Exposition (ECCE)* (2017), pp. 4447–4452.

[103] M. G. Kashani, S. Bhattacharya, J. Matamoros, D. Kaiser, & M. Cespedes. “Autonomous inverter voltage regulation in a low voltage distribution network”. *IEEE Transactions on Smart Grid* **PP** (2017).